

# Spectroscopic investigation of phytochromes and NIR fluorescent variants

vorgelegt von

MSc.

David Buhrke

von der Fakultät II-Mathematik und Naturwissenschaften

der Technischen Universität Berlin

zur Erlangung des akademischen Grades

Doktor der Naturwissenschaften

-Dr. rer. nat.-

genehmigte Dissertation

Promotionsausschuss:

Vorsitzender: Prof. Dr. Matthias Drieß

Gutachter: Prof. Dr. Peter Hildebrandt

Gutachter: Prof. Dr. Franz Bartl

Gutachter: Prof. Dr. Thomas Friedrich

Tag der wissenschaftlichen Aussprache: 13.03.2019

Berlin 2019

Love hides in molecular structure.  
- Jim Morrison, the Doors

---

## Publications

### Publications included in this thesis:

- D. Buhrke, F. Velázquez Escobar, L. Sauthof, S. Wilkening, N. Herder, N. N. Tavraz, M. Willoweit, A. Keidel, T. Utesch, M. Mroginski, F. Schmitt, P. Hildebrandt, and T. Friedrich. *The role of local and remote amino acid substitutions for optimizing fluorescence in bacteriophytochromes : A case study on iRFP*. in: *Scientific Reports* **6**.Article number: 28444 (2016). DOI: 10.1038/srep28444
- D. Buhrke, U. Kuhlmann, N. Michael, and P. Hildebrandt. *The Photoconversion of Phytochrome Includes an Unproductive Shunt Reaction Pathway*. In: *ChemPhysChem* **Volume 19**.Issue 5 (2018). DOI: 10.1002/cphc.201701311
- D. Buhrke, N. Tavraz, D. Shcherbakova, L. Sauthof, M. Moldenhauer, F. Velázquez Escobar, V. Verkhusha, P. Hildebrandt, and T. Friedrich. *Chromophore binding to two cysteines increases quantum yield of near-infrared fluorescent proteins*. In: *Scientific Reports* **9**.Article number: 1866 (2019). DOI: 10.1038/s41598-018-38433-2
- F. Velázquez Escobar, D. Buhrke, M. Fernández López, S. M. Shenkutie, S. von Horsten, L. O. Essen, J. Hughes, and P. Hildebrandt. *Structural communication between the chromophore-binding pocket and the N-terminal extension in plant phytochrome phyB*. in: *FEBS Letters* **Volume 591**.Issue 9 (2017), pp. 1258–1265. DOI: 10.1002/1873-3468.12642

### Related publications:

- F. Velázquez Escobar, D. Buhrke, N. Michael, L. Sauthof, S. Wilkening, N. N. Tavraz, J. Salewski, N. Frankenberg-Dinkel, M.-A. Mroginski, P. Scheerer, T. Friedrich, F. Siebert, and P. Hildebrandt. *Common Structural Elements in the Chromophore Binding Pocket of the Pfr State of Bathy Phytochromes*. In: *Photochem. Photobiol.* **93**.3 (2017), pp. 724–732. DOI: 10.1111/php.12742
- A. Schmidt, L. Sauthof, M. Szczepek, M. Fernández López, F. Velázquez Escobar, B. M. Qureshi, N. Michael, D. Buhrke, T. Stevens, D. Kwiatkowski, D. von Stetten, M. Mroginski, N. Krauss, T. Lamparter, P. Hildebrandt, and P. Scheerer. *Structural snapshot of a bacterial phytochrome in its functional intermediate state*. In: *Nat. Commun.* **9**.4912 (2018), pp. 1–13. DOI: 10.1038/s41467-018-07392-7

### Other publications:

- M. Moldenhauer, N. N. Sluchanko, N. N. Tavraz, C. Junghans, D. Buhrke, M. Willoweit, L. Chiappisi, F.-J. Schmitt, V. Vukojevic, E. A. Shirshin, V. Y. Ponomarev, V. Z. Paschenko, M. Gradzielski, E. G. Maksimov, and T. Friedrich. *Interaction of the signaling state analog and the apoprotein form of the orange carotenoid protein with the fluorescence recovery protein*. In: *Photosynth. Res.* (2017), pp. 1–15. DOI: 10.1007/s11120-017-0346-2
- M. Moldenhauer, N. N. Sluchanko, D. Buhrke, D. V. Zlenko, N. N. Tavraz, F.-J. Schmitt, P. Hildebrandt, E. G. Maksimov, and T. Friedrich. *Assembly of photoactive orange carotenoid protein from its domains unravels a carotenoid shuttle mechanism*. In: *Photosynth. Res.* (2017), pp. 1–15. DOI: 10.1007/s11120-017-0353-3

---

## Zusammenfassung

In dieser Arbeit wurden schwingungsspektroskopische Methoden (Resonanz-Raman [RR] und Infrarotabsorption [IR]) für die Untersuchung von Phytochromen verwendet. Phytochrome sind bi-stabile Photorezeptorproteine, die Biline (BV, PCB, PΦB) als Chromophore binden. Diverse pflanzliche, cyanobakterielle und bakterielle Varianten regulieren biologische Prozesse durch das lichtabhängige Schalten zwischen metastabilen Zuständen, die rotes und fern-rotes Licht absorbieren (Pr und Pfr). Ziel der Arbeit war die Aufklärung der Mechanismen photoinduzierter Prozesse in unterschiedlichen Phytochromen.

Im ersten Teil der Arbeit wurden pflanzliche Phytochrome untersucht. Wie auch in vielen (cyano-)bakteriellen Varianten sind die Pr- und Pfr-Zustände pflanzlicher Phytochrome nicht homogen, sondern liegen jeweils als Konformationsgleichgewichte von Unterzuständen (I,II) vor. Wie in dieser Arbeit gezeigt wurde, wird bei pflanzlichen Phytochromen die Verteilung zwischen Pfr-I und Pfr-II u.a. durch die N-terminale Verlängerung und die Bindung von PIF-Proteinen (Phytochrom-Interaktions-Faktoren) beeinflusst, was wiederum die Lebensdauer des Pfr-Zustands moduliert. Desweiteren wurden die Photosensorkonstrukte mit und ohne PHY-Domäne (PAS-GAF-PHY [PGP] und PAS-GAF [PG]) in Lösung und im kristallinen Zustand analysiert. Während die jeweiligen Pr-Zustände unveränderte Chromophorstrukturen aufweisen, nimmt PCB im Photoprodukt der verkürzten PG-Variante eine Konfiguration an, die dem Meta-Rc Zustand ähnelt.

Die Untersuchungen an cyanobakteriellen Phytochromen im zweiten Teil der Arbeit konzentrieren sich auf das PCB-bindende Cyanobacteriochrom (CBCR) Slr-GAF3, welches nach Photoaktivierung ausgehend von Pr in einen metastabilen grün absorbierenden (Pg) Zustand konvertiert. Die ungewöhnlichen grünen Absorptionseigenschaften wurden an Hand von vier verschiedenen Modellen analysiert, die für den Pg-Zustand vorgeschlagen wurden. Eine plausible Erklärung für die hypsochrome Verschiebung der Absorptionsbanden ist eine verdrehte Konfiguration der Pyrrolringe A und D in Kombination mit einer hydratisierten Chromophorbindungstasche. Bei tiefen Temperaturen wandelt sich Slr-GAF3 in einen orange-absorbierenden (Po) Zustand um. Verschiedene mögliche Mechanismen dieser Umwandlung wurden diskutiert.

Die Arbeiten an bakteriellen Phytochromen (Bphs) im dritten Teil der Dissertation behandeln zum einen die Entschlüsselung der thermischen Reaktionsmechanismen des Photozyklus. Dazu wurde ein Aufbau für zeitaufgelöste Messungen entwickelt, der ein Durchflusssystem mit einem kommerziellen FT-Raman-Spektrometer kombiniert. Besonderheiten des Aufbaus sind die kontinuierliche Anregung in Kombination mit einem präresonanten NIR-Messlaser und der photochemischen Rückkonvertierung der Probe in einem Reservoir. Diese ist notwendig, um den dunkeladaptierten Zustand als Startpunkt für repetitive Experimente sicherzustellen. Mithilfe dieser Technik konnte gezeigt werden, dass der Zerfall der Meta-Zustände der Bphs Agp1 und Agp2 nicht ausschließlich zur Bildung des aktiven Zustands, sondern auch in einer unproduktiven Verzweigungsreaktion zurück zum jeweiligen dunkeladaptierten Zustand führt. Bei den Untersuchungen an der Phytochrom-aktivierten di-Guanylyl-Zyklase IsPadC lassen die IR Spektren auf eine reduzierte Strukturänderung der PHY-Domäne schließen, welche essentiell für die Bildung des aktivierten (Pfr) Zustands ist. Diese Ergebnisse bestätigen ein Meta/Pfr-Heterodimer-Modell, das auf der Grundlage zeitaufgelöster UV/Vis-Daten entwickelt wurde.

Im vierten Teil der Arbeit wurde untersucht, welche strukturellen Faktoren das



---

Verhältnis der verschiedenen Zerfallsprozesse des elektronisch angeregten Zustands ( $\text{Pr}^*$ ) beeinflussen, um das rationale Design NIR-fluoreszierender Bphs (iRFPs) zu ermöglichen. Der Pr-Zustand von Bphs umfasst eine Mischung von fluoreszierenden (Pr-I) und nicht-fluoreszierenden (Pr-II) Unterzuständen, die durch RR Spektroskopie unterschieden werden können. Die Erzeugung stark fluoreszenter Varianten für die Fluoreszenzmikroskopie erfordert daher die Verschiebung der Konformationsverteilung in Richtung Pr-I, wie für iRFP713 gezeigt wurde. Das Konformationsgleichgewicht wird durch die Substitution von Aminosäuren sowohl in der direkten Umgebung des Chromophors als auch an entfernten Positionen beeinflusst. Einige iRFP-Varianten mit sehr hohen Fluoreszenzquantenausbeuten (FQY) enthalten ein zweites Cystein in der GAF-Domäne, welches ebenfalls eine Thioetherbindung zu BV ausbilden kann. Hierbei liegen ca. 50% des gesamten Proteinensembles mit zweifach gebundenem BV vor. In dieser Arbeit wurde anhand von iRFP682 gezeigt, dass die resultierende interne Querverbindung zu einer starken Erhöhung der FQY (16,6%) führt. Mithilfe von RR-Spektroskopie konnte gezeigt werden, dass der Fluoreszenzgewinn, analog zu iRFP713, auf eine Gleichgewichtsverschiebung zu Pr-I zurückzuführen ist.

---

## Abstract

In this work, vibrational spectroscopic methods (resonance Raman [RR] and infrared absorption [IR]) were used for the investigation of phytochromes. Phytochromes are bistable photoreceptor proteins that bind bilins (BV, PCB, P $\Phi$ B) as chromophores. Various plant, cyanobacterial, and bacterial variants regulate biological processes through the light-dependent switching between metastable states that absorb red and far-red light (Pr and Pfr). The aim of the work was the elucidation of the mechanisms of photoinduced processes in different phytochromes.

In the first part of the work, plant phytochromes were investigated. As in many (cyano-)bacterial variants, the Pr and Pfr states of plant phytochromes are not homogeneous, but instead exist as conformational equilibria of sub-states (I, II). As shown in this work, the distribution between Pfr-I and Pfr-II in plant phytochromes is affected i.a. by the N-terminal extension and binding of PIF proteins (phytochrome interaction factors), which in turn modulates the lifetime of the Pfr state. Furthermore, the photosensor constructs with and without the PHY domain (PAS-GAF-PHY [PGP], PAS-GAF [PG]) were analyzed in solution and in the crystalline state. While the respective Pr states have unaltered chromophore structures, PCB adopts a configuration similar to the Meta-Rc state in the photoproduct of the truncated PG variant.

The investigations on cyanobacterial phytochromes in the second part of the work focused on the PCB-binding cyanobacteriochrome (CBCR) Slr-GAF3, which converts to a metastable green-absorbing (Pg) state after photoactivation of Pr. The unusual green absorption properties were analyzed on the basis of four different models proposed for the Pg state. A plausible explanation for the hypsochromic shift of the absorption bands is a twisted configuration of the pyrrole rings A and D in combination with a hydrated chromophore binding pocket. At low temperatures, Slr-GAF3 converts to an orange-absorbing (Po) state. Various possible mechanisms of this transformation were discussed.

The work on bacterial phytochromes (Bphs) in the third part of the dissertation comprises the decoding of thermal reaction mechanisms in the photocycle. For this purpose, a setup for time-resolved measurements was developed, which combines a flow-through system with a commercial FT-Raman spectrometer. Special features of the design are the continuous excitation in combination with a pre-resonant NIR measuring laser and the photochemical back-conversion of the sample in a reservoir. This is necessary to ensure that the dark-adapted state is the starting point for repetitive experiments. Using this technique, it was shown that the decay of the meta-states of the Bphs Agp1 and Agp2 not only leads to the formation of the active state, but also in an unproductive thermal shunt reaction back to the respective dark-adapted state. In the studies on the phytochrome-activated di-guanylyl cyclase IsPadC, the IR spectra suggest a reduced structural change of the PHY domain, which is essential for the formation of the activated (Pfr) state. These results confirm a Meta/Pfr heterodimer model, which was developed on the basis of time-resolved UV/vis data.

In the fourth part of the thesis, the structural factors that influence the ratio of the different decay processes of the electronically excited state (Pr\*) were investigated in order to allow the rational design of NIR-fluorescent Bphs (iRFPs). The Pr state of Bphs comprises a mixture of fluorescent (Pr-I) and non-fluorescent (Pr-II) substates that can be distinguished by RR spectroscopy. Therefore, the generation of highly fluorescent variants for fluorescence microscopy requires the shift of the conformational distribution towards Pr-I, as shown for iRFP713. The conformational equilibrium

---

is affected by the substitution of amino acids both in the direct environment of the chromophore and at remote positions. Some iRFP variants with very high fluorescence quantum yields (FQY) contain a second cysteine in the GAF domain, which can also form a thioether bond to BV. Here, about 50% of the total protein ensemble contains the double-bound BV. It was shown in this work that the resulting internal cross-linking leads to a strong increase of FQY (16.6%) in iRFP682. RR spectroscopy indicates that the fluorescence gain, analogous to iRFP713, is due to an equilibrium shift towards Pr-I.

---

## Abbreviations

aa	amino acid
<i>ABS</i>	IR absorbance spectrum
Agp	<i>Agrobacterium fabrum</i> phytochrome
AnPixJ	CBCR from <i>Anabaena</i> sp. PCC7120
Arg	arginine
As	<i>Avena sativa</i>
At	<i>Arabidopsis thaliana</i>
Bph	bacteriophytochrome
BV	biliverdin IX $\alpha$
CBCR	cyanobacteriochrome
CC	coiled coil
CCD	charge-coupled device
c-di-GMP	cyclic-di-guanosine monophosphate
Cph	cyanobacterial phytochrome
cw	continous-wave
Cys	cysteine
Dr	<i>Deinococcus radiodurans</i>
<i>E. coli</i>	<i>Escherichia coli</i>
DXCF	sub-class of CBCRs with conserved Asp-X-Cys-Phe motif
EPR	electron paramagnetic resonance
FQY	fluorescence quantum yield
fs	femtosecond
FSRS	femtosecond stimulated Raman spectroscopy
FT	Fourier-transform
FTIR	Fourier-transform infrared absorption
FTR	Fourier-transform Raman
GAF	c-GMP-specific phosphodiesterases, adenylate cyclases, formate hy- drogen lyase transcription activator
GFP	green fluorescent protein from <i>Aequorea victoria</i>
GGDEF	conserved amino acid motif in the di-guanylyl cyclase domain
GTP	guanosine-5'-triphosphate
HDX-MS	hydrogen-deuterium exchange coupled to mass spectrometry
HeNe	helium neon
His	histidine
HK(RD)	histidine kinase (related domain)
HOOP	hydrogen-out-of-plane (bending mode)
i.p.	in-plane (bending mode)
IR	infrared
iRFP	infrared flourescent protein
IsPadC	<i>Idiomarina</i> sp.A28L phytochrome-activated di-guanylyl cyclase
kDa	kilodalton
laser	light amplification through stimulated emission of radiation
LED	light emitting diode
LH	light harvesting complex
mg	milligram
MIR	mid-infrared
mm	millimeter
MO	molecular orbital
MST	microscale thermophoresis
$\mu$ s	microsecond
$\mu$ m	micrometer
Nd:YAG	neodymium-doped yttrium aluminium garnet

---

NIR	near-infrared
nm	nanometer
NMA	normal mode analysis
ns	nanosecond
NTE	N-terminal extension
OCP	orange carotenoid protein
OD	optical density
Pa	<i>Pseudomonas aeruginosa</i>
PAiRFP	photo-activatable iRFP
PALM	photoactivated localisation microscopy
PAS	PER/ARNT/SIM protein domain
PCB	phycocyanobilin
PΦB	phytochromobilin
PDB	protein data bank
PG	PAS-GAF
Pg	green-absorbing parent state of CBCRs
PGP	PAS-GAF-PHY
Phe	phenylalanine
PHY	phytochrome specific domain
PhyA-E	plant phytochrome A-E
PhyPIF	adduct of PIF3 and AtPhyB
PIF	phytochrome interaction factor
PMMA	polymethylmethacrylate
Pr (Pfr)	red-absorbing (far-red-absorbing) parent state of phytochromes
Pr* (Pfr*)	electronically excited state of Pr (Pfr)
ps	picosecond
PSM	photosensory module
PVB	phycoviolobilin
QCL	quantum cascade laser
QED	quantum electrodynamics
QM	quantum mechanics
RcaE	CBCR from <i>Fremyella</i>
Rec	CheY-homologous response regulator domain
Reg1(Reg2)	proteins derived from IsPadC
Rp	<i>Rhodopseudomonas palustris</i>
RR	resonance Raman
s	second
S/N	signal-to-noise (ratio)
SAXS	small-angle x-ray scattering
Sb	<i>Sorghum bicolor</i>
SEC	size-exclusion chromatography
Ser	serine
SERDS	shifted-excitation Raman difference spectroscopy
Slr1393	CBCR from <i>Synechocystis</i> sp. PCC6803
Slr-GAF3	third GAF domain of Slr1393
smURFP	small ultra red fluorescent protein
STED	stimulated-emission-depletion
STORM	stochastic optical reconstruction microscopy
Thr	threonine
Tyr	tyrosine
UV	ultraviolet
Vis	visible
Xc	<i>Xanthomonas campestris</i>
Z/E(s/a)	<i>Zusammen/Entgegen</i> ( <i>syn/anti</i> )

---

## Nomenclature

Generally, **bold** symbols refer to matrices or vectors,  $\langle bra|ket \rangle$  notation is used for wave functions, and operators are indicated by circumflexes ( $\hat{o}$ ).

$\mathbf{1}$	identity matrix
$A_i$	Cartesian displacement amplitude of atom $i$
$A, B$	Albrecht terms
$B(\nu)$	spectral decomposition of a signal
$\mathbf{A}$	Cartesian displacement amplitude vector
$[\alpha]_{fi}$	transition moment
$\alpha$	polarizability tensor
$D_e$	depth of a potential minimum
$\delta_{ij}$	Kronecker delta
$E$	energy
$\mathbf{E}$	incident electric field
$\epsilon$	molecular extinction coefficient
$ e\rangle,  g\rangle$	electronic wave functions
$f$	force constant
$ f\rangle,  i\rangle,  r\rangle$	vibronic wave functions
$f^m$	mass-weighted force constant
$\mathbf{f}$	Hessian force constant matrix
$\mathbf{f}^m$	mass-weighted Hessian force constant matrix
$\Gamma_r$	damping rate
$h$	Planck constant
$\hbar$	reduced Planck constant
$\Delta H^0$	reaction enthalpy
$I$	intensity of light
$i, j, n$	running numbers for atoms
$k$	running number for normal modes or normal coordinates
$K_D$	equilibrium constant
$l_0$	photochemical conversion rate
$\lambda_k$	eigenvalue of $\mathbf{f}^m$
$\lambda$	wavelength
$\mu$	reduced mass
$\hat{\mu}_q$	electric dipole moment operator
$\mu_{ind}$	induced dipole moment
$m$	atomic or molecular mass
$M$	electronic transition dipole moment
$\mathbf{m}$	atomic mass matrix
$\mathbf{M}$	transition moment
$N$	number of atoms in a molecule/ interferogram points
$n_\nu$	vibrational quantum number
$\nu$	frequency
$ \nu\rangle$	vibrational wave function
$\hat{\Omega}$	interaction operator
$P_{fi}$	transition probability
$P$	laser power
$\Psi$	wave function
$\psi$	phase angle
$q$	mass-weighted Cartesian displacement coordinate
$Q$	normal coordinate
$\mathbf{q}$	mass-weighted Cartesian displacement vector
$r$	radius

---

$R$	universal gas constant
$\rho_f$	density of final states
$\rho, \sigma$	Cartesian components of $\boldsymbol{\alpha}$
$S_t$	internal coordinate
$S_n$	excited electronic state
$\Delta S^0$	reaction entropy
$\mathbf{s}_{tn}$	transformation vector for internal coordinate
$\Delta s$	spatial separation
$T$	kinetic energy
$t$	time
$V$	potential energy
$v$	velocity
$x$	Cartesian displacement coordinate
$\mathbf{x}$	Cartesian displacement vector
$x_e$	anharmonicity constant

## Contents

<b>Publications</b>	<b>3</b>
<b>Zusammenfassung</b>	<b>4</b>
<b>Abstract</b>	<b>6</b>
<b>Abbreviations</b>	<b>8</b>
<b>Nomenclature</b>	<b>10</b>
<b>1 Phytochromes</b>	<b>14</b>
1.1 Motivation . . . . .	14
1.2 Introduction . . . . .	16
1.3 Plant Phytochromes . . . . .	18
1.4 Cyanobacterial Phytochromes . . . . .	25
1.5 Bacterial Phytochromes . . . . .	28
1.6 Biotechnological Applications of Phytochromes . . . . .	30
<b>2 Theoretical Background: Vibrational Spectroscopy</b>	<b>34</b>
2.1 Frequencies of Molecular Vibrations . . . . .	34
2.2 Intensities and Selection Rules . . . . .	39
2.3 Raman Intensities . . . . .	41
2.4 The Resonance Raman Effect . . . . .	42
2.5 Fourier-Transform Spectroscopy . . . . .	44
2.6 Time-Resolved Vibrational Spectroscopy . . . . .	46
2.7 Application of Vibrational Spectroscopy to Phytochrome Samples . . . . .	48
<b>3 Materials and Methods</b>	<b>52</b>
3.1 Phytochrome Samples . . . . .	52
3.2 IRFP Samples . . . . .	54
3.3 Sample Handling . . . . .	55
3.4 UV/Vis and Fluorescence Spectroscopy . . . . .	57
3.5 FT-Raman Setup . . . . .	57
3.6 FT-IR Setup . . . . .	59
3.7 Figure Notation . . . . .	60
<b>4 Results: Plant Phytochromes</b>	<b>61</b>
4.1 Structural Communication of Plant PhyB with the N-terminal Extension	62
4.2 Interaction of <i>Arabidopsis thaliana</i> Phytochrome B with the Phytochrome Interaction Factor 3 . . . . .	71
4.3 The PAS-GAS Construct of <i>Sorghum bicolor</i> Phytochrome B . . . . .	79
<b>5 Results: Cyanobacterial Phytochromes</b>	<b>92</b>
5.1 The Cyanobacteriochrome Slr-GAF3 . . . . .	92



---

<b>6</b>	<b>Results: Bacterial Phytochromes</b>	<b>101</b>
6.1	Time-Resolved FT-Raman Spectroscopy of Bacteriophytochromes Agp1 and Agp2 . . . . .	102
6.2	The Phytochrome-Activated di-Guanylyl Cyclase from <i>Idiomarina</i> . . .	108
<b>7</b>	<b>Results: Infrared Fluorescent Proteins Derived from Phytochromes (iRFPs)</b>	<b>117</b>
7.1	Mutagenesis Study on iRFP713 . . . . .	118
7.2	Attachment of the Biliverdin Cofactor to two Cysteine Residues . . . .	131
<b>8</b>	<b>Conclusions</b>	<b>140</b>
<b>9</b>	<b>Supplementary Data</b>	<b>145</b>
9.1	Supplements: Plant Phytochromes . . . . .	145
9.2	Supplements: Cyanobacterial Phytochromes . . . . .	150
9.3	Supplements: Bacteriophytochromes . . . . .	158
9.4	Supplements: IsPadC . . . . .	168
9.5	Supplements: IRFPs . . . . .	175
	<b>List of Figures</b>	<b>198</b>
	<b>List of Tables</b>	<b>200</b>
	<b>Bibliography</b>	<b>201</b>

# 1 Phytochromes

## 1.1 Motivation

The ability to sense light is an evolutionary advantage for organisms in most ecosystems. It provides the basis for a broad variety of adaptative responses in competitive environments, such as the efficient regulation of photosynthesis, protection from irradiation damage, or even vision. Therefore, different highly specialized photoreceptor proteins can be found in organisms across all domains of life. All sensory photoreceptors convert information about the physical properties of incident light (intensity and energy) into biochemical signals (e.g. production of second messenger molecules, ion-gradients across a membrane or phosphorylation of response regulators). The resulting biochemical signal is further processed on a cellular level to trigger a response in the respective organism. Thus, the investigation of light-driven processes on a molecular level contributes to our ability to understand and eventually modify how life senses and reacts to changes in environmental light conditions.

The biophysical studies in this thesis aimed to investigate the light-driven reactions in phytochromes, which are a class of biological photoreceptors utilized by plants[29], cyanobacteria[106], bacteria[86] and fungi.[49] In phytochromes, light is absorbed by a linear open-chain tetrapyrrole (bilin) cofactor embedded in a photosensory protein domain.[105] After absorption of a photon, bilin photoisomerization[249] starts a cascade of ground-state intramolecular rearrangements that ultimately lead to the activation of a catalytic output module and biochemical signaling.[162] In this thesis, vibrational spectroscopy techniques (resonance Raman (RR) and infrared (IR) spectroscopy) were employed, because these structure-sensitive methods allow for detailed investigations of the protein geometry and chemical state in different stages of the photocycle. Hence, IR and RR spectroscopy can provide crucial information about functional changes in chromophore and protein structure.[70] In combination with crystallographic, biochemical and theoretical methods, an overall picture of the structure-function relationships of phytochromes can be obtained. The central objective of this thesis is to determine key parameters that control the molecular functioning of the photoreceptor module in various representatives of the phytochrome family. In this way, the present thesis provides a contribution to the elucidation of structure-dynamics-function relationships of this class of photoreceptors.

In plants, phytochromes regulate many different processes like germination, (de-)etiolation or shade avoidance, which are desirable target phenotypes for bioengineering of crops.[107] A detailed knowledge about the factors that influence phytochrome photoconversion is therefore of high interest. Chapters 4.1 and 4.2 focus on the interaction of the P $\Phi$ B chromophore with the N-terminal extension domain and phytochrome interaction factor 3 (PIF3) and the resulting implications for phytochrome action.

While all isoforms of plant phytochrome share a bi-modal photochemistry between red- and far-red absorbing (Pr and Pfr) states, cyanobacterial variants are much more diverse in their absorption properties.[165] Here, the absorption bands can be found in a range from the (ultra)violet to the near infrared wavelengths.[170] The underlying molecular parameters that are responsible for the spectral tuning of photoreceptor chromophores are not only crucial for color-vision (in the case of retinal proteins[118]) but are also crucial for expanding the biotechnological toolkit, including phytochromes, to other wavelength regimes.[190] In this thesis, the unusual green-absorbing Pg state of a cyanobacteriochrome was investigated and discussed with emphasis on the color-

tuning mechanism (chapter 5.1).

The plant pathogen *Agrobacterium fabrum* is the causal agent of the crown gall disease in flowering plants.[108] This disease causes the growth of tumors in crops like walnuts, grapes or sugar beets and is therefore a major economical concern for the food industry. The motility and infectivity of *Agrobacterium* are regulated by two bacterial phytochromes (Bphs), Agp1 and Agp2.[150] Chapter 6.1 comprises a time-resolved Raman study of the photocycle reactions in these two systems, aiming at a deeper understanding of the photoactivation mechanism, which starts the signaling cascades that ultimately lead to plant infection.

Phytochromes also gained growing attention as tools for biotechnological applications such as optogenetics or fluorescence microscopy.[32] In optogenetic applications, a phytochrome photosensory domain is fused to a suitable catalytic output module, allowing a precise spatial and temporal control of cellular processes not only for fundamental research but also medical applications.[129] Some examples for such processes are cell morphology control[88], second messenger production[182] or kinase dimerization.[163] The recently discovered natural phytochrome-linked di-guanylyl-cyclase IsPadC from *Idiomarina* is capable of red-light activated production of c-di-GMP.[61] This second messenger molecule influences the regulation of diverse signaling pathways in a wide variety of bacteria, including biofilm formation, motility, and virulence.[61] The similarities and differences of these novel optogenetic tools to canonical phytochromes need to be understood to improve their efficiency and specificity. In chapter 6.2, IsPadC is compared to Agp1 with emphasis on the mechanism of the photoactivation reaction and the photoactivated state.

Marker-based fluorescence microscopy is an important tool for medical imaging and fundamental research, because the utilization of visible and NIR light is cheaper and less invasive than many other common techniques.[192] Fluorescence enhanced phytochromes (iRFPs) can be used as dyes that are required for fluorescence imaging.[196] Among all phytochromes, Bphs are preferential precursors because of their unique natural fluorescence in the near-infrared region and the natural abundance of the cofactor (biliverdin) in mammalian cells.[188] The quality of the images that are obtained with fluorescence methods depends crucially on the emission intensity of the dye.[97] Thus, it is desirable to artificially enhance the fluorescence quantum yield in iRFPs over the competing excited-state decay channels like photochemistry or thermal relaxation. For a rational design of highly fluorescent iRFPs, the underlying structural parameters that determine the excited-state decay mechanism must be analyzed and discussed. This thesis comprises two fundamental studies on the molecular aspects of iRFP fluorescence enhancement and color-tuning (chapters 7.1 and 7.2).

## 1.2 Introduction

The phytochrome photoreceptor was first described in 1959 as the “pigment controlling photoresponsive development of plants” in turnip seedlings (*Brassica rapa*).[29] Subsequent genetic studies revealed that higher plants *de facto* encode three different phytochrome genes (plant PhyA-C) and two additional, PhyD and PhyE, were found in the case of flowering plants and *Brassicaceae*, respectively.[187, 34, 126] According to endosymbiotic theory, photosynthetic cyanobacteria and plant chloroplasts originate from a common progenitor that performed oxygenic photosynthesis 2.75 billion years ago.[59] Hence it can readily be understood that phytochromes were not only present in the common progenitor[37, 116], but can also be found in cyanobacteria.[106, 250, 222] Anaerobic photosynthetic bacteria and marine diatoms also encode for phytochromes, indicating a general relationship between phytochrome photoreception and photosynthesis regulation.[86, 111, 48] In fact, phytochromes regulate gene expression for proteins of the photosynthetic apparatus in all these forms of life[56, 42], as well as developmental processes and phototaxis.[199] The discovery of phytochromes in non-photosynthetic organisms like eubacteria[36] and fungi was therefore rather surprising.[49, 16] Here, phytochromes regulate fundamentally different light dependent processes like phototaxis, biofilm formation[150, 101], or sexual development in the case of fungi.[16] This large variability in phenotypes together with the wide distribution over most forms of life, except for animals and archaea, enables broad phylogenetic studies and thus the development of evolutionary models for a variety of organisms.[125, 166, 91]

Despite these large variations in organization and function, all phytochromes share certain general features, defining them as a class of proteins with different sub-classes. For historical reasons, the definitions were adjusted multiple times over the years to match new discoveries and are, even today, not consistent in the literature. The following general features define phytochromes:

**Phytochromes are proteins that harbour an open chain tetrapyrrole (bilin) chromophore as a prosthetic group.**

However, phytochromes of different origin utilize chemically different chromophores. Plant phytochromes incorporate phytochromobilin (PΦB)[105], bacteria use biliverdin IX $\alpha$  (BV)[14] and cyanobacteria phycocyanobilin (PCB) (see fig. 1.2.1 for the different chemical formulae).[106]

**The chromophore binding pocket is formed by a GAF domain.**

In all phytochromes, the bilin is embedded in a specific protein environment called the chromophore binding pocket. The binding pocket is formed by a protein domain that adopts a GAF fold (cGMP-specific phosphodiesterases, adenylate cyclases, formate hydrogen lyase transcription activator).[239]

**The bilin chromophore is covalently bound to a cysteine residue by a thioether linkage.**

The chemical attachment proceeds *via* a nucleophilic addition of the cysteine thiol side chain to a chromophore double bond. The reaction does not require further maturation proteins or chaperones and is therefore termed autolyase-activity of phytochromes.[77] In some cyanobacteriochromes (CBCRs), a second cysteine attaches to other C=C bonds. This secondary thioether bridge is either permanent or can be formed and broken during the photocycle reactions.[223]

**Phytochromes adopt two distinct meta-stable states that can be interconverted by photochemical and thermal reactions.**

In plant phytochromes these states are Pr (red-absorbing parent state) and Pfr (far-red-absorbing parent state, see fig. 1.3.4 for the typical absorption spectra). In prokaryotes, other states are also observed, and always named according to their characteristic visible absorption spectra (e.g. Pg for a green-absorbing state, see chapter 5.1). A phytochrome sample in predominantly one state (X,Y) can be photochemically converted to the second state (Y,X) by absorption of a photon ( $h\nu_{X,Y}$ ) in resonance with the electronically excited state ( $X^*,Y^*$ ) (eqs. 1.1-1.2). The two states X and Y are not only photochemically interconvertible, but also in thermal equilibrium (eq. 1.3). In most cases, the thermal equilibrium is predominantly on one side, and this state is termed the “dark-adapted state” (an exception is e.g. the bacteriophytochrome (Bph) from the plant pathogen *Xanthomonas campestris*).[153] Thus, after photoactivation of the dark-adapted state, a thermal equilibration can be observed on time scales from seconds to days (the net reaction is termed “dark relaxation reaction”). The resulting photochemical and thermal equilibrium can be described by the following equations:



**The initial photoreaction is a Z/E isomerization at the C/D methine bridge.**

The Z/E photoisomerization of a C=C double bond takes place at the  $C_{15}$  and  $C_{16}$  atoms of the chromophore (see fig. 1.2.1) and is followed by thermal processes that ultimately lead to the formation of the final photoproduct. Other reaction mechanisms for the initial photoreaction were discussed in the literature[105], including isomerization at A/B methine bridge[224], but were discarded in favor of the isomerization at the C/D bridge.[203]

**Nomenclature** Like the definitions, the abbreviation nomenclature for different phytochrome variants is inconsistent due to the historical development of the literature. Usually, the first two letters refer to the initial letters of the organism name, but the abbreviation can be adjusted to avoid doubling and confusion with other popular species. An example for this exception are Agp1 and 2 from the plant pathogen *Agrobacterium fabrum*. The next letters indicate that the protein is a phytochrome, either “p” or “phy”, but also “Bph” for bacteriophytochromes is commonly used. Most organisms encode more than one phytochrome, and a last digit is used to define the isoform. In the case of plant phytochromes, letters (A-E) indicate the isoform, whereas numbers are used in procaryots. Examples for some different notations that appear in this thesis:

Agp1	=	<i>Agrobacterium fabrum</i> phytochrome 1
RpBphP2	=	<i>Rhodospseudomonas palustris</i> bacteriophytochrome 2
SbPhyB	=	<i>Sorghum bicolor</i> phytochrome B

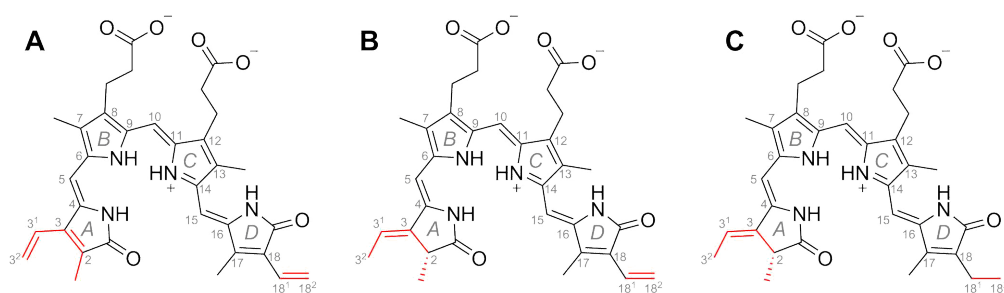


**Figure 1.2.1:** Chemical formulae of the tetrapyrrole chromophores. **A** biliverdin IX $\alpha$  (BV), **B** phytychromobilin (PΦB) and **C** phycocyanobilin (PCB). The three chromophores differ in conjugation length and saturation of the C<sub>32</sub> – C<sub>31</sub>, C<sub>3</sub> – C<sub>2</sub> and C<sub>181</sub> – C<sub>182</sub> bonds (marked in red).

### 1.3 Plant Phytochromes

After the discovery of phytochromes in *Brassica rapa*[29, 30], most subsequent pioneering work on purification and biochemical characterization was focused on rye (*Secale cereale*) and oat (*Avena sativa*) phytochromes. These early studies faced problems with proteolytic digestion in the endoprotease rich plant extracts, yielding non-functional protein fragments of variable sizes.[160] *Avena sativa* phyA (AsPhyA) was the first phytochrome to be purified intact and functional, when digestion in the oat extract could be inhibited efficiently with the use of protease inhibitors.[233, 234] Accordingly, AsPhyA was the first phytochrome to be cloned[66], sequenced[67] and overexpressed in transgenic tomatoes.[19] These fundamental developments in protein expression techniques and the resulting availability of purified protein samples facilitated numerous biochemical and biophysical studies, that lead to the state-of-the-art knowledge about phytochromes.

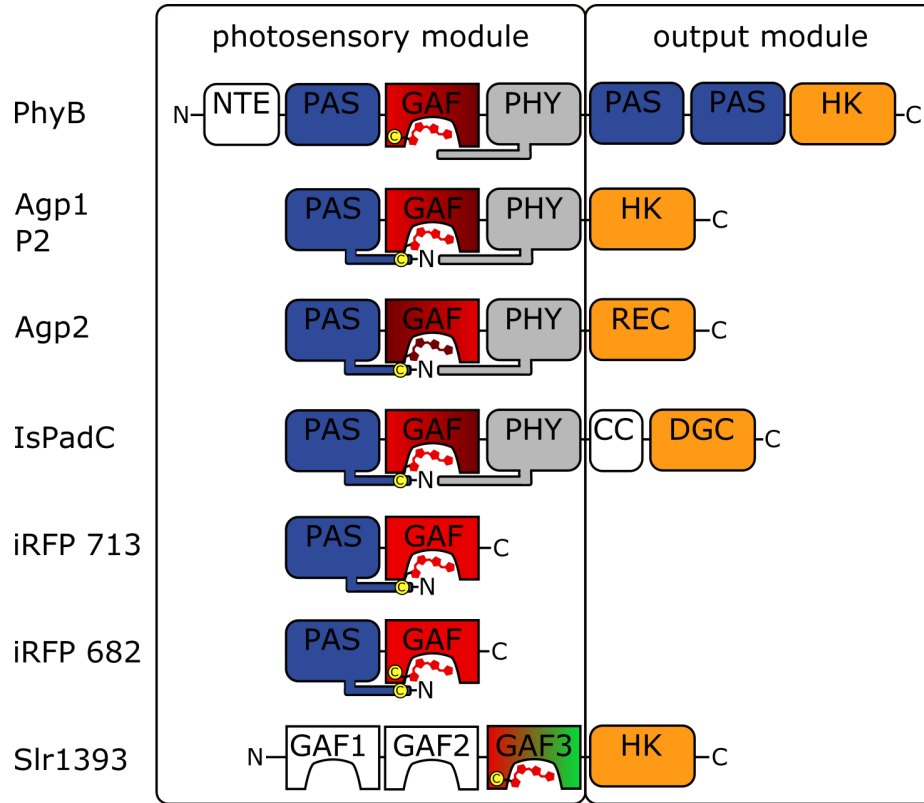


**Figure 1.3.1:** Domain structure of various natural and artificial phytochrome constructs. Functional phytochromes are structured into a photosensory module (PSM) and a catalytic output module. The chromophore (see fig. 1.2.1) binds to a GAF domain in the PSM. The type of photochemistry is indicated by the color coding of the GAF domain (e.g. red/dark red for Pr/Pfr). PAS domains are coded in blue, PHY domains in grey and catalytic output modules in orange. Non-binding GAF domains, the N-terminal extension (NTE) and the coiled-coil (CC) linker region are colored in white.

**Protein domains** All phytochromes are structured in a consecutive set of distinct protein domains that form the N-terminal photosensory module (PSM) and the C-terminal output module (see fig. 1.3.1).[79] In plant phytochromes, the PSM is composed of an N-terminal extension (NTE), followed by a PAS (PER/ARNT/SIM), a GAF and a PHY (phytochrome specific) domain.[129] All three PSM domains have a homologous fold motif composed of a central 5-stranded antiparallel  $\beta$ -sheet, a single  $\alpha$ -helix on one side and an  $\alpha$ -helical bundle on the other side and are beaded along a  $\alpha$ -helical spine (see fig. 1.3.3).[244] The PHY domain possesses a unique structural feature, called the tongue motif, which folds back to the chromophore binding pocket in the GAF domain and interacts with the chromophore. In the Pr state, the tongue adopts a  $\beta$ -sheet/ $\beta$ -hairpin fold,[26] and in Pfr the secondary structure is changed to an  $\alpha$ -helix/coil fold.[244] The output module in plant phytochromes is composed of a double-PAS motif (termed Quail module)[162] and a histidine kinase related domain (HK/HKRD).[78] Lower plants like ferns additionally encode for chimera proteins, where the phytochrome PSM is fused to the phototaxis protein phototropin. This sub-class of hybrid photoreceptor proteins is called “neochromes”.[129, 78]

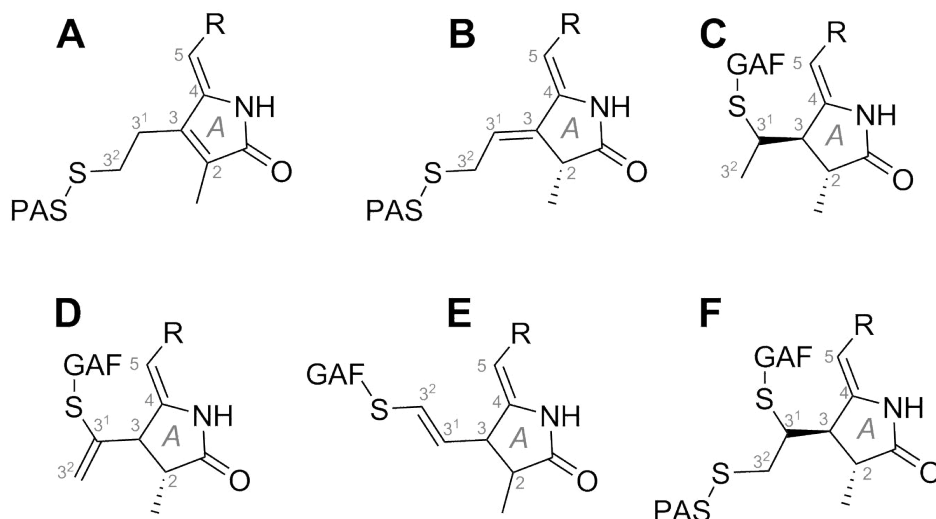


**Figure 1.3.2:** Chromophore attachment in different types of natural and artificial phytochromes. **A** and **B**: endo- and exocyclic attachment of BV in Bphs. **C**: Attachment of PCB and PΦB to the GAF domain in plant and cyanobacterial phytochromes. **D-F**: different artificial modes of attachment of BV found in infrared-fluorescent proteins (iRFPs) derived from phytochromes (see chapter 7.2 for a detailed discussion of these structures).

**Chromophores** Plant phytochromes utilize the unique tetrapyrrole phytochromobilin (PΦB) as chromophore, but the cyanobacterial cofactor phycocyanobilin (PCB) can also be assembled with the apoprotein *in vitro* (see fig. 1.2.1).[105, 77, 99] However, the chromophore is always covalently attached to a conserved cysteine (Cys) in the  $\alpha$ -helix of the GAF domain *via* a thioether linkage (see fig. 1.3.2 C).[105] In the Pr state, PΦB adopts the ZZZssa configuration.[26, 202] This nomenclature refers to the stereochemical configuration of the double (Z/E, German for *Zusammen/Entgegen*), and the single bonds (s/a Greek for *syn/anti*) at the three (A/B, B/C and C/D) methine bridges of the tetrapyrrole chromophore. In the Pfr state, the ZZE configuration was reported by NMR for AsPhyA chromopeptides[178], but the exact stereochemical configuration of the methine bridge single bonds remained a matter of debate, until x-ray crystal structures of the Pfr state were solved. Here the homologous Bph from *Pseudomonas aeruginosa* (PaBph) shows a ZZEssa configuration of BV in the Pfr state, reflecting the Pfr configuration of PΦB in plant phytochromes.[244] The long-used homology model was recently solidified for plants by NMR studies of AsPhyA.[200] Resonance Raman (RR) spectroscopy selectively probes the vibrational modes of the chromophore and thus is a powerful tool to access more detailed stereochemical information about the chromophore, always in conjunction with theoretical models.[134] The Pr and Pfr forms of AsPhyA were analyzed by RR [47] and Fourier-transform pre-resonance Raman (FTR) spectroscopy.[69] These investigations helped to refine the details of the chromophore configuration and demonstrated a double configuration within the ZZEssa geometry in Pfr. Here, PΦB adopts two spectroscopically distinguishable sub-states (Pfr-I and Pfr-II), characterized by subtle changes in the dihedral angle of the C/D methine bridge.[229] The equilibrium of Pfr-I and II and its implications are discussed in detail in chapters 4.1 and 4.2.



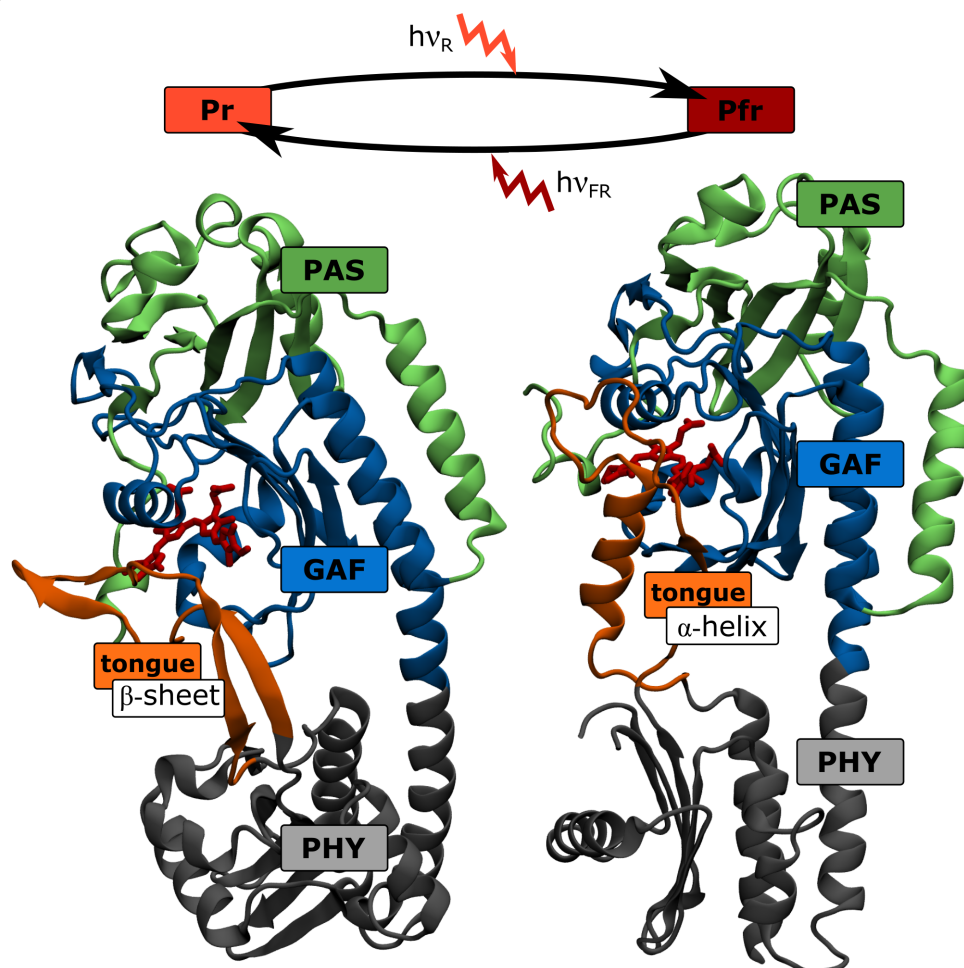


**Figure 1.3.3:** Photosensory module (PSM) crystal structures of the Pr and Pfr state of phytochromes (*Deinococcus radiodurans* bacteriophytochrome (DrBphP), protein data bank (PDB) entries 4O0P and 4O01).[217] The chromophore (red) is incorporated in the GAF domain (blue). The PAS and PHY domains are encoded in green and grey, respectively. The tongue motif is highlighted in orange to emphasize the secondary structure transition between the two parent states.

**Lumi state** Similar to other biological photoreceptors (e.g. rhodopsins[143, 121] or the orange carotenoid-binding protein (OCP)[123]), the interconversions of the Pr and Pfr parent states proceed *via* a series of intermediates (see fig. 1.3.5). The intermediates can be distinguished by different spectroscopic methods, but the nomenclature traces back to their first identification by cryogenical (cryo-)UV/Vis experiments.[39] Starting at Pr: After absorption of a photon in resonance with the Q- or Soret band, the delocalized  $\pi$ -electron system of the chromophore is electronically excited to the  $S_1$  state (Soret band excitation to the  $S_2$  relaxes rapidly to the  $S_1$  state), and the transition of an electron from a bonding to an antibonding molecular orbital (MO) weakens the bond order of the  $C_{15} = C_{16}$  bond (see fig. 1.2.1). Thus, the activation energy required for the Z/E isomerization at this position is lowered significantly and the reaction proceeds within the life time of the excited state.[249] The excited state thermally decays in the order of picoseconds (ps) to nanoseconds (ns)(ca. 30 ps in the case of phyA) either to the first ground-state intermediate termed Lumi-R, or back to the Pr state.[3] The decay of the excited state generally comprises a complex reaction network

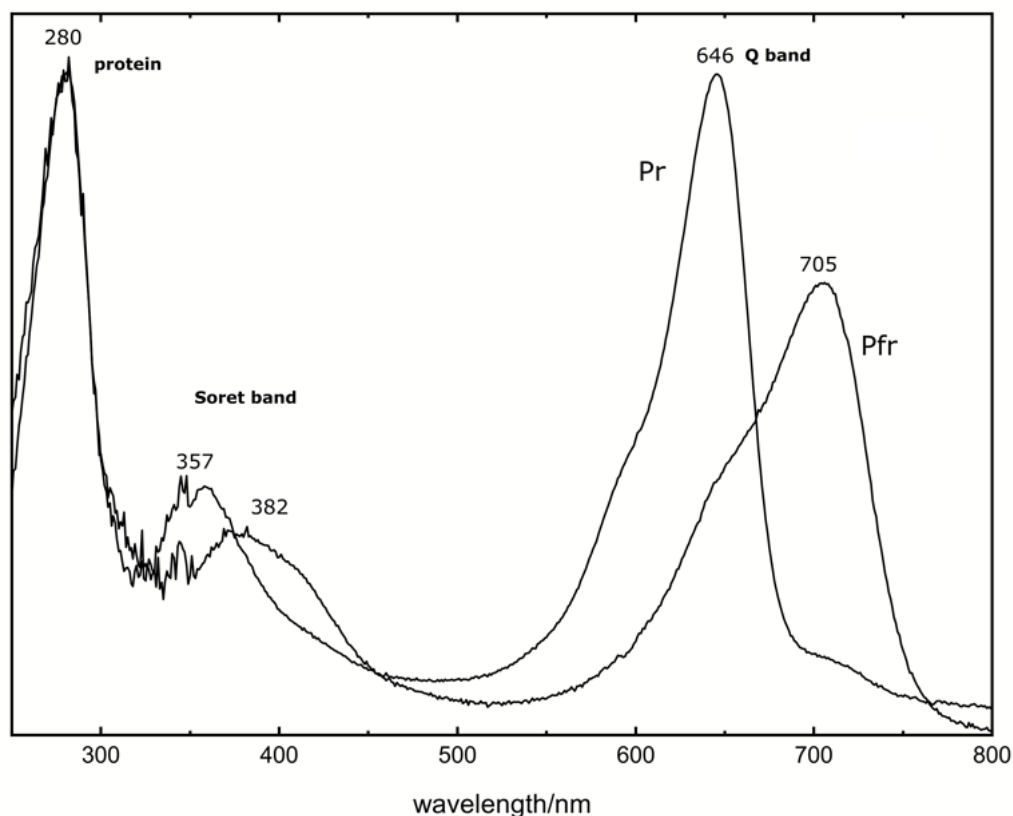


**Figure 1.3.4:** Room temperature UV/Vis spectra of *Sorghum bicolor* phytochrome B (SbPhyB) assembled with PCB in the Pr and in the Pfr states. The pure Pfr spectrum was obtained *via* spectral subtraction of residual Pr contributions.

that can only be disentangled by global analysis methods including multi-exponential fitting procedures.[46, 93, 197, 81] The lifetime of the excited state ( $\text{Pr}^*$ ) is also in the same order of magnitude as fluorescent decay, and thus most phytochromes are, to some extent, fluorescent from their  $\text{Pr}^*$  ( $S_1$ ) states (see chapter 7.1 for a detailed discussion of phytochrome fluorescence). The primary photoreaction from Pfr to Lumi-F is also complex and multiexponential, but by three orders of magnitude faster than in the case of Pr (femtoseconds (fs) to ps).[93] Accordingly, significant fluorescence was never observed from the  $\text{Pfr}^*$  state of any phytochrome. The first RR analysis of AsPhyA Lumi-R was carried out by a combined approach of cryo-trapping and room temperature flow techniques in conjunction with shifted-excitation Raman difference spectroscopy (SERDS).[4] The results of this study agree well with a cryo-trapping FTR analysis[99] and both studies indicate a highly distorted  $\text{P}\Phi\text{B}$  structure within an non-relaxed (still Pr-like) chromophore binding pocket environment.

**Meta states** The Lumi-R state subsequently decays *via* thermal reactions to further intermediates termed the Meta states: Meta-Ra, Rb and Rc.[39] Meta-Rb is formed by a photochemical side reaction and was only observed by cryo-UV/Vis experiments but could not be reproduced by any other analytical method, thus Meta-Rb is possibly a secondary photoproduct generated only under certain reaction conditions.[39] Later studies showed that even more intermediates can be resolved on the pathway from Pr to Pfr, but the most common nomenclature still refers to Meta-Ra and Meta-Rc for canonical phytochromes.[33] On the complementary side of the photocycle (Pfr to Pr), only one Meta state, termed Meta-F, was found.[39] The formation and decay of the Meta states proceed on a time scale of microseconds ( $\mu s$ ) to fractions of a second (s) and comprises rearrangements of the chromophore as well as the surrounding protein matrix. This specifically includes the refolding of the tongue segment (*vide supra*, see fig. 1.3.3).[217, 15] All intermediate transitions in phytochromes are temperature dependent[33], therefore the photocycle intermediates can be cryo-trapped by illumination at low temperatures. Intermediate/ parent state mixtures that allow the isolation of the Meta-Ra and Meta-Rc spectral contributions by subtraction procedures are obtained by illumination at  $-50^\circ\text{C}$  and  $-25^\circ\text{C}$ . FTR spectroscopy revealed transient de- and re-protonation of the P $\Phi$ B chromophore in the reaction sequence.[99] Protonation and deprotonation steps were also found in cyanobacterial[225, 95] and bacterial phytochromes[18, 256] by various spectroscopic methods. These reactions occur in all types of phytochromes and comprise a crucial factor necessary for signal transduction throughout the protein.[227] A scheme of the photocycle is summarized in figure 1.3.5. While the photocycle intermediates in phytochromes were initially proposed to decay in a linear sequential way,[39], thermal branching reactions for Bphs were observed in recent spectroscopic studies.[124, 216, 22] A detailed discussion of one exemplary thermal shunt reaction in the Bphs Agp1 and Agp2 is given in chapter 6.1.

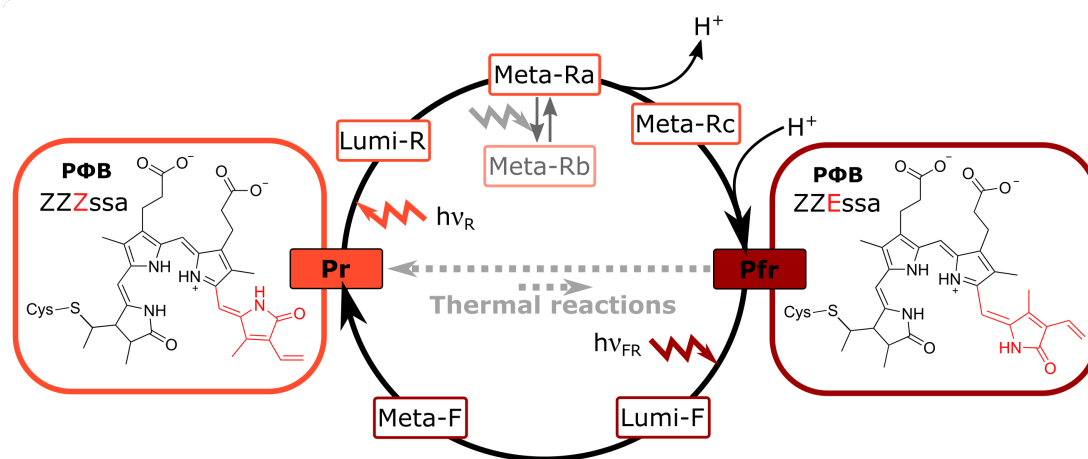


**Figure 1.3.5:** Photocycle scheme of plant phytochromes. The Pr and Pfr parent states interconvert either photochemically *via* a series of intermediates termed the Lumi and Meta states, or thermally in the dark (dashed arrows). Hereby, the stereochemical configuration of the P $\Phi$ B chromophore is changed (Z/E isomerisation). In canonical phytochromes, the dark reaction is predominantly on the side of the Pr state, thus it is termed the “dark-adapted” state. In the Meta-Rc state, P $\Phi$ B is deprotonated at the pyrrolic nitrogens (the positive charge is lost), the re-uptake of the proton occurs during the formation of Pfr.

**Phytochrome signaling** The downstream phytochrome signaling process in plants is quite complex and involves the transient binding of phytochrome interaction factors (PIFs), cellular translocation and kinase reactivity.[162] After photoconversion to the Pfr state, eukaryotic phytochromes relocate from the cytoplasm to the nucleus to interact with the DNA.[31] A study on PhyA demonstrated that the nuclear localization patterns can be altered *via* mutagenesis, and thus are highly dependent on the molecular properties of the photoreceptor itself.[254] In contrast to prokaryotic variants, plant phytochromes also interact with PIFs, but the reaction mechanism is under debate. Different phosphorylation reactions, such as phosphorylation of a tyrosine (Tyr)[147], or a serine (Ser) residue[127] by PIF3 are discussed. Also the reverse reaction, phosphorylation of PIF3 by the phytochrome, is under debate.[144, 181, 156] The output module HKRD is highly homologous to histidine (His) or threonine (Thr) kinases, which comprise the two-component signaling systems in prokaryotic organisms (see chapters 1.4 and 1.5). The proposed phosphorylation reactions of PIFs might be mediated in a similar manner by the HKRD domain.[195] Because the photocycle reactions are temperature dependent (*vide supra*), recent studies also proposed that phytochromes can act as thermosensors *in planta*. [87, 112, 28] The interaction of *Arabidopsis thaliana* PhyB (AtPhyB) with PIF3 and the implications for the chromophore geometry are discussed in detail in chapter 4.2.

**Limitations of protein crystallography** Although conventional x-ray crystallography is a powerful method for the investigation of protein structure, it is restricted to long-lived conformational states that do not undergo structural rearrangements during or after the crystallization procedure. Non-equilibrium conditions are mostly avoided because perturbations of homogeneous single crystals often damage or destroy the samples. An important historical example for this limitation is hemoglobin: this protein crystallizes readily in the reduced state, but when the crystals bind oxygen, the functional conformational toggle imposes strains on the crystal lattice and ultimately the protein crystals are damaged.[164] In contrast to chemical activation, phytochromes undergo light-induced structural rearrangements during the photocycle reactions, involving the  $\alpha$ -helix to  $\beta$ -sheet transition in the tongue region.[217] Therefore, the dark-adapted state can only be safely crystallized in darkness or under dim green light conditions. For canonical phytochromes like Agp1[138, 103], DrBph[239, 240, 27], RpBphP2 and P3[245, 11, 246], the cyanobacterial Cph1 [41] or plant PhyB [26], the dark adapted Pr-structures were obtained in this manner, whereas the bathy phytochromes from *Pseudomonas aeruginosa* (PaBph) and Agp2 were crystallized in their dark-adapted Pfr forms.[244, 185] Furthermore, Pfr structures from prototypical phytochromes were obtained either by crystal growth under defined periodical illumination with red light[217] or by introduction of distinct point mutations in the chromophore binding pocket that stabilize the Pfr state and inhibit thermal dark reversion to Pr.[24]

However, these approaches only yield static pictures of the parent states and no structural information about the photocycle intermediates or the molecular mechanism of their interconversion reactions. Recently developed techniques like room-temperature serial fs crystallography[38] or temperature scan cryo-crystallography [247] allow the investigation of the photoreaction and excited-state dynamics and could eventually even reveal information about the transition to the Lumi state, and possibly the subsequent Meta intermediates.

A promising approach to obtain structural information about the Meta states is the illumination of phytochrome crystals. Although illumination bears the risk of crystal lattice rupture, it was shown with RR spectroscopy for Agp1-M15 (PAS-GAF-PHY) that photo conversion to the Meta-Rc state can be achieved in crystalline samples. Here, the lattice restrains apparently restrict refolding of the tongue region and the photocycle is interrupted at the Meta-Rc intermediate.[237] Nevertheless, the potentially fatal lattice strains can be further reduced by the crystallization of artificial protein variants lacking the typical tongue transition reaction. This can be achieved in two ways: either by the introduction of amino acid substitutions that uncouple the chromophore binding pocket reactions from the tongue response[216, 185] or by the use of PAS-GAF-STOP constructs. Following both approaches, subsequent crystal illumination may yield photoproducts that serve as models for intermediate stages of the photocycle. In any case, the application of RR spectroscopy on crystalline samples is a useful tool for several reasons. First, the RR spectra may serve as a quality check for the dark-grown crystals: typical protein crystallization conditions can be quite harsh and therefore x-ray structures are prone to artifacts induced by high salt concentrations, precipitating agents or extreme pH conditions. However, RR spectra from the crystals can be readily compared with solution spectra of the same protein to identify or exclude differences induced by the crystallization conditions.[237] Second, the RR spectra of the illuminated crystals can be used to assign the photoproduct to an intermediate state or point out certain conformational differences.[237] Third, RR spectroscopy gives information about chromophore protonation states which is inaccessible by x-ray scattering due to the lack of electron density around protic hydrogen nuclei (additionally, x-ray radiation damage can lead to deprotonation and thus falsify the data).[117] Last, the structural information (bond lengths, angles, structural heterogeneities) which can be extracted from the analysis of RR spectra in combination with calculations provides complementary structural information to crystallographic data.[229]

## 1.4 Cyanobacterial Phytochromes

The discovery of the cyanobacterial phytochrome Cph1 from *Synechocystis* sp. PCC 6803 brought significant advantages for the basic studies in phytochrome biology. Milligram (mg) amounts of homogeneous, spectroscopically active Cph1 holoprotein were easily available by heterologous expression of the apoprotein in *Escherichia (E.) coli*, subsequent chromatographic purification and *in vitro* chromophore assembly.[80] Cph1 was therefore often used as a model system for plant phytochromes, albeit some differences between cyanobacterial and plant systems have to be kept in mind. Primarily, Cph1 lacks the NTE, which interacts with the chromophore in plant phytochromes. PhyB NTE deletion mutants show altered biophysical properties mainly in the Pfr state (see chapter 4.1 for a detailed discussion of the chromophore-NTE interactions). Secondly, Cph1 and other cyanobacterial phytochromes naturally incorporate (PCB) [77], instead of PΦB as a cofactor. Because these two chromophores only differ in the saturation of the  $C_{18^1} = C_{18^2}$  vinyl (ethyl in the case of PCB) side chain, which is located in a position remote to the attachment site, both chromophores assemble with Cph1 apo-protein *in vitro* (see fig. 1.2.1 for structural formulae).[106] Similar to plant phytochromes, the bilin is attached to a conserved Cys residue in a GAF domain when the holo-protein is formed.[64] A third difference between Cph1 and plant phytochromes is the lack of the double-PAS motif (Quail module) in the output module,

and in Cph1 the HKRD is directly connected to the PHY domain.[106] While the flexible NTE directly interacts with the chromophore, the Quail module is not in direct contact with the chromophore and exclusively important for the downstream signaling process in plant cells. While the signaling mechanism in plants is quite complex (see chapter 1.3), prokaryotic signal transduction proceeds *via* two component systems, consisting of a sensory kinase (the phytochrome) acting on a response regulator.[209]

**Cph1** Due to the high homology to plant phytochromes[41, 122] and the easy purification procedure[80], Cph1 was extensively used as a model system in diverse biophysical studies. In the Pr state, the ZZZssa configuration of PCB was reported first by NMR[63, 211] and later confirmed by protein x-ray crystallography.[41] Within the ZZZssa configuration, a homogeneous Pr state was reported for Cph1 only by RR intensity analysis [205, 204], but most spectroscopic studies imply a heterogeneous ground state configuration for Cph1.[237, 122, 93, 46, 249] Also, the proton release and uptake reactions in the photocycle were studied in greater detail with various spectroscopic techniques.[225, 95] Advanced time-resolved spectroscopic techniques like ultrafast polarized IR[248], femtosecond stimulated Raman spectroscopy (FSRS)[35, 248] and ultrafast UV/Vis absorption[197] allow tracking of the photoisomerization reaction in the excited state.

**Modular domain structure** In contrast to plant phytochromes, the PAS-GAF-PHY architecture of the PSM is not conserved in all cyanobacterial variants. Hence, different Cphs can be classified according to their PSM structure and subdivided into three groups:[5, 133]

- In **canonical** cyanobacterial phytochromes like Cph1, the PSM PAS-GAF-PHY motif is conserved.[80, 106]
- **Cph2-like** cyanobacterial phytochromes lack the PAS domain, here the PSM is only composed of a GAF and a PHY domain.[242, 6]
- In cyanobacteriochromes (**CBCRs**), the PSM consists only a GAF domain.[172, 174, 168, 169, 139, 141, 173, 51]

**Cyanobacteriochromes** While the chromophore is always embedded in a GAF domain in CBCRs, the surrounding domain structure is highly variable. A common motif in CBCRs is a multi-GAF repeat architecture, but not necessarily all GAF domains constituting a CBCR PSM bind chromophores or exhibit photoactivity.[168] The catalytic output module is also variable: some CBCRs carry a HK domain like Cph1 or other domains involved in classical two-component signaling pathways, others function as cyclases and some completely lack output modules.[174] Although most CBCRs covalently bind PCB, some are also capable to bind other bilins like phycoviolobin (PVB), bilirubin[165, 167] or biliverdin (BV).[141] This variability in prosthetic groups with different conjugation lengths results in drastically changed light absorption properties in CBCRs. While only a minor fraction of the PCB-binding CBCRs exhibit Cph1-like Pr/Pfr photochemistry[167], most display conversion between states of drastically shifted absorption bands.[165] Additional to the incorporation of PVB and bilirubin, some CBCRs are also able to form a second covalent Cys linkage at the C<sub>5</sub>[85, 223] or C<sub>10</sub>[139](see fig. 1.2.1 for notation) position, which eventually disrupts the conjugated system and leads to a hypsochromic shift in the absorption spectrum.[84] One example for this behavior is the CBCR sub-class termed DXCF CBCRs according to a

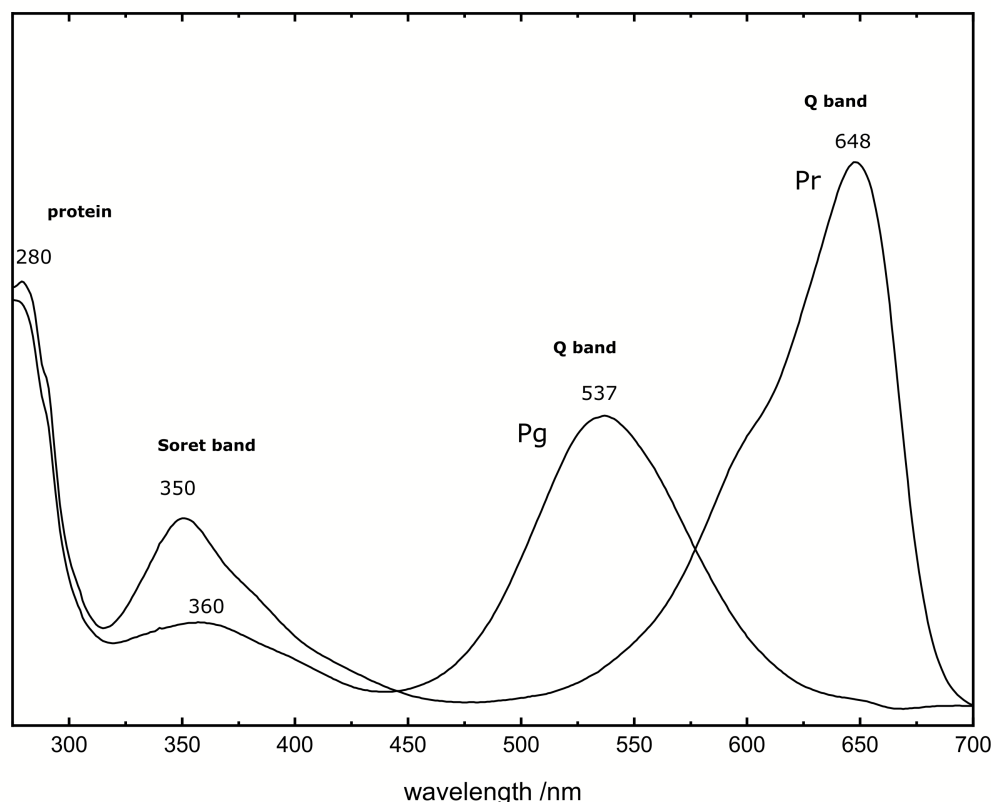


**Figure 1.4.1:** Room temperature UV/Vis spectra of Slr-GAF3 in the Pr and in the Pg state. The pure Pg spectrum was obtained by subtraction of residual Pr contributions.

conserved amino acid sequence (Asp-X-Cys-Phe) in the protein backbone. [172] DXCF CBCRs bind PCB or PVB and are able to sense blue, violet and near-UV light by the formation of a secondary Cys adduct at the C<sub>10</sub> position.[168, 174, 165] In some cases, the formation of the second thioether linkage is a reversible step within the photocycle, in others the attachment occurs during chromophore assembly and persists during the photocycle reactions.[172] While the canonical attachment site at the A ring is conserved in most CBCRs, some DXCF CBCRs also function without the canonical Cys.[51] Like retinal proteins, CBCR photochemistry spans the whole visible, near-IR and near-UV spectral range.[167] These highly specialized and unique properties enable CBCRs to regulate phototaxis[140], chromatic adaptation of the light-harvesting complexes[92, 72, 73, 52] or the remodeling of the entire photosynthetic apparatus in cyanobacteria.[53, 52]

**Red/green CBCRs** Another interesting subgroup of CBCRs incorporates PCB and exhibits red/green photochemistry without the secondary attachment of Cys residues to the chromophore. These bimodal photoreceptive proteins can be interconverted from the dark-adapted Pr state to a meta-stable green-absorbing (Pg) state and *vice versa* by illumination in the corresponding wavelength regions (the UV/Vis absorption spectrum of Slr-GAF3, a red/green CBCR, is shown in fig. 1.4.1).[140] Prominent and well-studied red/green CBCRs without secondary Cys are the phototaxis regulators AnPixJ from *Anabaena* sp. PCC7120[140], composed of four GAF domains and one MCP domain, or RcaE from *Fremyella*. [73] While the Pr state of these CBCRs is very

similar to Cph1 or other PCB-binding canonical phytochromes, the hypsochromic shift in the Pg is fundamentally different from the canonical conversion to the Pfr form. No attachment to secondary Cys residues was observed for these CBCRs, thus the unusual absorption properties of PCB in the Pg state can only be understood in terms of distinct interactions of PCB with the immediate protein environment. Albeit several different models were proposed[169], an unambiguous description of the color tuning mechanism in red/green CBCRs remains elusive. The different models and implications are discussed in detail in chapter 5.1 for Slr1393, a CBCR isolated from *Synechocystis* sp. PCC6803[243], which consists of three GAF domains, followed by a signaling C-terminal histidine kinase domain (see fig. 1.3.1). The third GAF domain of Slr1393 (denoted Slr-GAF3) binds PCB via a thioether bridge to the canonical cysteine residue (Cys 528).

### 1.5 Bacterial Phytochromes

In contrast to the rich variety of different PSM architectures in CBCRs, bacteriophytochromes (Bphs) share the conserved PAS-GAF-PHY sequence of plant phytochromes and canonical cyanobacterial phytochromes.[110] Bphs lack the long NTE (ca. 100 amino acids) that is found in plant phytochromes, but a shorter NTE (ca. 20 amino acids) folds to a unique figure-of-8 knot with the loop that connects the PAS and the GAF domains.[239] Although the specific function of the knot motif is still unknown, the short NTE element also comprises the chromophore attaching Cys residue in Bphs, which utilize biliverdin IX $\alpha$  (BV).[14, 110] Although the chromophore and attachment are different to plant and cyanobacterial variants (see figs. 1.2.1 and 1.3.2), Bphs also exhibit autolyase reactivity, and the cheap commercial availability of BV (compared to PCB and P $\Phi$ B) facilitates expression and *in vitro* assembly of Bphs in heterologous host systems like *E. coli*. [108] Like plant phytochromes, Bphs are generally homodimeric proteins[149], but distinct interface mutations can disrupt the non-covalent interactions at the dimerization sites and lead to artificial monomers.[214]

**Signaling** Although the PSM motif is conserved among Bphs, the output module is variable.[56] Like Cph1, most Bphs are histidine kinases (HKs)[235, 90] and comprise parts in prokaryotic two-component signaling pathways, but also other naturally occurring output modules like the diguanylyl cyclase GGDEF domain[61] or a direct attachment of a CheY-homologous regulator domain (REC) is possible (see fig. 1.3.1). The downstream regulation process in most Bphs is poorly understood compared to plants and only some case studies investigated the biological functions and phenotypes. In the photosynthetic purple bacterium *Rhodospseudomonas palustris*, the two Bphs RpBphP2 and P3 regulate the synthesis of the light harvesting complex LH4.[57]. In non-photosynthetic bacteria, like the plant pathogen *Agrobacterium fabrum*, motility and infectivity are regulated by the Bphs Agp1 and Agp2 *via* expression of flagella genes.[150, 101] The kinase activity of Agp1 is temperature dependent, with higher turnover numbers at 25 °C and lower turnover at higher temperatures (40 °C), suggesting that Bphs also might act as thermosensors.[148]



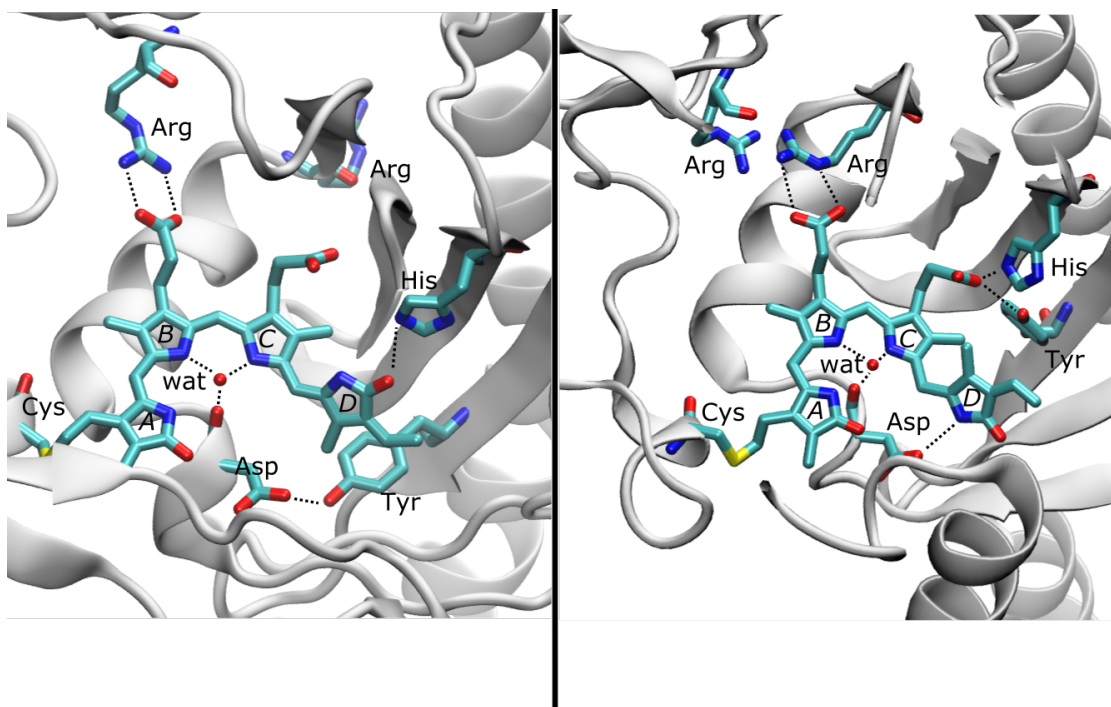


**Figure 1.5.1:** Chromophore binding pocket of the canonical Bph Agp1 (pdb entry: 5HSQ) in the Pr state (left panel) and the bathy phytochrome PaBph (pdb entry: 3C2W) in the Pfr state (right panel). BV adopts the ZZZssa (Pr state) and ZZEssa configurations (Pfr state), respectively. The reorientation of conserved amino acids, the covalent attachment to a Cys residue and the pyrrolic water (wat) molecule are highlighted. Dashed lines indicate hydrogen bonding distances.

**Canonical Bphs** In most Bphs, the thermal equilibrium reaction in the dark is predominantly on the side of the Pr state. Due to their high similarity to plant phytochromes or Cph1, these Bphs are termed canonical Bphs. Prominent, well-studied examples of canonical Bphs are the phytochromes from the extremophile bacterium *Deinococcus radiodurans* (DrBph) or *Agrobacterium fabrum*. The PAS-GAF (PG) construct of DrBph was the first phytochrome fragment to be successfully analyzed by x-ray crystallography[239, 240], revealing the unique knot motif and providing a basis for theoretical homology modeling studies. Later also the PAG-GAF-PHY (PGP) structure was solved (a close up view of the chromophore and surrounding amino acids in the Pr state is given in fig. 1.5.1).[27, 217] Crystallographic studies on Bphs were carried out in conjunction with electron microscopic studies of the Pr-Pfr activation[27], size-exclusion chromatography (SEC)[213] and small-angle x-ray scattering (SAXS) analysis[217, 15, 215], to investigate the structural rearrangements during the photocycle in the solution phase. Additionally, the photoactivation reaction in canonical Bphs was extensively studied by time-resolved and static difference (diff.) IR spectroscopy[215, 210, 159, 186, 220, 119], electron paramagnetic resonance (EPR) techniques using spin-labeling (PELDOR)[89, 68], RR spectroscopy[241, 18, 238], fluorescence line narrowing spectroscopy (FLN) [145] and UV/Vis techniques.[18] These studies unraveled a series of events during the Lumi, Meta-Ra and Rc transitions linking the chromophore isomerization to the secondary structure transition of the tongue and ultimately the activation of the catalytic output module, including (de)protonation steps similar to Cph1 and plant phytochromes. Despite the high similarity of the spectroscopic properties and the photocycle to Cph1, the isomerization

reaction in DrBph proceeds *via* a different pathway and yields  $\beta$ -facial chirality in the Pfr, in contrast to the  $\alpha$ -facial PCB in the Pfr state of Cph1.[171]

**Bathy phytochromes** In the Bph from the plant pathogen *Xanthomonas campestris* (XcBph), the thermal dark equilibrium reaction is less on the side of the Pr state compared to canonical phys, affording a Pr/Pfr mixture in the dark.[17, 153] In so-called bathy phytochromes, the thermal dark relaxation is completely reversed, thus defining Pfr as the dark-adapted state, albeit *in vitro* BV assembly yields Pr as a meta-stable initial product.[90] Bathy Bphs are found predominantly in rhizobial soil bacteria like *Agrobacterium fabrum* (Agp2) or *Rhodopseudomonas palustris* (RpBphP6)[177, 90], but also in the mammalian pathogen *Pseudomonas aeruginosa* (PaBph). The PaBph PGP construct was successfully crystallized in the dark-adapted Pfr state[244] and early intermediates in the light activated reaction sequence could be identified using temperature-scan x-ray crystallography.[247] A close up view of BV and the surrounding amino acids in the Pfr state is given in figure 1.5.1. Bathy Bphs share highly homolog sequences, resulting in a conserved chromophore environment in this sub-class and unique photochemical features among them.[177] Agp2, PaBph and RpBphP6 all share distinct features like a protonated propionic side chain at ring C within a homogeneous Pfr state[227] and all display a characteristic sequential H/D exchange pattern in their RR and IR spectra.[228, 227] Furthermore, the Pr state of bathy Bphs comprises a pH-dependent equilibrium of tautomeric keto- and enol-forms at the ring D carbonyl group.[256, 227] The enolic tautomer is formed by a proton exchange with a nearby conserved histidine (His) residue and presumably initiates the thermal dark-relaxation reaction to the Pfr state.[227]

## 1.6 Biotechnological Applications of Phytochromes

Phytochromes have unique photophysical and biological properties making them promising precursor proteins for various biotechnological applications.[193] The proteins and chromophores are not cytotoxic and the required pigment molecules can be supplied in sufficient amounts in pro- and eukaryotic host systems.[196] Especially Bphs are advantageous for application in mammalian cells because BV is the first intermediate product in the cellular heme degradation pathway and therefore ubiquitously available.[196] If required, it is also possible to synthesize PCB in mammalian cells, thus the biotechnological phytochrome toolkit also includes the cyanobacterial and plant variants.[137] While some applications like photoacoustic tomography[104], the production of for ZZE-BV in bacteria[109], or biofilm photography[115] are rather exotic, phytochromes are mostly utilized for popular technologies like optogenetics or fluorescence microscopy.

**Optogenetics** The control of cellular processes by light (optogenetics) requires the introduction of a protein construct composed of a photo-switchable component and a suitable output module to the target system.[130] These requirements are perfectly met by the PSM and the output module of Bphs. Furthermore, the coiled-coil (CC) motif that connects the output module with the PSM in Bphs can also be used to develop general design strategies for artificial protein constructs, e.g. to functionally fuse the phytochrome PSM to alternative output modules.[130] Utilizing these protein chimeras, the synthesis of cyclic-di-guanosine monophosphate (c-di-GMP) in *E.coli*[182], the dynamics of mammalian cell morphology[88] or the dimerization of two receptor tyrosine kinases[163] in mammalian cells can be controlled with red and near-infrared (NIR) light.

**IsPadC** Just recently, genome sequencing of the marine bacterium *Idiomarina* sp.A28L revealed the existence of naturally occurring phytochrome-activated di-guanylyl cyclases (e.g. IsPadC), which are readily suitable for the optogenetic regulation of the second messenger molecule c-di-GMP.[61] IsPadC was recently crystallized as a Pr homodimer (pdb entry: 5LLW) and as Guanosine-5'-triphosphate (GTP)-bound enzyme-substrate complex (pdb entry: 5LLX).[61] Hydrogen-deuterium exchange coupled to mass spectrometry (HDX-MS) experiments led to the conclusion that conformational dynamics in the functionally relevant state and the relative population of two register configurations in the coiled-coil (CC) region tune the cyclase activity.[61, 76] The register configuration influences the positioning of functionally important residues of the cyclase domain (the conserved Gly-Gly-Asp-Glu-Phe, or GGDEF, motif) and is influenced by the secondary structure of the tongue. Furthermore, two mutant proteins carrying amino acid substitutions in the CC-domain, called Reg1 and Reg2, exhibit cyclase inhibition or activation independent of light, by stabilizing either one of the register configurations. IsPadC Reg2 crystallizes in the form of an asymmetric Pfr/Pr heterodimer, indicating that this form might be the functionally relevant active state of the cyclase.[60] Anyhow, acidic urea denaturation experiments yielded over 90% ZZEssa (Pfr) chromophore in the light-activated wild-type protein, arguing against the Pr/Pfr heterodimer as the predominant activated state. Underpinned by a detailed analysis of the non-isosbestic recovery kinetics in UV/Vis experiments, a Pfr/Meta-R heterodimer was proposed for the activated state. In order to test this working hypothesis, IsPadC was characterized by means of RR and difference IR spectroscopy (chapter 6.2).

**Fluorescence imaging of biological samples** Fluorescence imaging comprises a powerful set of techniques for the investigation of biological samples on scales from several millimeters (mm) of tissue down to the single-molecule level. To reach this high spatial resolution beyond the diffraction limit, a donut-shaped pulse of light is used to create a ring of stimulated emission and inhibit fluorescence processes in the outer regions of a confocal excitation point, restricting the emission area to a few nm (stimulated-emission-depletion, STED microscopy).[97, 20] Based on STED, further sophisticated techniques like photoactivated localization microscopy (PALM)[12] or stochastic optical reconstruction microscopy (STORM) [180] were developed, yielding even higher spatial resolutions down to the single-molecule level. However, all these techniques are fluorescence-based and thus require dye molecules with suitable fluorescence properties.

Since the green fluorescent protein (GFP) from the jellyfish *Aequorea victoria* was first isolated[194] and biochemically characterized[161], a high number of related dyes with different photophysical properties was developed to keep up with the rapid microscope developments.[176] GFP and its spectral variants cover the visible spectrum, allowing multi-color imaging with fluorescence quantum yields (FQY) of up to 93 %.[55, 58] Although these multi-color techniques are useful for the parallel imaging of several analytes *in vivo*, it is important to consider that chemical attachment of dyes might impact structure, dynamics and therefore the biological function. The interaction of analyte and dye might be complex and therefore the applicability on a mechanistic molecular level is limited.

In contrast to high-resolution techniques, the development of fluorescence imaging through thick layers of biological tissues (e.g. mammalian skin) is of high interest for medical applications. To penetrate biological tissue efficiently, the fluorescence excitation and emission wavelengths need to be in the “near-infrared (NIR) transparent window” between 650 and 900 nm.[189] NIR radiation is advantageous compared to visible light because the competing absorption and fluorescence of natural pigments, mostly heme proteins, is low in this region. Further red-shifted IR radiation ( $> 900\text{nm}$ ), is mainly absorbed by water and therefore also not suitable for deep tissue imaging.[189] The major advantages of medical *in vivo* studies with NIR light (e.g. in living mice) are good targeting, low invasivity and low instrument costs compared to x-ray or tomographic imaging methods like magnetic resonance tomography (MRT) and positron-emission tomography (PET).[32]

The superior signal-to-noise (S/N) ratio in the NIR region makes the development, improvement and understanding of bright and stable NIR dyes highly desirable scientific objectives. Despite their high FQY in the visible region, far-red shifted GFP homologues lack brightness and photostability and therefore need to be further improved by bioengineering methods to meet the requirements for deep tissue studies.[128, 189, 212] An alternative approach to the development of far-red shifted GFP homologues is the utilization of bioengineered biliproteins derived from phytochromes.[157, 32, 188]

**iRFPs** The natural FQY of phytochromes in the NIR transparent window is in the order of about 1 % and can be enhanced by mutagenesis to yield bright and photostable NIR-fluorescent protein variants for applications in mammalian tissue.[157, 32] In the cyanobacterial phytochrome Cph1, the exchange of one single amino acid (Y167H) leads to a strong increase in PCB fluorescence (FQY higher than 10 %)[45]. Strong fluorescence (FQY=18 %) was also reported for a PCB-binding allophycocyanin derivate termed “small ultra red fluorescent protein” (smURFP).[175] In general, the synthesis of PCB in mammalian cells is possible but requires the introduction of a PCB:ferredoxin oxidoreductase to the host cell to catalyze the reduction of BV to PCB.[137] This step is not required if Bphs are used as precursors, because these proteins incorporate the ubiquitous BV (*vide supra*) without the requirement for any further chemical modification.

This major advantage led to the development of several NIR-fluorescent proteins derived from Bphs. The proteins were developed in different research institutions around the world by a combined approach of domain truncation, random mutagenesis steps and rational directed-site mutagenesis. Figure 1.6.1 depicts a complete scheme of the design strategy and introduction to the mammalian host system (e.g. a mouse).

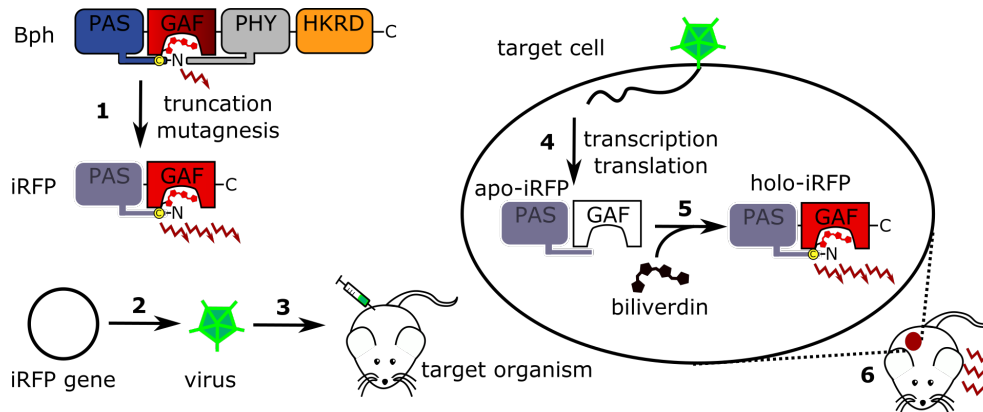


**Figure 1.6.1:** Fluorescence imaging with iRFPs. **1** in a first step, iRFPs are generated from Bph precursors by truncation (either PAS-GAF or GAF only), random mutagenesis and directed mutagenesis steps. Promising variants are screened for high fluorescence *in vitro*. The iRFP gene is introduced into a viral genome (**2**) and the mammalian host system (e.g. mouse liver cells) are transfected (**3**). After expression of the apo-iRFP by the host system (**4**), the protein autocatalytically attaches BV (**5**), and the fluorescent holo-iRFP is obtained. **6**: Fluorescence can be detected from the target cells of the host system *in vivo*.

- The IFP series derived from DrBph in the Shu Lab (University of California, San Francisco), including IFP1.0-1.4[196], IFP 2.0 [251] and iBlueberry, which bears second Cys in a monomeric variant.[252]
- The Wisconsin-phytochrome series derived from DrBph in the Forest Lab (University of Wisconsin, Madison), including Wi-Phy[8] and Wi-Phy 2.0.[114]
- The iRFP series derived from various different Bphs in the Verkhusha Lab (Einstein College, New York), including the auto-fluorescent variants iRFPXXX (XXX denotes the wavelength of the fluorescence emission maximum)[44, 190], the photo-activatable PAiRFP proteins[158], a GAF-only iRFP[179] and the monomeric group of mIRFPs.[191]

Furthermore, the rapid development of these proteins motivated further studies to understand the origin and mechanism of fluorescence enhancement.[221, 219, 113, 184, 13, 206, 207, 208, 192, 255, 74, 154, 232, 23] Two fundamental studies on the structural parameters that control the fluorescence in iRFPs are part of this thesis (chapters 7.1 and 7.2).[21]

## 2 Theoretical Background: Vibrational Spectroscopy

The term vibrational spectroscopy refers to analytical techniques that probe the interaction of matter with incident electromagnetic radiation by exploration of lattice or molecular vibrations. The two most common experimental techniques, infrared (IR) absorption and Raman scattering, rely on two different physical processes: the absorption and the inelastic scattering of photons, respectively (see fig. 2.1.1). Over the past centuries, these processes were described on various levels of theory, ranging from the classical treatment (microscopic Maxwell equations)[7] to a relativistic, time-dependent, quantum mechanical treatment of both matter and photons (the theory of quantum electrodynamics, QED).[43] Both of these theoretical approaches include major drawbacks: the classical treatment confines electromagnetic fields and oscillating dipoles but fails to account for the quantization of vibrational energy and therefore cannot explain any of the observables in vibrational spectroscopy.[7] The complexity of the QED approach, on the other hand scales exponentially with system size and is therefore restricted to either very small or very symmetric model systems in theoretical physics.[43] Hence, both approaches are not feasible to explain vibrational spectra of biomolecules. An appropriate combination of different levels of theory is necessary to obtain meaningful semi-classical models. The most common models treat the molecules quantum mechanically within the Born-Oppenheimer approximation, while the electromagnetic radiation is expressed as a field perturbing the electronic structure (perturbation theory).[70, 120, 2, 1]

The three basic observables in vibrational spectroscopy that require theoretical description are: the frequency  $\nu$  of a molecular vibration, the intensity of the corresponding transition  $I$ , and the line shape that describes the variation of  $I$  in the frequency domain  $I(\nu)$ .

### 2.1 Frequencies of Molecular Vibrations

Despite the mechanistic differences of IR absorption and Raman scattering, both techniques probe a re-population of vibrational energy levels of an analyte caused by the interaction with light. In IR spectroscopy, absorption of an IR photon  $h\nu_{IR}$  by the sample leads to the transition from an initial vibrational level  $|\nu_i\rangle$  to a final state  $|\nu_f\rangle$  within the electronic ground state  $S_0$ . Raman scattering of a photon ( $h\nu_{Raman}$ ) is a concerted two-photon process that also leads to an excitation (Stokes scattering) or de-excitation (anti-Stokes scattering) of a vibrational energy level (see fig. 2.1.1). Anyhow, the structure and distribution of the vibrational levels is independent of the technique and solely relies on the chemical properties of the analyte, thus the theoretical treatment of both methods initially requires a profound understanding of vibrational energy levels.

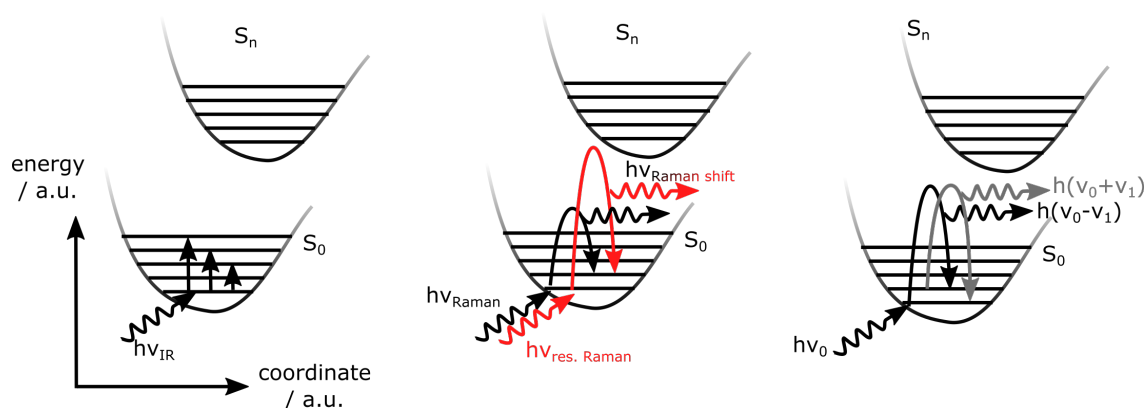


**Figure 2.1.1:** Jablonski diagram of different vibrational absorption and scattering processes. Left panel: absorption of IR photons ( $h\nu_{IR}$ ) excites vibrational levels of the electronic ground state  $S_0$ . Middle: Raman scattering of photons ( $h\nu_{Raman}$ ) is a concerted two-photon process. If the photon energy is in resonance with an excited electronic state ( $S_n$ ), the scattering intensity is enhanced (resonance Raman effect, see chapter 2.4). The RR process is depicted in red. Right panel: incident radiation can either excite (black line) or de-excite (gray) a vibrational state. The energy of the scattered photon is equal to the difference (Stokes scattering) or the sum (anti-Stokes scattering) of the incident photon energy  $h\nu_0$  and the vibrational energy difference  $\nu_1$ .

**Normal modes** All molecules oscillate in characteristic patterns that contain valuable information about their chemical structure and interactions with the molecular environment. A useful theoretical description for the complex vibrational patterns of molecules are so-called vibrational normal modes.[70] A normal mode  $k$  of an oscillator is defined as a pattern of motion in which all parts (atoms) of the oscillator (molecule) move sinusoidally with the same frequency  $f$  and with a fixed phase relation.[7] A nonlinear molecule consisting of  $N$  atoms has  $3N$  degrees of motional freedom,  $3N - 6$  of which correspond to vibrational motion. The remaining six degrees of freedom convey the dimensions of rotational and translational motion. Every vibrational motion within the  $3N - 6$  vibrational degrees of freedom can be represented by a linear combination of the  $3N - 6$  normal modes.[7] Although normal modes are per definition concerted oscillations of all atoms within the molecule, the relative displacement amplitudes for the individual atoms vary over several orders of magnitude.[70] Hence some vibrational modes are delocalized with significant participation of many atoms (e.g. the C=C stretching vibrations in long conjugated systems like carotenoids[96]), while other modes are in good approximation localized to smaller groups of atoms. Localized modes are often named according to the functional group and the corresponding motion (e.g. C=O stretching of a single keto group). The frequencies of these normal modes are governed by the masses of the displaced atoms and the forces between them. Consider for example a diatomic molecule  $\alpha - \beta$  with only one vibrational degree of freedom, namely the stretching of the bond. Assuming the harmonic motion of two point masses connected by a spring, the frequency of the vibration can be described classically by Hooke's law:

$$\nu = \frac{1}{2\pi} \sqrt{\frac{f}{\mu}} \quad (2.1)$$

Here,  $f$  is the stretching force constant,  $\mu$  is the reduced mass, which is related to the atomic masses  $m_\alpha$  and  $m_\beta$  by

$$\mu = \frac{m_\alpha m_\beta}{m_\alpha + m_\beta} \quad (2.2)$$

In this minimal model, the force constant  $f$  and atomic masses  $m_i$  depend on the composition and configuration, i.e. the bonding and non-bonding interactions of the atoms with each other and the environment. Hence, vibrational spectroscopic techniques that excite and probe the vibration provide very accurate information on molecular structure (such as bond lengths or angles in complex molecules).[7]

**The harmonic approximation** Equation 2.1 is an approximation based on a parabolic potential curve

$$V_{para} = \frac{1}{2}f\Delta x^2, \quad (2.3)$$

where  $\Delta x$  denotes the symmetric displacement of the masses along the x-axis from the equilibrium position. The Schrödinger equation for the motion of  $m_\alpha$  and  $m_\beta$  with  $V_{para}$  is

$$-\frac{\hbar^2}{2\mu} \frac{d^2\Psi}{dx^2} + V_{para}\Psi = E\Psi \quad (2.4)$$

with the reduced Planck constant  $\hbar = h/2\pi$  and the vibrational wave function  $\Psi$ . The energies  $E_\nu$  of the permitted vibrational energy levels  $|\nu\rangle$  are obtained as solutions of eqn. 2.4:

$$E_\nu = \left(n_\nu + \frac{1}{2}\right) \hbar \left(\frac{f}{\mu}\right)^{1/2}. \quad (2.5)$$

At high vibrational excitations (high values of the vibrational quantum number  $n_\nu$ ), the parabolic approximation is poor because it does not accurately represent spread of the vibrational wavefunction and also does not include a dissociation limit. The motion then becomes anharmonic and the force is no longer proportional to the displacement  $\Delta x$ . One approach to take the anharmonicity of an oscillation into account is to use a Morse potential instead of the parabolic:

$$V_{Morse} = D_e(1 - e^{-a\Delta x})^2, \quad (2.6)$$

where  $D_e$  is the depth of the potential minimum and

$$a = \left(\frac{f}{2D_e}\right)^{1/2}. \quad (2.7)$$



Solution of the Schrödinger eqn. 2.4 with respect to  $V_{Morse}$  yields an according set of energy levels:

$$E_{\nu,Morse} = \left(n_{\nu} + \frac{1}{2}\right) \hbar \left(\frac{f}{\mu}\right)^{1/2} - \left(n_{\nu} + \frac{1}{2}\right)^{1/2} x_e \hbar \left(\frac{f}{\mu}\right)^{1/2}, \quad (2.8)$$

with the anharmonicity constant  $x_e$ :

$$x_e = \frac{a^2 \hbar}{2(f\mu)^{1/2}}. \quad (2.9)$$

Although the harmonic approximation is inaccurate at high vibrational excitations, is widely used for *in silico* calculations of molecular vibrational frequencies. The approximation is useful, because the resulting error for the energies of fundamental  $|\nu_0\rangle \rightarrow |\nu_1\rangle$  transitions that dominate IR and Raman spectra at room or cryogenic temperatures is small.

**Normal Mode Analysis** Normal mode frequencies of complex systems like a tetrapyrrole molecule can be calculated *in silico* by normal mode analysis (NMA). Within the harmonic approximation, the NMA formalism follows three fundamental steps[70]: **(1)** A three-dimensional expression for the energy is derived. **(2)** The classical equations of motion are set up accordingly. **(3)** Frequencies and atomic displacement are calculated from the eigenvalue equation of a force constant matrix. The NMA formalism is commonly expressed in mass-weighted Cartesian coordinates  $q_i$  for the individual atoms  $i$ :

$$q_i = \sqrt{m_i} x_i. \quad (2.10)$$

The  $q_i$  of all atoms within the molecule can be written in matrix notation as vector  $\mathbf{q}$  that is calculated from the (diagonal) matrix  $\mathbf{m}$  containing atomic masses  $m_i$  and the vector  $\mathbf{x}$  containing atomic positions  $x_i$ ,

$$\mathbf{q} = \sqrt{\mathbf{m}} \mathbf{x}. \quad (2.11)$$

**(1)** The expression for the kinetic energy  $T$  is derived from  $q_i$  or  $\mathbf{q}$ ,

$$T = \frac{1}{2} \sum_{i=1}^{3N} \dot{q}_i^2 = \frac{1}{2} \dot{\mathbf{q}}^T \dot{\mathbf{q}}, \quad (2.12)$$

where dots above variables indicate time derivatives and  $\dot{\mathbf{q}}^T$  the trace of the matrix  $\dot{\mathbf{q}}$ . It is convenient to expand the potential energy  $V$  of a molecule within a local energy minimum in a Taylor series around the minimum position:

$$V = V_0 + \sum_{i=1}^{3N} \left( \frac{\partial V}{\partial q_i} \right)_0 q_i + \frac{1}{2} \sum_{i,j=1}^{3N} \left( \frac{\partial^2 V}{\partial q_i \partial q_j} \right)_0 q_i q_j + \dots \quad (2.13)$$

$V_0$  refers to the potential energy at equilibrium, which can be omitted because only changes of  $V$  caused by displacements of the individual atoms contribute to the NMA.

Also infinitesimal changes in  $q_i$  (second term) do not cause a change in  $V$  when the molecule is in equilibrium, thus this term is also zero. For small displacements  $q_i$  within the harmonic approximation, higher order terms can be neglected, such that eqn. 2.13 yields

$$V \approx \frac{1}{2} \sum_{i,j=1}^{3N} \left( \frac{\partial^2 V}{\partial q_i \partial q_j} \right)_0 q_i q_j = \frac{1}{2} \sum_{i,j=1}^{3N} f_{ij}^m q_i q_j = \frac{1}{2} \mathbf{q}^T \mathbf{f} \mathbf{q}, \quad (2.14)$$

where  $f_{ij}^m$  are the mass-weighted force constants (second partial derivatives of  $V$  with respect to the coordinates  $q_i$  and  $q_j$ , in matrix notation the (Hessian) force constant matrix  $\mathbf{f}$ ). Note the resemblance with eqn. 2.3 for a diatomic molecule.

## (2) The Lagrangian formalism

$$\frac{d}{dt} \left( \frac{\partial T}{\partial \dot{q}_j} \right) + \left( \frac{\partial V}{\partial q_j} \right) = 0 \quad (2.15)$$

allows the derivation of the  $3N$  Newtonian equations of motion in the form of second order coupled linear homogeneous differential equations,

$$\ddot{q}_j + \sum_{i=1}^{3N} f_{ij}^m q_i = 0. \quad (2.16)$$

The general solution for the coordinate  $i$  of the vibrational mode  $k$  with the frequency  $\nu = \sqrt{\lambda_k}/2\pi$ , the amplitude  $A_{ik}$  and the phase angle  $\psi_{ik}$  is given by

$$q_i = A_{ik} \cos(\sqrt{\lambda_k} t + \psi_{ik}). \quad (2.17)$$

Inserting the solution of eqn 2.17 back into eqn. 2.16 yields

$$\sum_{i=1}^{3N} (f_{ij}^m - \delta_{ij} \lambda_k) A_{ik} = 0. \quad (2.18)$$

With the Kronecker delta  $\delta_{ij}$ , which equals unity if  $i = j$  and zero in all other cases, eqn. 2.18 can be rewritten

$$-A_{jk} \lambda_k + \sum_{i=1}^{3N} f_{ij}^m A_{ik} = 0. \quad (2.19)$$

Eqn 2.19 corresponds to  $3N$  linear equations for  $A_{jk}$ , that can be rewritten in matrix notation as

$$(\mathbf{f}^m - \lambda_k \mathbf{1}) \mathbf{A}_k = 0. \quad (2.20)$$

Here, the mass-weighted Hessian matrix  $\mathbf{f}^m$  contains the mass-weighted force-constants  $f_{ij}^m$ ,  $\mathbf{1}$  denotes the identity matrix and  $\mathbf{A}$  is a vector containing the Cartesian displacement amplitudes  $A_{ik}$ . Expression 2.20 is an eigenvalue equation that defines eigenvalues  $\lambda_k$  for each eigenvector  $\mathbf{A}$  of the matrix  $\mathbf{f}^m$ .

(3) The vibrational frequency  $\nu = \sqrt{\lambda_k}/2\pi$  and amplitudes of atomic displacement  $A_{ik}$  for the normal mode  $k$  can be determined according to the general approach for eigenvalue problems.  $3N - 6$  non-zero eigenvalues  $\lambda_k$  can be obtained from the determinant of the secular equation

$$|\mathbf{f}^{\mathbf{m}} - \lambda_k \mathbf{1}| = 0. \quad (2.21)$$

By inserting the eigenvalues  $\lambda_k$  into eqn. 2.20, the eigenvectors  $\mathbf{A}_k$ , which describe atomic displacement amplitudes of the vibrational modes, are obtained. Thus, experimental frequencies  $\nu$  can be assigned to individual normal modes  $k$  and the included Cartesian atom displacements  $x_i$ . Unfortunately, the description of molecular motions in Cartesian coordinates is not very descriptive. A representation of the atomic displacements in internal coordinates  $S_t$  (such as bond lengths and angles) is more instructive and can be obtained *via* coordinate transformation from the Cartesian coordinates  $x_n$ :

$$S_t = \sum_{n=1}^N \mathbf{s}_{tn} \mathbf{x}_n, \quad (2.22)$$

where  $\mathbf{s}_{tn}$  are adequate transformation vectors that maximize  $S_t$ .

## 2.2 Intensities and Selection Rules

For a typical protein like phytochrome with ca. 500 amino acids (aa) with an average number of 15 atoms per aa, a rough estimate yields more than 20 000 normal modes ( $3N-6$ ). [10] Although this value is very large, the number of observable modes and thus the complexity of the vibrational spectrum is naturally reduced by certain quantum mechanical (QM) and symmetry-derived selection rules to a dimension that is feasible for analysis and interpretation. Because neither the phytochrome protein, nor the linear tetrapyrrole are symmetric (point group  $C_1$  in both cases), only the QM derivation of the signal intensities is discussed and symmetry considerations are omitted.

The intensity  $I$  of a any fundamental vibrational mode in a Raman or IR spectrum is proportional to the probability of the transition  $P_{fi}$  from the initial vibrational energy level  $|\nu_i\rangle$  to the final level  $|\nu_f\rangle$ .  $P_{fi}$  can be generally described according to Fermi's golden rule

$$I \propto P_{fi} = \frac{2\pi}{\hbar} |\mathbf{M}_{fi}|^2 \rho_f, \quad (2.23)$$

where  $\rho_f$  is the density of final states. The transition moment  $\mathbf{M}_{fi}$ , which represents the coupling between  $|\nu_i\rangle$  and  $|\nu_f\rangle$ , can then be written as an integral

$$\mathbf{M}_{fi} = \langle \nu_f | \hat{\mathbf{\Omega}} | \nu_i \rangle. \quad (2.24)$$

The interaction operator  $\hat{\mathbf{\Omega}}$  is determined by the interaction mechanism of the analyte with the electromagnetic radiation. Thus, the probability of vibrational transitions in IR absorption (one-photon process) and Raman scattering (two-photon process) have different  $\hat{\mathbf{\Omega}}$  and consequently different QM selection rules.

The intensities of QM allowed transitions depend on the redistribution of electrons and nuclei with the vibrational transition from  $|\nu_i\rangle$  to  $|\nu_f\rangle$ : while large changes in the electrical dipole moment  $\hat{\boldsymbol{\mu}}$  lead to strong IR bands, large changes of the polarizability  $\boldsymbol{\alpha}$  lead to strong Raman signals.

**IR absorption intensities** If the energy of incident IR radiation  $h\nu_{IR}$  equals the energy difference between the vibrational energy levels  $|\nu_i\rangle$  and  $|\nu_f\rangle$ , the resonance condition

$$h\nu_{IR} = h\nu_{\nu_f} - h\nu_{\nu_i} \quad (2.25)$$

is fulfilled. Additional to the resonance condition, the transition moment  $\mathbf{M}_{fi}$  (see eqn. 2.23) must be non-zero to facilitate the absorption of  $h\nu_{IR}$  and transition from  $|\nu_i\rangle$  to  $|\nu_f\rangle$  (see fig. 2.1.1, left panel). In absorption processes,  $\mathbf{M}_{fi}$  depends on the electrical dipole moment operator  $\hat{\boldsymbol{\mu}}_q$

$$\hat{\boldsymbol{\mu}}_q = \sum_{n=1}^N z_n \mathbf{r}_n, \quad (2.26)$$

where  $z_n$  is the effective charge and  $\mathbf{r}_n$  the Cartesian position vector of each atom  $n$ . Within the harmonic approximation, equation 2.24 yields

$$\mathbf{M}_{fi} = \sum_{k=1}^{3N-6} \hat{\boldsymbol{\mu}}_{qk} \langle \nu_f | Q_k | \nu_i \rangle, \quad (2.27)$$

where  $\hat{\boldsymbol{\mu}}_{qk}$  is the derivative of the molecular dipole moment with respect to the normal coordinate  $Q_k$ . For an IR absorption process, two criteria need to be fulfilled: primarily,  $\hat{\boldsymbol{\mu}}_{qk}$  has to be non-zero, so that the atomic displacements included in normal mode  $k$  must be accompanied by a net change of the molecular dipole moment and the intensity of the resulting absorption band will scale with  $\hat{\boldsymbol{\mu}}_{qk}$

$$I_{IR} \propto \left( \frac{\partial \hat{\boldsymbol{\mu}}_{qk}}{\partial Q_k} \right)^2. \quad (2.28)$$

Secondly,  $\langle \nu_f | Q_k | \nu_i \rangle$  needs to be non-zero. Within the harmonic approximation, this is the case when the vibrational quantum numbers of  $|\nu_i\rangle$  and  $|\nu_f\rangle$  differ by exactly one. This selection rule is a consequence of the conservation of angular momentum, because the spin of the absorbed photon must be compensated by the analyte.

### 2.3 Raman Intensities

In contrast to IR absorption, Raman spectroscopy is based on the inelastic scattering of incident photons  $h\nu_0$ . [120] Therefore the energy of an incident photon is not required to be equal to the energy corresponding to the difference between the two vibrational states. As shown in figure 2.1.1 (right panel), there are two forms of Raman scattering: Stokes scattering (scattering of a photon with the energy  $h(\nu_0 - \nu_1)$ ) and anti-Stokes scattering (scattering of a photon  $h(\nu_0 + \nu_1)$ ). In this thesis only Stokes-scattering is discussed, where  $h\nu_1$  equals the energy difference between the vibrational levels  $|\nu_i\rangle$  and  $|\nu_f\rangle$ , and the scattered radiation  $h\nu_R$  follows the relation

$$h\nu_1 = h\nu_f - h\nu_{\nu_i} = h\nu_0 - h\nu_R. \quad (2.29)$$

Experimentally, the accurate measurement of the Raman shift  $\nu_1$  and thus the spectral resolution depends on the bandwidth of the incident radiation  $\nu_0$ . Therefore, narrow-band excitation is crucial for Raman spectroscopy, mostly laser sources are employed (laser is an acronym for “light amplification by stimulated emission of radiation”).

**Polarizability theory** The most common approach for the theoretical description of Raman scattering is a semi-classical second-order perturbation theory of molecular polarizability (developed by Placzek). The incident electromagnetic radiation  $\mathbf{E}$  perturbs the electronic structure of the molecule and induces a dipole moment  $\boldsymbol{\mu}_{ind}$

$$\boldsymbol{\mu}_{ind} = \boldsymbol{\alpha}\mathbf{E}. \quad (2.30)$$

The oscillating dipole subsequently re-radiates scattered light  $h\nu_R$ . Hereby,  $\boldsymbol{\mu}_{ind}$  depends on the polarizability  $\boldsymbol{\alpha}$  of the molecule. The molecular polarizability tensor  $\boldsymbol{\alpha}$  with the Cartesian (molecule-fixed) components  $\alpha_{\rho,\sigma}$

$$\alpha_{\rho,\sigma} = \begin{pmatrix} \alpha_{xx} & \alpha_{xy} & \alpha_{xz} \\ \alpha_{yx} & \alpha_{yy} & \alpha_{yz} \\ \alpha_{zx} & \alpha_{zy} & \alpha_{zz} \end{pmatrix} \quad (2.31)$$

is unique for each molecule, and the tensor elements represent all molecular properties that have impact on  $h\nu_R$ . Expansion of  $\boldsymbol{\alpha}$  into a Taylor series of the normal coordinates  $Q_k$  yields

$$\boldsymbol{\alpha} = \boldsymbol{\alpha}_0 + \sum_{k=1}^{3N-6} \left( \frac{\partial \boldsymbol{\alpha}}{\partial Q_k} \right)_0 Q_k + \dots, \quad (2.32)$$

where the  $\boldsymbol{\alpha}_0$  term is responsible for elastic Rayleigh scattering and the first order term for Raman scattering. The intensity of the scattered radiation  $I$  is proportional to the square of  $\boldsymbol{\mu}_{ind}$

$$I \propto (\boldsymbol{\mu}_{ind})^2 = (\boldsymbol{\alpha}\mathbf{E})^2. \quad (2.33)$$

Applying the first order terms of equation (2.32) to this expression, the Raman scattering intensity  $I_{Ra}$  can be described.

Significant Raman intensity is observed for a normal mode  $k$  when the molecular polarizability  $\alpha$  changes along its normal coordinate  $Q_k$ ,

$$I_{Ra} \propto \left( \left( \frac{\partial \alpha}{\partial Q_k} \right)_0 Q_k \right)^2. \quad (2.34)$$

For a transition from an initial vibrational state  $|i\rangle$  to a final state  $|f\rangle$ , the transition moment  $[\alpha]_{fi}$  is defined as

$$[\alpha]_{fi} = \langle i | \alpha | f \rangle. \quad (2.35)$$

**Dispersion theory** Applying the Kramers-Heisenberg-Dirac dispersion theory (second order perturbation theory [102]), the matrix elements  $[\alpha_{\rho,\sigma}]_{fi}$  of the polarizability tensor can be expressed as

$$[\alpha_{\rho,\sigma}]_{if} = \frac{2\pi}{h} \sum_r \left( \frac{\langle f | \mu_\rho | r \rangle \langle r | \mu_\sigma | i \rangle}{(\nu_r - \nu_i) - \nu_0 + i\Gamma_r} + \frac{\langle f | \mu_\sigma | r \rangle \langle r | \mu_\rho | i \rangle}{(\nu_r - \nu_i) + \nu_0 + i\Gamma_r} \right), \quad (2.36)$$

for a transition from an initial vibrational state  $|i\rangle$  to a final state  $|f\rangle$ . The summation is performed over the vibrational states  $|r\rangle$  of all connecting vibronic states  $|r\rangle$ . The damping rate  $\Gamma_r$  correlates the lifetime of state  $|r\rangle$  and its spectral broadness.

## 2.4 The Resonance Raman Effect

If the excitation frequency  $\nu_0$  equals the frequency corresponding to an electronic transition  $|g\rangle \rightarrow |e\rangle$  of the analyte, the resonance condition is fulfilled (see fig. 2.1.1, middle panel). This phenomenon leads to a significant intensity enhancement of certain vibrational modes that are associated with the electronic transition and is called the resonance Raman effect.[70, 120]

**Albrecht vibronic theory** The summation over all other electronic transitions except the resonant transitions  $|r\rangle$  and the second term in equation (2.36) can be neglected in the resonant case, thus eqn. 2.36 simplifies to

$$[\alpha_{\rho,\sigma}]_{if} = \frac{2\pi}{h} \sum_{\nu_r} \left( \frac{\langle f | \mu_\rho | r \rangle \langle r | \mu_\sigma | i \rangle}{(\nu_r - \nu_i) - \nu_0 + i\Gamma_r} \right). \quad (2.37)$$

Application of the Born-Oppenheimer approximation allows the separation of the vibronic wave functions  $|i\rangle$ ,  $|r\rangle$ , and  $|f\rangle$  into the vibrational wave functions  $|\nu_i\rangle$ ,  $|\nu_r\rangle$ , or  $|\nu_f\rangle$  (with eigenfrequencies  $\nu_i$ ,  $\nu_r$  and  $\nu_f$ ), and the electronic ground and excited state wave functions,  $|g\rangle$  and  $|e\rangle$ , respectively

$$|i\rangle = |g\rangle |\nu_i\rangle \quad (2.38)$$

$$|r\rangle = |e\rangle |\nu_r\rangle \quad (2.39)$$

$$|f\rangle = |g\rangle |\nu_f\rangle. \quad (2.40)$$

The transition dipole moments in equation (2.37) can be expressed as

$$\langle f|\mu_\rho|r\rangle = \langle \nu_f|\langle g|\mu_\rho|e\rangle|\nu_r\rangle = \langle \nu_f|M_\rho|\nu_r\rangle \quad (2.41)$$

$$\langle r|\mu_\sigma|i\rangle = \langle \nu_r|\langle e|\mu_\sigma|g\rangle|\nu_i\rangle = \langle \nu_r|M_\sigma|\nu_i\rangle, \quad (2.42)$$

with the electronic transition dipole moments

$$M_\rho = \langle g|\mu_\rho|e\rangle \quad (2.43)$$

$$M_\sigma = \langle e|\mu_\sigma|g\rangle. \quad (2.44)$$

This leads to a simplified version of the resonant Raman tensor, where the electronic transition dipole moments  $M$  are effectively separated from the Franck-Condon factors  $\langle \nu_f|\nu_r\rangle$

$$[\alpha_{\rho,\sigma}]_{if} = \frac{2\pi}{h} \sum_{\nu_e} \left( \frac{\langle \nu_f|\nu_r\rangle M_\rho \langle \nu_r|\nu_i\rangle M_\sigma}{(\nu_r - \nu_i) - \nu_0 + i\Gamma_r} \right). \quad (2.45)$$

The inaccuracy of the Born-Oppenheimer approximation is compensated by expanding the electronic transition dipole moment into a Taylor series of the normal coordinates  $Q_k$ , the Herzberg-Teller equation.

$$M(Q) = M_0 + \sum_{k=1}^{3N-6} \left( \frac{\partial M}{\partial Q_k} \right)_0 Q_k + \dots \quad (2.46)$$

Inserting eqn. 2.46 into 2.45, one obtains

$$[\alpha_{\rho,\sigma}]_{if} = A + B + \dots \quad (2.47)$$

Here,  $A$  and  $B$  are the Albrecht terms:

$$A = M_{0\rho} M_{0\sigma} \sum_{\nu_e} \left( \frac{\langle \nu_f|\nu_r\rangle \langle \nu_r|\nu_i\rangle}{(\nu_r - \nu_i) - \nu_0 + i\Gamma_r} \right) \quad (2.48)$$

$$\begin{aligned} B = & M_{0\rho} \left( \frac{\partial M_\sigma}{\partial Q_k} \right)_0 \sum_{\nu_e} \left( \frac{\langle \nu_f|\nu_r\rangle \langle \nu_r|Q_k|\nu_i\rangle}{(\nu_r - \nu_i) - \nu_0 + i\Gamma_r} \right) + \\ & + \left( \frac{\partial M_\rho}{\partial Q_k} \right)_0 M_{0\sigma} \sum_{\nu_e} \left( \frac{\langle \nu_f|Q_k|\nu_r\rangle \langle \nu_r|\nu_i\rangle}{(\nu_r - \nu_i) - \nu_0 + i\Gamma_r} \right). \end{aligned} \quad (2.49)$$

The A-term depends on the overlap integrals  $\langle \nu_f|\nu_r\rangle$  (Franck-Condon factors) and becomes large for vibrational modes involving coordinates that change upon transition to the resonant state. In contrast, resonance enhancement through the B-term occurs when the resonant state couples to another vibronic state,

$$\langle \nu_r|Q_k|\nu_i\rangle \neq 0 \quad (2.50)$$

$$\langle \nu_f|Q_k|\nu_r\rangle \neq 0 \quad (2.51)$$

Both, the A and B-terms, contribute to the resonance enhancement.[2, 1, 120, 70, 75, 236]

## 2.5 Fourier-Transform Spectroscopy

Any kind of spectroscopy requires the decomposition of many superimposed plane waves of different frequencies into spectral components. In dispersive spectrometers, the scattered (Raman) radiation is decomposed by a grating, and subsequently projected on a detector element (typically a charge coupled device, CCD camera). An alternative way to decompose the electromagnetic radiation is Fourier-transform (FT) spectroscopy, a method which is routinely applied in IR spectroscopy (FTIR). Fourier-transform Raman spectroscopy (FTR), is less common than FTIR, because it is restricted to NIR excitation (see chapter 2.7). In FT spectrometers, the polychromatic radiation passes an interferometer and an interferogram (intensity  $I$  as a function of mirror position  $x$ ) is recorded. The interferogram is subsequently Fourier-transformed by a computer routine to yield the vibrational spectrum in the frequency domain. All vibrational spectra presented in this thesis were recorded with FT spectrometers (see figs. 3.5.1 and 3.6.1 for technical details).

**Fourier transformation** Fourier transformation is a mathematical operation that connects radiation intensity at a position in space  $I(x)$  with its spectral decomposition in the frequency domain (k-space)  $B(\nu)$

$$I(x) = \int_{-\infty}^{\infty} B(\nu) \cos(2\pi\nu x) d\nu \quad (2.52)$$

$$B(\nu) = \int_{-\infty}^{\infty} I(x) \cos(2\pi\nu x) dx \quad (2.53)$$

Generally, the FT determines the frequency components making up a continuous waveform. Experimentally, a discrete interferogram consisting of  $N$  values for light intensity as a function of  $N$  equidistant mirror displacement points is sampled ( $I(\Delta x)$ ). Thus, a discrete version of the FT has to be applied in practice,

$$B(k\Delta\nu) = \sum_{n=0}^{N-1} I(n\Delta x) \exp(i2\pi nk/N), \quad (2.54)$$

where the continuous variables  $x$ , and  $\nu$  are replaced by  $n\Delta x$  and  $k\Delta\nu$ , respectively.

**Advantages** FT spectroscopy has three major practical advantages over dispersive spectroscopy.

- **Fledgett (Multiplex) advantage** The Fourier transformation distributes the total noise over the entire spectral range, while in dispersive spectrometers, the full noise intensity is recorded at each data point. Thus, the signal-to-noise (S/N) ratio is higher by a factor of  $\sqrt{N}$  in a spectrum with  $N$  resolution elements ( $N$  is defined as the quotient of resolution and spectral range) measured with a FT spectrometer compared to the corresponding spectrum obtained with a dispersive spectrometer.[70, 236]
- **Jaquinot (Throughput) advantage** Dispersive spectrometers require a monochromator with a slit, which largely reduces the light throughput. Because FT spectrometers do not require the dispersion of radiation, these instruments can operate with large apertures and circular beam profiles, and consequently have a higher throughput.[70, 236]



- **Connes (Calibration) advantage** The interferogram produced by an internal Helium-Neon (HeNe) laser allows precise detection of the mirror position at all times. The wavenumbers are therefore accurately defined with respect to the HeNe zero-crossings and do not require further calibration.[70, 236]

On the other hand, the FT technique also bears drawbacks compared to the dispersive methods which have to be kept in mind when working with this method.

- **FT Parameters** The discrete FT (eqn. 2.54) only approximates the continuous FT, and can therefore lead to spectral artifacts, such as the picket-fence effect, aliasing and leakage. To overcome this drawback, additional corrections are introduced into the computational procedure, such as spectral apodisation or zero-filling.[65]
- **Resolution** While the spectral resolution of dispersive techniques depends on the grating, the optical pathlength and the resolution of the detector, in FT spectroscopy the accurate control of the mirror position and movement are crucial. To ensure interference, the mirrors and the beam splitter must be precisely adjusted such that the deviations from the ideal arrangement are considerably smaller than the shortest wavelength of the desired spectrum. Thus, FT methods are only practical in the IR region, where short wavelengths are on the  $\mu m$  length scales, but not for shorter, visible wavelengths.[70, 65]
- **Temporal resolution** In contrast to dispersive techniques, where the acquisition time for one spectrum is arbitrarily small, the minimal acquisition time of one FT-spectrum is equal to the time of one interferogram scan. In the conventional operation modus, one single interferogram is obtained within a few ms (rapid scan technique). One approach to overcome this limitation is the step scan technique, where the position of the mirrors is moved in discrete steps. Here, the process that is monitored in a time-resolved manner needs to be triggered at each fixed position and the time-resolved change of the interferogram at this mirror position is recorded.[70]

## 2.6 Time-Resolved Vibrational Spectroscopy

In contrast to many other analytical techniques like mass spectrometry, x-ray scattering or atomic force microscopy, vibrational spectroscopy can operate at moderate temperatures in the condensed phase and is generally non-destructive. Thus, IR and Raman spectroscopy are employed to investigate not only the structure of samples in physiological buffer solutions, cells or tissues, but also the reaction dynamics within these environments. In order to probe the dynamics of a reaction, a trigger event that starts the reaction needs to be synchronized with the subsequent detection of a time-resolved signal.[70]

**Trigger** Chemical reactions proceeding *via* the electronic ground state can be triggered either by a swift readjustment of the environmental conditions that change the chemical equilibrium (temperature or pressure jump) or by a temporal defined addition of a reactant. After this initial perturbation of the equilibrium, the relaxation can be monitored by a variety of techniques, e.g. vibrational spectroscopy. Other reactions require the electronically excited state, these can be triggered by absorption of a photon (see fig. 2.7.1, left panel). One example for an excited-state reaction is the Z/E isomerization in phytochromes (see also chapter 1.3). Compared to other trigger mechanisms, photochemical triggering is advantageous because modern light sources permit an unequaled spatial and temporal control of the trigger pulse.[253] These techniques are widely applied in both, RR and IR spectroscopy. In Raman spectroscopy, the development of femtosecond-pulsed Ti:sapphire laser systems in the visible region facilitated the investigation of ultrafast events such as the Z/E isomerisation of the phytochrome cofactor by femtosecond stimulated Raman spectroscopy (FSRS).[35] In IR spectroscopy, the development of tunable IR quantum cascade laser (QCL) systems extended the time resolution beyond the ns-time regime of step scan FTIR (see chapter 2.5). Ultrafast QCL-IR techniques were applied to the investigation of the primary events in the phytochrome photocycle.[248, 249]

**Flow-cell system** The most instructive way to obtain information about a time-resolved process is to apply a temporally defined sequence of pump and probe light pulses. However, time resolution can also be achieved by a spatial separation of the pump and the probe events. Hereby, the flowing sample solution with the velocity  $v$  first passes the pump laser spot and then the spatially separated ( $\Delta s$ ) probe laser spot. Hereby, continuous-wave (cw) lasers are employed. The delay time  $\Delta t$  between the pump and the probe events can be calculated accordingly,

$$\Delta t = \frac{\Delta s}{v}. \quad (2.55)$$

A schematic representation of such an experimental setup for RR spectroscopy is given in figure 2.6.1 (adapted from [70]).

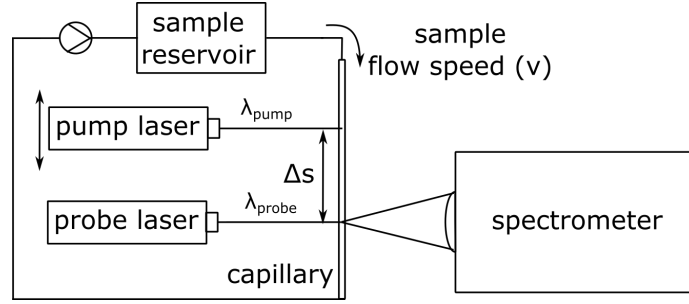


**Figure 2.6.1:** Pump-probe flow system for time-resolved RR spectroscopy with cw-laser excitation. The flowing sample (velocity  $v$ ) passes the pump laser spot and subsequently (after moving over a distance  $\Delta s$  in the time  $\Delta t$ ) the probe laser spot. The scattered radiation from the probe event is collected by collimation optics and focused into a Raman spectrometer.

According to eqn. 2.55, the maximum time resolution or minimum delay time  $\Delta t_{\min}$  of such a set-up can be achieved with maximum flow rate and when the distance between the pump and the probe laser spots  $\Delta s$  is minimal. Both laser spots cannot be infinitely focused, but have a certain radius  $r$  ( $r_p$  for the probe laser and  $r_P$  for the pump laser). Assuming a Gauss beam profile for both,  $r$  is defined as the distance from the center where the intensity is  $I(r) = I_0/e$ . Then the minimum delay time is

$$\Delta t_{\min} = \frac{r_p + r_P}{v}. \quad (2.56)$$

Another important parameter in the cw pump-probe flow system is the photochemical conversion rate of the sample in the pump laser spot  $\Delta t l_{0,P}$ , which is the product of the photochemical rate constant  $l_{0,P}$  at the pump wavelength  $\lambda_P$  and the residence time of the sample in the pump laser spot

$$\Delta t_P = \frac{2r_P}{v}. \quad (2.57)$$

To obtain minimum residual contributions of the initial state in the resulting spectrum, it is desirable to achieve maximum photoconversion during the residence time in the pump laser spot. The maximum photochemical conversion rate  $\Delta t l_{0,P}$

$$\Delta t_P l_{0,P} \propto \frac{\epsilon(\lambda_P) P_P \lambda_P}{r_P^2} \quad (2.58)$$

depends on the molecular extinction coefficient of the sample  $\epsilon(\lambda_P)$  at the pump laser wavelength  $\lambda_P$  and the pump laser power  $P_P$ . On the other hand,  $\Delta t_P l_{0,P}$  needs to be minimized in the probe laser ( $p$ ) spot to minimize the perturbation of the system by the measurement.

## 2.7 Application of Vibrational Spectroscopy to Phytochrome Samples

When static and time-resolved vibrational spectroscopy techniques are applied to phytochromes or other types of photoreceptors, the experimental procedures have to be adapted according to the photochemical properties of these molecules.

**IR difference spectroscopy** According to the IR selection rules (see chapter 2.2), normal modes which include a large change of the molecular dipole moment lead to strong IR absorption bands. In most proteins, this refers to normal modes which are dominated by C=O stretching coordinates of the protein backbone, termed amide I (ca. 1650 cm<sup>-1</sup>) and amide II (ca. 1530 cm<sup>-1</sup>) vibrations.[10] Especially the position and shape of the amide I band is sensitive to the protein fold, and the band envelope can be analyzed to obtain information about the secondary structure composition of the protein.[70, 10] In phytochromes, the C=O stretching of the carbonyl groups at rings A and D of the bilin contribute to this region, but the relative intensity compared to the amide I signal is small because the chromophore only comprises two oscillators of this type, while the number of C=O groups that contribute to amide I equals the number of amino acids. To obtain information about structural changes during the photocycle reactions, the IR spectra of two states of interest are compared. Therefore, absorbance (*ABS*) spectra before (1) and after illumination (2) are calculated from the transmitted intensity (*I*), where

$$ABS = \log_{10} \left( \frac{I}{I_0} \right). \quad (2.59)$$

Typical changes in a photoreceptor absorbance spectrum ( $\Delta ABS$ ) caused by such a procedure are small relative to the absolute absorbance *ABS* (in the order of  $\Delta ABS/ABS \approx 1/1000$ ), and therefore  $ABS_1$  and  $ABS_2$  seem very similar when compared directly.[70] To overcome this obstacle, IR difference spectra are calculated from the *ABS* spectra

$$IR_{diff} = ABS_2 - ABS_1. \quad (2.60)$$

Thus, in the  $IR_{diff}$  spectrum, negative features refer to the bleach of a signal originating from (1) and positive features attribute to (2).

**RR spectroscopy** Two broad bands are generally observed in the UV/visible absorption spectra of phytochromes, termed the Soret (300-450 nm) and the Q-band (550-800 nm), corresponding to electronic excitations (see fig. 1.3.4 for an exemplary absorption spectrum of SbPhyB). Thus, phytochromes are good candidates for RR spectroscopic measurements. Here, the RR effect can be used to enhance the chromophore bands over non-resonant protein bands, allowing the directed investigation of the chromophore structure. However, Q-band RR spectroscopy of phytochromes is experimentally challenging, because resonant irradiation does not only facilitate RR scattering, but also the absorption of  $h\nu_{UV/Vis}$  and excitation of the  $S_n$  state (fig. 2.7.1, left panel).

If the photon is absorbed instead of scattered, two competing processes aggravate RR spectroscopy of a defined state:

- **Fluorescence** The main problem of Q-band RR spectroscopy arises from the fluorescent decay of the  $S_n$  state (fig. 2.7.1, second panel). Phytochromes are fluorescent in the Pr state (see chapters 7.1 and 7.2), and the fluorescence background is in most cases stronger than the RR signal by several orders of magnitude.[70] This problem can be overcome by shifted-excitation Raman difference spectroscopy (SERDS).[4] The interference of fluorescence can be also minimized by Soret-band excitation, because fluorescence occurs predominantly from the lowest excited state (Q-band) after fast relaxation from the higher (Soret) levels (Kasha's rule).[70] Thus, the spectral overlap of fluorescence and the RR signals is negligible for Soret-band excitation.[236, 40]
- **Photochemistry** Additionally, the  $S_n$  state can also photochemically react to the Lumi\* state *via* crossing of a conical intersection (fig. 2.7.1, right panel). Consequently, the state of interest (Pr or Pfr) is depopulated and thus the RR signal will decrease. Additionally, other intermediate or parent states will be populated and appear in the spectrum, thus no pure spectrum can be obtained. Usually, cryogenic conditions are applied to prevent photochemical interconversion, because the Lumi-state formation exhibits a thermal barrier.[4] Hence pure Pr and Pfr spectra can be obtained at  $-140^\circ\text{C}$  and  $-195^\circ\text{C}$ , respectively (see chapter 1.3).[40]

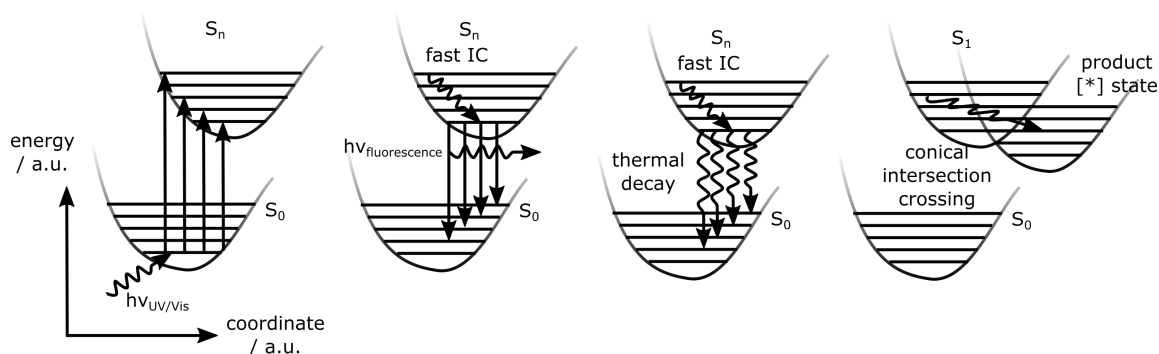


**Figure 2.7.1:** Jablonski diagram of excited-state processes in phytochromes. After absorption of a resonant photon  $h\nu_{UV/Vis}$ , the vibrational levels of the electronically excited state  $S_n$  are populated according to the Franck-Condon principle. After fast internal conversion (IC) to the vibrational ground state of  $S_n$ , the further decay to  $S_0$  proceeds either under emission of a fluorescence photon  $h\nu_{fluorescence}$  or thermally without the emission of radiation (middle panels). A competing process is a photochemical reaction in the excited state (right panel) *via* conical intersection crossing. In phytochromes, this corresponds to the Z/E isomerisation reaction, yielding the Lumi\* state.

**Pre-resonant excitation** An alternative approach is the excitation with a laser that is not directly in resonance, but close to a resonant transition (pre-resonant).[69] There is no sharp borderline between non-resonance Raman and RR scattering. When the frequency dependence of the Raman intensity  $I_{Ra}$  under strict non-resonant conditions and the intensity provided by the A-term enhancement mechanism  $I_{RR}$  are compared, an expression for the frequency dependent resonance enhancement  $I_{RR}/I_{Ra}(\nu_R)$  can be obtained[1, 70]

$$\frac{I_{RR}}{I_{Ra}} \propto \frac{(\nu_0 - \nu_k)^2(\nu_0^2 + \nu_R^2)}{(\nu_R^2 - \nu_0^2)^2} \quad (2.61)$$

Here,  $\nu_R$  is the excitation frequency,  $\nu_0$  the frequency of the electronic transition and  $\nu_k$  the frequency of the normal mode of interest.  $I_{RR}/I_{Ra}(\nu_R)$  decays when the difference  $\nu_R^2 - \nu_0^2$  is large, thus low enhancement is still observed when the resonance condition is not strictly fulfilled (2-3 orders of magnitude, compared to 5-6 orders of magnitude under strictly resonant conditions).

**FT-Raman spectroscopy** A common experimental solution is to use the 1064 nm line of a neodymium-doped yttrium aluminum garnet (Nd:YAG) solid state laser. While the 1064 nm laser does not induce fluorescence or unwanted photochemical processes, this wavelength still is in (pre-)resonance with the first electronic transition (Q-band) of the bilin chromophores. The resonance enhancement of the bilin Raman bands is sufficient for an effective discrimination from the (non-resonant) Raman bands of the much larger apoprotein, so that almost exclusively Raman signals of the chromophore are observed in the spectra.[69] Thus, these spectra are termed as RR spectra in the following. Furthermore, the NIR wavelength of the Raman laser permits the use of the FT technique (see chapter 2.5) and all Raman spectra that are presented in this thesis were acquired with an FT-Raman spectrometer (see chapter 3.5 for a detailed description of the experimental set-up).

**RR spectral regions** Relevant vibrational bands of the bilin chromophores appear in the region between 400 and 1800  $\text{cm}^{-1}$ . However, not all parts of this spectral range are equally informative. Different regions allow conclusions with respect to different aspects of the chromophore geometry and chemical structure (protonation state).[236]

- **1500-1800  $\text{cm}^{-1}$**  The marker region is particularly important because the position and intensity of the C=C stretching modes between 1590 and 1640  $\text{cm}^{-1}$  carries information about the geometry of the methine bridges.[69] Furthermore, the the protonation state (cationic vs. neutral form of the tetrapyrrole) is reflected by the existence or absence of N-H in-plane (NH i.p.) bending modes of rings B and C between 1550 and 1590  $\text{cm}^{-1}$ . This mode is strongly H/D sensitive, and the corresponding N-D peak is found between 1050 and 1080  $\text{cm}^{-1}$ . [99] The N-H i.p. modes of the rings A and D couple with the C=C stretching coordinates in these rings and the adjacent methine bridges, thus these modes are also H/D sensitive.

The C=O stretching vibrations of the ring A and D carbonyl groups are found at higher frequencies (1680 - 1740  $\text{cm}^{-1}$ ) with considerably lower intensity than the C=C stretching modes. These modes are very sensitive to the chemical environment of the carbonyl groups and are also found in the respective IR difference spectra.[40]

- **1000-1500  $\text{cm}^{-1}$**  This region includes in-plane modes of the tetrapyrrole carbon-skeleton and the ring substituents. The underlying modes include a large number of different internal coordinates and it is therefore difficult to extract structural information from this spectral region.[236] The identification and comparison of RR bands can be further complicated in some cases due to the interference of Raman bands from the apoprotein (mostly amide III).[236, 40] The symmetric ring breathing mode of phenylalanine (Phe) is found at  $1004 \text{ cm}^{-1}$ . The intensity of this band is a reliable reference to determine the relative RR scattering cross section of the chromophore of parent states or intermediates.[40]
- **600-1000  $\text{cm}^{-1}$**  This spectral region includes torsional and out-of-plane (OOP) modes that are sensitive towards subtle changes in the methine bridge conformations. Especially in the Pfr state, the most prominent feature is the hydrogen-out-of-plane (HOOP) mode of the C/D methine bridge which shows an inverse correlation with the  $C_{15} = C_{16}$  torsional angle.[183] Additionally, modes involving the propionate side chains and S-C stretching modes contribute to this region.[236, 40]

**Time resolved RR spectroscopy** The transitions between the photocycle states in phytochromes occurs on time scales from femtoseconds (photon absorption and population of the excited state) to hours or even days (thermal relaxation of the parent states in plant phytochromes). Obviously, it is hardly possible to cover 15 orders of magnitude in time with one single experimental set-up. Thus it is necessary to design time-resolved methods that are suitable for the investigation of specific time windows of interest. While ultrafast IR and Raman techniques are suitable to investigate the primary events in the excited and Lumi states[248, 35], they fail at longer time scales, and do not access the later photocycle intermediates such as the Meta states. However, the dynamic interconversion of the Meta states is of interest for the molecular mechanism of signal transduction throughout the protein.[216, 22] One fundamental problem with time-resolved studies of phytochromes is the bi-stability in the Pr and Pfr states and the slow thermal relaxation of the parent states (seconds to days). Most time-resolved techniques suffer from a low S/N ratio which can only be overcome by repeated signal accumulation. Hence, the samples are excited multiple times, and in phytochromes this leads to an unwanted accumulation of meta-stable states during the measurements. If the waiting time between two repeated measurements is adjusted to match the thermal relaxation and to ensure fresh sample conditions, the calculated duration of an experiment is not feasible (days) and additionally sample degradation becomes a major problem.[22] Thus, pulse-based time resolved RR or IR techniques that are applied routinely to other photoreceptors like retinal proteins[143, 70] can not be readily transferred to phytochromes. Another approach is the application of a flow-cell system with a sample reservoir as described in chapter 2.6 (see fig. 2.6.1). Here, the fresh sample conditions are ensured by photochemical back-conversion in the reservoir. Such a set-up was developed and applied to the two Bphs Agp1 and Agp2 in this thesis (chapter 6.1, and technical details are given in the supplementary section 9.3).

### 3 Materials and Methods

#### 3.1 Phytochrome Samples

All purified phytochrome samples were kindly provided by co-workers from the Friedrich and Hildebrandt groups and by collaborators from other research institutes. An overview of all investigated phytochrome variants is given in table 3.1. IRFP constructs are listed separately in table 3.2.

Protein	Organism	Cofactor	Domains
Agp1	<i>Agrobacterium fabrum</i>	BV	PAS-GAF-PHY-HK (FL)
		BV	PAS-GAF-PHY (PGP)
		BV	PAS-GAF (PG)
Agp2	<i>Agrobacterium fabrum</i>	BV	PAS-GAF-PHY (PGP)
RpBphP2	<i>Rhodospseudomonas palustris</i>	BV	PAS-GAF (PG)
AtPhyB	<i>Arabidopsis thaliana</i>	PCB	NTE-PAS-GAF-PHY (PSM)
		PCB	PAS-GAF-PHY ( $\Delta$ NTE)
SbPhyB	<i>Sorghum bicolor</i>	PCB	PAS-GAF-PHY (PGP)
		PCB	PAS-GAF (PG)
IsPadC	<i>Idiomarina</i> sp.A28L	BV	PAS-GAF-PHY-DGC (FL)
		BV	PAS-GAF (PG)
Slr1393	<i>Synechocystis</i> sp.PCC6803	PCB	GAF3 (GAF3)

**Table 3.1:** List of investigated phytochrome samples. Organism, respective tetrapyrrole cofactor and different available truncation constructs are listed for each protein. The nomenclature that is used throughout the thesis for specific constructs is given in brackets.

**Agp1** Samples of the prototypical *Agrobacterium fabrum* phytochrome 1 (Agp1) were kindly provided by Norbert Michael from the Hildebrandt group (TU Berlin). Molecular cloning, heterologous over-expression in *E. coli*, purification *via* Ni-NTA affinity chromatography and *in-vitro* chromophore (BV) assembly were performed as described elsewhere.[110] Three different protein constructs were investigated:

- **Agp1 FL**, the full length protein contains the photosensory module (PAS-GAF-PHY) and the catalytic output module, a histidine kinase (HK) domain. The protein contains 754 amino acids (87 kDa) and forms dimers in solution. In the literature, this construct is sometimes termed Agp1-M1 (mutant 1).[159]
- **Agp1 PGP** refers to the PAS-GAF-PHY construct, containing only the photosensory module (PSM). This deletion mutant contains 504 amino acids (56 kDa) and forms dimers in solution. In the literature, this construct is sometimes termed Agp1-M15.[159]
- **Agp1 PG** refers to the PAS-GAF construct. This deletion mutant contains 313 amino acids (33 kDa). In the literature, this construct is sometimes termed Agp1-M20.[159]



**Agp2 PGP** Samples of the bathy *Agrobacterium fabrum* phytochrome 2 (Agp2) were also kindly provided by Norbert Michael (TU Berlin). Molecular cloning, heterologous over-expression in *E. coli*, purification *via* Ni-NTA affinity chromatography and *in-vitro* chromophore (BV) assembly were performed similar to Agp1.[110] Only the PAS-GAF-PHY construct, a truncated protein lacking the natural response regulator module (Rec), was investigated (507 amino acids, 57 kDa). In the literature, this construct is sometimes termed Agp2-M2.[256]

**RpBphP2** *Rhodospseudomonas palustris* bacteriophytochrome 2 (RpBphP2, short:P2) samples were provided by Dr. Neslihan Tavraz, Luisa Sauthof, Nico Herder, Svea Wilkening and Mario Willoweit from the Friedrich group (TU Berlin). Molecular cloning, heterologous over-expression in *E. coli* and purification *via* Ni-NTA affinity chromatography were performed as described elsewhere.[232, 23] The PAS-GAF construct (316 amino acids, 37 kDa) and the following mutant proteins were investigated:

- D202T, Y258F, D202T/I203V, D202T/Y258F, D202T/I203V/Y258F (see chapter 7.1)
- D202H, D202N, Y258F/D202N (see chapter 9.5)

**Slr-GAF3** Samples of the red/green Cyanobacteriochrome Slr1393 from *Synechocystis* sp.PCC6803[243] were kindly provided by Svea Wilkening from the Friedrich group (TU Berlin). The cloning and purification procedure is given in the supplementary section 9.2. The Slr1393 full-length protein contains 577 aa (GenBank entry BAM50929.1). Only the third GAF domain (160 aa from 417 to 577) is capable to bind PCB and exhibits the characteristic red/green photochemistry. The spectral properties of Slr-1393 are unchanged when the other protein domains are cleaved and GAF3 is investigated separately.[243] Therefore, only this domain, denoted Slr-GAF3 in the following, was used for all experiments in this thesis.

**AtPhyB** *Arabidopsis thaliana* phytochrome B (AtPhyB) and phytochrome interaction factor 3 (PIF3) were kindly provided by Dr. Silke von Horsten and Christine Kupschus from the group of Prof. Dr. Lars-Oliver Essen (Philipps-Universität Marburg). Heterologous protein expression in *E. coli* and purification were performed according to previous studies.[76, 62] Although P $\Phi$ B is the natural chromophore for plant phytochromes, co-expression with PCB (fig. 1.2.1) yields a photoactive holo-protein.[76] Two protein constructs were investigated: the PSM (651 aa, 72.6 kDa) and a protein variant lacking the N-terminal extension domain ( $\Delta$ NTE), which is equivalent to the PGP variant of SbPhyB. The NTE comprises the first 90 aa of the sequence, hence the resulting SbPhyB  $\Delta$ NTE construct has a remaining sequence length of 561 aa (63.5 kDa).

**SbPhyB** Samples of *Sorghum bicolor* phytochrome B (SbPhyB) were kindly provided by Dr. Soshichiro Nagano from the group of Prof. Dr. Jon Hughes (Justus-Liebig-Universität Gießen). The PGP construct is analogous to the AtPhyB ( $\Delta$ NTE) discussed in section 4.1, the notation was changed in chapter 4.3 to emphasize the difference to the PG construct. The expression and purification conditions are analogous for the PGP and PG variants and given in chapter 4.1.[231] SbPhyB PGP and PG contain 542 and 338 aa, respectively (60.4 and 38.8 kDa).

**IsPadC** *Idiomarina sp. A28L* phytochrome-activated di-guanylyl cyclase (IsPadC)[61] samples were kindly provided by Geoffrey Gourinchas from the group of Prof. Dr. Andreas Winkler (TU Graz). Two different protein variants were investigated, the FL (683 amino acids, 78 kDa) and a PG truncation construct (containing the first 312 aa of FL, 36 kDa). The protein expression and purification conditions are described elsewhere.[61]

### 3.2 iRFP Samples

All samples of infrared fluorescent proteins (iRFPs) derived from phytochromes were provided by Dr. Neslihan Tavraz, Luisa Sauthof, Nico Herder, Svea Wilkenning and Mario Willoweit from the Friedrich group (TU Berlin). DNA for the variants iRFP682 SC, iRFP682 CS, iRFP670 SC, iRFP670 CS, iRFP702, iRFP713 and iRFP720 were kindly provided by Prof. Dr. Vladislav V. Verkhusha and Dr. Daria Shcherbakova (Einstein College, New York). Further molecular cloning, heterologous over-expression in *E. coli* and purification *via* Ni-NTA affinity chromatography were performed as described in chapters 7.1 and 7.2.[23]

Construct	Derived from	AA exchange	Nomenclature	Chapter
iRFP713	RpBphP2		iRFP	7.1
		T202D	iRFP T202D	
		F258Y	iRFP F258Y	
		T202D/F258Y	iRFP T202D/F258Y	
		T202D/V203I	iRFP T202D/V203I	
		T202D/V203I/F258Y	iRFP T202D/V203I/F258Y	
iRFP682	RpBphP2		iRFP682 CC	7.2
		C249S	iRFP682 CS	
		C15S	iRFP682 SC	
		C15S/C249S	iRFP682 SS	
iRFP720	RpBphP2		iRFP720	9.5
iRFP670	RpBphP6		iRFP670 CC	9.5
		C244S	iRFP670 CS	
		C10S	iRFP670 SC	
		C10S/C244S	iRFP670 SS	
iRFP702	RpBphP6		iRFP702	9.5

**Table 3.2:** List of investigated iRFP constructs. The native Bphs used as templates for for iRFP design and available mutant proteins with the corresponding nomenclature are listed. iRFP720, 702 and 670, including the Cys/Ser exchange mutants are not discussed in the main part of the thesis, spectroscopic data is included in the supplementary section 9.5.

All iRFPs were derived from native phytochromes by truncation of the output module and the PHY domain, yielding PAS-GAF constructs (see fig. 1.3.1). Additionally, multiple amino acid residues are substituted, resulting in proteins with strongly altered photophysical properties.

The aligned protein sequences of all investigated iRFPs and their natural origins are given in the supplementary section 9.5. The investigated proteins can be organized in three different categories as follows:

- Binding pocket mutant proteins derived from iRFP713. Here amino acids in the chromophore binding pocket were selectively exchanged to probe the influence on the chromophore structure and fluorescence properties (see chapter 7.1).
- Cys/Ser exchange mutant proteins derived from iRFP682. Here the amino acids cysteine and serine were selectively interchanged to probe the effect on the chromophore attachment, geometry and fluorescence quantum yield (see chapter 7.2).
- Further proteins: the UV/Vis and RR spectra of iRFP670 and its variants, iRFP702 and iRFP720 are given in the supplementary section 9.5.

### 3.3 Sample Handling

After expression and purification, all samples were flash frozen in liquid  $N_2$  and further stored at  $-80^\circ\text{C}$ . All buffers were stored at  $4^\circ\text{C}$ . During preparation steps like centrifugation or buffer exchange, the samples were kept at  $4^\circ\text{C}$ . All sample preparation steps and spectroscopic measurements were performed under dim green light illumination (room illumination with light-emitting diodes (LEDs) of defined wavelength  $\lambda_{max} = 515\text{--}530\text{ nm}$  and half-width broadness  $\Delta\lambda = 20\text{ nm}$ ) to avoid unwanted photochemical processes.

**Buffers** Except for IsPadC, all phytochrome and iRFP samples were prepared in Tris buffer containing 50 mM TrisCl, 5 mM EDTA and 300 mM NaCl, adjusted with HCl and NaOH to  $\text{pH}=7.8$ .  $\text{D}_2\text{O}$  buffer was prepared with the use of 99.95%  $\text{D}_2\text{O}$  (Deutero GmbH). In  $\text{D}_2\text{O}$  buffer, the corresponding  $\text{pD}=7.8$  was adjusted with DCl according to equation 3.1 to an apparent  $\text{pH}$  of 7.4.

$$\text{pD} = \text{pH}_{app} - 0.4 \quad (3.1)$$

Accurate determination of the final  $\text{pH}(\text{pD})$  was performed with a  $\text{pH}$  meter (Denver Instruments, Model 225). To stay consistent with previous (H/D exchange-mass spectrometry and kinetic) studies[61], IsPadC samples were prepared by Geoffrey Gourinchas in a buffer containing 10 mM HEPES, 500 mM NaCl and 2 mM  $\text{MgCl}_2$  ( $\text{pH}=7.0$ ), or the appropriate  $\text{D}_2\text{O}$  buffer.

**Centrifugation** To optimize the signal-to-noise (S/N) ratio in the RR and IR experiments, the protein concentration was often increased by spinning in millipore filters (Amicon, 10 or 30 kDa depending on protein size) at about 1000 g for 30 to 60 minutes (Eppendorf centrifuge 5424 R). For some experiments the concentration had to be decreased by dilution in buffer, and all concentration adjustments were performed immediately prior to the measurements.

The final protein concentration was determined *via* UV/VIS measurements by analyzing the protein absorption at the protein peak (280 nm, absorption of aromatic amino acids) and the Q-band maximum (650-750 nm), depending on the molecular properties of the analyte and the planned experiment. For the time-resolved RR measurements the concentration was limited by viscosity and the degradation in the tubing and flow cell and was adjusted to an OD=10 at the Q-band absorption maximum corresponding to a concentration of 7 mg/mL for the Agp1 and Agp2 PGP constructs (see section 9.3). For the static cryo-RR and IR experiments, the concentration was up to 10x higher, depending on the size and solubility of the investigated protein. For the interaction experiments of AtPhyB with PIF3, the concentrations were considerably lower, and were calculated from the complex dissociation constant  $K_D$  (see chapter 4.2).

**H/D exchange** When exposed to D<sub>2</sub>O buffer, the chromophore pyrrolic protons exchange within minutes (or faster) with deuterons, except for bathy phytochrome samples, which exhibit a sequential H/D exchange behaviour.[228] Preparation of a sample in D<sub>2</sub>O buffer included three washing steps with 20x excess buffer in the same centrifugal filter units that were also used for the sample concentration procedure. Typically 20  $\mu$ L sample were centrifugated three rounds with 400  $\mu$ L buffer solution. H<sub>2</sub>O buffer exchange for samples that were prepared in different buffer (e.g. GAF3 was prepared in PBS buffer and later exchanged to Tris H<sub>2</sub>O buffer) proceeded in the same manner. The protein backbone protons generally exchange at slower time scales[227, 40], thus the procedure was adjusted for IR sample preparation. Here, two rounds of washing were preceded by overnight storage in 20x excess amount of buffer, and the last round of centrifugation followed on the next day. All D<sub>2</sub>O RR spectra shown in this thesis were recorded immediately after the last step of the re-buffering procedure.

**Sample illumination** All phytochrome samples are to some extent photoactive. Static photoproduct spectra were generated by illumination of the samples with a variety of different light sources, always according to the absorption properties. The light source and length of the illumination period always depended on the sample and were specifically adjusted to achieve maximal photo conversion. If the photo conversion was incomplete (visible residual contributions of dark-adapted state signals in the spectrum), another illumination period was added, until no differences were observed. All red/far-red samples were interconverted with LEDs and laser diodes with emission maxima at 660 nm, 750 nm, 780 nm (LEDs and LED arrays), or 685 nm and 785 nm (laser diodes). Typical illumination times were around 2 minutes (LEDs) or 10 seconds (laser diodes). The red/green photoreceptor Slr1393 GAF3 was interconverted with a green LED array (530 nm) and the same red-light sources described before. The spectral halfwidth of the light sources was typically 20 nm (LEDs) or 1 nm (laser diodes).

### 3.4 UV/Vis and Fluorescence Spectroscopy

**UV/Vis Absorption** The room-temperature absorption measurements were performed using either a Cary 50Bio- or a Cary 1E Varian spectrophotometer (Agilent Technologies) operated with the corresponding Agilent-Cary software package. Protein solutions were measured in UV quartz cuvettes with total volumina of 500  $\mu\text{l}$  and an optical pathlength of 1 cm (Blaubrand QS 1.000). Samples were diluted in the according buffer to an  $OD_{280} < 1$ , corresponding to a protein concentration of 1-2  $\mu\text{M}$ . In case of Slr-GAF3 cryo absorption measurements (chapter 5.1), a  $\text{N}_2$ -cooled cryostat (Oxford instruments) under protective Argon atmosphere was placed in the Cary 1E spectrometer. For these measurements, disposable polymethylmethacrylate (PMMA) semi-micro cuvettes with an optical pathlength of 1 cm were used (BRAND). Appropriate  $\lambda^4$  baselines were subtracted from some UV/vis spectra to correct the baseline for the effects of scattering in dense samples.

**Fluorescence Spectroscopy** Static fluorescence measurements for the determination of fluorescence quantum yields and spectra were performed with a Fluoromax 2 spectrophotometer (Horiba Scientific), and the according software. Parameters of individual experiments are specified in the according sections (7.1 and 7.2).

### 3.5 FT-Raman Setup

**FTR Setup** All RR spectra were recorded with a fourier transform (FT)-Raman spectrometer RFS100/S (Bruker GmbH) equipped with an cw diode-pumped Nd:YAG laser (DPY 301 II0.50 EM, Coherent) at 1064 nm with a line width of  $< 1 \text{ cm}^{-1}$ . Scattered light was collected in an  $180^\circ$  angle orientation of incident light (back-scattering geometry). Contribution of elastically scattered laser light (Rayleigh scattering) was mainly eliminated with a notch filter module between the interferometer and the detector. The remaining inelastically scattered radiation (Stokes Raman scattering) was detected with a liquid  $\text{N}_2$  cooled germanium element. The RFS 100/S spectrometer is equipped with a Rocksolid interferometer with rocking corner mirrors. Further technical details are shown in a schematic drawing of the spectrometer (fig. 3.5.1).

**Cryo-trap protocol** The experimental FT-RR protocol and setup were adapted from previous works[40, 236], and were established mostly by Prof. Dr. Peter Hildebrandt, Dr. David von Stetten and Dr. Francisco Velázquez Escobar. Specific details of non-standard experiments are indicated in the respective results section. For each measurement about 6.5  $\mu\text{l}$  of protein solution were used. The selected measurement temperatures ( $-140^\circ\text{C}$  or  $-190^\circ\text{C}$ ) prevent any undesired thermal conversion during RR spectra accumulation (see sections 1.3 and 2.7). The laser power was set to 800 mW by the spectrometer software (OPUS) and was measured 690 mW at the sample (determined with a COHERENT FieldMax-II power meter with PM100-19C sensor). To monitor possible laser induced damages, samples were measured several times and over long time periods. Despite the strong laser power, no changes in the spectra could be detected, even after a series of spectra. The spectral resolution of the spectrometer was set to  $4 \text{ cm}^{-1}$ . For a single spectrum, generally 2000 interferometer scans were averaged prior to the Fourier transformation.

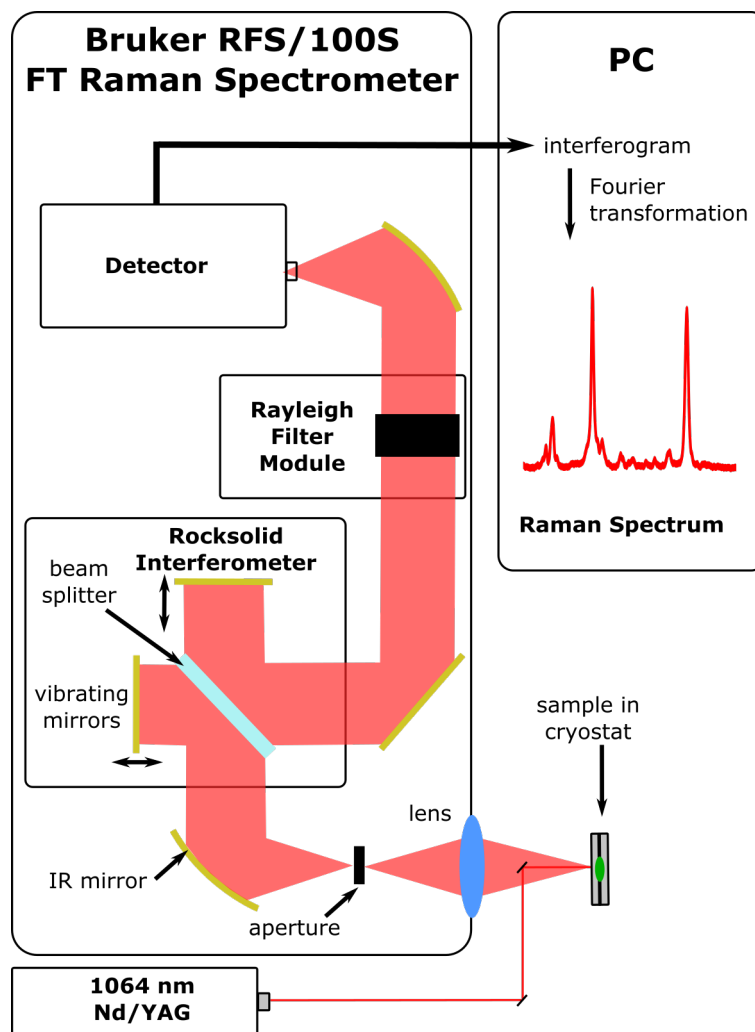


**Figure 3.5.1:** Schematic drawing of the Bruker RFS/100S FTR spectrometer. 1064 nm NIR laser light was focused on a sample in a Linkam cryostat (or on a capillary in the case of time-resolved measurements, see chapter for 9.3 details). The scattered NIR radiation was focused by a lens, passes the interferometer and the Rayleigh filter module and was detected by a liquid nitrogen cooled germanium element. The recorded interferogram was processed by a PC to yield the RR spectrum.

**TR-FTR setup** To obtain time-resolved (TR)-RR spectra, the RFS100/S spectrometer was equipped with a sample flow cell and a spatially adjustable cw-pump laser. The time resolution (max. 8 ms) was adjusted by flow speed, laser spot size and the spatial distance between pump and probe laser spots. After the pump-probe process, the sample was photochemically converted back to the dark state to achieve fresh sample conditions. Although protein concentration in the TR experiments was lower by a factor of 10, all other parameters (laser power and FT-parameters) were similar to the cryo-trap experiments. A detailed description of the development and the final setup parameters is given in chapter 9.3.

## 3.6 FT-IR Setup

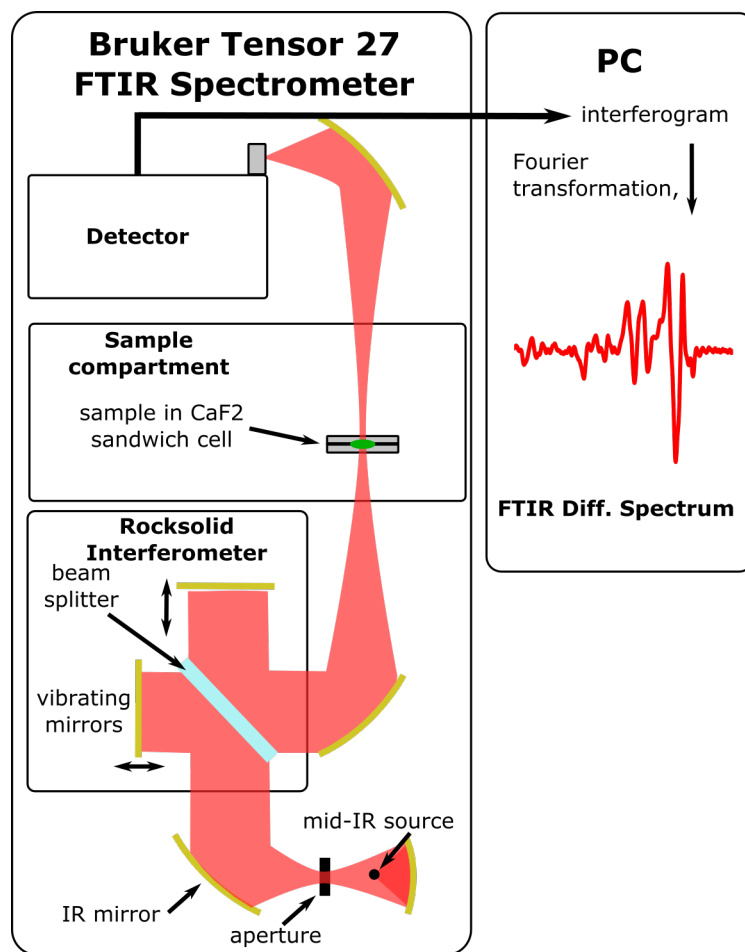


**Figure 3.6.1:** Schematic drawing of the Bruker Tensor27 FTIR spectrometer. Here, the mid-IR radiation emitted by a globar passed the interferometer unit before transmission through the sample, which was placed in a CaF<sub>2</sub> sandwich cell. The transmitted IR radiation was focused by a mirror and detected by a liquid nitrogen cooled MCT detector. The interferogram is processed by a PC to obtain an IR absorbance spectrum.

**Difference-IR setup** All IR spectra were recorded in a TENSOR 27 FTIR spectrometer (Bruker). A schematic drawing of the spectrometer is given in figure 3.6.1. All IR measurements given in this work were performed at room temperature in transmission mode: polychromatic infrared radiation emitted by a globar was focused on the sample after passing through a Rocksolid interferometer. The IR signal was recorded with a liquid N<sub>2</sub> cooled MCT detector. The following protocol for photo-induced difference-IR measurements was developed and established by Dr. Francisco Velázquez Escobar, Prof. Dr. Friedrich Siebert and Lars Paasche and is described elsewhere in more detail.[40] 2  $\mu$ L of protein sample (preparation identical to RR) were deposited on a CaF<sub>2</sub> window with a 2  $\mu$ m deepening and the sample film was sealed with a plain CaF<sub>2</sub> window. To avoid sample dehydration, additional isolation of the sample was provided by a thin layer of silicone grease between both windows around the sample. The CaF<sub>2</sub> sandwich cell was placed in a suitable window holder. Unlike the FTR conditions, sample photo conversion was achieved by light exposure during data accumulation and automatically executed and processed via an OPUS macro script developed by

Dr. Francisco Velázquez Escobar and Lars Paasche.[40] After a stabilization period of 3 h (monitored by continuous acquisition of IR spectra), a series of 5 spectra (each 200 scans) was recorded per illumination period. After a short period of dark relaxation (200 scans or 88 seconds), the illumination wavelength was changed and a second series of 5 spectra was recorded, to investigate whether the photoswitching process is reversible. The whole experiment was repeated twice to ensure reproducibility.

**Data treatment** Analysis and treatment of RR and IR data was performed using the OPUS software (Bruker) and the Origin software package (Origin labs).[151] Prior to the Fourier transformation, bad interferogram scans were automatically discriminated, a zero filling was added to the interferogram and an apodization function was multiplied. In the case of RR experiments, a trigonal apodization function and a zero filling factor of 2 were used. IR spectra were apodized with a Blackman-Harris 3-Term function and the zero filling factor was set to 4. For RR spectra, the background and baseline effects were corrected manually with a polynomial function. Spectra were cut to the region of 400-2000  $\text{cm}^{-1}$  and normalized to the peak with the highest intensity. For IR spectra, atmospheric compensation was performed for each spectrum using the OPUS software package. Subsequently, the difference spectra were calculated using the absorption spectrum prior to irradiation as reference and subtracting it from the irradiated absorption spectrum (see section 2.7). Subsequent background correction of the IR difference spectrum was performed manually using a linear background in the region of 1000-2000  $\text{cm}^{-1}$ .

### 3.7 Figure Notation

All figures containing vibrational or electronic spectra were generated using the Origin[151] software package. Further graphical modifications were included with the Inkscape software package (Inkscape project).[82]

- **Black color** indicates that this spectrum was recorded in  $\text{H}_2\text{O}$  buffer.
- **Red color** indicates that this spectrum was recorded in  $\text{D}_2\text{O}$  buffer.
- **Blue spectrum** indicates that an additional reagent was added to the solution, e.g. phytochrome interaction factor 3 (PIF3, see chapter 4.2) or imidazole (see chapter 9.2).
- **Gray spectrum** indicates the measurement of apoprotein or other non-resonant samples (e.g. buffer or PIF3).

Notation for the vibrational mode composition in each spectrum is shortened as follows:

- **A, B, C** or **D** refers to modes localized in the corresponding pyrrole ring,
- **A,B, B,C** or **C,D** indicates C=C stretching modes of the methine bridges,
- **i.p.** terms all in-plane vibrational modes,
- **OOP** denotes the general description for out-of-plane bending vibrations
- **HOOP** indicates solely **OOP** vibrations involving C-H groups of the methine bridges.



---

## 4 Results: Plant Phytochromes

The following section comprises three spectroscopic studies of plant phytochrome B from the dicotyledon *Arabidopsis thaliana* (AtPhyB) and the monocotyledon *Sorghum bicolor* (SbPhyB). The three studies investigated different parameters that fine-tune the structure of the bilin chromophore (PΦB and PCB) in the Pr and Pfr states and the interconversion between them. Here, special emphasis is laid on factors that influence the conformational equilibrium in the Pfr state (Pfr-I and Pfr-II) and the implications on the dark-relaxation reaction.

Chapter 4.1 contains a publication that focuses on the influence of the N-terminal extension domain (NTE) on the structure of PCB and PΦB in AtPhyB and SbPhyB. This study aimed to explore whether and how the presence or absence of the NTE influences the chromophore structure in the Pfr and Pr states. Here, RR spectra of full-length PSM constructs and NTE-deletion mutants were comparatively analyzed. These considerations are logically continued in a second study (chapter 4.2), where the influence of the transiently binding phytochrome interaction factor 3 (PIF3) on PCB-AtPhyB are investigated. The structural changes of PCB that are caused by PIF-binding are compared to the findings from the NTE-deletion study with a focus on the same RR spectral marker bands.

In a third part, the role of the PHY-domain for the photoproduct formation in PCB-SbPhyB is investigated (chapter 4.3). Here, vibrational spectra of the PAS-GAF-PHY (PGP) and PAS-GAF (PG) variants are analyzed in solution and in protein crystals. The RR and IR spectra of the PG photoproduct are compared to the Pfr and Meta-Rc states of the PGP construct, and the photoactivation *in crystallo* is discussed.

#### 4.1 Structural Communication of Plant PhyB with the N-terminal Extension

This research was originally published in FEBS letters:

F. Velázquez Escobar, D. Buhrke, M. Fernández López, S. M. Shenkutie, S. von Horsten, L. O. Essen, J. Hughes, and P. Hildebrandt. *Structural communication between the chromophore-binding pocket and the N-terminal extension in plant phytochrome phyB*. in: *FEBS Letters* **Volume 591**. Issue 9 (2017), pp. 1258–1265. DOI: 10.1002/1873-3468.12642

- Francisco Velázquez Escobar, **David Buhrke** and Maria Fernández López performed RR experiments.
- Sintayehu Manaye Shenkutie and Silke von Horsten prepared the samples.
- Peter Hildebrandt, Lars-Oliver Essen and Jon Hughes conceived and supervised the study and wrote the manuscript.
- All the authors discussed the results and commented on the manuscript.

© Reprinted with permission of John Wiley and Sons publishing (license number 4427081118525).

## Structural communication between the chromophore-binding pocket and the N-terminal extension in plant phytochrome phyB

Francisco Velázquez Escobar<sup>1</sup>, David Buhrke<sup>1</sup>, Maria Fernandez Lopez<sup>1</sup>, Sintayehu Manaye Shenkutie<sup>2</sup>, Silke von Horsten<sup>3</sup>, Lars-Oliver Essen<sup>3,4</sup>, Jon Hughes<sup>2</sup> and Peter Hildebrandt<sup>1</sup>

<sup>1</sup> Institut für Chemie, Technische Universität Berlin, Germany

<sup>2</sup> Plant Physiology, Justus-Liebig University Gießen, Giessen, Germany

<sup>3</sup> Fachbereich Chemie, Strukturbiochemie, Philipps-Universität Marburg, Marburg, Germany

<sup>4</sup> LOEWE Center for Synthetic Microbiology, Philipps-Universität, Marburg, Germany

### Correspondence

P. Hildebrandt, Technische Universität Berlin, Institut für Chemie, Sekr. PC14, Straße des 17. Juni 135, D-10623 Berlin, Germany  
Fax: +49 30 31421122  
Tel: +49 30 31421419  
E-mail: hildebrandt@chem.tu-berlin.de

(Received 5 March 2017, revised 25 March 2017, accepted 28 March 2017, available online 16 April 2017)

doi:10.1002/1873-3468.12642

Edited by Miguel De la Rosa

The N-terminal extension (NTE) of plant phytochromes has been suggested to play a functional role in signaling photoinduced structural changes. Here, we use resonance Raman spectroscopy to study the effect of the NTE on the chromophore structure of B-type phytochromes from two evolutionarily distant plants. NTE deletion seems to have no effect on the chromophore in the inactive Pr state, but alters the torsion of the C-D ring methine bridge and the surrounding hydrogen bonding network in the physiologically active Pfr state. These changes are accompanied by a shift of the conformational equilibrium between two Pfr substates, which might affect the thermal isomerization rate of the C-D double bond and, thus, account for the effect of the NTE on the dark reversion kinetics.

**Keywords:** chromophore structure; N-terminal extension; plant phytochrome; resonance Raman spectroscopy

Light-dependent development in plants is regulated principally by phytochromes, a family of photoreceptors harboring the tetrapyrrole phytochromobilin (PΦB) as the light-absorbing chromophore [1–3] (Fig. 1). A photoinduced reaction cascade, starting with a double bond isomerization of the cofactor, leads to the conversion of the red-absorbing Pr state to the far-red absorbing Pfr state which is the physiologically active form. Important insight into the molecular processes of the photosensor module (PSM) has been obtained from bacterial and cyanobacterial representatives of this photoreceptor family [1–3]. However, despite similar reaction steps and structural changes in

the chromophore-binding pocket, the signaling process by which the PSM transduces its structural changes to the cell is quite different in prokaryotic and plant phytochromes [4–6]. In particular, although most prokaryotic phytochromes are light-repressed histidine protein kinases signaling from the C-terminal transmitter module, plant phytochromes are active in the Pfr state, signaling from the PSM directly. The domain structure of plant phytochromes is also more complex, with an additional PAS-PAS module separating the PSM and the transmitter-like module. Moreover, although prokaryotic phytochromes carry an N-terminal extension (NTE) of only about 20 residues, in plant

### Abbreviations

A-B/C-D, C=C stretching of the AB/CD methine bridge; ARR, Arabidopsis response regulator; GAF, cGMP phosphodiesterase/adenylyl cyclase/FhlA; HDX, H/D exchange with mass spectrometry; HOOP, hydrogen-out-of-plane; N-H ip, N-H in-plane bending; NTE, N-terminal extension; PAS, Per/Arnt/Sim; PCB, phycocyanobilin; phyA/B, phytochrome A/B; PHY, phytochrome-specific; PIF, phytochrome interaction factor; Pr/Pfr, red/far-red absorbing form of phytochrome; PSM, photosensory module; PΦB, phytochromobilin; RR, resonance Raman.

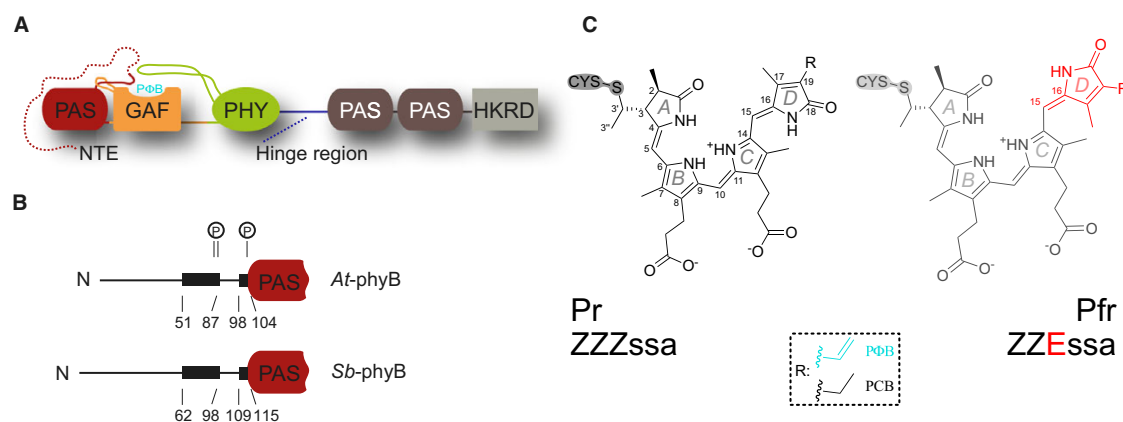


**Fig. 1.** (A) Domain organization of phyB; PAF denotes the chromophore binding site (adapted from ref. [8]), (B) NTEs in Sb-phyB and At-phyB ('P' refers to putative phosphorylation sites and the black boxes mark conserved regions), (C) structure of the bilin chromophores PAF (R = vinyl) and PCB (R = ethyl) in the ZZEssa configuration of the Pfr state.

phytochromes this is much larger, comprising ca. 110 and 70–75 residues in B- and other types, respectively (Fig. 1). In phyB, the NTE is likely to interact with the PSM since it affects the dark reversion from the Pfr to the Pr state [7]. Furthermore, recent H/D exchange probed by mass spectrometry (HDX) provided evidence for Pr/Pfr-dependent differences [8]. In *Arabidopsis*, the NTE is bound by the response regulator-like protein ARR4 which also thereby regulates the rate of reversion [9,10]. Furthermore, it contains phosphorylation sites that affect the spectral characteristics as well as the binding of the phytochrome interaction factor 3 (PIF3) [11,12]. 3D structural information about the NTE and its interaction with the PSM are not yet available. Despite its limited resolution, the recently determined PSM crystal structure for *Arabidopsis* phyB in the Pr state [7] reveals far-reaching similarities in particular to Cph1 from the cyanobacterium *Synechocystis* 6803 [13] on account of their similar protein-chromophore linkage. However, crystallized variants of phyB and Cph1 are devoid of any structural information for NTE.

The present work focuses on the role of the NTE in phyB using resonance Raman (RR) spectroscopy, a method that selectively probes the structure of the chromophore and its interactions with the molecular environment [14–16]. By comparing phyB from evolutionarily distant plants, the dicotyledon *Arabidopsis thaliana* (AtphyB) and the monocotyledon *Sorghum bicolor* (SbphyB) and their deletion variants lacking the NTE (AtΔNTE, SbΔNTE) with phytochrome A3 from *Avena sativa* (AsphyA), we provide insight into structural details of the chromophore-binding pocket

of plant phytochromes and the impact of the NTE on the photoinduced formation of the functional Pfr state.

## Materials and methods

### Protein expression and purification

AtphyB with and without the NTE was expressed, purified, and assembled with PCB as described previously [8]. The photosensory module SbphyB with or without the NTE was produced from pCDFDuet-based constructs together with PAF or PCB in *Escherichia coli* to form the holoprotein *in vivo* following procedures similar to those established for prokaryotic phytochromes [17,18]. Both recombinant phytochromes carried a C-terminal His<sub>6</sub>-tag for Ni-affinity purification, followed by size-exclusion chromatography to give a chromophore/protein absorbance ratio of ca. 1.4 and 1.15 for the variants with and without the NTE, respectively (Fig. S1). In the case of the PCB adducts, close similarities are apparent between the equivalent PSM constructs from *Sorghum* and *Arabidopsis* with and without the NTE. In the case of SbphyB, the native PAF adduct showed the expected bathochromic shifts in the red and far-red peaks of Pr and Pfr concomitant with the  $\pi$  electron system extending into the D-ring side chain.

### Resonance Raman spectroscopy

Samples were concentrated in aqueous TS50 buffer (50 mM Tris-Cl, 300 mM NaCl, 5 mM EDTA, pH = 7.8). Pr-to-Pfr (Pfr-to-Pr) conversion was achieved by continuous (2 min, LED) light exposure at 670 nm (Pr) or 750 nm (Pfr) at 20 °C. RR measurements of phyB phytochrome were

performed with an RFS-100 FT-Raman spectrometer (Bruker Optics, Ettlingen, Germany), equipped with an 1064 nm Nd-YAG laser (670 mW) and a Linkam (Resultec, Illerkirchberg, Germany) cryostat. Measurements were performed at  $-140^{\circ}\text{C}$ . Each spectrum is based on 1000–2000 single interferometer scans, corresponding to accumulation times between 30–60 min per spectrum. All spectra processing was performed using the OPUS suite. Further experimental details are given elsewhere [14–16].

## Results

The RR spectra of the Pr and Pfr parent states of PΦB and PCB adducts of *Avena* (oat) phyA3 (*AsphyA*) have been analyzed in detail previously [15,16] and now serve as a reference for the comparison with the corresponding data for phyB with and

without the larger NTE. Here, we focus on three spectral regions characteristic of the specific structural parameters of the chromophore and its interactions with the immediate molecular environment. In the region between 1520 and 1680  $\text{cm}^{-1}$ , the spectra of the Pr state are dominated by three peaks originating from the N-H in-plane bending of rings B and C (N-H ip), and the C=C stretching modes of the CD and AB methine bridges (Fig. 2A; see Fig. 1C for ring notation). In *AsphyA*, these modes are found at 1575 (N-H ip), 1626 (C-D), and 1646  $\text{cm}^{-1}$  (A-B), reflecting the *ZZZ<sub>ssa</sub>* geometry of the fully protonated PΦB chromophore (Fig. 1) [15]. Between 750 and 850, the spectra display less intense bands including the C-H out-of-plane deformation coordinates (HOOP). In *AsphyA*, the most pronounced band at 802  $\text{cm}^{-1}$  is a HOOP mode of the CD methine bridge and is

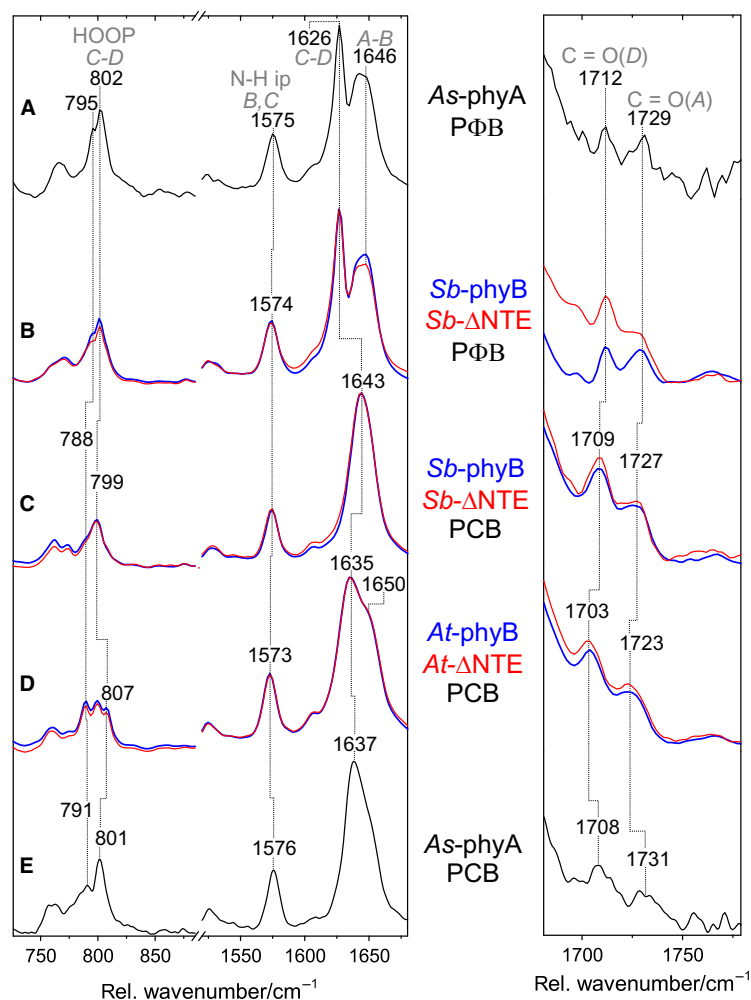


**Fig. 2.** Resonance Raman spectra of the Pr state of (A) *As-phyA* and (B) *Sb-phyB* including the PΦB chromophore, and (C) *Sb-phyB*, (D) *At-phyB*, and (E) *As-phyA* including the PCB chromophore. The red traces in (B), (C), and (D) refer to the variants lacking the NTE segments ( $\Delta\text{NTE}$ ). The spectra in (A) and (E) have been published earlier [15].

accompanied by a shoulder at  $795\text{ cm}^{-1}$ . Finally, the carbonyl stretching modes of the terminal pyrrole rings give rise to weak RR bands at  $1712$  and  $1729\text{ cm}^{-1}$ . On the basis of previous IR studies [19], these bands are readily assigned to the C=O stretching of ring *D* and *A*, respectively.

### The Pr state of phyB

The spectra of the PΦB adducts of *SbphyB* and *AsphyA* (Fig. 2B) are nearly identical, indicating that even structural details of the chromophore and its interactions with the protein environment agree well. For *AsphyA*, structural models revealed very similar chromophore geometries for PΦB and PCB, implying that the different substitution at ring *D* (vinyl vs. ethyl) does not perturb the interactions with the protein [15,16,20]. Thus, the differences in the RR spectra between the *AsphyA* adducts can mainly be attributed to the intrinsic effect of the side chain difference on the cofactor modes, including the frequency upshift of the *C-D* ( $1626\text{--}1637\text{ cm}^{-1}$ ) and *A-B* ( $1646$  to ca.  $1650\text{ cm}^{-1}$ ) stretching modes in the PCB adduct due to the reduced length of the delocalized  $\pi$ -electron system that is also reflected by the UV-vis absorption spectra (Fig. S1). The notable differences between the PCB adducts of *SbphyB* and *AsphyA* (Fig. 2C, E) are, therefore, quite surprising. In *SbphyB*, a distinctly larger upshift of the *C-D* stretching to  $1643\text{ cm}^{-1}$  is observed, such that the putatively invariant *A-B* stretching mode (ca.  $1650\text{ cm}^{-1}$ ) is largely obscured. This finding points to a structural change at the *CD* methine bridge leading to a decrease in the N(C)-C-C-C(*D*) dihedral angle, according to previous theoretical analyses [14,15]. Most likely, this distortion originates from the specific structure of the chromophore-binding pocket in *SbphyB* in the vicinity of ring *D*, which stabilizes a similar PΦB structure to that in *AsphyA* but, unlike in the latter, small geometrical adjustments are necessary to accommodate PCB. Subtle structural alterations compared to *AsphyA* seem to occur also in *AtphyB* (Fig. 2D). Here, however, the *C-D* stretching remains unchanged, whereas the  $6\text{ cm}^{-1}$  upshift of the *CD* HOOP mode compared to *AsphyA* may be taken as a small decrease in the C(C)-C-C-N(*D*) dihedral angle. Thus, we conclude that the chromophore structure differs only in small details between oat phyA and the two phyB orthologs. These small differences also include the hydrogen bonding network as reflected by minor differences between the C=O stretching frequencies of the rings *A* and *D*. In the Pr state, the RR spectra show no significant differences between the *SbphyB* and *AtphyB* variants with regard to the presence of an NTE.

### The Pfr state of phyB

Both the Pr and the Pfr state of *AsphyA* display a structural heterogeneity in the chromophore binding site [16,21], but RR spectroscopy only distinguishes a temperature-dependent equilibrium between substates in the case of Pfr (Pfr-I, Pfr-II) [16]. Each of these Pfr substates adopts a protonated *ZZEssa* chromophore structure. However, the torsion between the rings *C* and *D* probably differs by ca.  $10^\circ$  as implied by two bands originating from the HOOP mode, separated by  $16$  and  $8\text{ cm}^{-1}$  in the PΦB and PCB adducts, respectively (Figs 3A and 4A). The intensity ratio of these bands can be taken as a measure for the relative populations of the substates. This conformational heterogeneity is also reflected in the region between  $1600$  and  $1620\text{ cm}^{-1}$ , albeit less clearly visible due to the superposition of four components, that is, for each conformer a strongly RR-active C=C stretching mode of the *CD* methine bridge at lower frequency and a C=C stretching mode of ring *D* a higher frequency, which exhibits weaker RR intensity [16]. Based on isotopic labeling and temperature-dependent measurements, it could be shown that Pfr-I is associated with the low-frequency HOOP mode and the high-frequency *C-D* stretching component, whereas the high-frequency HOOP and low-frequency *C-D* stretching originate from Pfr-II. This interpretation may also be extended to the *SbphyB* and *AtphyB* variants including the NTE, which show a similar HOOP mode ratio and only small adduct-related frequency differences (Figs 3 and 4). Also, the other marker bands between  $1500$  and  $1800\text{ cm}^{-1}$  are similar within the experimental accuracy, and the most pronounced frequency shifts refers to the ring *D* C=O stretching, which is lowered by  $7\text{ cm}^{-1}$  in the PCB adducts of the phyB PSM.

### The effect of the NTE on the chromophore-binding pocket

Unlike Pr, the deletion of the NTE segment has a remarkable effect on the RR spectra of Pfr. For the PCB adducts, we note a downshift of the high-frequency HOOP component from  $816\text{ cm}^{-1}$  in *SbphyB* (*AtphyB*:  $814\text{ cm}^{-1}$  in) to  $811\text{ cm}^{-1}$ , accompanied by a reversal of the intensity ratio between the low and high-frequency components, which reflects an increase in the Pfr-I/Pfr-II population ratio (Fig. 3B–E). Accordingly, this shift of the conformational equilibrium is accompanied by a growth of the high-frequency *C-D* stretching component (*vide supra*), which can in fact account for the intensity increase in the

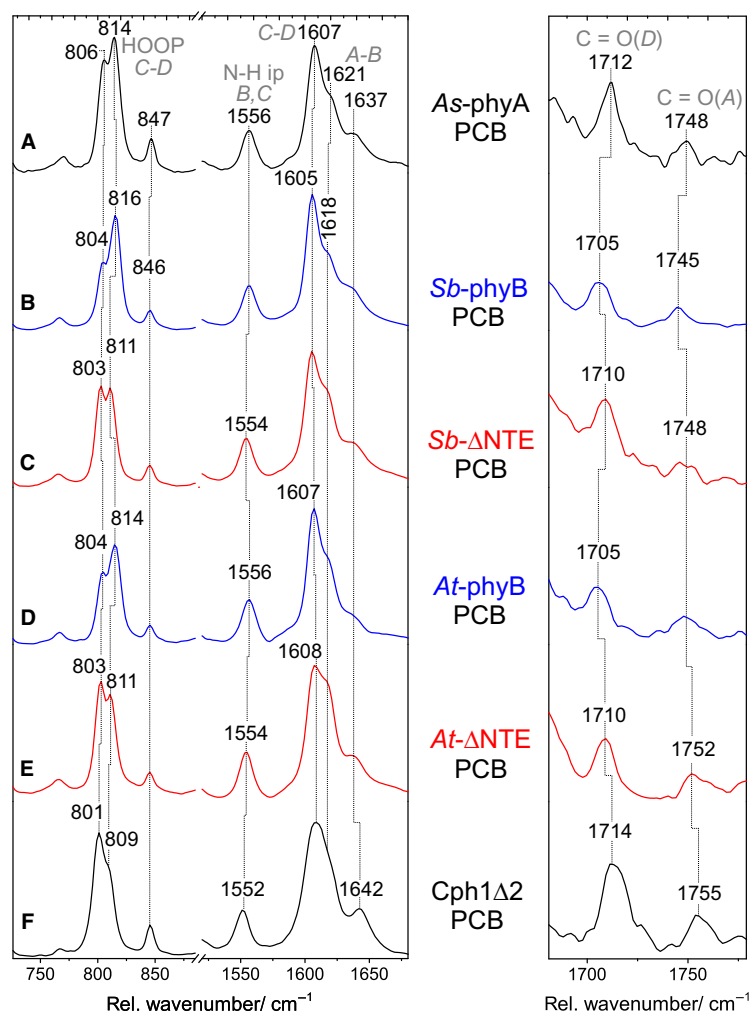


**Fig. 3.** Resonance Raman spectra of the Pfr state of phytochrome adducts including the PCB chromophore. (A) *As-phyA*, (B) *Sb-phyB*, (C) *Sb-ΔNTE*, (D) *At-phyB*, (E) *At-ΔNTE*, and (F) *Cph1Δ2*. The spectra in (A) and (F) have been published earlier [16].

1618-cm<sup>-1</sup> shoulder. Concomitant to the redistribution among the substate population, we note a small downshift of the N-H ip mode from 1556 to 1554 cm<sup>-1</sup>, indicating an alteration of the hydrogen bond interactions in the chromophore pocket [22]. The same interpretation may hold for the 5-cm<sup>-1</sup> upshift of the C=O stretching of ring *D* from 1705 to 1710 cm<sup>-1</sup>. Interestingly, upon deletion of the NTE, the RR spectra become very similar to that of the PSM of cyanobacterial phytochrome Cph1Δ2, including the distribution among the conformational substates (Figs 3F and 4D) [16,23]. In contrast, such far-reaching similarities with Cph1Δ2 do not exist for the RR spectra of the Pr state, neither for phyA nor for phyB [15,22,23].

For the PΦB adducts the effect of NTE deletion is smaller than for the PCB adducts, but with respect

to the changes in the substate populations the same tendency can be derived from intensity redistribution of the composite peak of the two HOOP modes (Fig. 4B, C).

## Discussion

The present results demonstrate a state-dependent interaction between the chromophore and the NTE in phyB. This interaction is similar for phyB from *A. thaliana* and *S. bicolor*, suggesting that it represents a general characteristic of phyB. The impact of these interactions on the chromophore-binding pocket is small and only observed in the Pfr state. It comprises a perturbation of the hydrogen bonding network and the *CD* portion of the chromophore, reflected by a

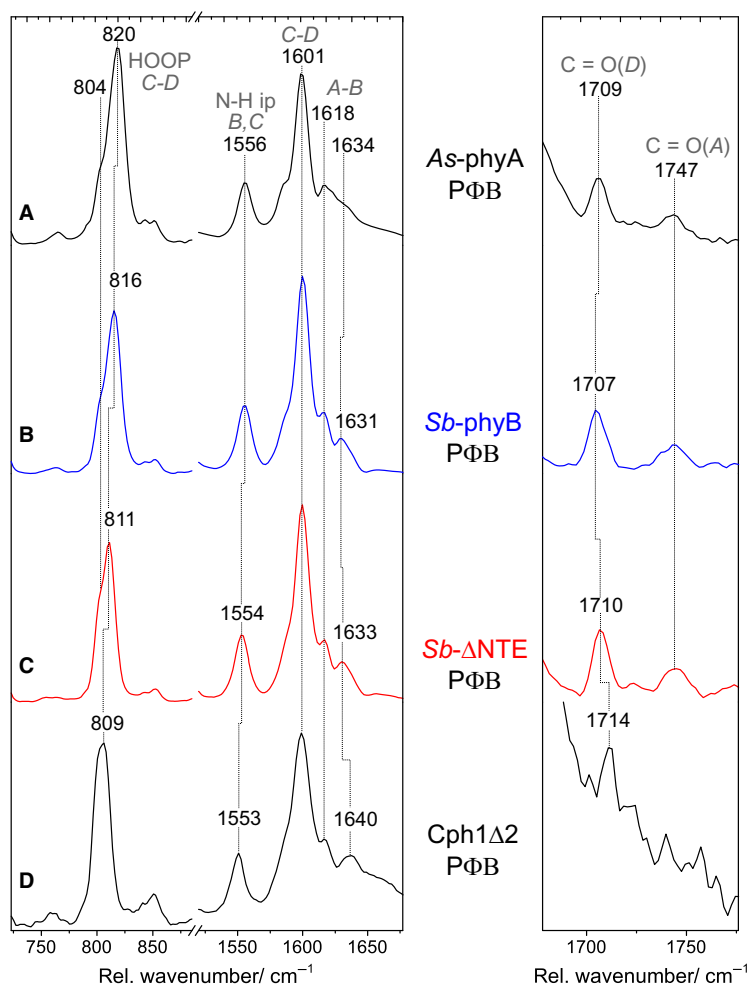


**Fig. 4.** Resonance Raman spectra of the Pfr state of phytochrome adducts including the PΦB chromophore. (A) *As-phyA*, (B) *Sb-phyB*, (C) *Sb-ΔNTE*, and (D) *Cph1Δ2*. The spectra in (A) and (D) have been published earlier [16].

shift in the conformational Pfr-I/Pfr-II equilibrium. Both effects, which most likely constitute the molecular basis for the hypsochromic shift of the electronic absorption in NTE deletion variants (Fig. S1) [7,8], are presumably linked although no conclusions can be drawn about possible cause-effect relationships between them. The NTE undergoes structural changes upon Pr → Pfr photoconversion as demonstrated by recent HDX experiments [8]. These studies identified several regions within the NTE that display a slower exchange in Pfr (compared to Pr), indicating a restructuring of the NTE.

One region close to the *AB* rings of the chromophore that displays changes in the HDX rates links the C terminus of the NTE with the start of the PAS domain (Y104-I108). However, the altered dynamics of this region does not affect the geometry at the *AB*

rings of the chromophore upon Pr → Pfr transition, consistent with the RR data. All other regions in the NTE with HDX rates altered by photoconversion probably lack direct contact with the chromophore itself [8]. This implies that only indirect interactions are able to explain the observed effect of the NTE on the structural changes of the bilin chromophore. Our packing model for the NTE/PSM interactions suggested that in the Pfr state a stretch with comparably slow intrinsic HDX rates (P28-Q36) may interact with the β1 strand of the GAF domain and its adjacent loop [8] (Fig. 5). A prominent part of this strand is Y276, which forms crucial interactions with the chromophore and which upon mutation to histidine forms a strongly fluorescent, Pfr-mimicking signaling state in darkness [24]. Interactions between the β1GAF strand and the NTE could hence affect the *CD* ring



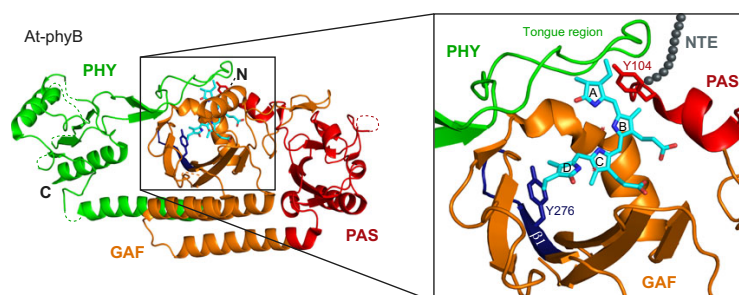


**Fig. 5.** Structure of At-phyB (PDB code: 4OUR); the PAS, GAF, and PHY domains are depicted in red, orange and green, respectively. The chromophore, phytochromobilin (PΦB), is colored in cyan. The inset enlarges the chromophore binding site. The  $\beta 1$  strand of the GAF domain is highlighted in blue and the N-terminal extension (NTE) in gray spheres.

surroundings and account for the RR spectroscopic differences between the wild-type and NTE deletion variants. A second candidate for an indirect interaction site for the NTE is the tongue region of the PHY domain (Fig. 5), which is thought to undergo major structural changes next to the chromophore upon photoconversion. Overall, it appears that indirect interactions of the CD ring surroundings with the NTE suffice to affect the chromophore geometry and thereby its photochemistry.

The conformational coupling of the NTE segment and the chromophore-binding pocket are probably of functional importance. It has been shown previously that dark reversion kinetics of phyB is substantially accelerated upon removal of the NTE segment [7]. This may in fact be related to the structural differences compared to the complete PSM, reflected by the shift of the conformational equilibrium between the substates Pfr-I/Pfr-II which mainly differ by CD methine bridge torsion and the hydrogen bond network around the chromophore. This conformational heterogeneity has only been observed for cyanobacterial and prototypical bacteriophytochromes that, like plant phytochromes, thermally revert to the Pr state. In contrast, bathy bacteriophytochromes exhibit a highly homogeneous chromophore structure in the Pfr state that does not decay to the Pr state [14]. It was, therefore, concluded that thermal CD methine bridge isomerization, which is presumably the rate-limiting step for dark reversion, runs via one of the Pfr substates. In phyB, NTE deletion increases the population of the substate associated with a larger C(14)-C(15)-C(16)-N (D) dihedral angle [14], which might lower the energy barrier for the rotation around the C(15)-C(16) bond as one important parameter promoting *E*  $\rightarrow$  *Z* isomerization. Also, the changes of the hydrogen bond interactions induced by NTE deletion might contribute to the acceleration of the dark reversion via favoring the transient formation of the enol form of the chromophore as the essential mechanistic step of thermal double bond isomerization [25].

## Acknowledgements

The authors acknowledge financial support by the Deutsche Forschungsgemeinschaft (SFB1078 B6 to PH, HU702/8 and/9 to JH and ES152/10 to LOE).

## Author contributions

PH, LOE, and JH conceived and supervised the study and wrote the manuscript. FVE, DB, and MFL performed the spectroscopic experiments. SMS and SvH prepared the samples.

## References

- 1 Briggs WR and Spudis JL (2005) Handbook of Photosensory Receptors. Wiley Verlag, Weinheim, Germany.
- 2 Nagatani A (2010) Phytochrome: structural basis for its functions. *Curr Opin Plant Biol* **13**, 565–570.
- 3 Auldridge ME and Forest KT (2011) Bacterial phytochromes: more than meets the light. *Crit Rev Biochem Mol Biol* **46**, 67–88.
- 4 Zhang J, Stankey RJ and Vierstra RD (2013) Structure-guided engineering of plant phytochrome B with altered photochemistry and light signaling. *Plant Physiol* **161**, 1445–1457.
- 5 Burgie ES and Vierstra RD (2014) Phytochromes: an atomic perspective on photoactivation and signaling. *Plant Cell* **26**, 4568–4583.
- 6 Hughes J (2013) Phytochrome cytoplasmic signaling. *Ann Rev Plant Biol* **64**, 377–402.
- 7 Burgie ES, Bussell AN, Walker JM, Dubiel K and Vierstra RD (2014) Crystal structure of the photosensing module from a red/far-red light-absorbing plant phytochrome. *Proc Natl Acad Sci USA* **111**, 10179–10184.
- 8 von Horsten S, Straß S, Hellwig N, Gruth V, Klasen R, Mielcarek A, Linne U, Morgner N and Essen LO (2016) Mapping light-driven conformational changes within the photosensory module of plant phytochrome B. *Sci Rep* **6**, 34366.

- 9 Sweere U, Eichenberg K, Lohrmann J, Mira-Rodado V, Bäurle I, Kudla J, Nagy F, Schäfer E and Harter K (2001) Interaction of the response regulator ARR4 with phytochrome B in modulation red light signaling. *Science* **294**, 1108–1111.
- 10 Fankhauser C (2002) Light perception in plants: cytokinins and red light join forces to keep phytochrome B active. *Trends Plant Sci* **7**, 143–145.
- 11 Medzihradsky M, Bindics J, Ádám E, Viczián A, Klement E, Lorrain S, Gyula P, Mérai Z, Fankhauser C, Medzihradsky KF *et al.* (2013) Phosphorylation of phytochrome B inhibits light-induced signaling via accelerated dark reversion in Arabidopsis. *Plant Cell* **25**, 535–544.
- 12 Kazumasa N, Wong CCL, Yates JR III and Chory J (2013) Tyrosine phosphorylation regulates the activity of phytochrome photoreceptors. *Cell Rep* **3**, 1970–1979.
- 13 Essen LO, Maillat J and Hughes J (2008) The structure of a complete phytochrome sensory module in the Pr ground state. *Proc Natl Acad Sci USA* **105**, 14709–14714.
- 14 Salewski J, Velazquez F, Kaminski S, von Stetten D, Keidel A, Rippers Y, Michael N, Scheerer P, Piwowarski P, Bartl F *et al.* (2013) The structure of the biliverdin cofactor in the Pfr state of bathy and prototypical phytochromes. *J Biol Chem* **288**, 16800–16814.
- 15 Mroginski MA, Kaminski S, von Stetten D, Ringsdorf S, Gärtner W, Essen LO and Hildebrandt P (2011) The structure of the chromophore binding pocket in the Pr state of plant phytochrome phyA. *J Phys Chem B* **115**, 1220–1231.
- 16 Velazquez Escobar F, von Stetten D, Günther M, Keidel A, Michael N, Yang Y, Heyne K, Lamparter T, Essen LO, Hughes J *et al.* (2015) Conformational heterogeneity of the Pfr chromophore in plant and cyanobacterial phytochromes. *Front Mol Biosci* **2**, 37.
- 17 Landgraf FT, Forreiter C, Hurtado Picó A, Lamparter T and Hughes J (2001) Recombinant holophytochrome in *Escherichia coli*. *FEBS Lett* **508**, 459–462.
- 18 Song C, Psakis G, Kopycki J, Lang C, Matysik J and Hughes J (2013) The D-ring, not the A-ring, rotates in Synechococcus OS-B' phytochrome. *J Biol Chem* **289**, 2552–2562.
- 19 Schwinté P, Foerstendorf H, Gärtner W, Mroginski MA, Hildebrandt P and Siebert F (2008) Fourier transform infrared studies of the photoinduced processes of phytochrome phyA using isotopically labelled chromophores and density functional theory calculations. *Biophys J* **95**, 1256–1267.
- 20 Kneip C, Mozley D, Hildebrandt P, Gärtner W, Braslavsky SE and Schaffner K (1997) Effect of chromophore exchange on the resonance Raman spectra of recombinant phytochromes. *FEBS Lett* **414**, 23–26.
- 21 Rohmer T, Lang C, Hughes J, Essen LO, Gärtner W and Matysik J (2008) Light-induced chromophore activity and signal transduction in phytochromes observed by <sup>13</sup>C and <sup>15</sup>N magic-angle spinning NMR. *Proc Natl Acad Sci USA* **105**, 15229–15234.
- 22 Mroginski MA, von Stetten D, Velazquez Escobar F, Strauss HM, Kaminski S, Scheerer P, Günther M, Murgida DH, Schmieder P, Bongards C *et al.* (2009) Chromophore structure of cyanobacterial phytochrome Cph1 in the Pr state: reconciling structural and spectroscopic data by QM/MM calculations. *Biophys J* **96**, 4153–4163.
- 23 Velazquez Escobar F, Lang C, Takiden A, Schneider C, Balke J, Hughes J, Alexiev U, Hildebrandt P and Mroginski MA (2017) Protonation-dependent structural heterogeneity in the chromophore binding site of cyanobacterial phytochrome Cph1Δ2. *J Phys Chem B* **121**, 47–57.
- 24 Su Y and Lagarias JC (2007) Light-independent phytochrome signaling mediated by dominant GAF domain tyrosine mutants of Arabidopsis phytochromes in transgenic plants. *Plant Cell* **19**, 2124–2139.
- 25 Velazquez Escobar F, Piwowarski P, Salewski J, Michael N, Fernandez Lopez M, Rupp A, Qureshi BM, Scheerer P, Bartl F, Frankenberg-Dinkel N *et al.* (2015) A protonation-coupled feedback mechanism controls the signaling process in bathy phytochromes. *Nat Chem* **7**, 423–430.

## Supporting information

Additional Supporting Information may be found online in the supporting information tab for this article:

**Fig. S1.** Absorption spectra of *SbphyB* assembled with PCB and PΦB.

## 4.2 Interaction of *Arabidopsis thaliana* Phytochrome B with the Phytochrome Interaction Factor 3

The phytochrome signaling process in plants is complex and poorly understood. After photoconversion to the Pfr state, plant phytochromes translocate from the cytoplasm into the nucleus and transiently bind so-called phytochrome interaction factors (PIFs).[162, 31] The molecular mechanism and location of PIF binding and eventual chemical reactions with the phytochrome, such as (de)phosphorylation reactions, are still controversial in the literature and not known in detail. In case of PhyB and PIF3, phosphorylation of a tyrosine (Tyr) [147] or serine (Ser) [127, 144] residue of PIF3 by the PhyB was proposed, but also the reverse reaction, dephosphorylation of PIF by phytochromes, was observed.[181, 156] To disentangle these contradicting results, molecular investigations of the active complex (denoted PhyPIF in the following) are necessary. *In vitro* studies of the molecular interaction serve as models and therefore eventually contribute to a more profound understanding of phytochrome signaling pathways *in planta*.

**PhyPIF complex formation** *Arabidopsis thaliana* phytochrome B (AtPhyB) interacts with PIF3 and transiently forms the PhyPIF complex in the Pfr state. The complex formation reaction (eqn. 4.1) was investigated by means of analytical microscale thermophoresis (MST), and the equilibrium constant in the Pfr state was determined ( $K_D=6.8 \mu M$ ) for the reaction in TES- $\beta$ -buffer. No interaction was found in the Pr state with this analytical technique.[62] To probe the effects of PIF3 binding on the chromophore (PCB) configuration, RR spectra were recorded for PIF3 and mixtures of PIF3 with AtPhyB in the Pr and Pfr states (see fig. 4.2.2). The initial concentration of PIF3 and AtPhyB (denoted Phy for simplicity in the following) was adjusted accordingly. The complex formation reaction



is reversible, and the dissociation constant  $K_D$  is defined as

$$K_D = \frac{[Phy][PIF]}{[PhyPIF]}. \quad (4.2)$$

To analyze the interaction of PIF3 and AtPhyB with RR spectroscopy, a high portion of PhyPIF relative to unbound [Phy] must be obtained at sufficiently high concentrations. At least a 10:1 ratio of is needed

$$\frac{[PhyPIF]}{[Phy]} = 10. \quad (4.3)$$

Inserting eqn. 4.3 into eqn. 4.2 yields

$$K_D = 0.1[PIF] = 0.1([PIF]_0 - [PhyPIF]). \quad (4.4)$$

Additionally, a high concentration of [PhyPIF] is required to obtain RR spectra of reasonable quality

$$[PhyPIF] = 10^{-4}M. \quad (4.5)$$

Within the boundary condition 4.5, eqn. 4.4 can be rewritten

$$[PIF]_0 = 10 \cdot K_D + [PhyPIF] = 1.7 \cdot 10^{-4}M, \quad (4.6)$$

by inserting eqn. 4.3, one obtains the initial concentration  $[Phy]_0$

$$[Phy] = 0.1 \cdot [PhyPIF] = 10^{-5}M \quad (4.7)$$

$$[Phy]_0 = [Phy] + [PhyPIF] = 1.1 \cdot 10^{-4}M \quad (4.8)$$

**Sample preparation** The samples of PhyB and PIF3 both had an initial concentration of 40  $\mu$ M. For one RR sample, 55  $\mu$ L AtPhyB and 85  $\mu$ L PIF3 were mixed, illuminated with a 660 nm LED to generate the complex and subsequently concentrated in a 10 kDa cutoff Amicon centrifugal filter unit to a final amount of 20  $\mu$ L to obtain the initial concentrations  $[Phy]_0$  and  $[PIF]_0$  (see eqns. 4.6 and 4.8). Raman signals originating from PIF3 are not pre-resonance enhanced and therefore weak compared to the enhanced PCB bands. Nevertheless, under the present experimental conditions with PIF3 excess (ca. 1.5x) and a low concentration of AtPhyB (relative to the conditions used for the pure AtPhyB spectra in chapter 4.1), the intensity of strong PIF3 bands (e.g. amide III at 1464  $\text{cm}^{-1}$ ) is in the order of magnitude of the PCB bands or even higher (see fig. 4.2.1).

To investigate the potential influence of PIF3 on the structure of PCB in the PhyPIF complex, the PIF contribution was subtracted from the mixture (see fig. 4.2.2). Although PIF3 bands are not detected after the subtraction procedure, they substantially contribute to the spectral underground and thus lead to more overall noise and spectral artifacts (marked with asterisks (\*)) in the subtracted spectra. Therefore, only the strongest PCB bands in the marker region (1500-1700  $\text{cm}^{-1}$ ) and in the HOOP region (600-900  $\text{cm}^{-1}$ ) are discussed, where even small changes in frequencies or intensities can be discriminated unambiguously (see figs. 4.2.3 and 4.2.4 for expanded views of the marker and the HOOP regions). The C=C stretching and HOOP signals in these spectral regions are sensitive to chromophore geometry and protonation state. When PIF is added, the overall mode composition and shape of the Pr and Pfr spectra remains unchanged, indicating that PCB persists in the respective ZZZssa and ZZEssa configurations with a fully protonated (cationic) PCB chromophore. Yet, small but reproducible differences are observed in the Pfr and Pr spectra upon PIF3 addition.

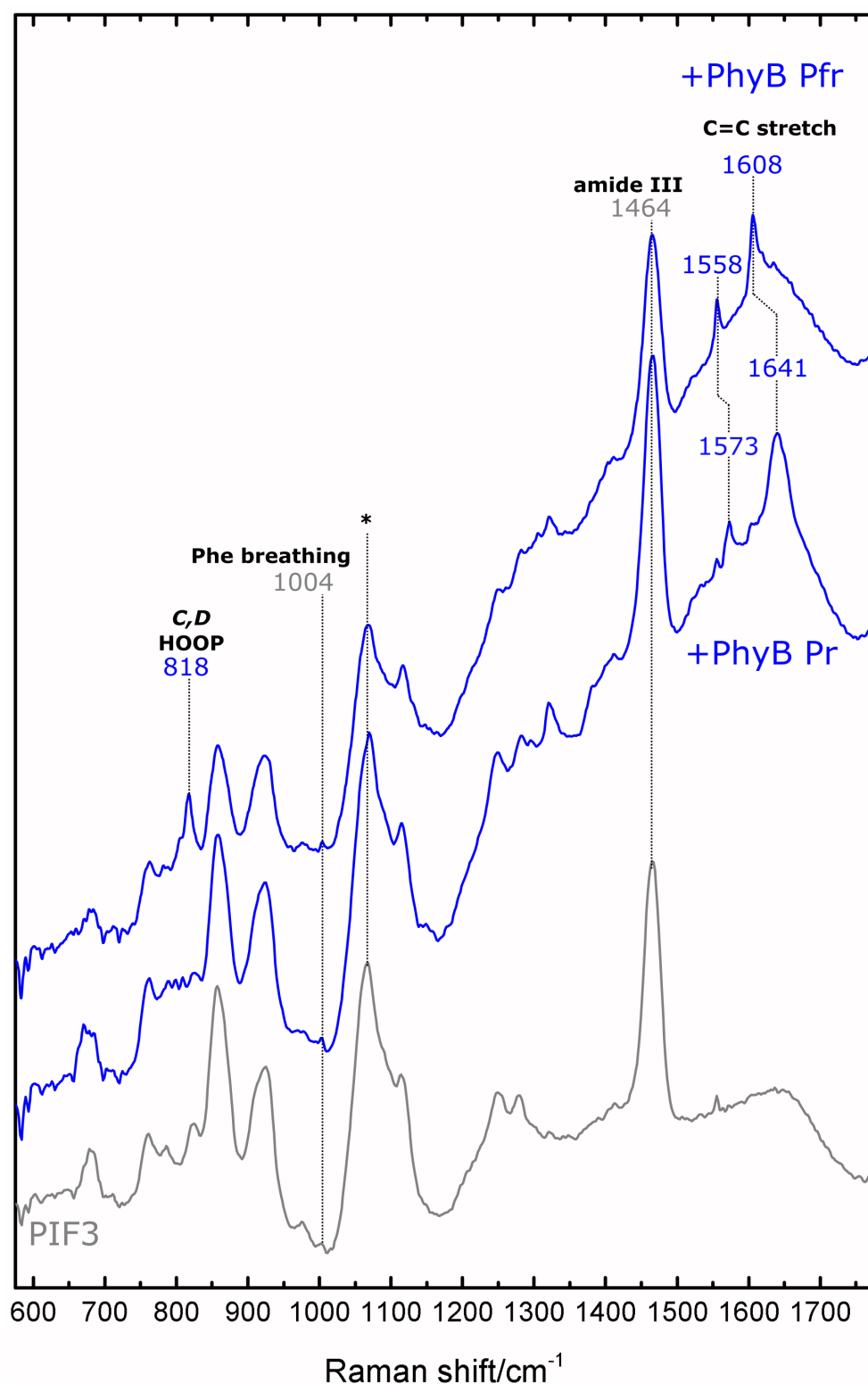


**Figure 4.2.1:** The Raman spectra of PIF3 and AtPhyB/PIF3 mixtures. The gray spectrum shows pure PIF3 ( $[PIF3] = 10^{-4} M$ ). The lower blue spectrum is directly obtained after addition of AtPhyB to PIF3 in the dark, and represents a spectral superposition of PIF3 and AtPhyB in the Pr form. The topmost blue spectrum is obtained after illumination of the mixture with red light (660 nm LED). Here the shifted C=C stretching signals and the appearance of the HOOP mode are indicative for the Pfr form.

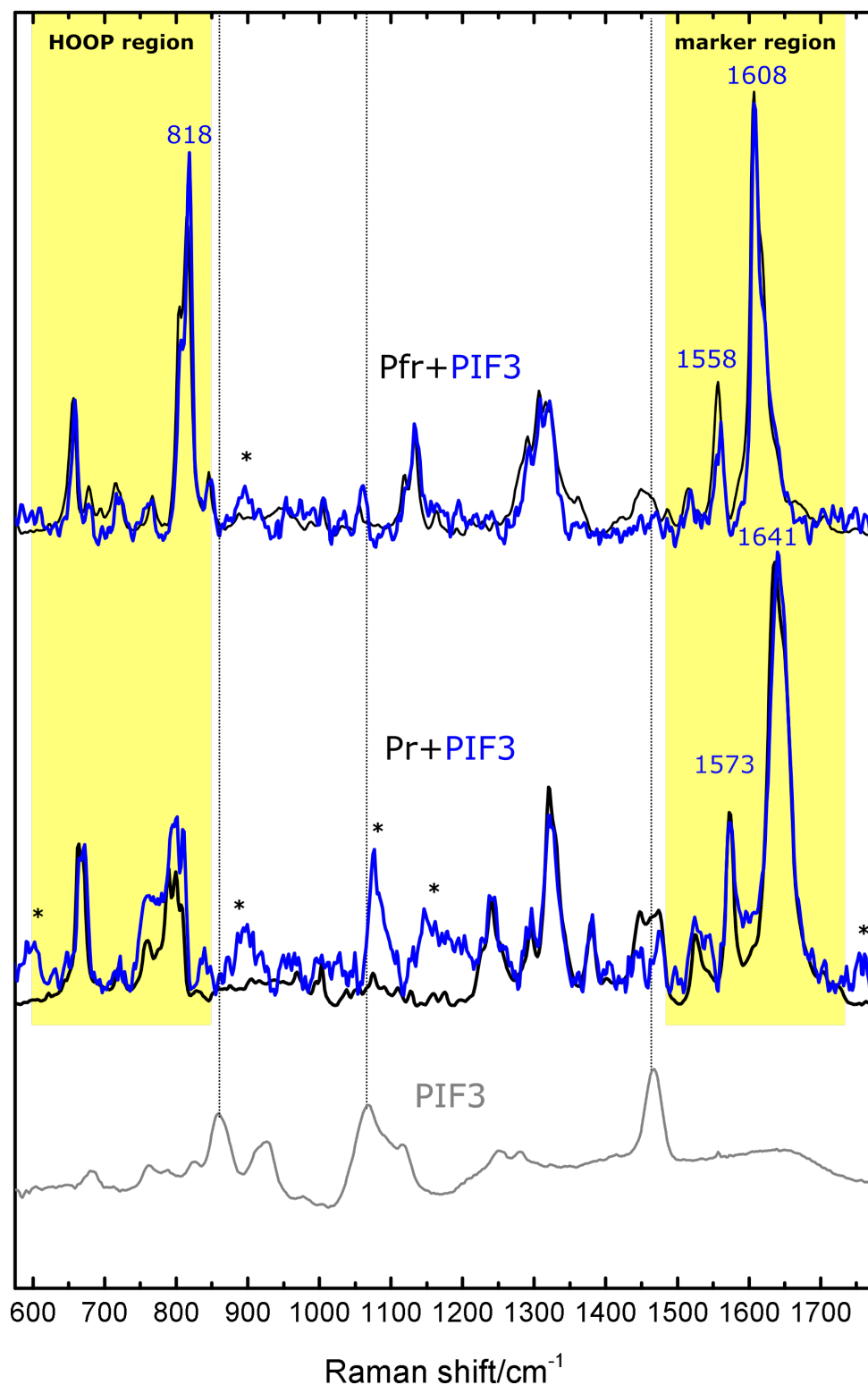


**Figure 4.2.2:** Full range RR spectra of AtPhyB with and without PIF3 (subtracted). The gray spectrum shows pure PIF3 (scaled down for comparison). The black and blue spectra show AtPhyB in the Pr and Pfr state without and with the addition of PIF3, respectively. PIF3 contribution was subtracted to obtain the blue spectra. Possible subtraction artifacts are marked with asterisks (\*). In the HOOP and marker regions (highlighted in yellow), PCB bands can be detected unambiguously (see figs. 4.2.4 and 4.2.3).

**PhyPIF formation in the Pfr state** The Pfr-PIF3 complexes were generated by two different approaches in order to exclude diffusion rate limiting effects on the PhyPIF adduct formation reaction (see eqn. 4.1) in the highly concentrated Raman sample. In a first approach, the unconcentrated AtPhyB sample was illuminated with red light (660 nm LED) before mixing with PIF3 and subsequent concentration. In the second approach, the mixed and concentrated sample was illuminated in a last step. Both approaches led to similar spectral changes, indicating that reaction 4.1 is not diffusion-limited under the present conditions.

In *Avena sativa* phytochrome A, the heterogeneous Pfr state comprises an equilibrium of two distinct chromophore configurations (denoted Pfr-I and Pfr-II) characterized by a differences in the C,D methine bridge torsional angle of about  $10^\circ$ . [229] This equilibrium is also observed in PhyB regardless of the assembled chromophore (PCB or the native P $\Phi$ B) or whether the construct comprises the NTE. The relative contribution of the two sub-states shifts in the NTE deletion mutants ( $\Delta NTE$ ). [231] Both species can be readily detected in RR spectra because different modes are influenced by the conformation of ring D. This applies to the most prominent band in the marker region, the C=C stretching mode doublet at 1607 and 1618  $\text{cm}^{-1}$  (see fig. 4.2.3), and also to the C,D hydrogen-out-of-plane (HOOP) doublet at 804 and 818  $\text{cm}^{-1}$  (see fig. 4.2.4). Hereby, the low-frequency HOOP mode and the high-frequency C,D stretching component were assigned to Pfr-I, whereas the high-frequency HOOP and low-frequency C,D stretching originate from Pfr-II (see also chapter 4.1). [229, 231] Upon addition of PIF3, A small upshift ( $+1 \text{ cm}^{-1}$ ) of the band at 1607  $\text{cm}^{-1}$  and a relative intensity loss in the 1618  $\text{cm}^{-1}$  mode are observed. The second effect can be attributed to a shift of the conformational equilibrium from Pfr-I towards Pfr-II. This interpretation is underpinned by the HOOP region, where a concomitant intensity redistribution from the low-frequency mode (804  $\text{cm}^{-1}$ , marker for Pfr-I) to the higher frequency mode (818  $\text{cm}^{-1}$ , marker for Pfr-II) is observed. Additionally, both C,D HOOP bands shift up by 3 and 4  $\text{cm}^{-1}$ , and a small upshift (2  $\text{cm}^{-1}$  from 1556 to 1558  $\text{cm}^{-1}$ ) in B,C N-H i.p. bending mode is observed, indicating further minor structural adjustments in the chromophore binding pocket upon PIF3 interaction.

Interestingly, the mode composition indicating the Pfr conformational equilibration, is also influenced by NTE deletion. The effect of PIF addition is exactly reversed: NTE deletion shifts the conformational equilibrium more towards Pfr-I, while PIF3 adduct formation favors Pfr-II. [231] Remarkably, NTE deletion was found to accelerate the Pfr to Pr dark reversion reaction [26], while the process is slowed down when PIF3 is added to the sample. [62] Both findings can be rationalized within the two-states model, and it can be concluded that Pfr-I has a faster dark reversion kinetics compared to Pfr-II.

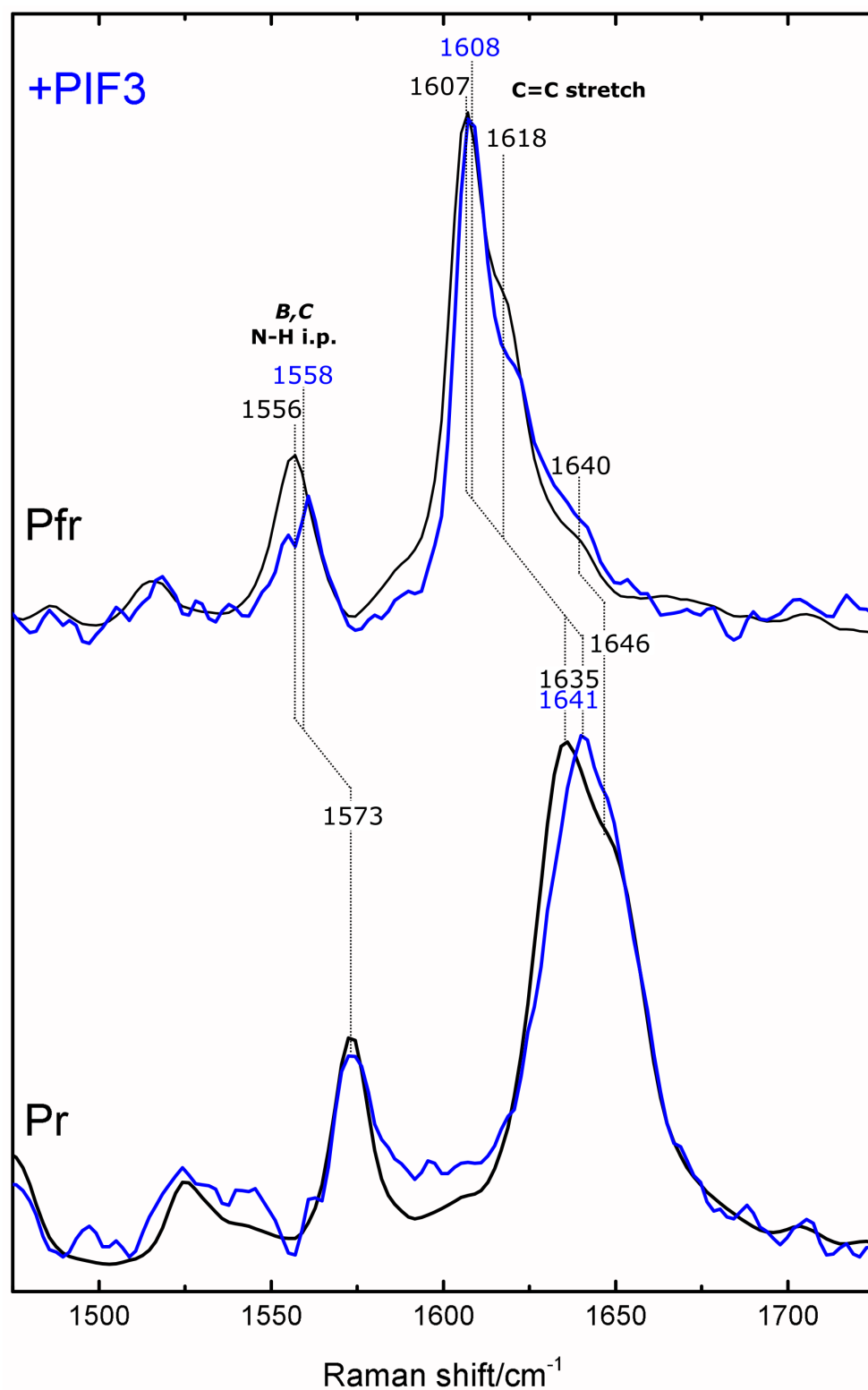


**Figure 4.2.3:** RR spectra of AtPhyB with PIF3 in the marker region (detail of fig. 4.2.2). The overlaid black and blue spectra show AtPhyB in the Pr and Pfr state without and with the addition of PIF3, respectively. Top: Pfr state. Bottom: Pr state.



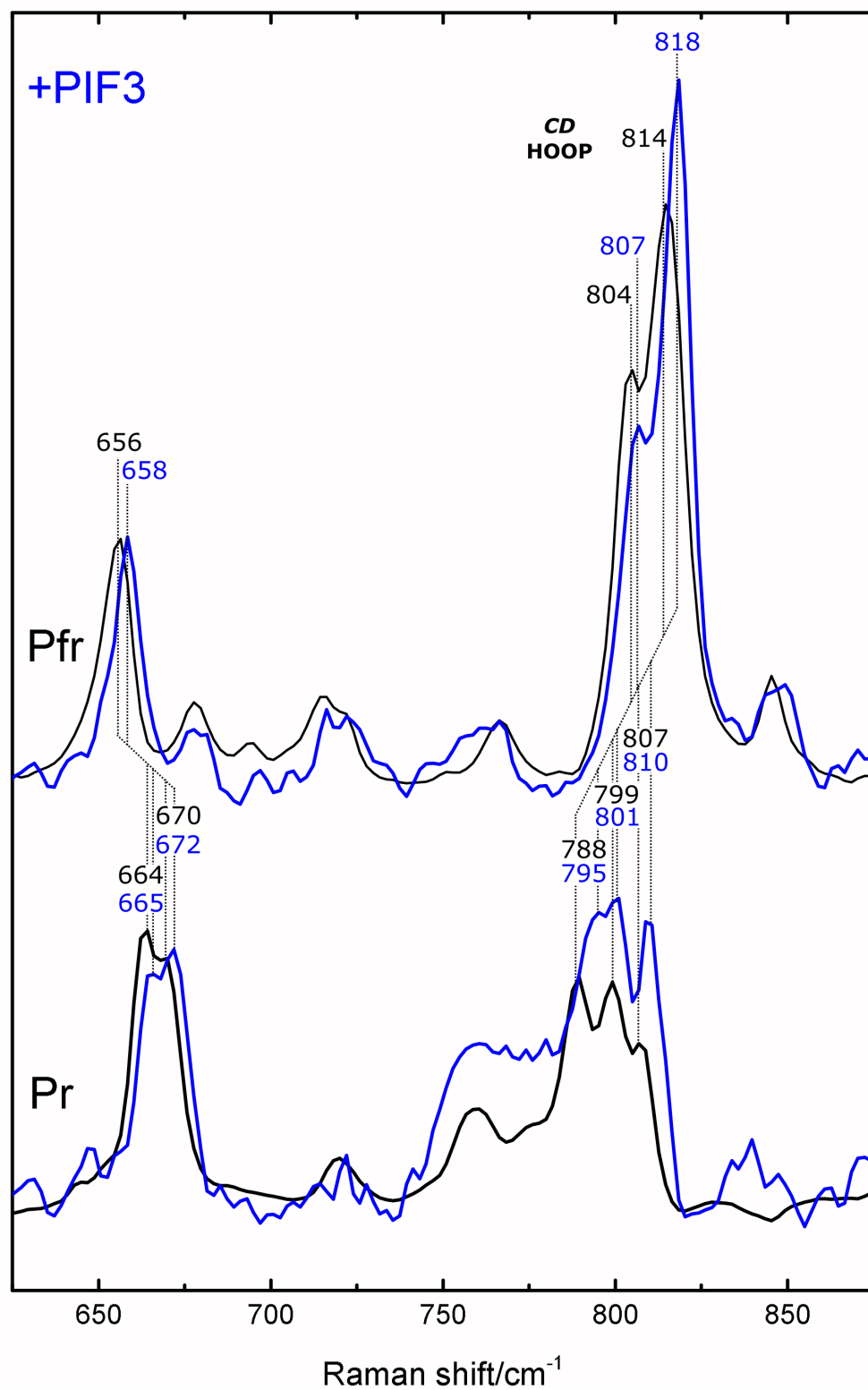


**Figure 4.2.4:** RR spectra of AtPhyB with PIF3 in the HOOP region (detail of fig. 4.2.2). The overlaid black and blue spectra show AtPhyB in the Pr and Pfr state without and with the addition of PIF3, respectively. Top: Pfr state. Bottom: Pr state.

**Possible interaction in the Pr state** In the Pr state, no PhyPIF complex formation was observed in the MST experiments and no equilibrium constant could be determined.[62] Additionally, deletion of the NTE had no effect on the Pr state RR spectra.[231] Therefore it is rather surprising, that spectral changes are also detected in the Pr marker and HOOP regions upon PIF addition.

In contrast to Pfr, the C=C stretching doublet in the Pr marker region is not assigned to two distinct bilin conformations. Here, the doublet originates from two different normal modes with major contribution from the C,D methine bridge ( $1635\text{ cm}^{-1}$ ) and the A,B methine bridge ( $1646\text{ cm}^{-1}$ ) C=C stretching vibrations.[136] The latter mode is detected in the Pfr only as a small shoulder at  $1640\text{ cm}^{-1}$ , while in Pr the relative intensity is higher. The C,D C=C stretching mode shifts up to  $1641\text{ cm}^{-1}$  upon PIF addition, indicating that the torsional angle of ring D is affected. This effect is also reflected in the HOOP region where small upshifts of all bands (in the order of  $4\text{ cm}^{-1}$ ) are observed. These results indicate that a PhyPIF complex is also formed in the Pr state under the present experimental (RR) conditions.

PIF3 can also bind in the Pr state of *Avena sativa* PhyA, and the differential binding is strongly buffer-dependent.[195] Taking the far-reaching similarities of PhyA and PhyB into account, these findings probably also hold for AtPhyB.[231] The different buffer conditions and concentrations are most likely the reason for PhyPIF complex formation in the RR experiments, but not in MST. In the RR experiments, the samples are concentrated by up to 100-fold higher than in UV/Vis absorption (*vide supra*), corresponding to viscous suspensions rather than real solutions. Thus, a weakened specific ion efficacy and different diffusion rates, may influence the rate and equilibria of chemical reactions like the PhyPIF adduct formation (eqn. 4.2). Regarding the fundamentally different situation in a molecular crowded environment in living plant cells from the *in vitro* MST or the RR experimental conditions, no conclusions can be drawn at this point whether PIF3 forms transient complexes with AtPhyB in the Pr state *in vivo*.

### 4.3 The PAS-GAS Construct of *Sorghum bicolor* Phytochrome B

This chapter focusses on the spectroscopic characterization of plant phytochrome B from the monocotyledon *Sorghum bicolor* (SbPhyB), in particular the truncated PAS-GAF (PG) protein variant assembled with PCB. The PGP construct is identical with the PSM without the N-terminal extension (which is denoted SbPhyB  $\Delta$ NTE in chapter 4.1), the nomenclature was changed in this chapter to stay consistent with the nomenclature for unpublished results throughout the thesis. Recently, SbPhyB PG was successfully crystallized in the Pr state, and a promising high-resolution x-ray structure was solved (1.4 Å resolution, unpublished results, private communication with Dr. Soshichiro Nagano and Prof. Dr. Jon Hughes). A cartoon representation of the overall protein fold and a figure of the electron density distribution within the chromophore binding pocket were kindly provided by Dr. Soshichiro Nagano (fig. 4.3.1). Upon red-light illumination in solution, the PG protein construct forms a long-lived photoproduct and thus is a good candidate to obtain a crystal structure of a light-activated state. To investigate whether this photoproduct can be used as a model for a photocycle intermediate of the PGP construct, UV/Vis, RR and IR difference spectroscopy were employed.

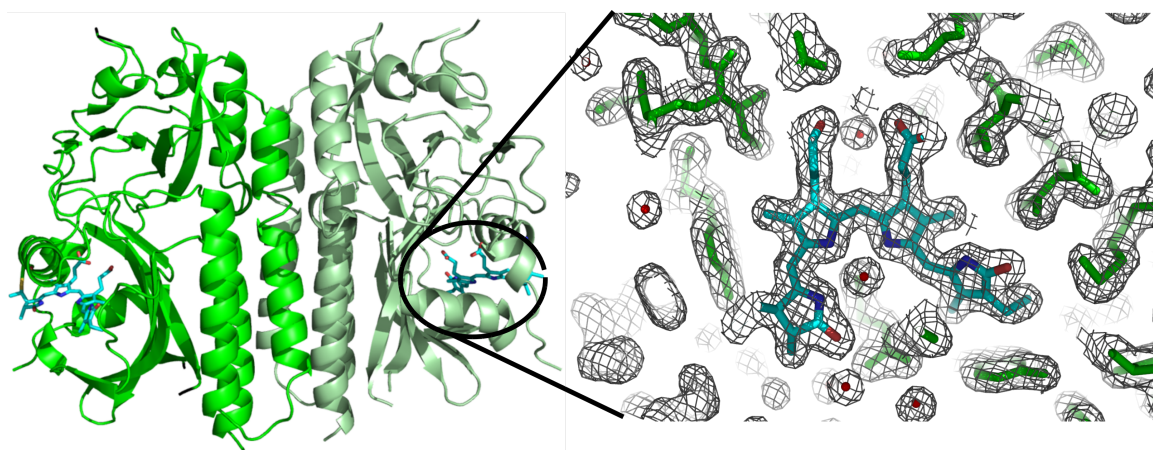


**Figure 4.3.1:** SbPhyB PG crystal structure. The left panel shows an overall picture of the protein fold with the two monomeric subunits represented in different shades of green. The right panel depicts a close-up view of the PCB chromophore (cyan) and the side-chains of the surrounding amino acids (green). Electron density cutoff is represented by a black mesh. This figure was kindly provided by Dr. Sochichiro Nagano.

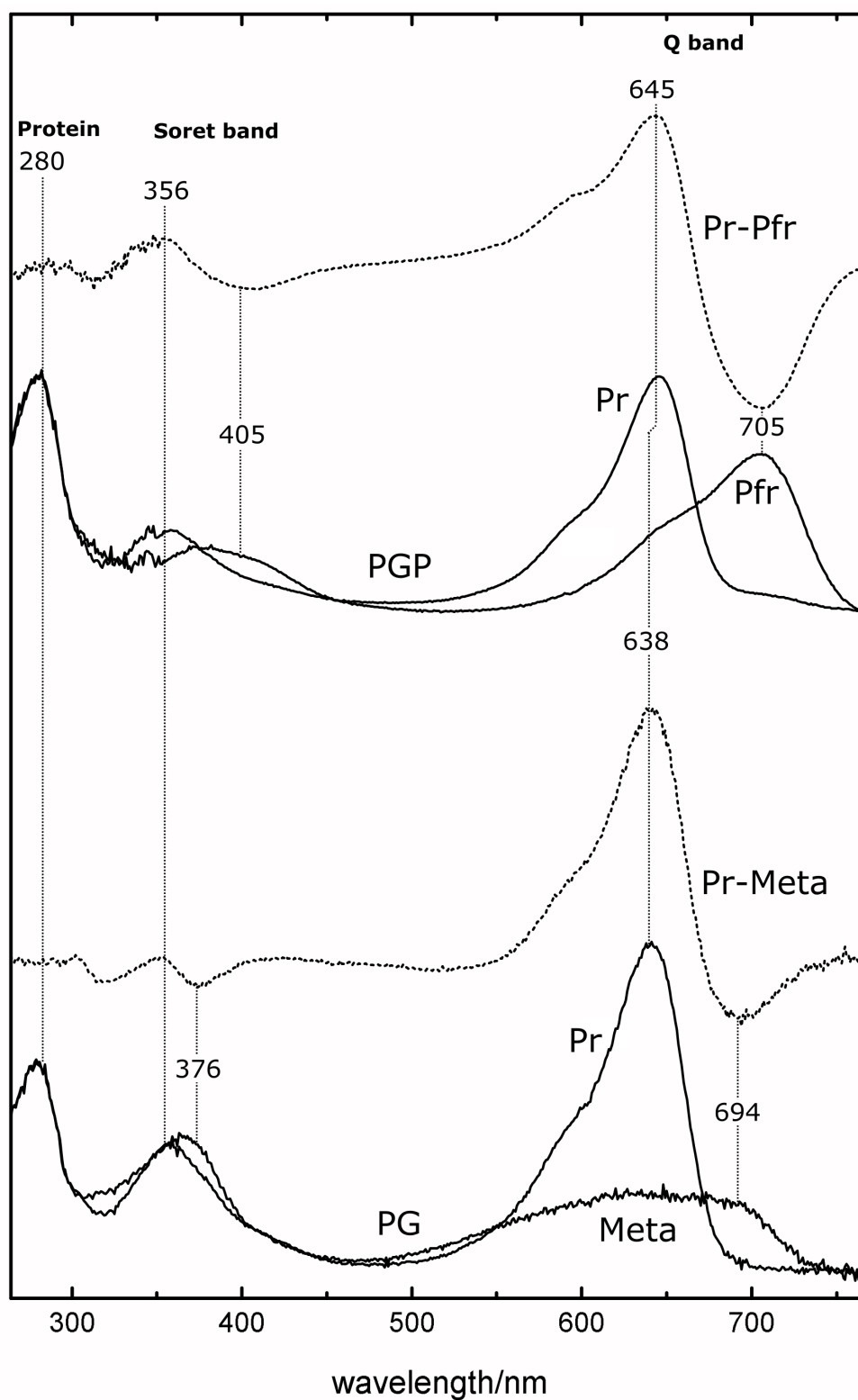


**Figure 4.3.2:** UV/Vis absorption and difference spectra of the SbPhyB PG (bottom) and PGP constructs (top). The absorption spectra of the Pfr and Meta states were generated by spectral subtraction of residual Pr contributions. For the original, unsubtracted spectra, see supplementary fig. 9.1.1 Pr-minus-Pfr (for PGP) and Pr-minus-Meta (for PG, bottom). Difference spectra are indicated by dashed lines.

**UV/Vis spectroscopy** In agreement with previously published results[231], the Pr and Pfr spectra of the PGP construct exhibit Q-band absorption maxima at 645 and 705 nm, respectively (see fig. 4.3.2). However, complete photoactivation was achieved neither in the PGP nor PG constructs. Hence, the pure photoproduct spectra were obtained *via* subtraction of residual Pr contributions (for unsubtracted spectra, see supplementary fig. 9.1.1). In the PG variant, the Pr Q-band maximum is shifted down by 7 nm upon PHY domain deletion, indicating only minor changes in the dark-adapted state. The PG photoproduct spectrum displays a broad and unstructured low-intensity Q-band. Similar spectra were observed for the Meta-Rc state of *Avena sativa* phyA or the Bph Agp1.[39, 18] Concomitantly, the Soret band features a smaller upshift from 356 to 376 nm and no characteristic broadening like in PGP Pfr, accompanied by an upshift to 405 nm. These shifts can be detected with higher accuracy in the Pr-minus-Pfr and Pr-minus-Meta difference spectra (dashed lines in fig. 4.3.2). Despite the truncation of the output module and the NTE, a Pfr state is formed in the PGP construct (albeit with changed sub-populations of Pfr-I and Pfr-II, see chapter 4.1).

The shape and intensity of the Q-band of the PG construct photoproduct differ significantly from the typical Pfr spectrum. Taking the similarity to Meta-Rc into account, all photoproduct spectra (UV/Vis, RR and IR) of PG are denoted “Meta” in the following. The use of this notation is not intended to assign the photoproduct to a specific state in the PGP photocycle and solely expresses the observation that no characteristic Pfr is formed. In Agp1, the low intensity Q-Band was associated with chromophore deprotonation in the Meta-Rc state[18], but in the cyanobacteriochrome AnPixJg2, only small changes UV/Vis absorption spectra have been observed despite of chromophore deprotonation.[201] Anyhow, the de- and re-protonation reactions of the bilin during the photocycle reactions probably play a crucial part in the signal transduction through the protein (see chapter 1.3). Because the structure and intensity of the Q-band are not conclusive for the chromophore protonation pattern, application of RR spectroscopy is useful because this technique can assess the protonation state directly by probing of the corresponding N-H vibrations.

**Solution RR spectroscopy** The following discussion is restricted on the RR signals characteristic for the structure of the PCB chromophore. These are found in the marker (see fig. 4.3.3), HOOP (see fig. 4.3.5) and C=O regions (see fig. 4.3.4). The full range RR spectra are given in the supplementary figure 9.1.2.

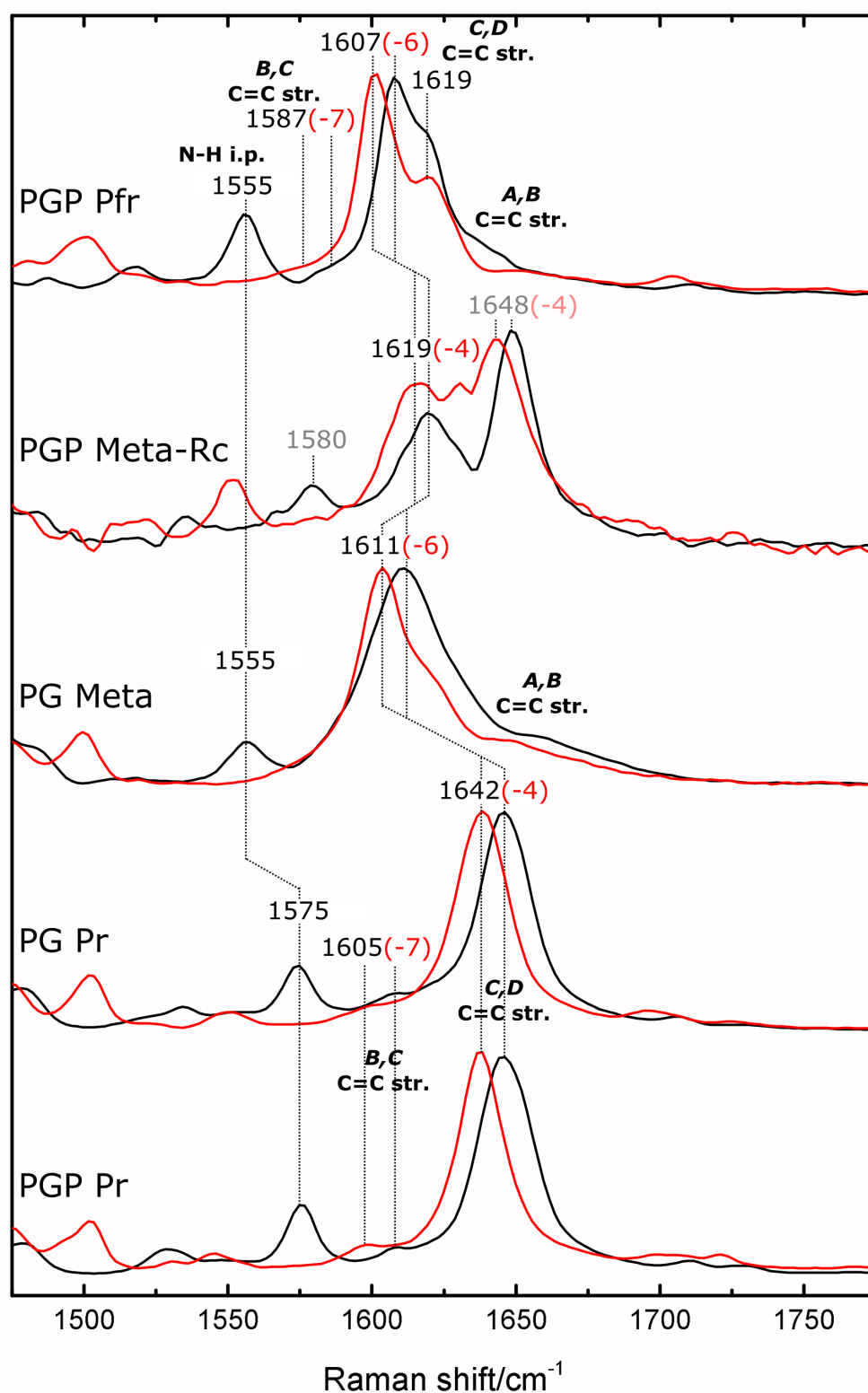


**Figure 4.3.3:** SbPhyB RR spectra in the marker region. Spectra were recorded in  $\text{H}_2\text{O}$  and  $\text{D}_2\text{O}$  buffer. From bottom to top: The Pr spectra of the PGP and PG variants in the Pr form and the photoproduct (Meta) of the PG variant. The PGP Meta-Rc spectrum of PGP was generated according to published cryo-trap conditions.[99] Topmost panel: the PGP Pfr spectrum.

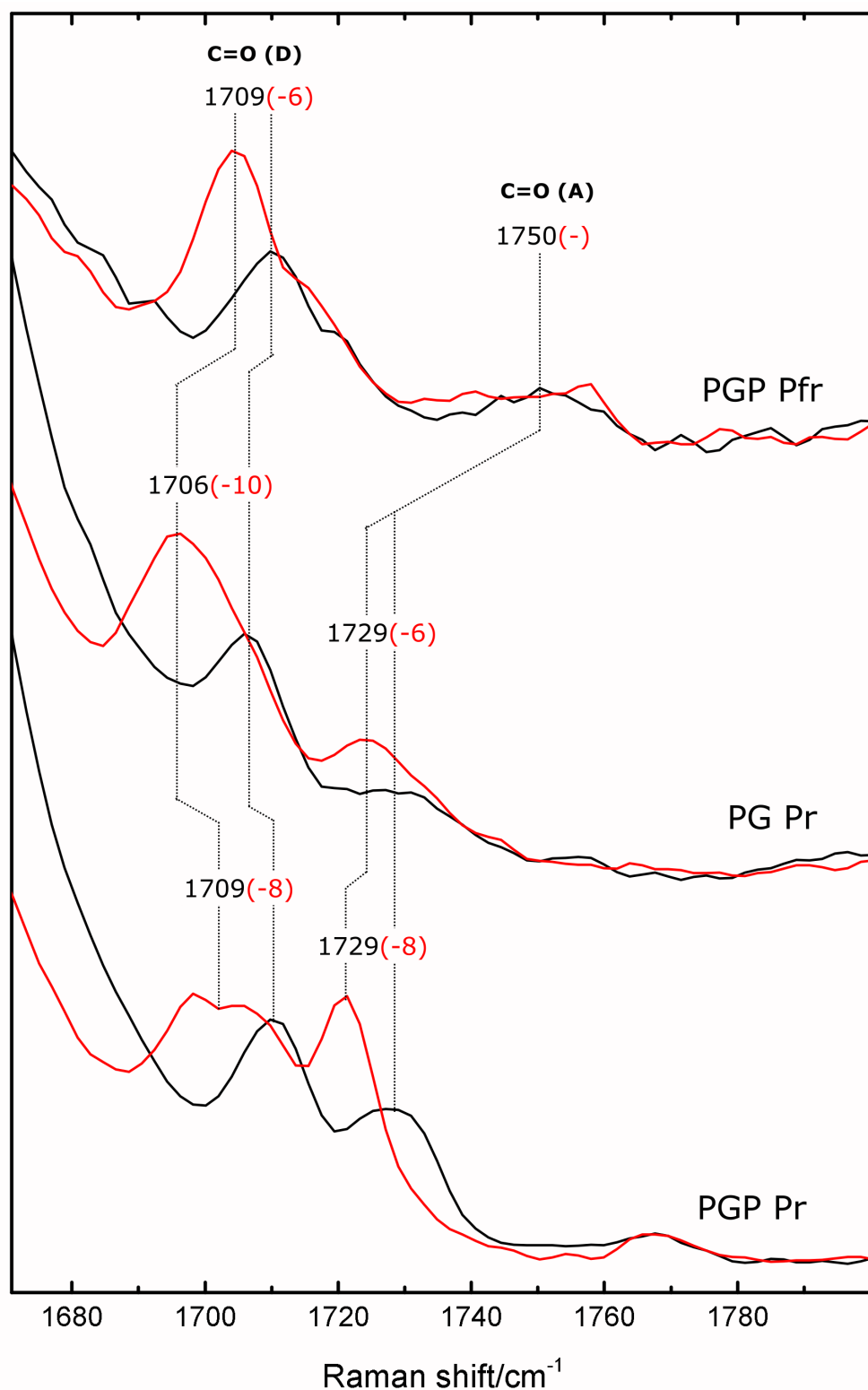


**Figure 4.3.4:** SbPhyB RR spectra in the CO region. Spectra were recorded in  $\text{H}_2\text{O}$  and  $\text{D}_2\text{O}$  buffer. Only spectra of the Pr forms (bottom: PGP, middle: PG) and the PGP Pfr are shown. In the Meta forms of PG and PGP, the C=O stretching bands are not detected due to a poor S/N ratio in the spectra and are therefore omitted in this figure.

**Pr** In the Pr state, the PG construct appears identical to PGP in all spectral regions consistent with the published RR data (see chapter 4.1).[231] The C=C stretching band positions at  $1605\text{ cm}^{-1}$  and  $1642\text{ cm}^{-1}$  and the N-H i.p. bending at  $1575\text{ cm}^{-1}$  as well as their corresponding isotopic shifts when measured in  $\text{D}_2\text{O}$  buffer are indicative of a protonated (cationic) PCB chromophore in the ZZZssa configuration.[135] Only a small downshift in the CO region from  $1709\text{ cm}^{-1}$  to  $1706\text{ cm}^{-1}$  construct can be noted in the PG construct. The C=O stretching bands of ring A and D are extremely sensitive to even small changes of the carbonyl oxygen atoms (e.g. by the coordinating water molecules or the surrounding protein) and therefore often hard to predict by frequency calculations even on the QM/MM level.[135, 183] The lower-frequency band was assigned to the carbonyl stretching of ring D by isotopic labeling IR experiments in Cph1.[226] The mode appears as a strong negative signal in the IR spectra at  $1701\text{ cm}^{-1}$  (PGP) and  $1702\text{ cm}^{-1}$  (PG, see fig. 4.3.6). The apparent frequency in the difference IR spectra deviates from the RR data because the signal is obscured by the contiguous positive signals. The corresponding Pfr signal for ring D C=O stretching ( $1721\text{ cm}^{-1}(+)$ ) is weak and broad in the PG construct compared to PGP ( $1711\text{ cm}^{-1}(+)$ ) and does not exceed the noise level in RR (therefore not plotted in fig. 4.3.4). This results in a stronger bias of the adjacent (-) signals in the IR spectra and therefore the band appears to be more downshifted in PGP when compared to the RR signals. Because the C=O stretching bands are well separated in the RR, the band positions are less biased and therefore probably more accurate, although the CO modes have intrinsically weak RR activity. Additionally, the experimental conditions are different in RR and IR experiments, thus a temperature effect on the band positions cannot be ruled out (see chapter 3 for the experimental conditions).

**Pfr** In the Pfr state, the PGP construct displays the characteristic RR spectrum composed of two protonated ZZEssa configured PCB species with slight conformational differences at the C,D methine bridge (Pfr-I and Pfr-II) The Pfr spectrum of SbPhyB PGP is discussed in detail in chapter 4.1, thus another discussion is omitted at this point.[231] To analyze the PG photoproduct spectrum, it will be compared not only to the PGP Pfr but also to the Meta-Rc RR spectrum of PGP.



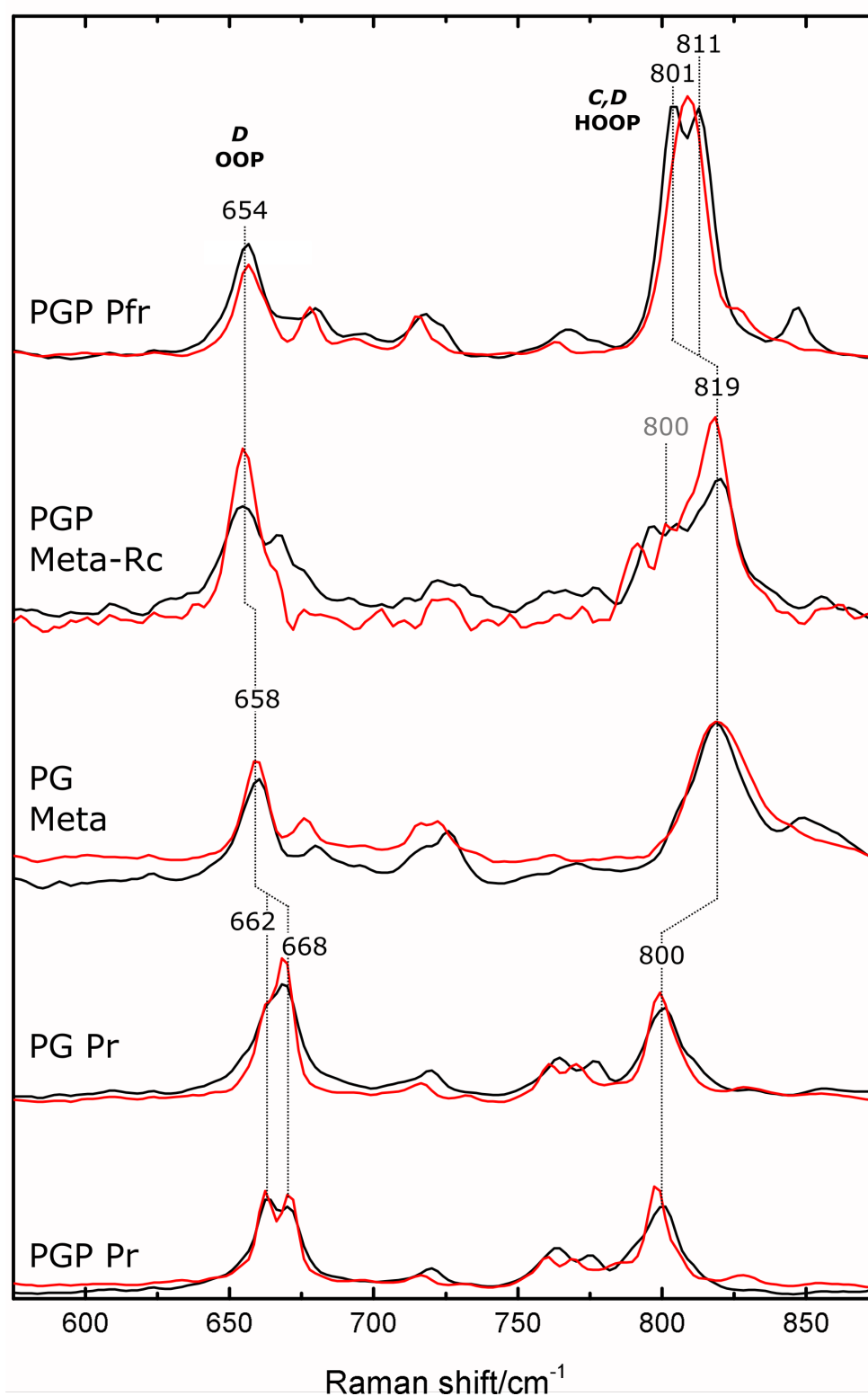


**Figure 4.3.5:** SbPhyB RR spectra in the HOOP region. Spectra were recorded in  $\text{H}_2\text{O}$  and  $\text{D}_2\text{O}$  buffer. From bottom to top: The Pr spectra of the PGP and PG variants in the Pr form, followed by the photo product of the PG variant (denoted Meta). The PGP Meta-Rc spectrum of PGP was generated according to published cryo-trap conditions.[99] Topmost panel: the PGP Pfr spectrum.

**The Meta-Rc state** The Meta-Rc photoproduct was generated according to the experimental conditions and subtraction procedure published for the phytochromobilin (PΦB) adduct of *Avena sativa* PhyA (AsPhyA).[99] Generally, the photochemical quantum yield for the Pr to Meta reactions and the scattering cross section of the Meta-chromophore itself are quite low compared to Pfr, resulting in a low signal-to-noise (S/N) ratio and significant apo-protein contribution in the Meta RR spectra. In these cases, the sharp band at  $1004\text{ cm}^{-1}$ , corresponding to the phenylalanine (Phe) breathing mode of the protein can be used as a marker to assess apo-protein contribution to the Meta spectra and estimate the resonance enhancement factor. Additionally, the spectral subtraction procedure is quite complex and includes several free parameters like tentative subtraction factors and is therefore prone to systematic errors and spectral artifacts.[40, 236, 98] The Meta-Rc of the PCB adduct of AsPhyA is a good example for these obstacles, and yields spectra with poor S/N ratio and broad, heterogeneous features in all spectral regions.[236, 98] Similar difficulties were faced for the Meta-Rc of SbPhyB PGP and discussed briefly in the following.

The most prominent band in the Meta-Rc marker region of SbPhyB PGP is composed of two major features at  $1619\text{ cm}^{-1}$  and  $1648\text{ cm}^{-1}$ , with corresponding downshifts in  $\text{D}_2\text{O}$  buffer by  $4\text{ cm}^{-1}$ , indicating that both signals originate from normal modes including mainly C=C stretching character of the methine bridges (see fig. 4.3.3). These two peaks are found in a variety of Meta-Rc spectra from different PCB binding phytochromes.[236] While the lower frequency band ( $1619\text{ cm}^{-1}$ ) is in reasonable agreement with a ZZEssa C/D methine bridge stretching mode (like in the Pfr state), the intense peak at  $1648\text{ cm}^{-1}$  is not easy to rationalize. At least three different origins for spectral contributions to this band have to be taken into account:

- A contribution from the protein amide I band (see diff. IR spectra in fig. 4.3.6) is expected in this region. However, the protein backbone contributions to the Meta-Rc spectrum can be estimated from the intensity of the  $1004\text{ cm}^{-1}$  Phe breathing mode (full range RR spectra given in supplements fig. 9.1.2) and are quite low in this case.
- Some contribution can originate from the A,B C=C stretching mode, which is also seen as shoulder in Pfr and the PG Meta at similar frequencies, albeit with much lower intensities. In principle, this band could have a much higher relative intensity in the Meta-Rc state compared to the parent states and thus be a major contribution to this feature.
- A third possibility is that the band partly originates from an incomplete subtraction of another, Pr-like, state. If this is the case, other spectral artifacts are expected at positions close to prominent Pr bands.

Indeed, bands are found at  $1580\text{ cm}^{-1}$  and  $800\text{ cm}^{-1}$ , closely resembling the Pr N-H i.p. bending and HOOP bands. Furthermore, the relative intensity distribution between these three bands resembles the Pr or a Pr-like state, thus it is very likely that a large contribution to this feature is caused by incomplete spectral subtraction.

**Difficulties of spectral subtraction** When parent-state contributions are subtracted to obtain spectra of intermediate states, the procedure implicitly requires that the spectra of the parent states do not change during the experimental procedure. In the case of Meta-Rc cryo-trapping in SbPhyB PGP, the Pr spectrum is therefore required to be identical before and after a temperature change by +90 K, red light illumination and another temperature change by -90 K, in order to be subsequently removed completely by spectral subtraction. Unfortunately, the Pr state of PCB binding phytochromes is generally not homogeneous and the heterogeneities can be detected *via* spectroscopic methods.[93, 94] If two or more distinguishable Pr sub-states have different photochemical reaction coordinates and therefore different rate constants, the prerequisite of an identical Pr RR spectrum before and after illumination is not met. The overall Pr spectrum, a superposition of the sub-states, will change in favour of the Pr sub-state with the slower reaction rate, because this state reacts less and therefore contributes more to the spectrum. The overall composition of the Pr spectrum will therefore be affected by the experimental procedure, even if the difference in reaction rates is small. This argumentation is further validated by the D<sub>2</sub>O spectra: here the artifacts are less intense relative to the signals that are tentatively assigned to real Meta-Rc bands. Both peak doublets, at 1615/1644 cm<sup>-1</sup> and 819/800 cm<sup>-1</sup> have a changed intensity distribution in favour of the presumably real bands (1615 and 819 cm<sup>-1</sup>). The changed ratio in D<sub>2</sub>O can be rationalized as a kinetic isotope effect in the reaction rates of the Pr sub-states to Meta. In fact, a kinetic isotope effect can be anticipated because this reaction involves a deprotonation event which should be accelerated in D<sub>2</sub>O.[99] With the assignment of the 1580 cm<sup>-1</sup> band to a spectral artifact and no corresponding band in the region of 1555 cm<sup>-1</sup>, the Meta-Rc chromophore is most likely in a deprotonated form like in Agp1 or other prototypical phytochromes.[18]

**PG photoproduct** Taking these considerations into account, the Meta spectrum of the PG construct can be compared to the PGP variants Pfr spectrum and the real peaks in the Meta-Rc spectrum. The PG Meta is protonated at all four pyrrole rings as indicated by the characteristic B,C N-H i.p band at 1556 cm<sup>-1</sup> and in a Pfr-like ZZE<sub>ss</sub> configuration (C,D C=C stretching band at 1611 cm<sup>-1</sup>). These two features, as well as the low-intensity A,B C=C stretching high-frequency shoulder (ca. 1640 cm<sup>-1</sup>) in the marker region resemble the Pfr state of PGP quite well, including the according isotopic downshifts when measured in D<sub>2</sub>O. The C,D HOOP region, however, does not display the characteristic intense doublet at 801 and 811 cm<sup>-1</sup> indicative for the Pfr-I/Pfr-II equilibrium (see fig. 4.3.5). In contrast, a broad and upshifted feature, similar to the Meta-Rc spectrum is detected at 819 cm<sup>-1</sup>. The C,D HOOP frequency exhibits a sensitive negative correlation with the C(14)-C(15)-C(16)-N(D) dihedral angle and is therefore a marker band for the chromophore configuration at the C,D methine bridge.[183]

The C=O bands are detected neither in the Meta-Rc nor in the PG Meta RR spectra, probably because they are broad and not intense, but are clearly detected in the IR difference spectrum at 1721 cm<sup>-1</sup> (+)(*vide supra*). Taken together, the RR data implies that PCB adopts a ZZE<sub>ss</sub> configuration in-between Meta-Rc and Pfr in the PG photoproduct and is protonated.

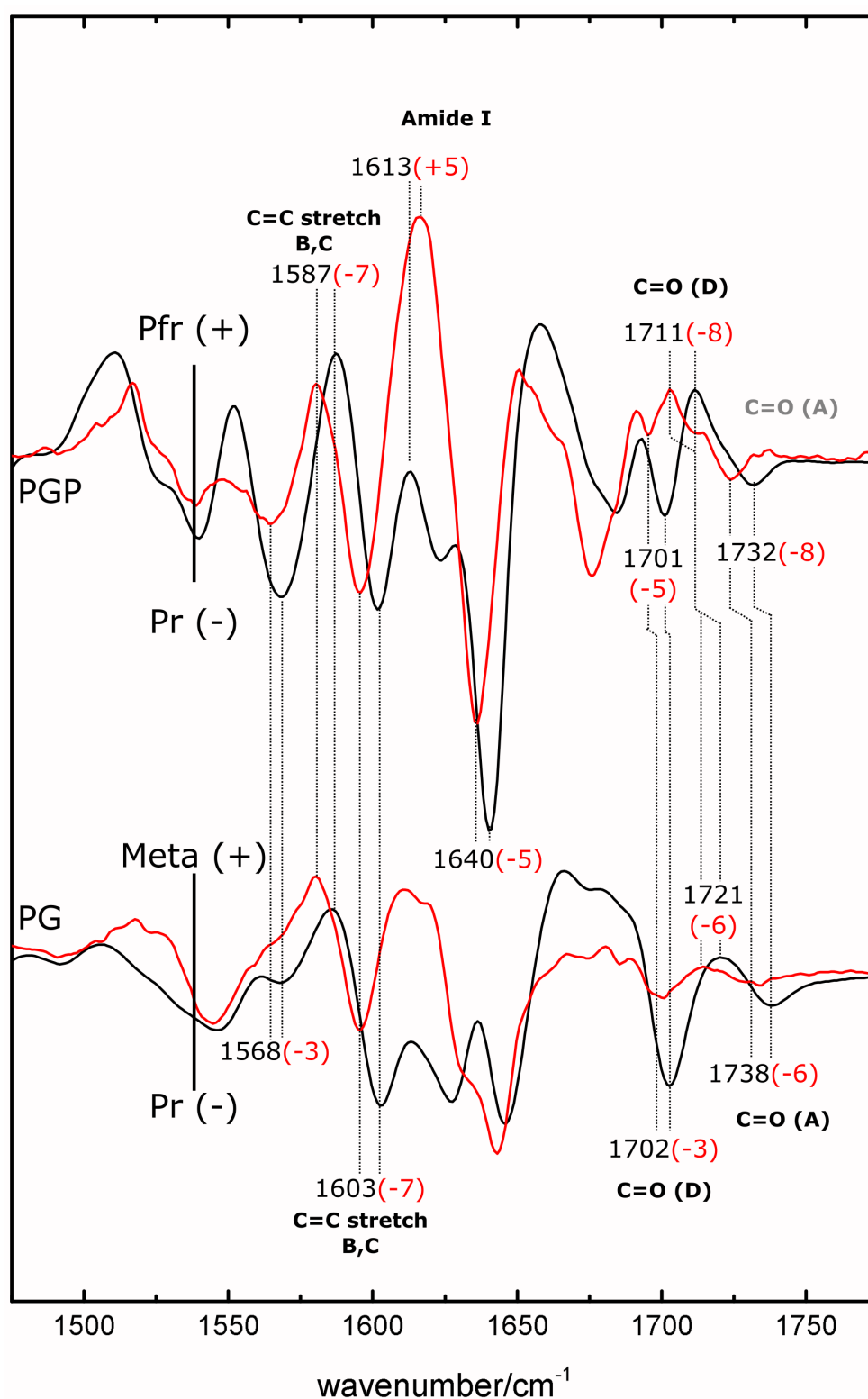


**Figure 4.3.6:** IR difference spectra of SbPhyB PG (bottom) and PGP (top). Spectra were recorded in  $\text{H}_2\text{O}$  and  $\text{D}_2\text{O}$  buffer. Negative (-) bands originate from a bleach of singals corresponding to the dark-adapted state (Pr), while positive features originate from the photoproduct (Pfr for PGP or Meta for PG).

**IR difference spectroscopy** Additional to the C=O stretching signals, the IR difference spectra display more interesting features that can be used to assign the state of the PG photoproduct (see fig. 4.3.6). The B,C C=C stretching vibration is IR active and detected as a strong difference signal at the same position (1578(+)/1603 cm<sup>-1</sup> (-)) in both protein constructs with an isotopic shift of -7 cm<sup>-1</sup> in D<sub>2</sub>O. This mode is only sparsely Raman active and forms a small shoulder at 1587 cm<sup>-1</sup> in the Pfr and 1605 cm<sup>-1</sup> in the Pr state (see fig. 4.3.3). The characteristic isotopic shift of -7 cm<sup>-1</sup> in the D<sub>2</sub>O RR spectra is in good agreement with the IR data. The strongest bands in the PGP IR difference spectrum are in the amide I region between 1600 and 1650 cm<sup>-1</sup>. These signals are caused by the secondary structure transition of the PHY domain tongue motif during the photocycle (see chapter 1.3). This transition comprises four events with overlapping spectral signatures: the loss of the  $\beta$ -sheet and  $\beta$ -hairpin motives and the concomitant formation of the  $\alpha$ -helix and the coil region of the tongue (personal communication with Prof. Dr. Peter Hildebrandt and Prof. Dr. Friedrich Siebert, see also chapter 6.2). These features overlap additionally with the smaller amide I difference signals that can also be seen in the PG Meta-minus-Pr difference spectra, probably originating by smaller structural adjustments in the PAS and GAF domains. Hence, the band pattern in this region is very complex and hard to interpret in detail, but the association of the large difference signal 1613(+)/1640 cm<sup>-1</sup>(-) to the tongue secondary structure transition is reasonable. A possible interpretation of these results is that the chromophore reprotonation precedes the tongue restructuring. This conclusion is only valid if the reaction mechanism of the re-protonation in the PG and the PGP constructs is the same.

**RR on crystal samples** As discussed in chapter 1.3, RR spectroscopy is an excellent tool to validate x-ray crystal structures by comparison of the RR spectra obtained from samples in solution and crystalline form. All RR spectra from SbPhyB PG crystals discussed in the following were kindly provided by Anastasia Kraskov and crystallization was performed by Dr. Soshichiro Nagano.

The dark spectrum of the crystals resembles the solution Pr spectrum (see fig. 4.3.7) in overall bandshape and position of the peaks very well, e.g. the C,D C=C stretching peak at 1644 cm<sup>-1</sup> and B,C N-H i.p. band at 1573 cm<sup>-1</sup>. The crystals were subjected to illumination with a 660 nm LED array to generate a photoproduct *in crystallo*. After the illumination procedure, the spectra displayed distinct differences originating from two processes. Primary, photoconversion to the Meta product, indicated by the upcoming C,D C=C stretching marker band at 1607 cm<sup>-1</sup>. Secondly, the relative contribution of buffer bands is higher in the spectra of the illuminated crystals. The crystallization buffer contains high amounts of the precipitant polyethyleneglycol (PEG), leading to Raman signals in the region 800-1500 cm<sup>-1</sup>, that were marked with asterisks (\*) in figure 4.3.7.[100] In the Pr spectrum, the contribution of these PEG bands is negligibly small and no intensive PEG bands are observed in the spectral region from 1000 to 1200 cm<sup>-1</sup>.

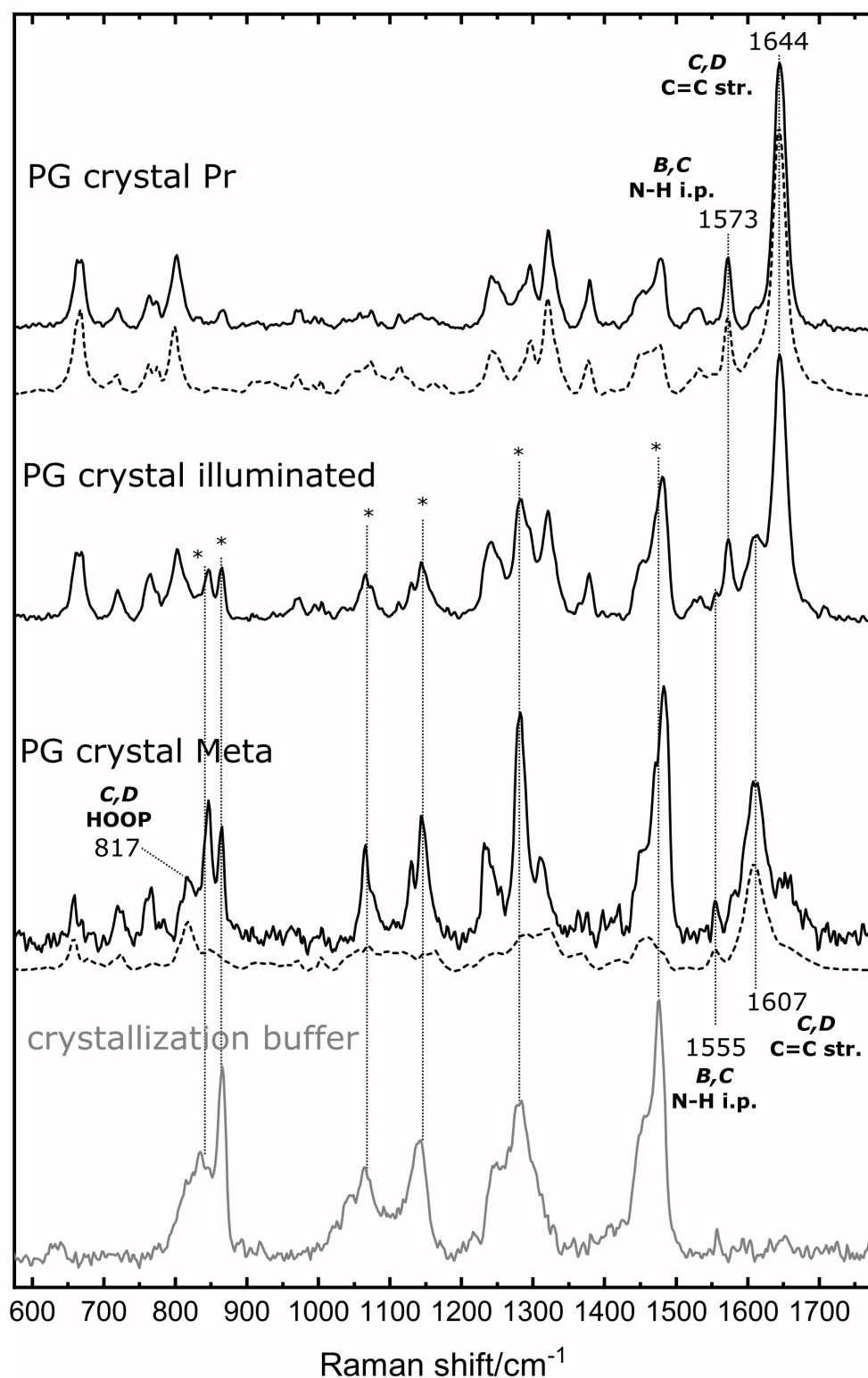


**Figure 4.3.7:** RR spectra of SbPhyB crystals. Bottom: the crystallization buffer (gray spectrum) contains PEG and thus contributes to the other spectra (PEG bands are marked with asterisks (\*)). From top to bottom: the dark crystal spectrum is essentially identical with the solution spectrum (dashed line). After illumination (660 nm LED array), the crystals are photoconverted to a certain extent (middle). Subtraction of the dark crystal spectrum yields the Meta crystal, albeit with large buffer contributions. The solution Meta spectrum (dashed line) is given as a reference. All crystal spectra were kindly provided by Anastasia Kraskov and crystallization was performed by Dr. Soshichiro Nagano.

The RR intensity of the Meta crystals is much lower compared to Pr, therefore the relative contribution of PEG bands to the overall spectrum is magnified when the Pr sample is photoconverted to Meta. After subtraction of residual Pr from the illuminated crystal spectrum, a superposition of the PEG bands and the Meta spectrum is obtained. Unfortunately, the PEG bands cannot be further subtracted to yield the pure Meta spectrum without generating massive spectral artifacts for two reasons:

- The S/N ratio in the buffer spectrum and the PG crystal Meta spectrum is low and the error multiplies in every step of spectrum manipulation, such as subtraction.
- The Raman spectrum of PEG is probably changed when PEG interacts with protein crystals, and thus cannot be subtracted without the generation of subtraction artifacts such as negative or very sharp bands.

**Outlook** Nevertheless, these results clearly demonstrate that photoactivation of Sb-PhyB PG crystals is possible and yields a product with a chromophore geometry comparable to the Meta of PG in solution. Hence, to obtain an activated crystal structure that can be used to model the Meta-Rc state of plant phytochromes, experimental conditions need to be further optimized. First, the illumination conditions (light intensity, wavelength and sample temperature) can be further optimized to obtain a higher amount of photoconverted molecules per crystal. From the RR spectra in figure 4.3.7, photoconversion of about 50% can be estimated, judging by the enlargement of the PEG bands in the spectral region 1000-1200  $\text{cm}^{-1}$ . Furthermore, it could be advantageous to investigate the spectral artifacts in Meta-Rc more systematically and to find an efficient way to subtract the PEG contribution from the Meta RR spectrum of the PG crystals.

## 5 Results: Cyanobacterial Phytochromes

The studies on cyanobacteriochromes (CBCRs) focused on the PCB-binding GAF-protoreceptor Slr1393 from *Synechocystis* sp. PCC6803. In the following chapter, RR and cryo-UV/Vis spectroscopy were employed to investigate the structural parameters that govern the unusual red/green photochemistry.

### 5.1 The Cyanobacteriochrome Slr-GAF3

The third GAF domain of the CBCR Slr1393 from *Synechocystis* sp. PCC6803 (Slr-GAF3) and the well characterized second GAF domain of AnPixJ from *Anabaena* sp. PCC7120 (AnPixJg2) are highly homologous.[140, 50, 230, 201] Photoactive AnPixJg2 holoprotein can be purified in two different ways: PCB can either be assembled *in vivo* by introduction of a PCB-producing protein apparatus into the heterologous host system *E.coli*, or *in vitro*, by adding PCB to a purified apoprotein solution. In AnPixJg2, these two different purification procedures lead to significant differences in the RR and NMR spectra of the resulting holoprotein. This effect was attributed to partial protein misfolding due to the artificial buffer environment in the *in vitro* procedure and misfold-induced deprotonation of the chromophore.[201] To avoid the error of potential misfolding in Slr-GAF3, the preparation for this thesis followed the *in vivo* protocol (see supplementary section 9.2 for details) and all AnPixJg2 spectra that are shown for comparison were also collected from *in vivo* assembled samples. At room temperature (20 °C), Slr-GAF3 displays the typical red-green photochemistry with Q-band absorption maxima at 684 nm in the Pr and 530 nm in the Pg state (fig. 5.1.1 for Q band, see introductory fig. 1.4.1 for the full range UV/Vis absorption spectra).

**The Pr state** In the red-absorbing state, the PCB chromophore in Slr-GAF3 adopts the typical ZZZssa configuration, and the RR spectra in the marker region are nearly identical to AnPixJg2 Pr (fig. 5.1.3, full spectral range is given in the supplements fig. 9.2.1), except for a small downshift ( $-3\text{ cm}^{-1}$ ) and broadening of the B,C N-H i.p. bending peak, indicating that the coordination sphere of pyrrolic nitrogens is slightly changed. In the case of AnPixJg2, the N-H i.p. band at this position together with complementing results from magic-angle spinning nuclear magnetic resonance (MAS-NMR) experiments led to the conclusion that Pr-PCB is protonated at all four pyrrolic nitrogens and therefore bears a net charge of +1 within the conjugated  $\pi$ -electron system.[201] In contrast to prototypical phytochromes, the pyrrolic protons in AnPixJg2 are not coordinating a conserved water molecule (termed “pyrrole water”) but instead directly interact with the conserved Asp residue (also conserved in canonical phytochromes in the PASDIP motif, see fig. 1.5.1), that presumably also acts as a counterion for the positive charge.[142] Aside from this, the Pr in Slr-GAF3 and AnPixJg2 closely resembles the Pr state of PCB binding plant phytochromes like PhyA-PCB [230] or PhyB-PBC (see chapters 4.1 - 4.3), albeit with a larger torsional angle of ring D with respect to the chromophore plane ( $61^\circ$ ), that is reflected in the RR spectra by a downshift of the C,D HOOP mode by  $9\text{ cm}^{-1}$ . [230]



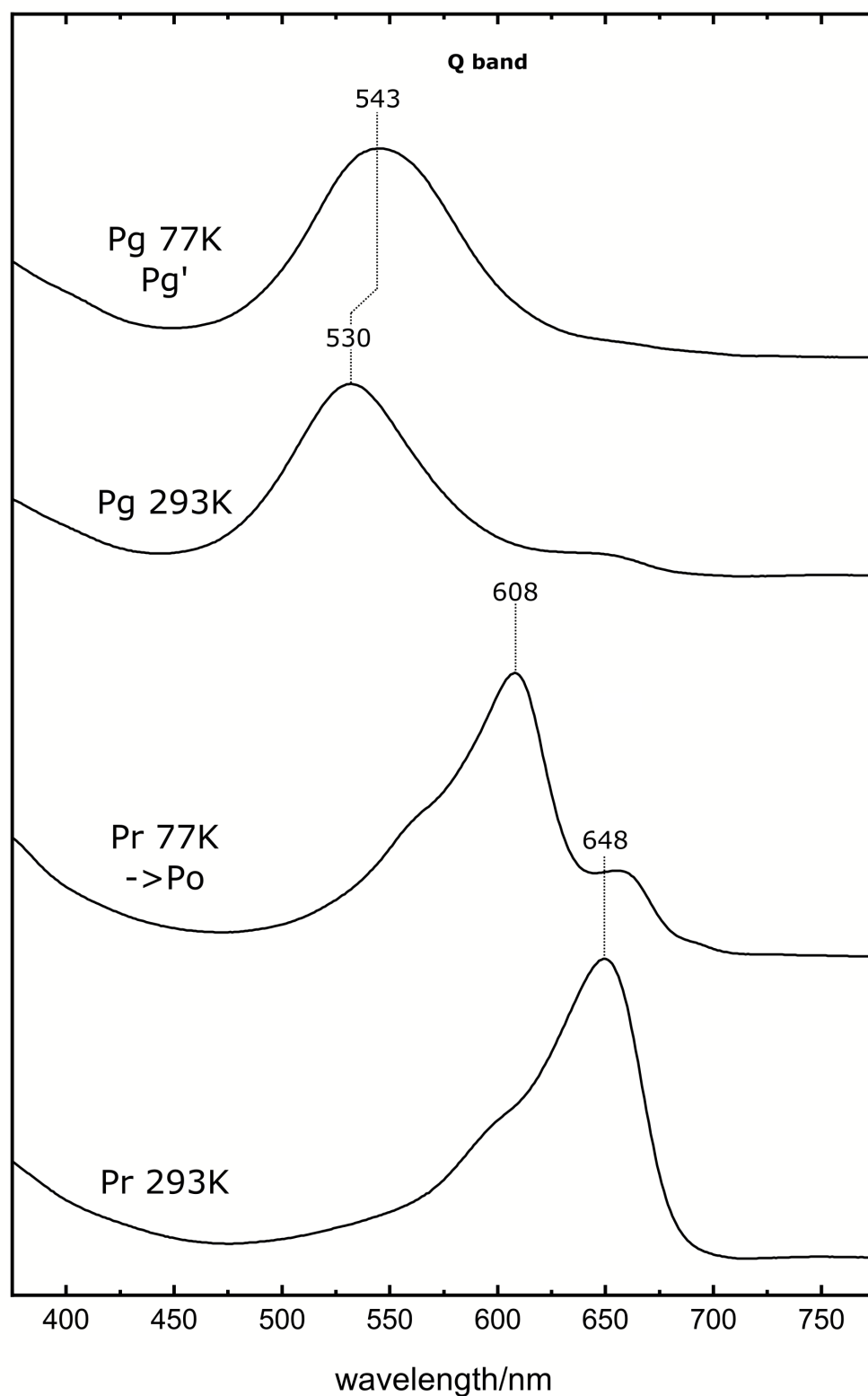


**Figure 5.1.1:** UV/Vis spectra of Slr-GAF3. Bottom: the Pr spectrum of Slr-GAF3 measured at room temperature (293 K) changes when the sample is frozen in the dark (77 K) to an orange absorbing state, denoted Po. Top: the Pg state changes during freezing in a similar manner, the resulting Pg' has a red-shifted absorption maximum.

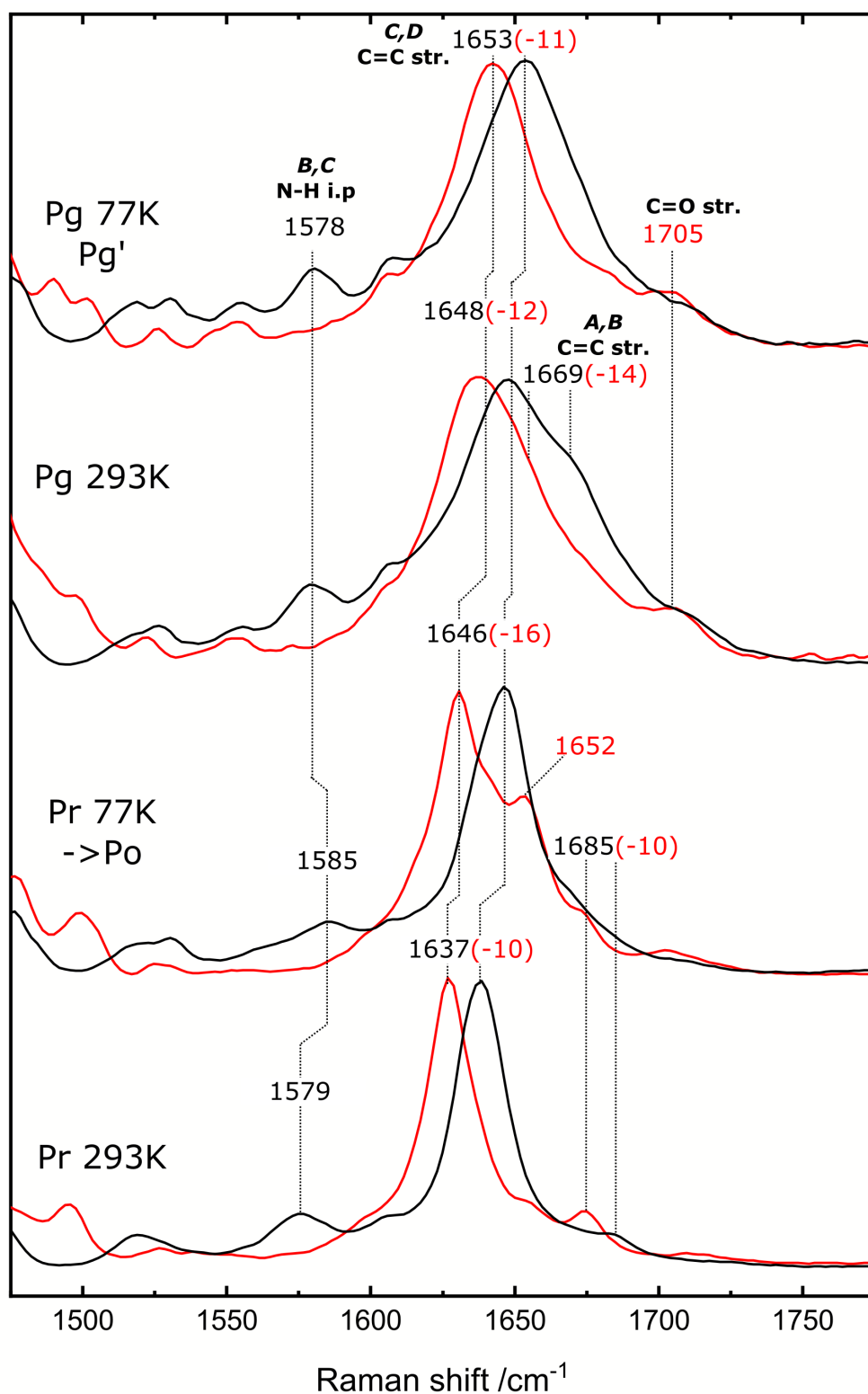


**Figure 5.1.2:** Temperature dependent RR spectra of Slr-GAF3 in the marker region. Spectra were recorded in  $\text{H}_2\text{O}$  and  $\text{D}_2\text{O}$  buffer. From bottom to top: the Pr spectrum of Slr-GAF3 at 293 K changes when it is frozen in the dark (77 K). The Pg state is also changed during freezing to the Pg' state at 77 K (top).

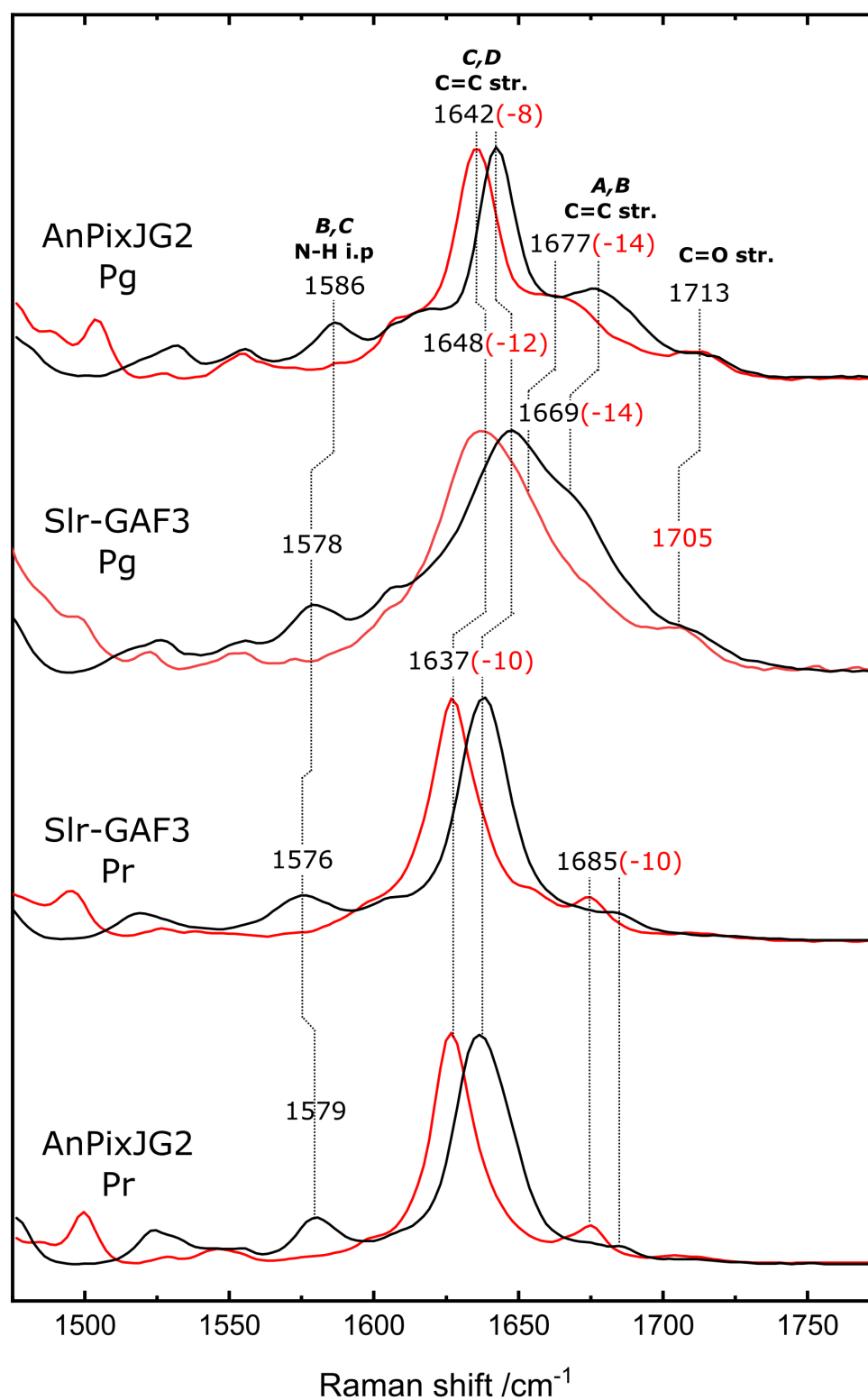


**Figure 5.1.3:** RR spectra of Slr-GAF3 and AnPixJg2 in the marker region. Bottom: the Pr spectra of AnPixJg2 and Slr-GAF3. Top: Pg spectra of AnPixJg2 and Slr-GAF3. Spectra were recorded in H<sub>2</sub>O and D<sub>2</sub>O buffer. Slr-GAF3 spectra were recorded at 293 K, AnPixJg2 spectra were recorded at 133 K.

**The Po state** Unlike AnPixJg2 or any other phytochrome, the typical spectral properties of the Pr state of Slr-GAF3 are not preserved when the sample is frozen. Instead, the Q-band absorption maximum shifts down by 40 nm to 608 nm and the Pr maximum at 648 nm is merely observed as a small shoulder (see fig. 5.1.1). The freezing-induced state is further denoted as Po (orange-absorbing), and reverses slowly (minutes) to Pr when thawed again. Some possibilities for the formation of the Po are discussed in the following:

*Photoreaction* Although the sample is kept in darkness under the best possible conditions during the freezing procedure, small amounts of light from the instruments or surroundings can never be completely excluded. Other samples treated under the same conditions do not photoconvert, therefore this contribution is probably negligible. Additionally, the photochemical quantum yield of Slr-GAF3 is naturally quite low (0.08), and instead, the protein is strongly fluorescent in the Pr state.[198, 155] Hence, a photochemical reaction mechanism *via* the excited state is probably not the pathway for the Pr-to-Po conversion.

*Acid-base reaction* The cryogenic UV/Vis measurements were performed in the phosphate buffered saline (PBS) elution buffer, which is prone to significant acidification when cooled down.[152, 71] Although the spectral properties of red/green CBCRs are pH-dependent in general [73], the highly homologous AnPixJg2 preserves the Pr under acidic conditions.[201] Furthermore, the RR spectra were recorded in Tris buffer (see chapter 3.3 for the exact buffer conditions), which does not exhibit a strong pH-drop like PBS during freezing. Still, significant changes are also seen upon freezing in the RR spectra (marker region in fig. 5.1.2, for full spectral range see supplements fig. 9.2.4). Albeit a pH-drop-induced acid-base reaction could be the reason for the changes in the UV/Vis spectra, it cannot explain the temperature effect in the RR spectra and is therefore excluded as a reason for the transition to the Po state.

*Thermal reaction* A third possible explanation for the state transition is that the Pr and Po states are in a temperature dependent thermal equilibrium



The temperature dependent equilibrium constant  $K$  is defined as:

$$K = \frac{[Po]}{[Pr]} \quad (5.2)$$

At 20 °C, the equilibrium must be strongly on the Pr side, whereas the equilibrium is shifted towards Po at lower temperatures. The temperature dependence of the thermal equilibrium constant  $K$  is derived from the van't Hoff-equation and is governed by the reaction enthalpy  $\Delta H^0$  and entropy  $\Delta S^0$  of the reaction 5.1

$$\ln K = -\frac{\Delta H^0}{R} \frac{1}{T} + \frac{\Delta S^0}{R}. \quad (5.3)$$

If a thermal equilibrium is the reason for the observed reaction, it is possible to estimate the order of magnitude of the thermodynamic quantities of the reaction.

Suppose that at room temperature ( $T = 293\text{ K}$ ), the equilibrium is strongly on the Pr side ( $K = 0.25$ ). If the equilibrium is shifted predominantly to the Po side ( $K = 4$ , judged from the Q-band intensity ratio at cryogenic temperatures, see fig. 5.1.1) at  $T = 77\text{ K}$ , the order of magnitude for  $\Delta H^0$  and  $\Delta S^0$  can be estimated from eqn. 5.3

$$\Delta H^0 \approx 2.4\text{ kJ/mol}, \Delta S^0 \approx 19\text{ J/molK}. \quad (5.4)$$

These estimated quantities are reasonably small for an intermolecular rearrangement reaction and therefore it can be concluded that the thermal pathway is, at this point, the best possible explanation for reaction 5.1. The small thermodynamic quantities ( $\Delta H^0$  and  $\Delta S^0$ ) of the equilibrium reaction indicate that the chromophore structure deviates on a small scale and thus an isomerization reaction can be excluded. The differences in the absorption spectra of Pr and Po are probably due to a changed electrostatic chromophore environment in the Po state. However, a thermal reaction of Pr is not observed in AnPixJg2 upon freezing, despite the high similarity of the two proteins.

The high similarity of the RR and UV/Vis spectra of AnPixJg2 and Slr-GAF3 implies that the geometry and therefore the thermodynamic properties, such as  $\Delta H^0$  and  $\Delta S^0$ , should not deviate largely in these two systems. According to this model, the different freezing behavior of the two systems must originate from a significantly lowered activation energy barrier for reaction 5.1 in Slr-GAF3 compared to AnPixJg2. A detailed investigation of the freezing behaviour and an accurate determination of  $\Delta H^0$  and  $\Delta S^0$  with an van,t Hoff plot is an interesting goal for the future. Then, temperature-dependent kinetic UV/Vis experiments of the light-induced back-reaction from Po to Pr can be used to determine the activation energy with an Arrhenius plot. Furthermore, a specific interaction of PCB in the Pg state of Slr-GAF3 with molecular imidazole was observed in the RR spectra. A detailed discussion is given in the supplements section 9.2.

**The Pg state** In line with the findings for AnPixJg2, the RR spectra of Slr-GAF3 show a characteristic N-H i.p. bending peak in both the Pg ( $1578\text{ cm}^{-1}$ ) and the Pr state, indicating that PCB carries protons on all four pyrrole rings in both parent states at the given conditions (see fig. 5.1.3).[230] This assignment is further confirmed by the results from  $\text{D}_2\text{O}$  buffer exchange and subsequent disappearance of this band in both parent states. Due to vibrational uncoupling from the vanished N-H i.p. mode, the C=C stretching bands in the marker region display an isotopic downshift (from  $1637\text{ cm}^{-1}$  to  $1627\text{ cm}^{-1}$  in Pr, and from  $1648\text{ cm}^{-1}$  to  $1636\text{ cm}^{-1}$  in Pg). The broad, unstructured feature at  $1677\text{ cm}^{-1}$  was assigned to a normal mode that mainly includes C=C stretching character from the A,B methine bridge in AnPixJg2, and the bandshape was traced back to a double-conformation in the Pg state.[230] In Slr-GAF3, this band is downshifted to  $1669\text{ cm}^{-1}$ , thus only detected as a shoulder of the broad peak at  $1648\text{ cm}^{-1}$ . This band is broadened compared to AnPixJg2, indicating that Pg is also heterogeneous in Slr-GAF3, but the heterogeneity is not only localized at the A,B methine bridge but instead affects also the conformation of ring D.

The first event of the photochemical conversion from Pr to the green state is a Z/E isomerization of the ring D methine bridge, similar to the photoreaction of canonical phytochromes. The ZZE<sub>ssa</sub> configuration in the Pg state was predicted by different spectroscopic methods[230, 73, 198] and on the basis of acidic urea denaturing experiments[140] for different red/green CBCRs. While in canonical phytochromes ZZE<sub>ssa</sub> is characteristic for the far-red absorbing (Pfr) state[183], the hypsochromic shift of the absorption maximum despite the similar chromophore photochemistry can only be rationalized by distinct interactions of PCB with the protein surroundings that differ from canonical phytochromes.

To understand the molecular basis of color tuning in CBCRs generally, and in particular the nature of the Pg in AnPixJg2 and Slr-GAF3, the well-developed theory of color tuning in retinal proteins can be adapted for biliproteins.[146] Three factors contribute to the color of retinal binding proteins:

- distortion of the chromophore enforced by the protein binding pocket
- interaction of the chromophore with the counterion that balances its positive charge
- interaction of the chromophore with polar amino acids and water molecules constituting the protein binding pocket

All three factors apply to CBCRs, with one additional factor that was not found in retinal binding proteins: For the blue/green CBCR TePixJ (from *Thermosynechococcus elongatus*), the strong hypsochromic shift was explained by a second thioether formation to the chromophore and a resulting disruption of the conjugation.[85, 223, 25] However, the formation of a second thioether was not reported for red/green CBCRs. For AnPixJg2, the reduction of the A,B methine bridge (affording phycoviolobilin (PVB)) by any mechanism was excluded on the basis of the fundamentally different Pg state RR spectra of TePixJ and AnPixJ.[223, 230]. Thus, this mechanism can be safely ruled out also for Slr-GAF3.

Four additional models that aim to explain the electronic properties of the Pg state in red/green CBCRs in accordance with the retinal theory were proposed and are discussed in the following paragraphs.[169, 201]

- deprotonation of the chromophore
- hydration of the chromophore binding pocket
- trapped-twist of ring D
- geometrical distortion of ring A

*Deprotonation* In retinal binding proteins, deprotonation of the chromophore usually results in a blue-shift in the absorption maximum. This behavior can be explained *via* a strong stabilization of the deprotonated excited state compared to a weaker stabilization of the electronic ground state, and thus a reduction of the energy difference between the highest occupied and lowest unoccupied molecular orbitals (HOMO and LUMO, respectively).[118, 146] This mechanism can be excluded for Slr-GAF3 for two reasons. Primary, RR spectroscopy shows that PCB is protonated also in the green state, and the positive charge is probably stabilized by an Asp residue acting

as a counterion (*vide supra*). Additionally, *in vitro* assembled AnPixJg2 preserves its absorption characteristics despite a pH-induced protonation state change of PCB in the green state.[201] The deprotonation of PCB is also possible in Slr-GAF3 when it is subjected to high concentrations of the base imidazole (see the results of the imidazole titration experiments in supplementary section 9.2), but unlikely the reason for the hypsochromic shift of the absorption maximum in Pg.

**Hydration** In AnPixJg2, the hypsochromic absorption shift coincides with water entry into the chromophore binding pocket and resulting hydration of the PCB environment. The binding pocket is gated by a conserved tryptophane (Trp) residue, which is also conserved in GAF3 (W496). In a classical molecular mechanics Pg state model, the hydrophobic sidechain of the Trp lid opens up and the hydrated PCB environment creates a changed electrostatic situation.[230] However, a change to a more polar chromophore environment would stabilize a charged (protonated) PCB more strongly than an uncharged, deprotonated PCB. Because the hypsochromic shift in AnPixJg2 is independent of the protonation state, the hydration fails to explain the hypsochromic shift.[201]

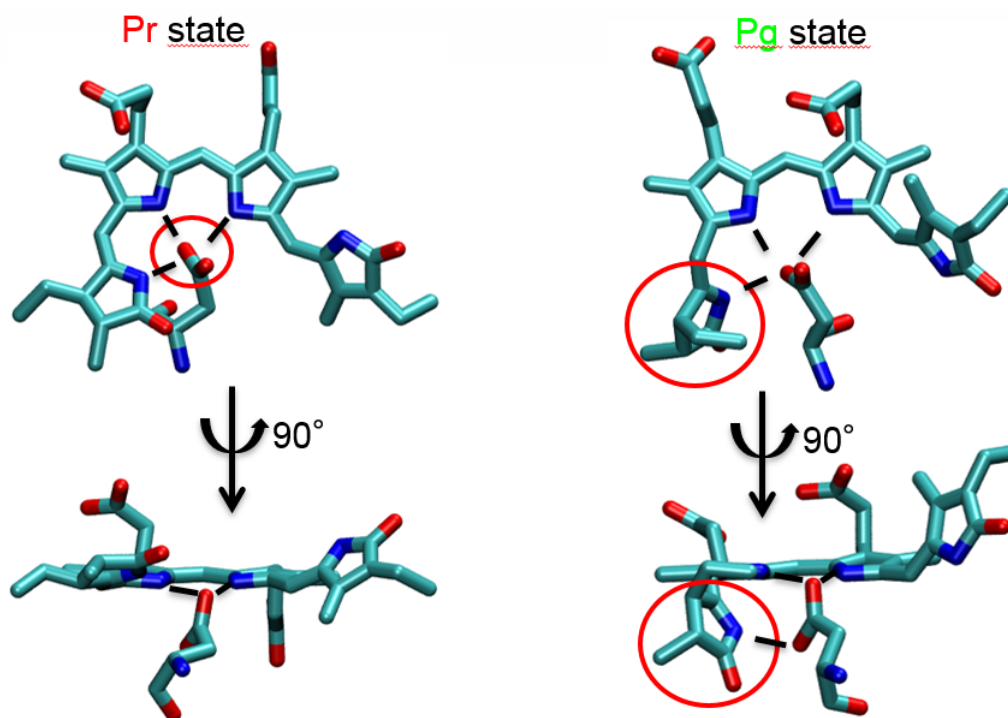


**Figure 5.1.4:** Crystal structure of Slr-GAF3 PCB chromophore in the Pr (*in vivo* assembled chromophore, PDB entry: 5DFX) and the photoproduct (presumably resembling the Pg state, PDB entry: 5M82) states. A conserved Asp residue coordinating the pyrrolic nitrogens and the tilted A-ring in the Pg structure are highlighted with red circles. Hydrogen bonding distances are indicated by black lines.

**Trapped-twist** In the trapped-twist model, changes in protein-chromophore interactions after initial photoisomerization trap a twisted PCB species, in which the bilin D ring cannot relax into full conjugation. [169] Here, the trapping of ring D is mediated by hydrophobic  $\pi$ -stacking interactions of the pyrrole ring with conserved phenylalanine (Phe) residues, which are also found in Slr-GAF3.[173] Unfortunately, the trapped-

twist model contradicts the RR results for AnpJg2 and Slr-GAF3, because a different frequency for the C,D HOOP band would be expected.[201]

*Distortion of ring A* Albeit a full reduction of PCB to PVB was excluded earlier in this section (*vide infra*), a strong distortion of the chromophore at the A,B methine bridge can also lead to a reduced effective length of the conjugated  $\pi$ -electron system and therefore to similar hypsochromic absorption properties. Accordingly, spectroscopic experiments with locked 5Za chromophores show that this artificial isomerization of ring A affords a blue-shift in the Q-band absorption maximum in Bphs.[83] Furthermore, a crystal structure of a photoproduct state of Slr-GAF3 was deposited in the protein data bank (PDB entry: 5M82), and exhibits a strongly tilted ring A configuration, stabilized by the conserved Asp residue (see fig. 5.1.4). Unfortunately, the experimental conditions for this crystal structure are not published, thus a more detailed discussion regarding the geometry is aggravated at this point.

In view of the strong conflicts of the other models, the changed geometry at the ring A might be the reason for green color, probably combined with the trapped twist of ring D. If a distortion of ring A is taken into account, the PCB normal mode composition is affected and the conflicts of the trapped-twist model with the RR results vanish. If both pyrrole rings A and D are in a trapped-twist configuration, this could account for the systematic upshifts of all C=C stretching frequencies in the marker region, due to an enhanced vibrational uncoupling of these normal modes. Here the strong tilting of the A and D rings out of plane reduces the effective conjugation length and the vibrations of the corresponding C=C double bonds are less coupled to the rings B and C, therefore the frequencies of all modes are higher.

**The Pg, state** Like the Pr, the Pg Q-band absorption maximum is also changed in frozen samples (from 530 nm to 543 nm, see fig. 5.1.1), albeit the effect is less pronounced. The product is therefore termed Pg,. In line with the previous argumentation regarding the Po state transition, the explanation for this reaction is most likely another thermal equilibrium with a meta-stable state.



---

## 6 Results: Bacterial Phytochromes

The following section comprises two studies of the bacterial phytochromes Agp1 and Agp2 from *Agrobacterium fabrum* and IsPadC, a bacterial phytochrome-activated di-guanylyl cyclase from *Idiomarina*. Both studies aim to correlate the structural changes of the chromophore during the photocycle reactions with the respective functional activation of the proteins.

Chapter 6.1 encloses a publication about the design of a time-resolved pre-resonance FT-Raman set-up for the investigation of the Meta-state decay pathways in Agp1 and Agp2. In these two proteins, the formation of the active state (Pfr in Agp1 and Pr in Agp2) from the Meta-precursor is the crucial last step in the reaction cascades and occurs on a ms time scale. The structural changes of the chromophore can be monitored with the novel set-up and provide insight into the mechanism of the functional activation.

The PSM domain of IsPadC is connected to a GGDEF di-guanylyl-cyclase as a catalytic output module instead of the typical histidine kinase or related protein domain (HKRD). Thus, IsPadC produces the bacterial second-messenger c-di-GMP when triggered by red light, whereas far-red light inhibits cyclase activity. The full-length protein and a PAS-GAF truncation construct were investigated with RR and IR spectroscopy to yield insight into the structural parameters that govern the activation of the cyclase module (chapter 6.2).

### 6.1 Time-Resolved FT-Raman Spectroscopy of Bacteriophytochromes Agp1 and Agp2

This research was originally published in ChemPhysChem:

D. Buhrke, U. Kuhlmann, N. Michael, and P. Hildebrandt. *The Photoconversion of Phytochrome Includes an Unproductive Shunt Reaction Pathway*. In: *ChemPhysChem* **Volume 19**. Issue 5 (2018). DOI: 10.1002/cphc.201701311

- **David Buhrke** performed RR experiments.
- Norbert Michael prepared the protein samples.
- **David Buhrke** and Uwe Kuhlmann designed and assembled the set-up for time resolved RR experiments.
- Peter Hildebrandt and **David Buhrke** designed the project, analysed the data and wrote the manuscript.
- All the authors discussed the results and commented on the manuscript.

© Reprinted with permission of John Wiley and Sons publishing (license number 4427080904253).

# The Photoconversion of Phytochrome Includes an Unproductive Shunt Reaction Pathway

David Buhrke, Uwe Kuhlmann, Norbert Michael, and Peter Hildebrandt<sup>\*[a]</sup>

Phytochromes are modular bimodal photoswitches that control gene expression for morphogenetic processes in plants. These functions are triggered by photoinduced conversions between the inactive and active states of the photosensory module, denoted as Pr and Pfr, respectively. In the present time-resolved resonance Raman spectroscopic study of bacterial representatives of this photoreceptor family, we demonstrate that these phototransformations do not represent linear processes but include a branching reaction back to the initial state, prior to (de)activation of the output module. Thus, only a fraction of the photoreceptors undergoing the phototransformations can initiate the downstream signaling process, consistent with phytochrome's function as a sensor for more durable changes of light conditions.

Phytochromes are ubiquitous photoreceptors that use light as a trigger to initiate biological processes.<sup>[1–3]</sup> Although originally considered as typical plant photoreceptors, phytochromes were meanwhile also discovered in (cyano)bacteria, fungi, and algae. Common to all phytochromes is a sensor domain (PAS-GAF-PHY) harbouring a tetrapyrrole chromophore that undergoes photo-induced interconversions between a red-absorbing (Pr) and a far-red absorbing (Pfr) state (Figure 1). These photoconversions occur on comparable time scales and include similar intermediates in plant and bacterial phytochromes despite different chromophores and binding sites. The underlying molecular events start with the photoisomerisation of the C-D methine bridge double bond to afford the Lumi intermediates with the chromophore in a highly tensed geometry, followed by thermal relaxation of the chromophore and the immediate protein environment, leading to the formation of the Meta intermediates on the microsecond time scale. The subsequent decay to the final product of the Pr→Pfr (Pfr→Pr) photoconversion involves proton translocation steps in the chromophore pocket and a  $\alpha$ -helix (Pfr) and  $\beta$ -sheet (Pr) transition in the tongue region of the PHY domain, thought to be functional for (de)activating the downstream signaling chain.<sup>[4–7]</sup>

The current state of knowledge on the mechanism and dynamics of the photoconversion results from numerous spectroscopic studies, which can be grouped into two categories. Time-resolved investigations at ambient temperature were pre-

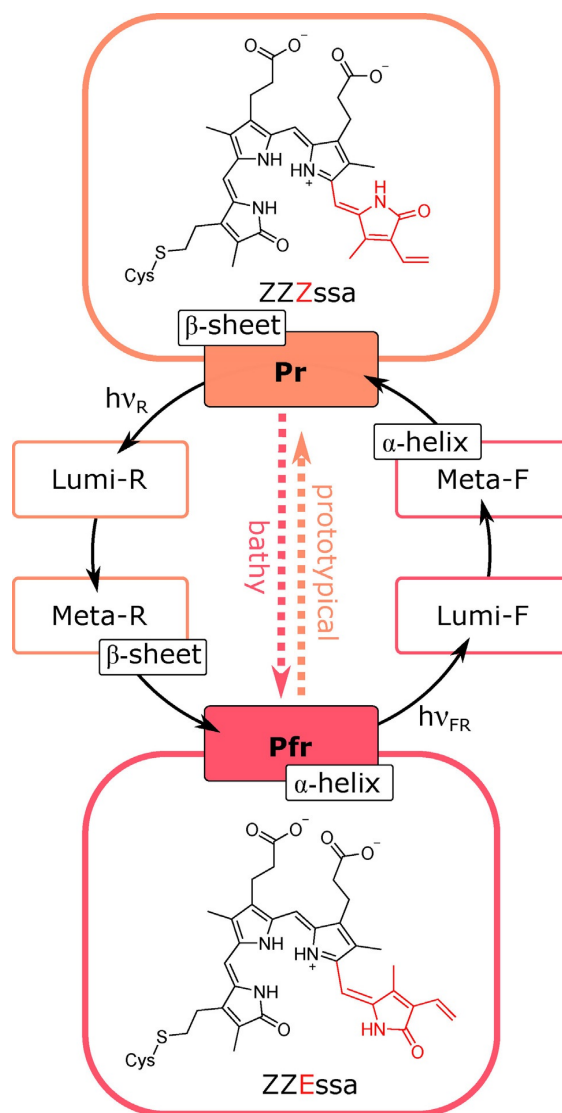


**Figure 1.** Schematic representation of the photoinduced reaction sequences of phytochromes.<sup>[1–6]</sup> The first step refers to the double bond photoisomerization of the ZZZssa (top inset) and ZZEssa configuration (bottom inset) in Pr and Pfr, respectively (the C-D methine bridge and ring D are highlighted in red). The final step includes a secondary structure change between  $\beta$ -sheet (Pr, Meta-R) and  $\alpha$ -helix (Pfr, Meta-F). Thermal Pfr→Pr and Pr→Pfr reactions of prototypical and bathy phytochromes are indicated by bold arrows.

[a] D. Buhrke, Dr. U. Kuhlmann, N. Michael, Prof. Dr. P. Hildebrandt  
Institut für Chemie, Sekr. PC14  
Technische Universität Berlin  
Straße des 17. Juni 135, 10623 Berlin (Germany)  
E-mail: hildebrandt@chem.tu-berlin.de

Supporting Information and the ORCID identification number(s) for the author(s) of this article can be found under <https://doi.org/10.1002/cphc.201701311>.

dominantly based on transient UV/Vis absorption spectroscopy which, however, provided only limited structural information

about the species involved.<sup>[8,9]</sup> Significantly more insight into the molecular structure changes was derived from low temperature resonance Raman (RR) spectroscopy which in turn did allow for analyzing the dynamics of the processes.<sup>[7,10–12]</sup> As a consequence, the results from time-resolved and low-temperature studies are partly difficult to correlate.

The present work aimed at overcoming these drawbacks by employing, for the first time, time-resolved continuous-wave (cw) pump-probe RR spectroscopy to study the late events of the photoinduced reaction cascades of phytochromes. The setup is based on a flow system (time resolution: 10–700 ms) but, in contrast to previous approaches,<sup>[13–15]</sup> a pre-resonant probe wavelength (1064 nm) was used that did not induce photochemical processes (Supplementary Note 1). The studies focused on the photosensor modules of two biliverdin IX $\alpha$  (BV)-binding bacteriophytochromes from *Agrobacterium fabrum*, Agp1 and Agp2.<sup>[16,17]</sup> These phytochromes are representatives of the classes of prototypical (Agp1) and bathy phytochromes (Agp2) in which Pr and Pfr are the stable dark states, respectively. In both phytochromes, a histidine kinase serves as the output module that is (de)activated via the secondary structure change of the tongue in the last step of the photoconversion (Figure 1). It is shown that in both phytochromes, the Meta intermediates represent a branching point in the respective reaction sequence: these states may either decay to the final photoconversion products or revert directly to the initial dark state via a thermal route that circumvents the functional structural transition.

The decay reactions of the Meta intermediates are the target processes of the present study. Previous flash photolysis experiments have shown that they occur on the long millisecond time scale,<sup>[12,18]</sup> which is within the time resolution of the present set-up (vide supra). In Agp1, similar to other prototypical phytochromes, the Pr  $\rightarrow$  Pfr photoconversion runs via the intermediate Meta-Rc that is formed with a time constant of ca. 3 ms whereas its decay to the final product was reported to take place with a time constant of ca. 300 ms.<sup>[12]</sup> The subsequently formed Pfr thermally reverts to the initial Pr state within minutes. Therefore, the sample was irradiated with far-red light after the probe event to accelerate recovery of the Pr state (Supplementary Note 1; Figure S1).

Earlier cryo-trap RR studies revealed that Meta-Rc includes a deprotonated chromophore in which a proton of the ring B or C nitrogen is removed.<sup>[11,12]</sup> As a consequence the resultant neutral BV exhibits a significantly reduced oscillator strength of the first electronic transition, corresponding to a weak resonance enhancement of the Raman spectrum at 1064 nm excitation (Supplementary Note 3). In fact, the pump-probe spectra that were measured with the shortest possible time-resolution (10–20 ms) predominantly display the depletion of the initial Pr state as indicated by the negative signal at 1623 cm<sup>-1</sup>, whereas the concomitantly formed Meta-Rc cannot be detected (Figure 2, top). With increasing delay time we did not only observe the expected formation of the Pfr state as shown by the intensity increase at 1600 cm<sup>-1</sup>, but also the unprecedented recovery of the initial Pr state on the millisecond time scale, reflected by the decrease of the negative difference signal at

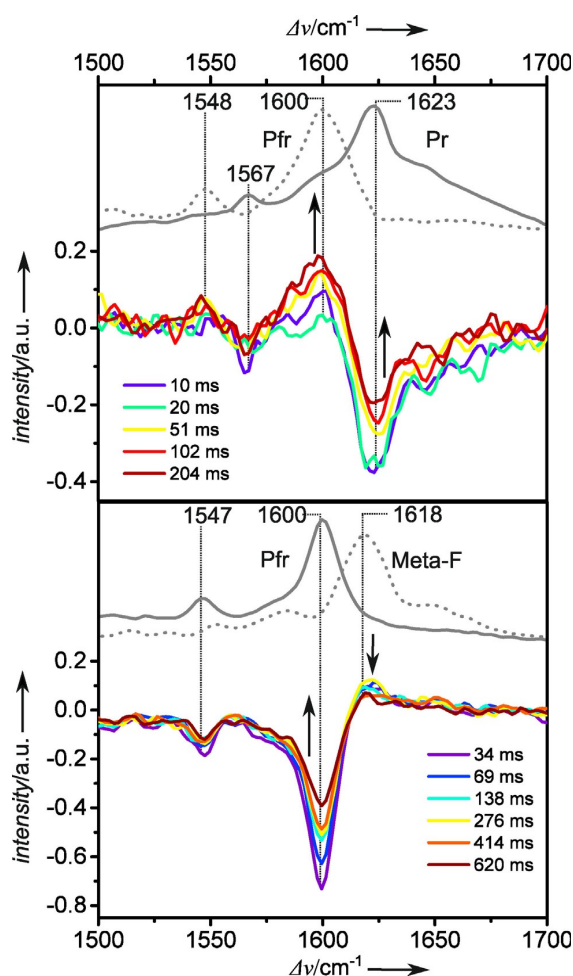


**Figure 2.** Time-resolved RR spectroscopic measurements of the photoinduced conversion (top) of Pr of Agp1 and (bottom) of Pfr of Agp2. RR spectra were measured at ambient temperature with 1064 nm excitation at various pump-probe delay times and presented as difference spectra with respect to the probe-only spectrum. Absolute spectra are shown in the Supplementary Information (Figures S3, S4). The sum of all probe-only spectra is shown as grey solid line (top: Pr, bottom: Pfr). The dotted grey lines represent the spectra of (top) Pfr of Agp1, obtained in separate experiments, and (bottom) Meta-F of Agp2, measured at  $-190^{\circ}\text{C}$ , after cryogenic trapping at  $-30^{\circ}\text{C}$ .<sup>[7]</sup>

1623 cm<sup>-1</sup>. This reaction, which is much faster than the Pfr  $\rightarrow$  Pr dark reversion,<sup>[16,19]</sup> cannot be attributed to a secondary photo-reaction of Meta-Rc back to Pr (Supplementary Note 1). Thus, we conclude that there are two thermal decay channels of Meta-Rc leading to Pfr and Pr. For an approximate quantitative analysis of the spectral changes, we have plotted the difference signals at 1600 cm<sup>-1</sup> (Pfr) and 1623 cm<sup>-1</sup> (Pr) as a function of the delay time (Figure 3A and B). Exponential fits to this data afford a time constants of 56 ms for the formation of Pr. A similar value, albeit associated with a larger error, is obtained for the Pfr formation. Since the RR bands of Meta-Rc, albeit weak (vide supra), overlap with both the 1600 and 1623 cm<sup>-1</sup> bands, the true relaxation times are presumably slightly longer

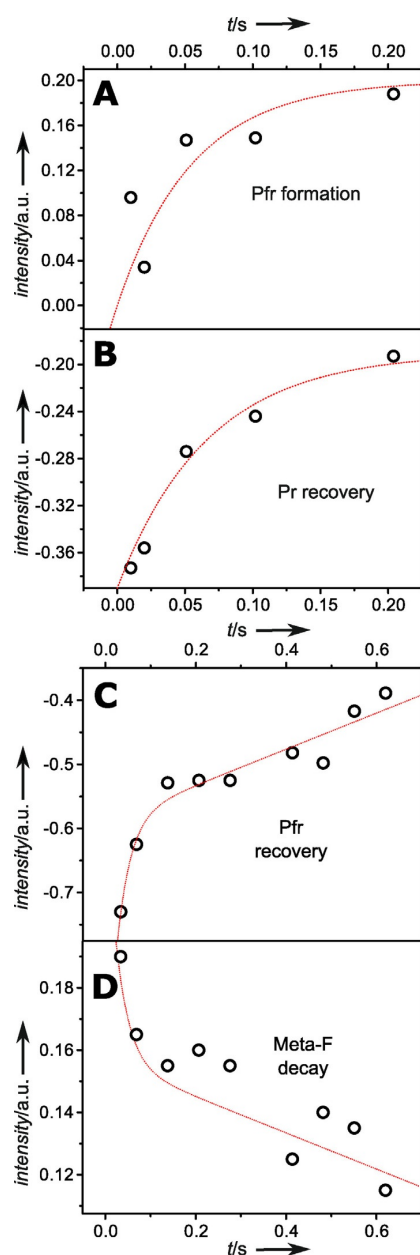


**Figure 3.** A, B) Analysis of the intensities of the difference signals of (A) Pfr and (B) Pr, determined from the time-resolved RR spectra (Figure 2, top) as a function of the delay time for the Pr  $\rightarrow$  Pfr photoconversion of Agp1. The red lines in A and B represent fits of mono-exponential functions to the experimental data affording time constants of 56 and 67 ms for Pfr and Pr formation, respectively. C, D) Analysis of the intensities of the difference signals of (C) Pfr and (D) Meta-F, determined from the time-resolved RR spectra (Figure 2 bottom) as a function of the delay time for the Pfr  $\rightarrow$  Pr photoconversion of Agp2. The red line in C represents the fit of a bi-exponential function to the experimental data affording a time constant of 30 ms for the fast phase of Pfr recovery. The red line in D shows the mirror image of the same fit function.

and shorter for Pfr and Pr formation, respectively. Despite these uncertainties, we estimate a branching ratio of ca. 50%.

The rate of Pfr formation determined in this work is faster by a factor of ca. 6 compared to the data derived from previous flash photolysis and rapid scan IR experiments.<sup>[12,19]</sup> This discrepancy possibly roots in the different types of spectral signals that are monitored by the two techniques, that is, electronic transitions of the chromophore and IR-active vibrational modes of the chromophore and the protein. Thus it may be that the main structural properties of the Pfr chromophore as reflected by the characteristic RR bands at  $1600\text{ cm}^{-1}$  (C=C stretching of the *C-D* methine bridge) and  $1548\text{ cm}^{-1}$  (N-H in-plane bending of rings *B* and *C*),<sup>[20]</sup> are established within ca. 60 ms. However, further structural adjustments of the chromophore and its immediate environment due to hydrogen bond changes of the ring *D* C=O and ring *C* propionate as probed by IR spectroscopy may occur with some delay,<sup>[21]</sup> and eventually lead to the characteristic UV-vis absorption monitored by flash photolysis.<sup>[12]</sup> We also like to remind that these kinetic studies tacitly assumed a single decay route of Meta-Rc although first indications for a more complex reaction pattern of Meta-Rc have been noted.<sup>[12]</sup>

As for Agp1, flash photolysis experiments on the bathy phytochrome Agp2 showed that the formation of the Meta-F intermediate is too fast (7.5 ms) to be detected with the present setup.<sup>[18]</sup> Thus, the early time-resolved RR spectra, shown as difference spectra in Figure 2 (bottom), reveal a large negative signal at  $1600\text{ cm}^{-1}$  corresponding to the prominent Pfr peak. Also in this case, the resonance enhancement for the intermediate is lower than for Pfr, but still the strongest RR band of Meta-F can be detected as a weak positive shoulder at ca.  $1618\text{ cm}^{-1}$ .<sup>[7]</sup>

Again, we note the recovery of the initial Pfr state with increasing delay time, accompanied by the decay of the Meta-F intermediate. Already the visual inspection of the difference spectra indicates an initial rapid decrease of the negative Pfr signal (ca. 30% within ca. 150 ms), followed by a distinctly slower recovery phase that is not completed within the time range of the present experiments. Accordingly, only for the initial fast phase a time constant (ca. 30 ms) can be obtained from a bi-exponential fit (Figure 3 C and D). Interestingly, a satisfactory description of the distinctly weaker Meta-F signals can be achieved by the same fit function albeit with opposite sign. The much slower intensity changes at delay times greater than ca. 130 ms seem to follow a nearly linear behavior up to the longest delay time of the time-resolved experiments (600 ms), where only ca. 50% of the total photoconverted Pfr is recovered. This suggests that the slow recovery phase results from a more complex mechanism including reaction steps with time constants in the range of seconds. We therefore attribute this process to the reaction sequence Meta-F  $\rightarrow$  Pr  $\rightarrow$  Pfr, which is consistent with previous time-dependent UV-vis absorption spectroscopic experiments (Supplementary note 2).<sup>[7,18]</sup> Thus, we conclude that, like Meta-Rc of Agp1, Meta-F of Agp2 exhibits two decay channels leading either directly or via Pr to the initial Pfr state.

In this context, we would like to refer to a recent study on bacterial phytochrome from *Stigmatella aurantiaca*.<sup>[22]</sup> The authors found a thermal Lumi-R  $\rightarrow$  Pr back reaction. The distorted

C-D methine bridge geometry of the primary photoproduct (between a *Z* and *E* configuration) could account for the short time constant (ca. 100 ns) of the reaction. In the present case, however, the back reaction starts from a structurally relaxed chromophore (Meta states). It thus requires a higher energy barrier for isomerization corresponding to a much slower time constant of the reaction.

Phytochromes exert their biological functions by switching between the physiologically inactive and active states. In addition to the photoinduced conversions, there is a thermal pathway between the parent states. Except for a phytochrome from *Xanthomonas campestris* for which these transformations proceed in both directions to a detectable extent,<sup>[23]</sup> thermal Pr/Pfr conversions are essentially unidirectional such that the Pr and Pfr state are the stable ("dark") states in prototypical and bathy phytochromes, respectively (Figure 1). In this work, however, we provided evidence for an additional thermal recovery route of the dark state via the Meta intermediate which competes with the final step of the respective photoconversion (Figure 4). Branching of the reaction sequence at the stage of Meta-Rc/Meta-F is directly related to the physiological functions of phytochromes. The conversion of Meta-Rc (Meta-F) to Pfr (Pr) is associated with the  $\beta$ -sheet to  $\alpha$ -helix ( $\alpha$ -helix to  $\beta$ -sheet) transition of the tongue segment that in turn is postulated to (de)activate the histidine kinase output module in Agp1 (Agp2). The two decay pathways of the Meta intermediates, therefore, imply that only a fraction, that is, 50–70%, of the photoconverted phytochromes can induce the (de)activation of the output module. For Agp1, the quantum yield for the photochemical isomerization Pr $\rightarrow$ Lumi-R was determined to be 9.4%,<sup>[24]</sup> such that at best just 5% of the absorbed photons may lead to a functional response of the photoreceptor. Essentially the same estimate holds for Agp2 assuming that the photochemical quantum yield (Pfr $\rightarrow$ Lumi-F) is similar as for Agp1 (ca. 8%).<sup>[25]</sup> Such a low efficiency for utilizing absorbed photons is likely to be a common property of all prototypical phytochromes taking into account the far-reaching sim-

ilarities in structure and reaction dynamics of the photosensor module. Specifically, it may also hold for plant phytochromes although here the primary event for triggering downstream signaling is the activation of bound phytochrome interaction factors (PIF proteins).<sup>[26]</sup> However, also this activation is associated with the formation of Pfr and would not occur for that fraction of photoconverted proteins that runs through the unproductive shunt pathway back to Pr. On the first sight, this "waste" of photons might be surprising since other sensory photoreceptors like the visual pigment rhodopsin or the phototaxis receptor sensory rhodopsin II exhibit photochemical quantum yields of 0.5 or larger.<sup>[27,28]</sup> These photoreceptors are optimized for efficient light-signal conversion and transduction, which must ensure an immediate physiological response. Instead, the biological functions of plant phytochromes and, as far as they are known also of (cyano)bacterial phytochromes, refer to the (de)activation of gene expression.<sup>[29]</sup> These energy demanding processes should, therefore, follow more durable changes in the environmental light conditions rather than single-photon sensitivity of the signaling cascade.

## Acknowledgements

The work was supported by the Deutsche Forschungsgemeinschaft via the SFB1078 (B6) and the Cluster of Excellence UniCat (EXC314). We thank Thomas Friedrich for helpful comments.

## Conflict of interest

The authors declare no conflict of interest.

**Keywords:** photochemistry · photoswitches · phytochromes · Raman spectroscopy · time-resolved spectroscopy

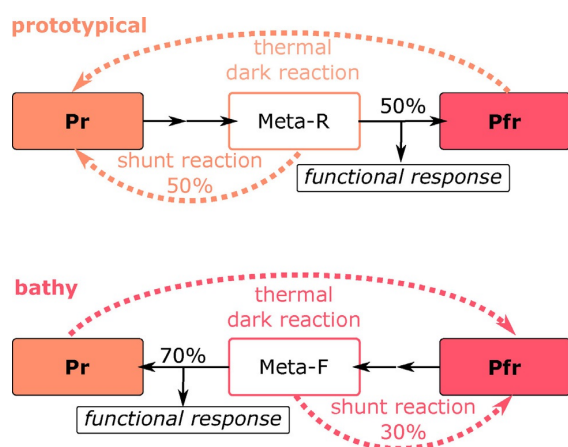


**Figure 4.** Branched reaction pathways of the photoinduced transformations in prototypical (Pr $\rightarrow$ Pfr; top) and bathy phytochromes (Pfr $\rightarrow$ Pr; bottom).

- [1] W. R. Briggs, J. L. Spudis, *Handbook of Photosensory Receptors*, Wiley Verlag, Weinheim, Germany, **2005**.
- [2] N. C. Rockwell, Y. S. Su, J. C. Lagarias, *Annu. Rev. Plant Biol.* **2006**, *57*, 837–858.
- [3] J. Hughes, *Annu. Rev. Plant Biol.* **2013**, *64*, 377–402.
- [4] H. Takala, A. Björling, O. Berntsson, H. Lehtivuori, S. Niebling, M. Hoernke, I. Kosheleva, R. Henning, A. Menzel, J. A. Ihalainen, S. Westenhoff, *Nature* **2014**, *509*, 245–248.
- [5] A. Björling, O. Berntsson, H. Lehtivuori, H. Takala, A. J. Hughes, M. Panman, M. Hoernke, S. Niebling, L. Henry, R. Henning, I. Kosheleva, V. Chukharev, N. V. Tkachenko, A. Menzel, G. Newby, D. Khakhulin, M. Wulff, J. A. Ihalainen, S. Westenhoff, *Sci. Adv.* **2016**, e1600920.
- [6] E. S. Burgie, J. Zhang, R. D. Vierstra, *Structure* **2016**, *24*, 448–457.
- [7] F. Velazquez Escobar, P. Piwowarski, J. Salewski, N. Michael, M. Fernandez Lopez, A. Rupp, Q. B. Qureshi, P. Scheerer, F. Bartl, N. Frankenberger-Dinkel, F. Siebert, M. A. Mroginski, P. Hildebrandt, *Nat. Chem.* **2015**, *7*, 423–430.
- [8] V. A. Sineshchekov, *Biochim. Biophys. Acta* **1995**, *1228*, 125–164.
- [9] I. Chizhov, B. Zorn, D. J. Manstein, W. Gärtner, *Biophys. J.* **2013**, *105*, 2210–2220.
- [10] M. A. Mroginski, D. von Stetten, S. Kaminski, F. Velazquez Escobar, N. Michael, G. Daminelli-Widany, P. Hildebrandt, *J. Mol. Struct.* **2011**, *993*, 15–25.
- [11] D. von Stetten, S. Seibeck, N. Michael, P. Scheerer, M. A. Mroginski, D. H. Murgida, N. Krauss, M. P. Heyn, P. Hildebrandt, B. Borucki, T. Lamparter, *J. Biol. Chem.* **2007**, *282*, 2116–2123.

- [12] B. Borucki, D. von Stetten, S. Seibeck, T. Lamparter, N. Michael, M. A. Mroginski, H. Otto, D. H. Murgida, M. P. Heyn, P. Hildebrandt, *J. Biol. Chem.* **2005**, *280*, 34358–34364.
- [13] T. Althaus, W. Eisfeld, R. Lohrmann, M. Stockburger, *Isr. J. Chem.* **1995**, *35*, 227–251.
- [14] M. Braiman, R. A. Mathies, *Biochemistry* **1980**, *19*, 5421–5428.
- [15] H. Naumann, M. Engelhard, D. H. Murgida, P. Hildebrandt, *J. Raman Spectrosc.* **2006**, *37*, 436–441.
- [16] T. Lamparter, N. Michael, F. Mittmann, B. Esteban, *Proc. Natl. Acad. Sci. USA* **2002**, *99*, 11628–11633.
- [17] B. Karniol, R. D. Vierstra, *Proc. Natl. Acad. Sci. USA* **2003**, *100*, 2807–2812.
- [18] B. Zienicke, I. Molina, R. Glenz, P. Singer, D. Ehmer, F. Velazquez Escobar, P. Hildebrandt, R. Diller, T. Lamparter, *J. Biol. Chem.* **2013**, *288*, 31738–31751.
- [19] E. S. Burgie, A. N. Bussell, J. M. Walker, K. Dubiel, R. D. Vierstra, *Proc. Natl. Acad. Sci. USA* **2014**, *111*, 10179–10184.
- [20] J. Salewski, F. Velazquez, S. Kaminski, D. von Stetten, A. Keidel, Y. Rippers, N. Michael, P. Scheerer, P. Piwowarski, F. Bartl, N. Frankenberg-Dinkel, S. Ringsdorf, W. Gärtner, T. Lamparter, M. A. Mroginski, P. Hildebrandt, *J. Biol. Chem.* **2013**, *288*, 16800–16814.
- [21] P. Piwowarski, E. Ritter, K. P. Hofmann, P. Hildebrandt, D. von Stetten, P. Scheerer, N. Michael, T. Lamparter, F. Bartl, *ChemPhysChem* **2010**, *11*, 1207–1214.
- [22] T. Mathes, J. Ravensbergen, M. Klotz, T. Gleichmann, K. D. Gallagher, N. C. Woitowich, R. St. Peter, S. E. Kovaleva, E. A. Stojković, J. T. M. Kennis, *J. Phys. Chem. Lett.* **2015**, *6*, 239–243.
- [23] L. H. Otero, S. Klinke, J. Rinaldi, F. Velázquez Escobar, M. A. Mroginski, M. Fernández López, F. Malamud, A. A. Vojnov, P. Hildebrandt, F. A. Goldbaum, H. R. Bonomi, *J. Mol. Biol.* **2015**, *428*, 3702–3720.
- [24] C. Schumann, R. Groß, N. Michael, T. Lamparter, R. Diller, *ChemPhysChem* **2007**, *8*, 1657–1663.
- [25] C. Schumann, R. Groß, M. M. N. Wolf, R. Diller, N. Michael, T. Lamparter, *Biophys. J.* **2008**, *94*, 3189–3197.
- [26] A. Castillon, H. Shen, E. Huq, *Trends Plant Sci.* **2007**, *12*, 514–521.
- [27] H. Kandori, Y. Katsuta, M. Ito, H. Sasabe, *J. Am. Chem. Soc.* **1995**, *117*, 2669–2670.
- [28] A. Losi, A. A. Wegener, M. Engelhard, W. Gärtner, S. Braslavsky, *Biophys. J.* **2000**, *78*, 2581–2589.
- [29] T. Lamparter, *BMC Biochem.* **2006**, *7*, 141.

Manuscript received: December 6, 2017  
Accepted manuscript online: January 12, 2018  
Version of record online: January 26, 2018



## 6.2 The Phytochrome-Activated di-Guanylyl Cyclase from *Idiomarina*

The full length (FL) and the PAS-GAF (PG) constructs of *Idiomarina* sp.A28L phytochrome-activated di-guanylyl cyclase (IsPadC) were investigated with RR and difference IR spectroscopy. The FL construct of this unusual phytochrome includes the PAS, GAF, PHY, coiled coil (CC) domains as a PSM, linked to a diguanylyl-cyclase (GGDEF) domain that acts as an output module (see fig. 1.3.1). For both IsPadC constructs, UV/Vis spectroscopy yielded two clearly distinguishable states, and pure Pr and Pfr (Meta-like in the case of PG) spectra were obtained by spectral subtraction. The spectra are compared to the corresponding constructs of the canonical Bph histidine kinase Agp1, Agp1-FL and Agp1-PG. The unsubtracted and pure (subtracted) UV/Vis spectra of all four protein constructs in the respective states are given in the supplements (see figs. 9.4.1 and 9.4.2).

**Pr state** In the Pr state, the IsPadC FL and PG constructs exhibit nearly identical RR spectra (marker region in fig. 6.2.1, the full spectral range and HOOP region are given in supplementary figs. 9.4.3 and 9.4.5). In H<sub>2</sub>O buffer, the bandshape in the C=C stretching region is very similar to Agp1 FL (except for small downshifts of the A,B and C,D C=C stretching modes by ca. 5 cm<sup>-1</sup>), and indicate the typical ZZZssa configuration of the BV cofactor and an overall geometry resembling Agp1. Furthermore, the position of the N-H i.p. bending mode at 1567 cm<sup>-1</sup> attributes to a protonated, cationic BV. For Agp1, the vibrational mode assignment was recently validated by isotopic labeling experiments complemented by state-of-the-art QM/MM calculations.[218] The position and D<sub>2</sub>O exchange behavior of the C=C stretching bands in the Pr of canonical phytochromes is discussed in detail for iRFPs in chapter 7.1.[23] In H<sub>2</sub>O, two fundamental normal modes involving mainly C=C stretching character at ring D and the C,D methine bridge are found as one heterogeneous broadened peak with maximum at 1627 cm<sup>-1</sup>. The broadening is less pronounced in the IsPadC constructs than in Agp1, but a heterogeneous low-energy flank is clearly visible. After buffer exchange to D<sub>2</sub>O, the C=C stretching modes localized at the C,D methine bridge and inside ring D downshift (-6 cm<sup>-1</sup>) and pronounced heterogeneous broadening is observed, albeit the two bands are not as well separated as in Agp1 (1623 and 1613 cm<sup>-1</sup>). In the A,B C=C stretching region, two bands (1640 and 1605 cm<sup>-1</sup> for Agp1) were assigned to two different conformers at the A,B methine bridge.[23]. The low-frequency component (around 1640 cm<sup>-1</sup>) originates from conformer I and the high-frequency component was assigned to conformer II (around 1650 cm<sup>-1</sup>). The two bands are also detected in IsPadC, albeit with a different relative intensity ratio, reflecting a change in the relative population of the two sub-states. In IsPadC, the conformational equilibrium is shifted slightly in favor of conformer I. Additionally, both A,B C=C stretching modes are downshifted to lower frequencies compared to Agp1, indicating slightly different tilt angles of ring A in both conformers (-2 and -5 cm<sup>-1</sup>).



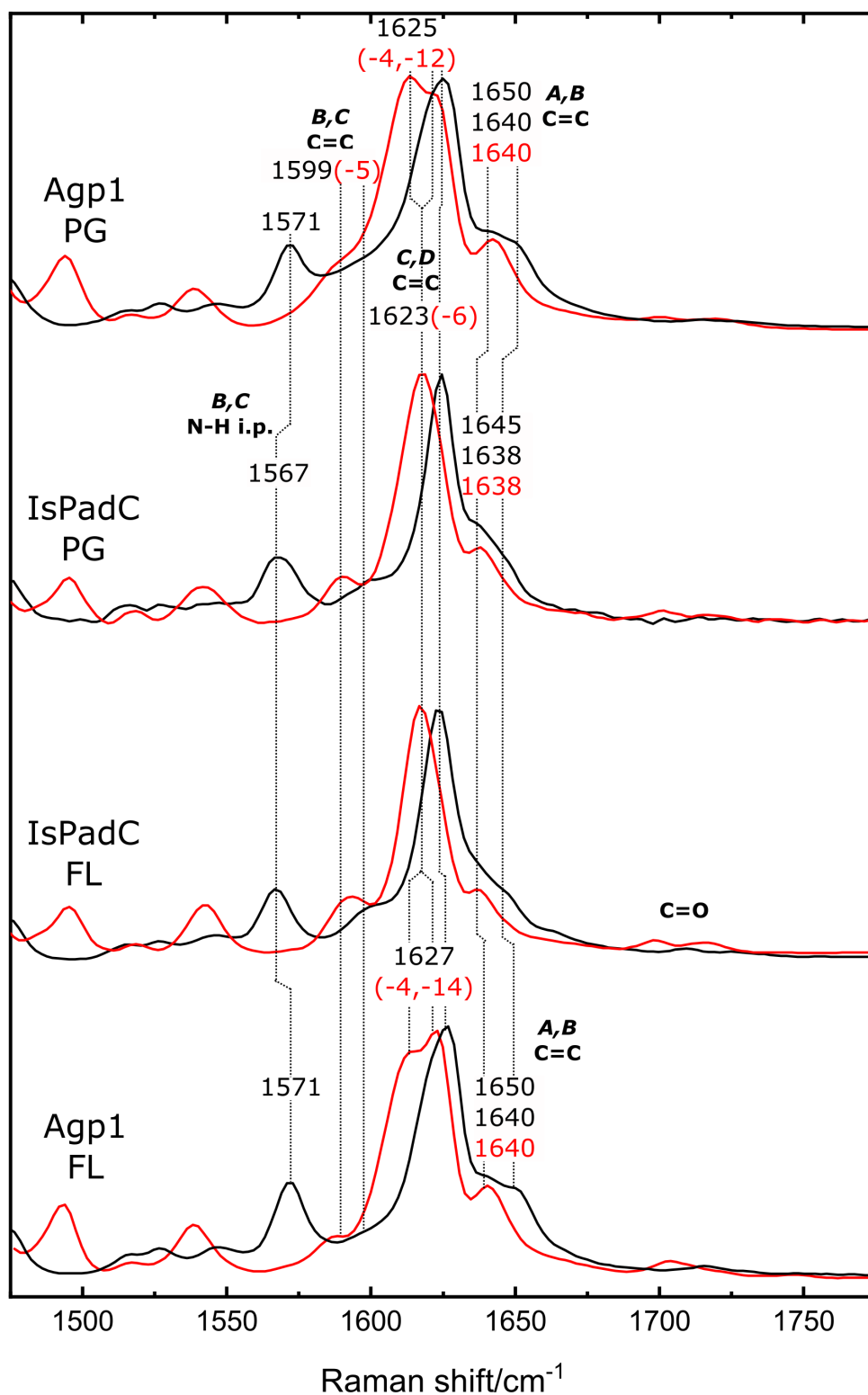


**Figure 6.2.1:** IsPadC and Agp1 RR spectra in the marker region in the Pr state. From bottom to top: Agp1 FL, IsPadC FL, IsPadC PG and Agp1 PG. Spectra were recorded in H<sub>2</sub>O and D<sub>2</sub>O buffer.

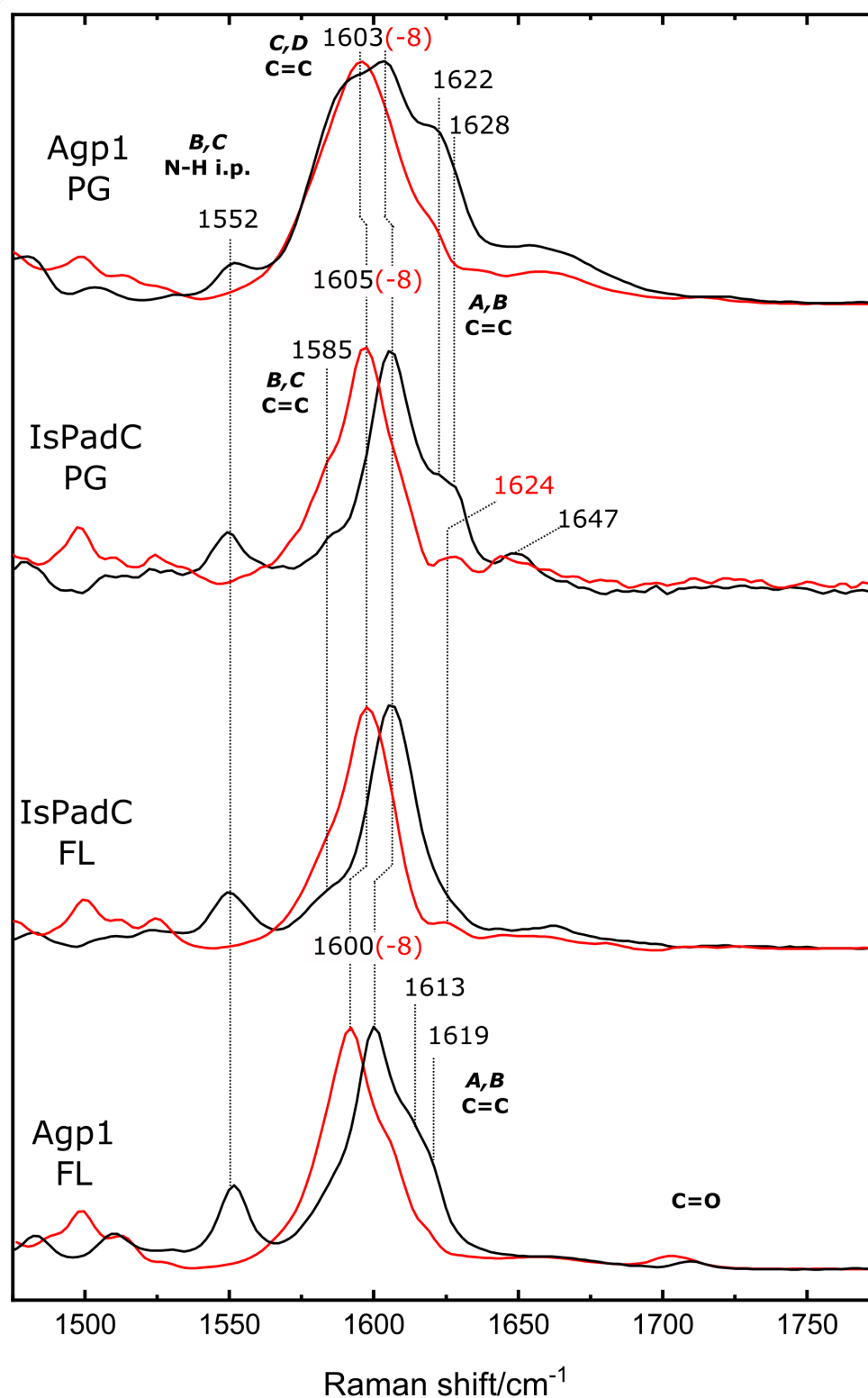


**Figure 6.2.2:** IsPadC and Agp1 RR spectra in the marker region in the photoactivated (Pfr and Meta for the FL and PG constructs, respectively) states. From bottom to top: Agp1 FL, IsPadC FL, IsPadC PG and Agp1 PG. Spectra were recorded in  $\text{H}_2\text{O}$  and  $\text{D}_2\text{O}$  buffer.

**Photoactivated state** While the RR spectra of Pr states of PG, PGP, and FL constructs Bphs are usually very similar or even identical, the photoproduct spectra in the PG constructs of most canonical phytochromes differ substantially from the Pfr state.[236, 40] The PG constructs lack the stabilizing interaction of the tongue and therefore rather convert to a Meta-Rc (like) state after photoactivation (see chapter 4.2 for a detailed discussion of the SbPhyB PG construct). In most prototypical phytochromes, the Meta-Rc is characterized by a deprotonated chromophore, where one N-H proton at the rings B and C is removed.[236, 40] Thus, the oscillator strength of the Meta-Rc chromophore is reduced, leading to weak Q-Band absorption (see supplementary fig. 9.4.2 or the UV/Vis absorption spectra of Agp1 PG or fig. 1.3.4 for SbPhyB PG). Interestingly, this is not the case for IsPadC PG. Here, the UV/Vis spectrum of the photoproduct does not display the characteristic reduced Q-band intensity, and this effect is pronounced when the UV/Vis difference spectra of the four constructs are compared (see fig. 9.4.2).

**PG photoproduct** Concomitant to the reduced oscillator strength in Meta-Rc, the RR spectra are only weakly resonance enhanced compared to the parent states, this results in a high intensity of apo-protein modes such as the Phe-breathing mode at  $1004\text{ cm}^{-1}$ . Due to the deprotonation, the vibrational band pattern of Meta-Rc differs to those of protonated chromophores, particularly that of Pfr. The first difference is obviously the lack of the characteristic N-H i.p. band at ca.  $1550\text{ cm}^{-1}$ . The resulting tautomeric forms of BV carry the remaining proton either at the B or C ring, and this leads to a doubling of all other normal modes which involve the respective N-H vibrations and thus very broad and unstructured RR spectra. During the formation of Meta-Rc in Agp1 and Cph1, a proton is transferred to the protein surface, and the re-uptake and chromophore re-protonation takes place with the decay of the Meta-Rc intermediate to Pfr.[225, 18] This transition also involves the secondary structure change of the tongue.[159, 218] However, the temporal sequence of the chromophore re-protonation and the tongue secondary structure change remains elusive.

However, in IsPadC PG, the Meta-like photoproduct is clearly protonated (N-H i.p. band at  $1552\text{ cm}^{-1}$ ), and the structure of the chromophore is already similar to the Pfr chromophore, as indicated by the C/D C=C stretching at  $1605\text{ cm}^{-1}$  with an isotopic shift of  $-8\text{ cm}^{-1}$  in  $\text{D}_2\text{O}$  buffer. Agp1 PG displays similar features, albeit with significantly broadened bands, probably originating from a heterogeneous chromophore environment. Assuming similar mechanistic patterns in prototypical phytochromes like Agp1 and IsPadC, a possible interpretation would be that the re-uptake of the proton by the chromophore precedes the tongue restructuring reaction. If the proton transfer is a functional toggle for the tongue structural change, the mechanism might be based on a transient protonation of a critical residue in the tongue. This interpretation is consistent with recent, unpublished cryo-trap and time-resolved IR results (personal communications with Zaneta Nogacz, Dr. Patrick Piwowarski and Prof. Dr. Franz Bartl from Charité Berlin).

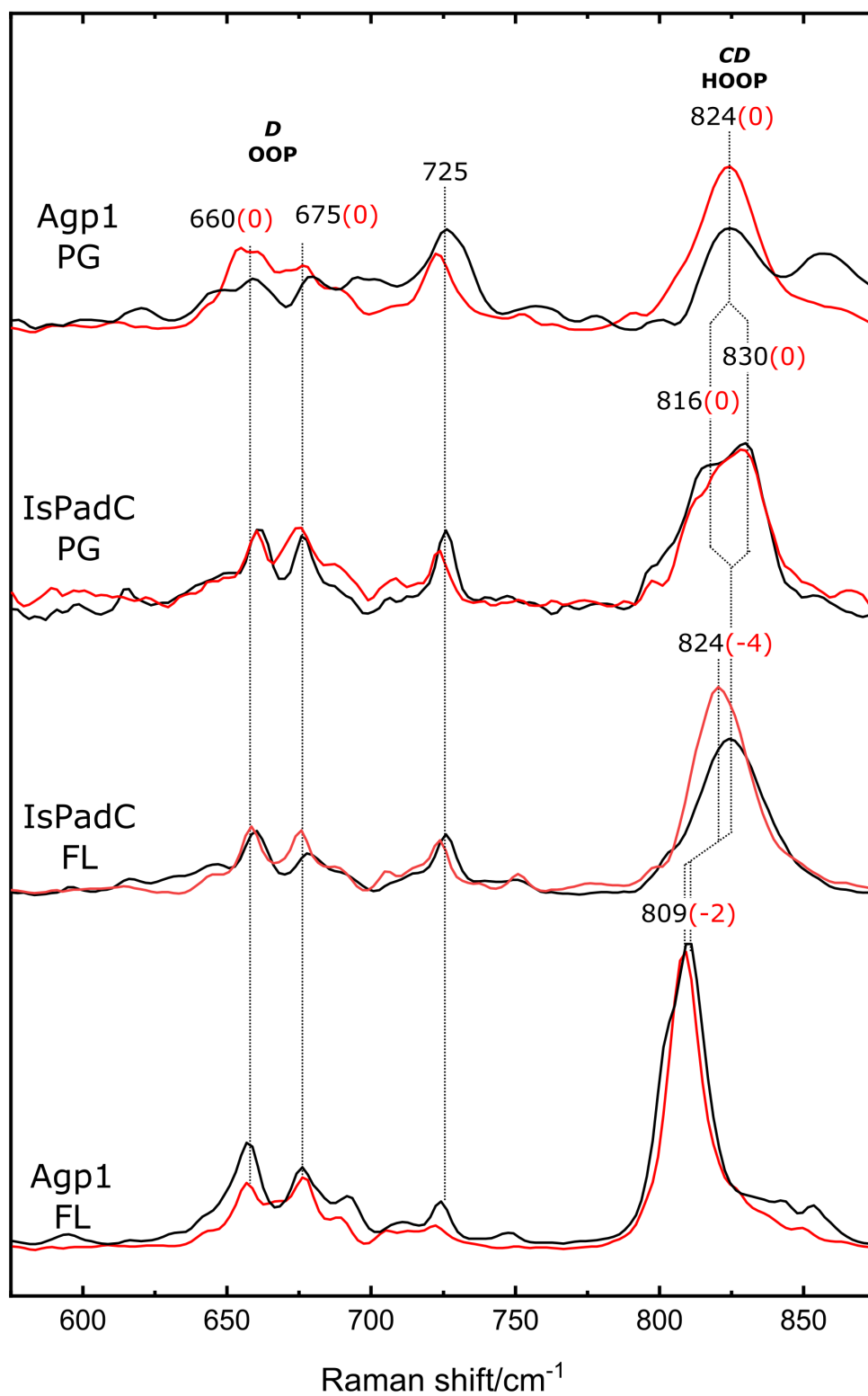


**Figure 6.2.3:** IsPadC and Agp1 RR spectra in the HOOP region in the (Pfr and Meta) states. From bottom to top: Agp1 FL, IsPadC FL, IsPadC PG and Agp1 PG. Spectra were recorded in  $\text{H}_2\text{O}$  and  $\text{D}_2\text{O}$  buffer.

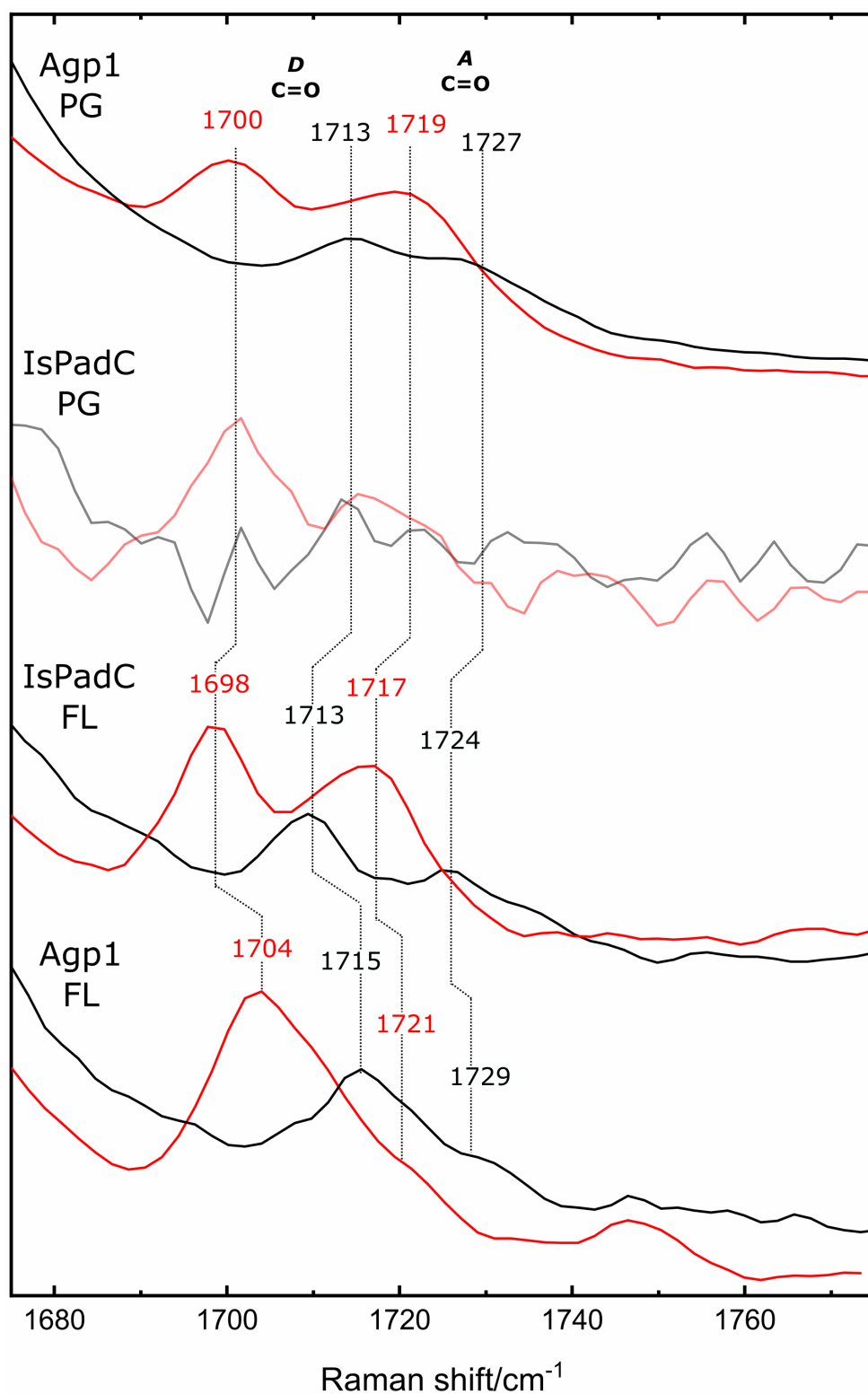


**Figure 6.2.4:** IsPadC and Agp1 RR spectra in the CO region in the Pr state. From bottom to top: Agp1 FL, IsPadC FL, IsPadC PG (lines are faded because of high noise level) and Agp1 PG. Spectra were recorded in H<sub>2</sub>O and D<sub>2</sub>O buffer.

**The Pfr/Meta heterodimer** According to UV/Vis spectroscopic experiments, the photoproduct of the FL protein is a heterodimer, consisting of one subunit in a Meta-R-like state and the other in the Pfr state.[60] Consequently, the spectrum of the FL photoproduct should represent a superposition of the Meta-R and Pfr RR spectra. The respective spectral contribution of Meta-R may be low due to the lower resonance enhancement conditions (*vide supra*). Under the assumption that the photoproduct spectrum of the PG construct constitutes a sufficient model for the Meta-Rc state in the FL protein, this hypothesis can be tested via a spectral subtraction procedure. In fact, the RR spectrum of the PG photoproduct can be partially subtracted (with a subtraction factor up to 0.2) from the FL photoproduct spectrum without introducing spectral artifacts such as negative or very sharp bands. The influence of the subtraction procedure on the FL photoproduct spectrum is negligible because the resulting spectra are essentially the same except for small shifts or intensity variations ( $< 2 \text{ cm}^{-1}$ , data not shown).

An interesting feature in the photoproduct spectrum of IsPadC FL is the broad and upshifted C/D HOOP band (see fig. 6.2.3). In canonical Bphs like Agp1, this high intensity band is found at  $809 \text{ cm}^{-1}$  with a characteristic double-band feature originating from a Pfr-I/Pfr-II conformational equilibrium at the C/D methine bridge (discussed in detail for plant PhyB in the chapters 4.1 and 4.2). In IsPadC FL, this band is upshifted to  $824 \text{ cm}^{-1}$ , which resembles the band position in the Meta-Rc state or in the PG constructs. Interestingly, the position and relative intensity of the C/D HOOP band is very similar to the dark-adapted state of bathy phytochrome PG constructs (e.g. RpBphP6 PG).[228] From the proposed Meta/Pfr heterodimer model, one would assume to observe a mixture of two HOOP bands, where one is located at lower frequencies with higher intensity (like characteristic  $809 \text{ cm}^{-1}$  for Agp1 Pfr) with a high-frequency ( $824 \text{ cm}^{-1}$ ), shoulder of low intensity. The position of the HOOP band correlates with the N(C)-C-C-C(D) dihedral angle, and thus with the tilt of ring D relative to the chromophore plane formed by the rings B and C.[183]

Accordingly, the IsPadC FL “Pfr” photoproduct also resembles a Meta-like configuration at the C/D methine bridge rather than a typical Pfr. This might be due to a reduced interaction of the chromophore with the tongue motif, which is necessary in IsPadC to uncouple the two transitions and allow the formation of the Meta-Rc/Pfr heterodimer. A (partial) uncoupling of these two structural transitions, which is also observed in the IsPadC Reg2 crystal structure (see chapter 1.6), was described for Agp1 and Agp2 (see chapter 6.1)[22] and a single-point mutant of DrBph.[216] In order to correlate the structural changes of the chromophore with the events in the tongue motif, difference IR spectroscopy was employed.

**IR spectroscopy** In the region between  $1600\text{--}1750 \text{ cm}^{-1}$  the IR spectra of phytochromes are dominated by modes that include substantial C=O stretching character. The bands originating from C=O stretching of the chromophores carbonyl groups (above  $1700 \text{ cm}^{-1}$ ) were assigned to the rings A and D on the basis of isotopic labeling experiments for Cph1[226] and agree well with previously published results for Agp1.[159] Due to the low polarizability of these highly polar functional groups, the corresponding C=O stretching modes are only sparsely Raman active and therefore the signal intensity is relatively low. The C=O stretching bands are only detected unambiguously when the sample quality and concentration are high, and often exceed the noise level only by a factor of 2-10.

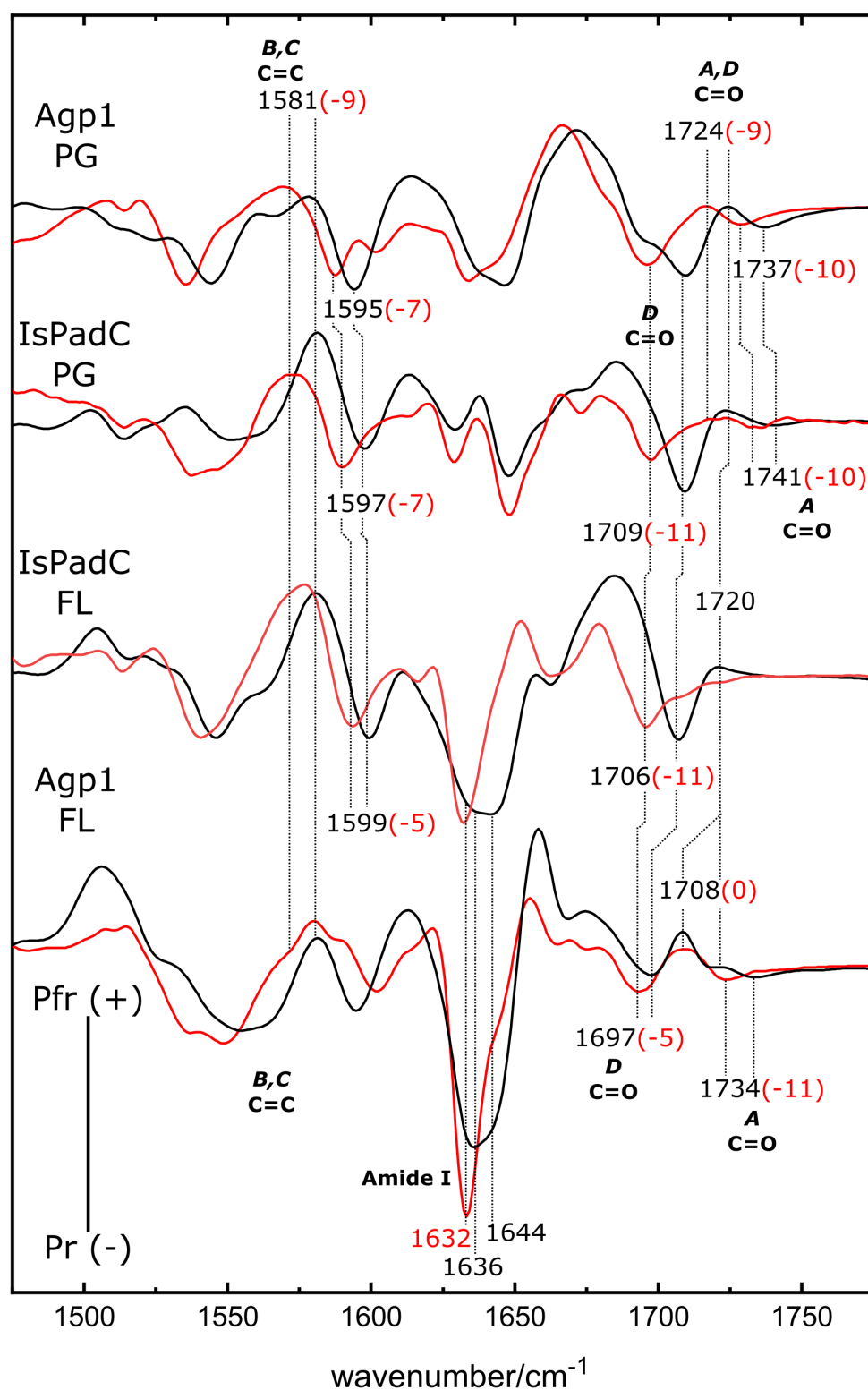


**Figure 6.2.5:** IsPadC and Agp1 difference IR spectra. Negative (-) bands originate from the Pr state bleach while positive bands (+) correspond to a gain of signals from to Meta or Pfr photoproducts. From bottom to top: Agp1 FL, IsPadC FL, IsPadC PG and Agp1 PG. Spectra were recorded in  $\text{H}_2\text{O}$  and  $\text{D}_2\text{O}$  buffer.

Although the C=O stretching bands are unambiguously detected in Agp1 PG and FL in both parent states (see figs. 6.2.4 and 9.4.6), the quality of the IsPadC samples permits a safe detection only in the Pr state RR spectrum of the FL construct at 1713 and 1724  $\text{cm}^{-1}$  (see fig. 6.2.4). The high polarity of the C=O double bond is accompanied strong IR absorption and the corresponding C=O stretching bands can be detected in the difference IR spectra of all four constructs (see fig. 6.2.5). As discussed in chapter 4.3, the band positions in the IR diff. spectra are unfortunately obscured by overlapping adjacent bands. Both IsPadC constructs are very similar with a strong negative signal at 1709  $\text{cm}^{-1}$  (1706  $\text{cm}^{-1}$  in the case of PG), originating from the bleach of the ring D C=O Pr signal (at 1713  $\text{cm}^{-1}$  for IspadC FL in the RR spectra). This is complemented by a weak positive signal at 1720  $\text{cm}^{-1}$ , resembling the position of the Pfr C=O stretching band of ring D in Agp1 PG (also see RR spectra fig. 6.2.4). This observation is in agreement with the interpretation of the HOOP band that points to a Meta-like configuration of ring D in both IsPadC photoproducts. In contrast, the Pfr state of Agp1 FL displays a much stronger positive signal at a lower frequency (1708  $\text{cm}^{-1}$  (+) in the diff. IR, fig. 6.2.5 and 1709  $\text{cm}^{-1}$  in the RR, fig. 9.4.6). The Pr bleach signal of the ring A carbonyl stretching at higher frequencies (1724  $\text{cm}^{-1}$  in IsPadC FL) overlaps strongly with the (+) signal and thus cancels out, leading to a reduced intensity and obscured band position (1737  $\text{cm}^{-1}$  for Agp1 PG and 1741  $\text{cm}^{-1}$  for IsPadC PG). In the region between 1620 and 1660  $\text{cm}^{-1}$ , C=O stretching vibrations of the protein backbone, termed amide I bands, are observed. The position, intensity and bandwidth of the amide I signal mainly depends on the secondary structure of the protein backbone.[70] This leads to a strong difference signal when the tongue region undergoes the transition from  $\alpha$ -helix to  $\beta$ -sheet (strong negative signal for Agp1 at 1636/1644  $\text{cm}^{-1}$ , fig. 6.2.5). The interpretation of phytochrome IR difference spectra is complicated, because the bands for the structural elements of the tongue in the Pfr and Pr states strongly overlap with opposite site. For the Pfr configuration, two broad bands at ca. (i) 1625 and (ii) 1655  $\text{cm}^{-1}$  are expected, corresponding to the loop-coil and the  $\alpha$ -helical regions of the tongue, respectively. For Pr, the corresponding bands are expected at ca. (iii) 1630  $\text{cm}^{-1}$ , corresponding to the formation of a  $\beta$ -sheet and (iv) 1640  $\text{cm}^{-1}$  for the  $\beta$ -hairpin motif. In addition, Pr (of both PG constructs) includes a band at ca. 1645  $\text{cm}^{-1}$  (-) which does not seem to be related to the tongue. Regarding the complete tongue transition, the contributions of the overlapping bands i-iv must partially cancel each other due to the opposite signs in the difference spectra (Unpublished results, personal communication with Prof. Dr. Peter Hildebrandt and Prof. Dr. Friedrich Siebert). However, in IsPadC FL, the resulting negative amide I band is present, but smaller (about half the intensity) than in Agp1 FL, which is consistent with the Meta/Pfr heterodimer hypothesis.



---

## 7 Results: Infrared Fluorescent Proteins Derived from Phytochromes (iRFPs)

The following section comprises two publications about the relationship between the chromophore structure and the fluorescence properties of near-infrared fluorescent proteins derived from phytochromes (iRFPs). A common method to enhance the fluorescence quantum yield in these proteins is the random introduction of amino acid substitution (e.g. error prone PCR) followed by a screening for highly fluorescent candidates.

In chapter 7.1, a mutagenesis study of the bacterial phytochrome RpBphP2 from *Rhodospseudomonas palustris* and the related fluorescence-enhanced protein iRFP713 aims to unravel the contribution of different amino acids exchanges to the overall fluorescence enhancement. Here, a combined approach of fluorescence and RR spectroscopy was employed to rationalize how the different substitutions change the structure of the chromophore and influence the fluorescence properties. The presented results are supported by theoretical modeling and time- and wavelength-correlated single photon counting (TWCSPC).

Chapter 7.2 is a logical continuation of chapter 7.1. Here, another iRFP with an unusual double-attachment of the biliverdin chromophore (iRFP682) is investigated with RR and fluorescence spectroscopy. This study aims to correlate the structural changes of the chromophore that are caused by the second covalent attachment with the fluorescence properties. For this purpose, iRFP682 was purified with a novel protocol and compared to several cysteine/serine exchange variants with different modes of chromophore attachment.

### 7.1 Mutagenesis Study on iRFP713

This research was originally published in Scientific Reports:

D. Buhrke, F. Velázquez Escobar, L. Sauthof, S. Wilkening, N. Herder, N. N. Tavraz, M. Willoweit, A. Keidel, T. Utesch, M. Mroginski, F. Schmitt, P. Hildebrandt, and T. Friedrich. *The role of local and remote amino acid substitutions for optimizing fluorescence in bacteriophytochromes : A case study on iRFP*. in: *Scientific Reports* **6**.Article number: 28444 (2016). DOI: 10.1038/srep28444

- **David Buhrke** performed RR, UV-Vis absorption and static fluorescence measurements and RR data analysis.
- Francisco Velázquez Escobar and Anke Keidel supervised RR measurements.
- Luisa Sauthof, Svea Wilkening and Nico Herder performed site directed mutagenesis, protein expression and purification under the supervision of Neslihan N. Tavraz.
- Mario Willoweit performed time- and wavelength-correlated single photon counting.
- Franz-Josef Schmitt and Thomas Friedrich performed TWCSPP data analysis.
- Tillmann Utesch, Francisco Velázquez Escobar, Maria-Andrea Mroginski and Peter Hildebrandt contributed to RR data analysis.
- **David Buhrke**, Francisco Velázquez Escobar, Thomas Friedrich and Peter Hildebrandt wrote the manuscript.
- Peter Hildebrandt designed the two-states-model.
- All authors discussed the results and commented on the manuscript.

© This work is licensed under a Creative Commons Attribution 4.0 International License.

# SCIENTIFIC REPORTS

OPEN

## The role of local and remote amino acid substitutions for optimizing fluorescence in bacteriophytochromes: A case study on iRFP

Received: 14 March 2016

Accepted: 03 June 2016

Published: 22 June 2016

David Buhrke, Francisco Velazquez Escobar, Luisa Sauthof, Svea Wilkening, Nico Herder, Neslihan N. Tavraz, Mario Willoweit, Anke Keidel, Tillmann Utesch, Maria-Andrea Mroginski, Franz-Josef Schmitt, Peter Hildebrandt & Thomas Friedrich

Bacteriophytochromes are promising tools for tissue microscopy and imaging due to their fluorescence in the near-infrared region. These applications require optimization of the originally low fluorescence quantum yields via genetic engineering. Factors that favour fluorescence over other non-radiative excited state decay channels are yet poorly understood. In this work we employed resonance Raman and fluorescence spectroscopy to analyse the consequences of multiple amino acid substitutions on fluorescence of the iRFP713 benchmark protein. Two groups of mutations distinguishing iRFP from its precursor, the PAS-GAF domain of the bacteriophytochrome P2 from *Rhodospseudomonas palustris*, have qualitatively different effects on the biliverdin cofactor, which exists in a fluorescent (state II) and a non-fluorescent conformer (state I). Substitution of three critical amino acids in the chromophore binding pocket increases the intrinsic fluorescence quantum yield of state II from 1.7 to 5.0% due to slight structural changes of the tetrapyrrole chromophore. Whereas these changes are accompanied by an enrichment of state II from ~40 to ~50%, a major shift to ~88% is achieved by remote amino acid substitutions. Additionally, an increase of the intrinsic fluorescence quantum yield of this conformer by ~34% is achieved. The present results have important implications for future design strategies of biofluorophores.

The development of fluorescence microscopy has opened novel possibilities for monitoring biochemical processes in cellular systems<sup>1–5</sup>. The availability of genetically encoded fluorescent proteins including photoswitchable variants provided new insights into the organization of living cells on the nanoscale by super-resolution fluorescence microscopy<sup>6–9</sup>. These techniques have a strong impact on fundamental research and are important diagnostic tools in medical science. In particular for high resolution imaging genetically encoded rather than synthetic fluorescence markers are preferred, because they can be expressed directly in the target cell and fused to the desired protein.

Fluorescent proteins emitting in the red or near-infrared spectral region gain increasing importance because they ensure a high penetration depth in tissues. Genetic engineering of the green fluorescent protein (GFP)<sup>10</sup> and its homologues from other species afforded numerous variants with emission maxima covering nearly the entire visible spectrum<sup>2</sup>. However, red-emitting biofluorophores suffer from limited photostability and low brightness<sup>11</sup>. Bacterial phytochromes may overcome these drawbacks, since the tetrapyrrole cofactor exhibits a strong electronic transition between 660 and 700 nm. Furthermore, biliverdin (BV) is ubiquitous in mammalian cells as an intermediate of the heme degradation pathway. Due to their function as sensory photoreceptors, bacteriophytochromes exhibit only a low fluorescence quantum yield ( $\Phi_{fl}$ , ~1%) but instead undergo a photoisomerisation upon electronic excitation. However, the approach to raise  $\Phi_{fl}$  by blocking the photocycle is not necessarily

Technische Universität Berlin, Institut für Chemie, Sekr. PC14, Straße des 17. Juni 135, D-10623 Berlin, Germany. Correspondence and requests for materials should be addressed to P.H. (email: hildebrandt@chem.tu-berlin.de) or T.F. (email: friedrich@chem.tu-berlin.de)

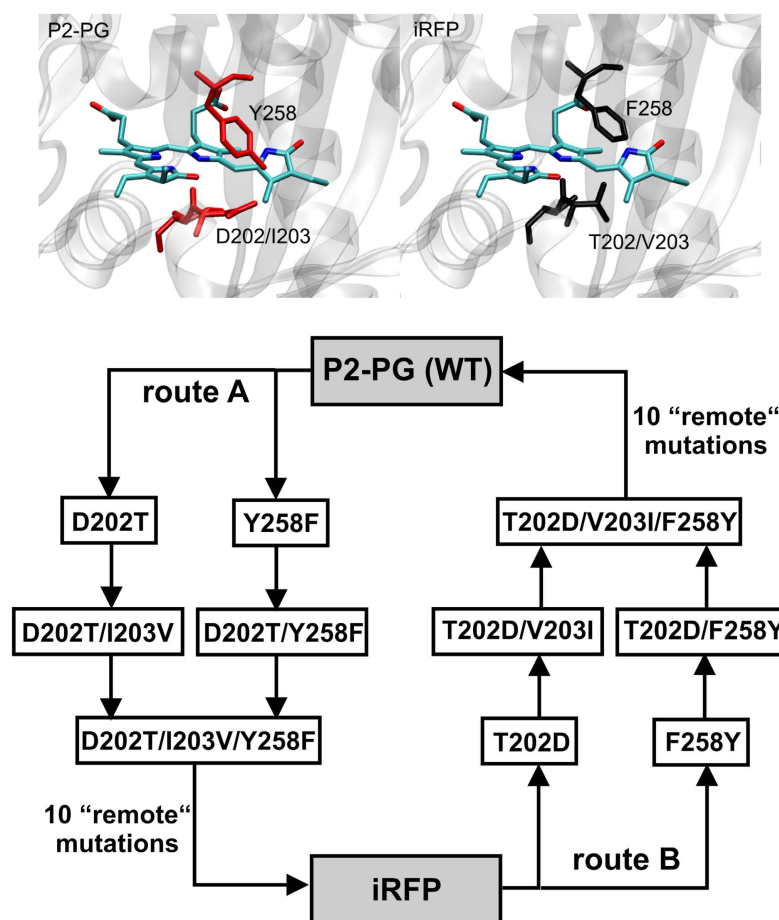


**Figure 1.** Top, structure of the chromophore binding pocket of P2PG (left) and iRFP (right), indicating the amino acid variations between both variants. The structural models<sup>18</sup> were derived from the crystal structure of the chromophore binding domain of RpBphP2 obtained by homologue-directed mutagenesis, which was termed RpBphP2-CBD\*<sup>29</sup>. Bottom, schematic presentation of the step-wise amino acid substitutions starting from P2PG WT (route A) and from iRFP (route B).

straightforward, since the photochemical conversion for BV-binding phytochromes of less than 10%<sup>12</sup> is still low compared to the non-radiative excited-state decay pathways. Nevertheless, a bacteriophytochrome variant with strongly reduced photochemical quantum yield, that is for instance achieved by substituting the highly conserved Asp-202 (amino acid [AA] numbering refers to *Rhodospseudomonas palustris* bacteriophytochrome photoreceptor 2, RpBphP2)<sup>13</sup>, served as a starting point for the development of bacteriophytochromes with improved fluorescence by using evolutionary mutagenesis. Promising results were obtained by genetic engineering of the chromophore-binding domain of RpBphP2, which produced an efficient phytofluor denoted iRFP713<sup>11,14</sup> (termed iRFP for brevity herein). This variant differs from the truncated wild-type (WT) protein RpBphP2 (including only the GAF and PAS domains, termed P2PG in the following) by a total of 13 mutations. These substitutions resulted in a  $\Phi_f$  of 5.9% compared to 0.7% for P2PG. Meanwhile, similar engineering strategies, also based on other bacteriophytochromes, have afforded variants with further improved fluorescence properties<sup>14–16</sup>, and the application as sensitive fluorescence probes for *in vivo* imaging has been demonstrated for some variants including iRFP<sup>11,17</sup>.

In parallel, attempts have been made to elucidate the structural basis for the altered photophysical properties in fluorescent bacteriophytochromes. Crystallographic and spectroscopic studies have consistently shown that an increased rigidity of the chromophore embedment in the protein matrix is one of the key parameters that favours fluorescence as the decay route of the electronically excited state<sup>15,16,18–21</sup>.

In this work, we continued our spectroscopic studies on iRFP<sup>18</sup> to specifically analyze the contributions of individual AA substitutions on the ground- and excited-state properties of the BV cofactor. We focused on three highly conserved AAs in the chromophore-binding pocket (CBP), Asp202, Ile203, and Tyr258, which in iRFP are replaced by Thr, Val, and Phe, respectively. Mutagenesis followed two main routes via stepwise substitutions (route A) in the truncated WT P2PG and (route B) the corresponding back substitutions in iRFP (Fig. 1). The variants along route A include single, double (with two out of three possible combinations), and triple mutations.

protein variant	absorption (nm)	fluorescence (nm)	$\Phi_{\text{fl}}$ (%)	photo-activity	ring D str. (cm <sup>-1</sup> )	A-B str. (cm <sup>-1</sup> )		Intensity ratio A-B str., conformer II/ conformer I ( $R = I_{\text{II}}/I_{\text{I}}$ )
						conformer I	conformer II	
P2-PG variants derived from P2-PG WT (route A)								
WT P2-PG	707	712	0.7	yes	1625	1651	1641	0.64
D202T	707	717	1.4	yes	1628	1655	1644	0.78
Y258F	706	717	1.9	very weak	1627	1656	1644	1.11
D202T/I203V	704	716	1.3	yes	1628	1655	1644	0.82
D202T/Y258F	707	719	2.2	very weak	1628	1655	1646	0.99
D202T/I203V/Y258F	701	715	2.5	no	1629	1655	1646	1.01
P2-PG variants derived from iRFP (route B)								
iRFP	692	708	5.9	no	1629	1656	1642	7.20
T202D	697	714	3.4	no	1627	1654	1642	3.81
F258Y	693	710	3.6	no	1628	1654	1642	7.22
T202D/V203I	702	716	3.0	no	1627	1655	1642	2.64
T202D/F258Y	697	710	2.8	no	1627	1652	1642	n.a.
T202D/V203I/F258Y	699	712	1.5	yes	1627	1652	1642	7.38

**Table 1. Absorption and fluorescence maxima, and fluorescence quantum yields of various P2-PG variants.** The variants (route A and B) are defined in Fig. 1. Absorption and fluorescence maxima were taken from Supplementary Figs S1 and S2 (Supporting Information); the fluorescence quantum yields ( $\Phi_f$  in %) were determined experimentally (see materials and methods). The stretching mode frequencies of the A-B methine bridge and of ring D as well as the intensity ratio  $R$  (intensity of the high [conformer II] vs. the low frequency component [conformer I] of the A-B mode) were determined from second derivatives of the RR spectra in Figs 5 and 6 (left panels). For the iRFP-T202D/F258Y variant, the error in the intensity determination was too large due to a close overlap of the respective bands (Fig. 5, left) and a very low intensity of the conformer I component (thus denoted as “n.a.” = not applicable).

Each of the variants obtained by the corresponding back substitutions along route B also included the additional 10 substitutions of iRFP that are more remote from the CBP. The objective was to correlate chromophore structural changes determined by resonance Raman (RR) spectroscopy with the properties of the static and time-resolved fluorescence of the individual variants. The results demonstrate the coexistence of a fluorescent and a non-fluorescent conformer. The intrinsic fluorescence quantum yields for the former and its relative population are affected by both, the AA substitutions in the CBP and the remote mutations, albeit in a qualitatively different manner. The findings have implications for optimizing strategies towards generating highly fluorescent bacteriophytochromes.

## Results

**Absorption and Fluorescence Properties.** In general, the electronic absorption spectra of the Pr state of all investigated P2PG and iRFP variants show very similar characteristics of the Q and Soret bands (see Supplementary Fig. S1), with variations in the Q band absorption maxima from 707 to 692 nm (Table 1). Among the P2PG-derived variants, mutations D202T and Y258F and their combination in D202T/Y258F had only a small impact on the absorption maximum, whereas the double D202T/I203V and triple D202T/I203V/Y258F mutation displayed a blue-shift by 3 and 6 nm, respectively. In a similar way, iRFP-T202D and others from route B including mutant V203I, showed markedly red-shifted absorption maxima compared to iRFP (Table 1).

The  $\Phi_f$  values of all investigated mutants were between those of native P2PG (0.7%) and iRFP (5.9%) (Tables 1 and 2, Supplementary Fig. S2). Interestingly, an increased  $\Phi_f$  seems to be accompanied with a blue-shift in the Q-band absorption maximum and an increasing Stokes shift (Table 1, Supplementary Figs S1 and S2).

None of the variants studied in this work can undergo a phototransformation to the Pfr state, but some are arrested at the Meta-R state as typically observed for phytochrome variants with substitutions of highly conserved AAs close to the chromophore<sup>22,23</sup>. Since the Qband transition of the Meta-R state exhibits reduced oscillator strength and its maximum nearly coincides with that of the parent state (Supplementary Fig. S1), IR difference spectroscopy is more reliable to detect even low photoconversion than UV-Vis absorption spectroscopy (Supplementary Fig. S5). Except for the triple mutant P2PG-D202T/I203V/Y258F, all variants generated from P2PG via route A are capable to undergo photoisomerisation to a small extent (Table 1, Supplementary Fig. S1). This observation suggests that the triple mutation D202T/I203V/Y258F represents a minimal set to completely inhibit photoconversion of P2PG, although  $\Phi_f$  is still relatively low. The reverse mutations starting from iRFP along route B represent a mirror image of this tendency, since the triple substitution T202D/V203I/F258Y in the CBP of iRFP is sufficient to recover photoactivity, irrespective of the 10 remote substitutions. However, blocking photoconversion alone is insufficient to optimize  $\Phi_f$ , since the 10 remote substitutions still exhibit a profound effect: Compared to the P2PG triple mutant D202T/I203V/Y258F,  $\Phi_f$  increases ~2.4-fold upon introduction of the additional 10 remote substitutions in iRFP. Conversely, the iRFP triple mutant T202D/V203I/F258Y, which comprises only the 10 remote substitutions, still has a more than 2-fold larger  $\Phi_f$  than P2PG.

Variants without remote substitutions			Variants with remote substitutions			Intrinsic fluorescence quantum yields $\Phi_{II}$	
Route A variants	$\Phi_{II}$ (%)	R	Route B variants	$\Phi_{II}$	R	$\Phi_{II}(A)$ (%)	$\Phi_{II}(B)$ (%)
P2-PG	0.7	0.64	T202D/V203I/F258Y	1.5	7.38	1.7	1.7
D202T	1.4	0.78	—	—	—	3.2	—
Y258F	1.9	1.11	T202D/V203I	3.0	2.64	3.6	4.1
D202T/I203V	1.3	0.82	F258Y	3.6	7.72	2.9	4.1
D202T/Y258F	2.2	0.99	—	—	—	4.4	—
D202T/I203V/Y258F	2.5	1.01	iRFP	5.9	7.20	5.0	6.7
—	—	—	T202D	3.4	3.81	—	4.3
—	—	—	T202D/F258Y	2.8	n.a.	—	—

**Table 2. Intrinsic fluorescence quantum yields of conformer II.** The intrinsic fluorescence quantum yields  $\Phi_{II}$  were evaluated according to eq. (4) using the experimentally observed fluorescence quantum yields  $\Phi_{II}$  and the intensity ratio  $R$  (see Table 1), taken to be equal to the population ratio of the conformers II and I.  $\Phi_{II}(A)$  and  $\Phi_{II}(B)$  refer to values determined for the variants of route A and B, given in the same row of the table. For the iRFP-T202D/F258Y variant, the error in the intensity determination was too large due to a close overlap of the respective bands (Fig. 5, left) and a very low intensity of the conformer I component (thus denoted as “n.a.” = not applicable).

**Fluorescence dynamics.** The fluorescence decays of all variants could consistently be approximated by three exponential decay components with distinct spectral dependence of the resulting decay-associated spectra (DAS, Fig. 2). The longest fluorescence lifetime was found to decrease along mutational route B from 910 ps in iRFP (Fig. 2a) to 440 ps in iRFP-T202D/V203I/F258Y (Fig. 2f). In addition, a short fluorescence decay time exists, which shortens from 350 ps in iRFP to 180 ps in iRFP-T202D/V203I/F258Y. A third component with ~100 ps present in iRFP and all route B samples without significant variations, exhibits a negative amplitude for iRFP and iRFP-F258Y in the whole spectral range (Fig. 2a,b, black curves). Such exclusively negative components in DAS are assigned to fluorescence rise effects in time<sup>24</sup>, representing population processes of excited states that occur in the 100 ps time regime. Since this value is close to the resolution limit of the employed TWCSPPC setup, this component might be even faster than 100 ps.

Considering that decay and rise components have similar spectral characteristics, iRFP exhibits a rather homogenous excited state (Fig. 2a) with two decay components that possibly carry (phonon) sidebands at 715 and 725 nm. Such biexponential excited-state relaxations are typical for pigment-protein-complexes and do not necessarily indicate different chromophore configurations<sup>24</sup>. However, the iRFP-F258Y mutant already shows a heterogeneous spectral distribution of both decay components with reduced lifetimes (Fig. 2b). This feature indicates a substructure of the ground- and/or excited-state potential surface that is, in the simplest case, described by a double-well potential<sup>24</sup>. However, since the 90 ps component does not exhibit a transition from positive to negative amplitude (*vide infra*), it cannot be attributed to a transition between two states within the lifetime of the excited state. The two spectrally distinguishable decay components might simply represent two non-coupled excited-state subpopulations.

DAS heterogeneity is even more pronounced in iRFP-T202D and iRFP-T202D/V203I (Fig. 2c,e). Here, the fastest component (130 ps) exhibits a transition from positive values (up to about 700 nm) to negative values above 710 nm representing a novel feature not observed in iRFP and iRFP-F258Y: During the excited-state lifetime, a red-shifted emitting state is populated at the expense of a blue-shifted one. This biphasic behaviour suggests an interconversion of two chromophore configurations in the excited state. The subsequent fluorescence decay occurs with 290 ps (705 nm), and 680 ps (715 nm) (Fig. 2c). In iRFP-T202D/F258Y (Fig. 2d), the DAS heterogeneity is reduced compared to iRFP-T202D, although the emission spectrum of its longest decay component shows a more profound shoulder at 740 nm compared to iRFP. Notably, the biphasic nature of the 70 ps component is absent suggesting that the effects of both mutations on the DAS partially neutralize each other.

A further dissection into several spectrally distinguishable states is observed in the triple mutant iRFP-T202D/V203I/F258Y, still carrying all remote substitutions of iRFP. Besides a remarkable acceleration of all fluorescence decay components, which accounts for the small  $\Phi_{II}$ , the DAS of this mutant distinguishes at least four spectral bands at ~695, ~705, ~715 and ~730 nm (Fig. 2f), indicating radiative decays from four distinct excited states or chromophore configurations. The pronounced biphasic nature of the 100 ps component indicates strong coupling and interconversion between the electronic states at 695 nm and at 715 nm, followed by a ~440 ps decay. Thus, already single back-substitutions in the CBP of iRFP entail substantial excited-state heterogeneity, which gradually increases with the number of mutations.

Notably, the DAS of iRFP-T202D/V203I/F258Y is similar to that of the parental P2PG (Fig. 2g), which also exhibits a biphasic component (180 ps) and two further decay components (280 ps and 690 ps). Among them, the faster one dominates in amplitude, in line with the lowest  $\Phi_{II}$  of P2PG. In total, four spectral features at 710, 730, 750, and 780 nm can be discriminated for P2PG. In contrast, the double mutant P2PG-D202T/F258Y, which only carries two CBP substitutions, already shows rather homogenous DAS (Fig. 2h), essentially similar to iRFP, despite the fact that the mutant still shows photoconversion. Figure 3a summarizes the average lifetimes and Fig. 3b compares the fast and slow fluorescence decay time constants of the constructs from Fig. 2.

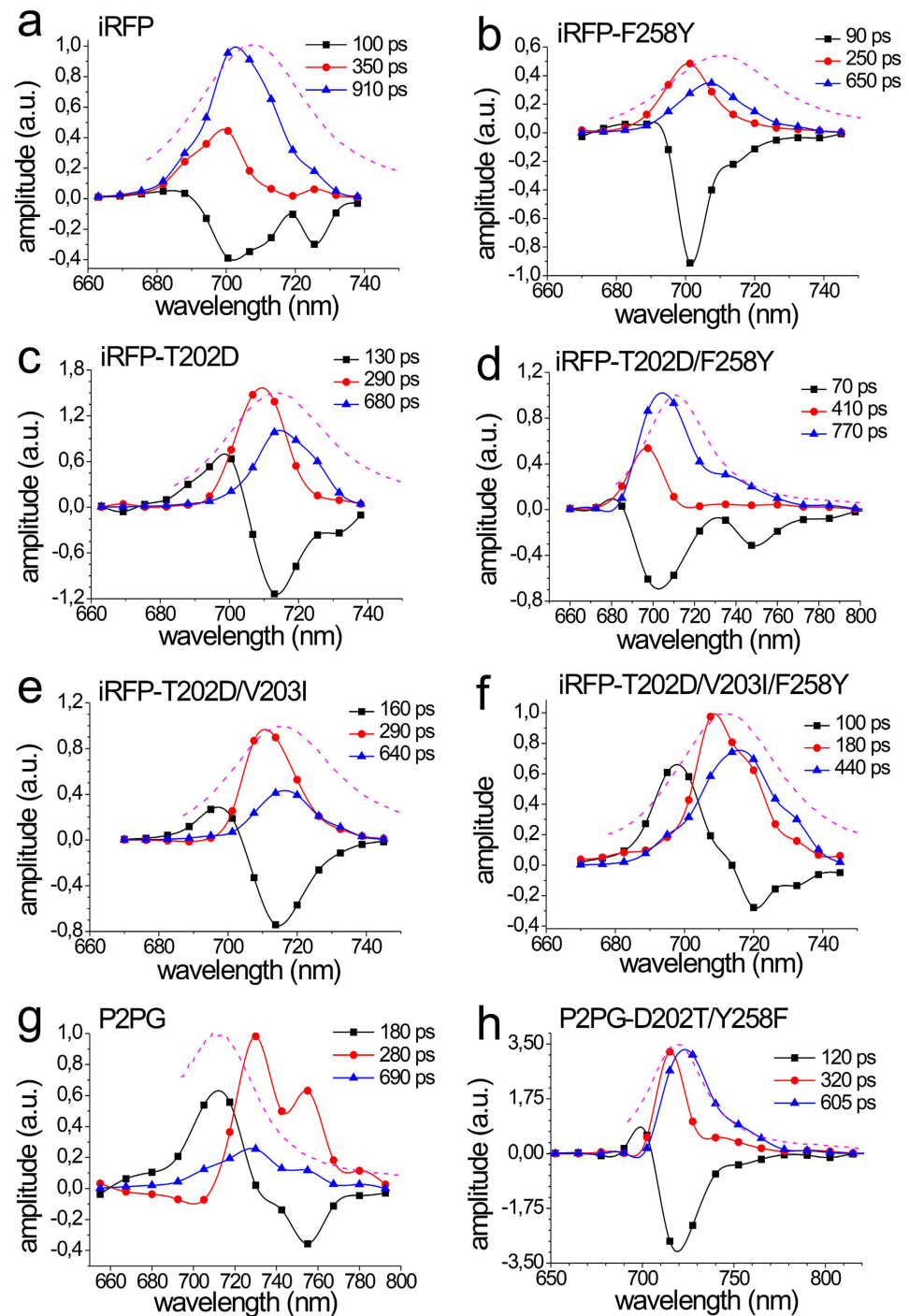


**Figure 2. Decay associated spectra (DAS) and fluorescence lifetimes of iRFP, P2PG and selected mutants from route A and B.** (a–h) The DAS were obtained from global fitting of the wavelength-resolved fluorescence decays recorded at 10 K with a sum of three exponentials. The relative amplitudes of the individual decay components (ultrafast: black; fast: blue; slow: red) from these fits are depicted for each wavelength channel, with time constants as given in the insets. The black, blue and red curves are included to guide the eye. Superimposed to the DAS are the corresponding fluorescence emission spectra (magenta) of the protein variants measured at room temperature.



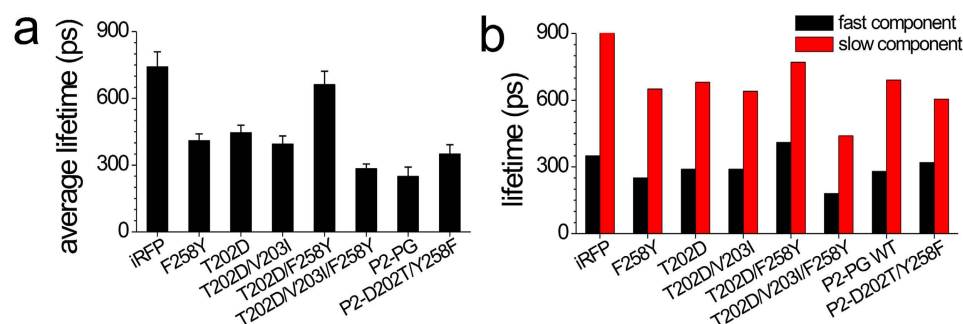


**Figure 3.** Average fluorescence lifetimes (a) and overview about the lifetimes (b) of the fast (black columns) and slow (red columns) component for each construct from Fig. 2a–h.

**Resonance Raman Spectroscopy.** All phytochrome variants studied in this work were in the Pr state as reflected by the characteristic vibrational band pattern of the chromophore in the *ZZZssa* configuration (see Supplementary Information). For a detailed vibrational assignment we therefore refer to previous analyses<sup>25,26</sup>. In this work we focus on the identification of selected modes that correlate with specific structural parameters of the tetrapyrrole. Between 1565 and 1580  $\text{cm}^{-1}$ , the protonation marker band of the Pr state is observed<sup>27,28</sup>. It is due to the in-phase N-H in-plane bending (N-H ip) of the ring B and C N-H groups and thus indicates that all pyrrole nitrogen atoms carry a proton and rings B and C share a positive charge (Figs 4 and 5). In P2PG and iRFP, this band is observed between 1571 and 1575  $\text{cm}^{-1}$ , and it shifts down to 1075 and 1079  $\text{cm}^{-1}$  in  $\text{D}_2\text{O}$ <sup>18</sup>, indicating a cationic (protonated) chromophore in each case. The same conclusion can be drawn for all P2PG or iRFP variants. Small frequency variations observed for the N-H ip indicate minor changes of the hydrogen bond interactions of the ring B and C N-H groups<sup>25</sup>.

The most intense peak in the Pr state of all variants is observed around 1620  $\text{cm}^{-1}$  (Figs 4 and 5, left). It is actually composed of two overlapping bands, which are more clearly discriminated in the second-derivatives (grey traces in Figs 4 and 5). The underlying modes include mainly the C=C stretching coordinates of the C-D methine bridge (C-D stretching) and of ring D and its vinyl substituent, albeit with different relative contributions. Since the C-D stretching couples with the N-H ip of rings C and D, the main character of the two modes can be distinguished on the basis of the H/D isotopic shifts (Figs 4 and 5). In all cases, the frequency downshifts of the band components at 1620 and 1627  $\text{cm}^{-1}$  is about 7 and 2  $\text{cm}^{-1}$ , respectively. Thus, the lower and higher frequency components may be considered as C-D stretching and ring D C=C stretching modes, respectively.

The corresponding C=C stretching mode of the A-B methine bridge (A-B stretching) is observed between 1640 and 1660  $\text{cm}^{-1}$ . In the Pr state of many BV-binding phytochromes including P2PG, this mode is split into two components, corresponding to two conformational sub-states. We denote the states represented by the low- and high-frequency component as state I and II, respectively. For P2PG these bands are found at 1641 and 1651  $\text{cm}^{-1}$  (Fig. 4, left). Due to the coupling of the A-B stretching with the N-H ip coordinates of rings A and B, these modes shift down by  $\sim 10 \text{ cm}^{-1}$  upon  $\text{D}_2\text{O}$  exchange. Thus, only one of these modes can be safely detected in the RR spectra measured in  $\text{D}_2\text{O}$  (i.e., 1641  $\text{cm}^{-1}$ ; Fig. 4, right), whereas the lower-frequency component overlaps with the (largely H/D-insensitive) C=C stretching mode of ring D.

Among the modes in the region between 1550 and 1670  $\text{cm}^{-1}$ , the A-B stretching and the ring D C=C stretching display the most notable differences between P2PG and iRFP. First, the two A-B stretching modes are of nearly equal intensity in P2PG, but the intensity of the high frequency component strongly increases in iRFP along with a frequency upshift from 1651 to 1656  $\text{cm}^{-1}$ . Inspection of the protein variants of route A (Fig. 4) indicates that the single substitution of either Asp202 or Tyr258 (D202T, Y258F) already causes this frequency upshift while the intensity ratio  $I_{\text{II}}/I_{\text{I}}$  ( $=R$ ; Table 1) of the two A-B stretching modes varies only slightly by the individual AA replacements in the CBP. However, the 10 remote substitutions that afford the iRFP variant cause a major intensity redistribution of the two bands. The latter effect appears to be independent of the CBP substitutions since all variants from route B, each involving the 10 remote substitutions, display very high  $I_{\text{II}}/I_{\text{I}}$  intensity ratios of the two A-B stretching modes (Fig. 5). Note that the low-frequency component at 1641  $\text{cm}^{-1}$  in P2PG also shifts up to higher frequencies upon substitutions in the CBP (1646  $\text{cm}^{-1}$  in P2PG-D202T/I203V/Y258F) but the additional remote substitutions revert this shift and keep the band position at 1642  $\text{cm}^{-1}$  (Figs 4 and 5; Table 1).

Also for the ring D C=C stretching, the frequency upshift from P2PG (1625  $\text{cm}^{-1}$ ) to iRFP (1629  $\text{cm}^{-1}$ ) is already complete in P2PG-D202T/I203V/Y258F, but not fully reversed in P2PG-D202T/I203V/Y258F. Further spectral data reflecting mutation-induced structural changes of the chromophore including the C-D methine bridges are provided in the Supporting Information (Supplementary Figs S3 and S4).

## Discussion

Phytochrome variants that display enhanced fluorescence quantum yield include two groups of AA substitutions. The first group refers to positions in the immediate environment of the chromophore (CBP substitutions). These are specifically D202, I203, and Y258 which all have contacts with the BV cofactor or with the surrounding H-bond network. In P2PG, substitutions at these positions account for a  $\Phi_{\text{fl}}$  increase from 0.7 to 2.5%. The further increase to 5.9% is only achieved by including a second group of 10 substitutions remote from the CBP.



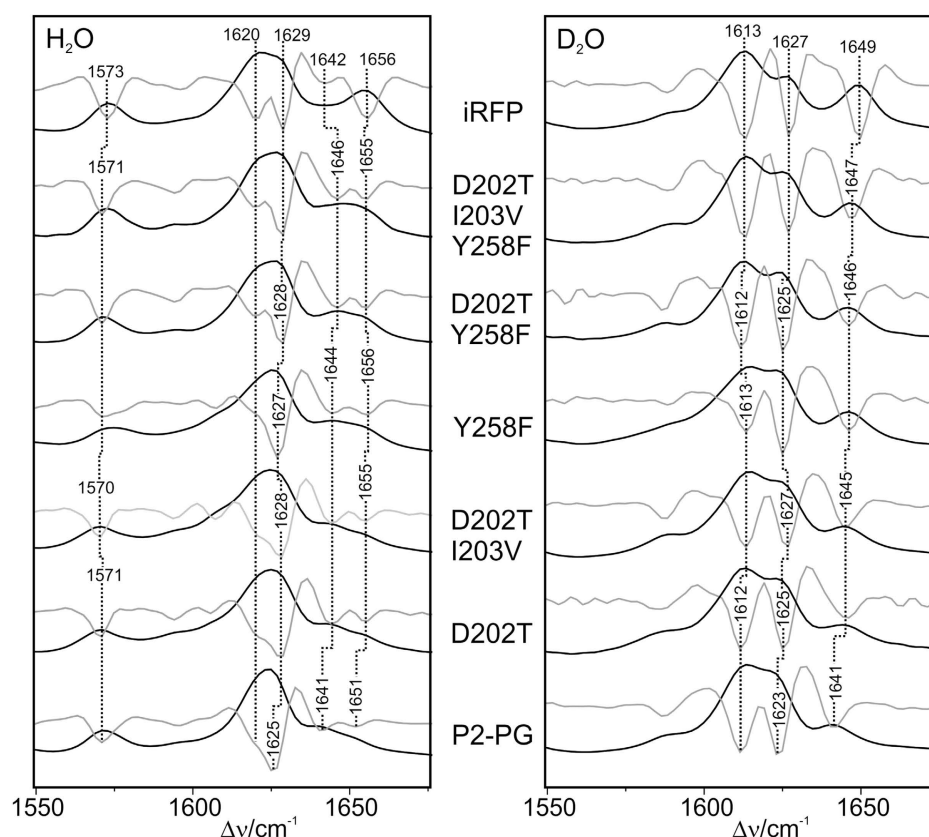


**Figure 4.** RR spectra of the P2PG variants obtained via route A (from bottom to top), compared to the spectra of P2PG WT and iRFP. The spectra, measured from the proteins in H<sub>2</sub>O (left) and D<sub>2</sub>O (right), display the region of the C=C stretching modes. Grey traces represent the second derivatives of the spectra.

The impact of substituting D202 and Y258 on the structure of the chromophore pocket has been recently analysed for the Pr state of the chromophore-binding domain CBD-DR<sup>15</sup> of the *Deinococcus radiodurans* bacteriophytochrome (AA numbering refers to P2PG). Crystal structures revealed a perturbation of the hydrogen bond network in the chromophore pocket, particularly affecting the interactions with the ring A carbonyl. This was suggested to impair excited-state proton transfer that competes with the radiative excited-state decay. As an additional factor responsible for the about 2-fold increased fluorescence in the D202H and Y258F single and D202H/Y258F double mutants, the *E* configuration at the *C-D* methine bridge was proposed to be destabilized, corresponding to a decrease of the photochemical quantum yield. Indeed, the structural changes of the chromophore refer to the *A-B* and *C-D* methine bridges. Specifically, the mutations cause an increase of the dihedral angle C(4)-C(5)-C(6)-N(B) from 6.7° (WT CBD-DR) to 10.4° and 14.0° in the D202H and D202H/Y258F mutants, respectively<sup>15</sup>. The dihedral angle C(14)-C(15)-C(16)-N(D) of the *C-D* methine bridge displays the opposite tendency as it decreases from 35.8° to 0.5° and 12.6° in the D202H and D202H/Y258F mutants, respectively. This geometric change corresponds to a substantial decrease of the tilt angle of ring *D* with respect to ring *C* by ~15°.

In view of the far-reaching structural similarities between CBD-DR and P2PG, one may expect similar mutation-induced structural changes also for P2PG, although in the latter case the ring *D* tilt angle is already rather low in the WT protein<sup>29</sup>. In fact, the vibrational modes localized at the *A-B* methine bridge and in ring *D* respond to substitutions of D202 and Y258. Note that the correlation with the structural changes in the CBD-DR mutants are justified since control experiments with the D202H mutant of P2PG display the same tendency in the RR spectra as threonine substitution at this position studied in this work (Supplementary Fig. S6). The single mutants P2PG-D202T and -Y258F as well as P2PG-D202T/Y258F show essentially the same frequency upshifts of these modes compared to P2PG (Table 1), and the additional I203V substitution in the triple mutant causes only a further 1-cm<sup>-1</sup> shift of the ring *D* mode. These findings may be rationalized in terms of an increased C(4)-C(5)-C(6)-N(B) dihedral angle at the *A-B* methine bridge and a reduced tilt angle of ring *D*. This conclusion is also consistent with the concomitant increase of the frequency of the *C-D* HOOP mode (Supplementary Figs S3 and S4) that has been shown to exhibit a negative correlation with the C(14)-C(15)-C(16)-N(D) dihedral angle<sup>30</sup>, thereby indicating a reduced torsion of the *C-D* methine bridge upon mutations in the CBP, particularly of either D202 or Y258. These chromophore structural changes as revealed by the RR spectra account for an increase of  $\Phi_{\text{fl}}$  from 0.7% (P2PG) to 2.5% (P2PG-D202T/I203V/Y258F) (Supplementary Fig. S7), in line with the

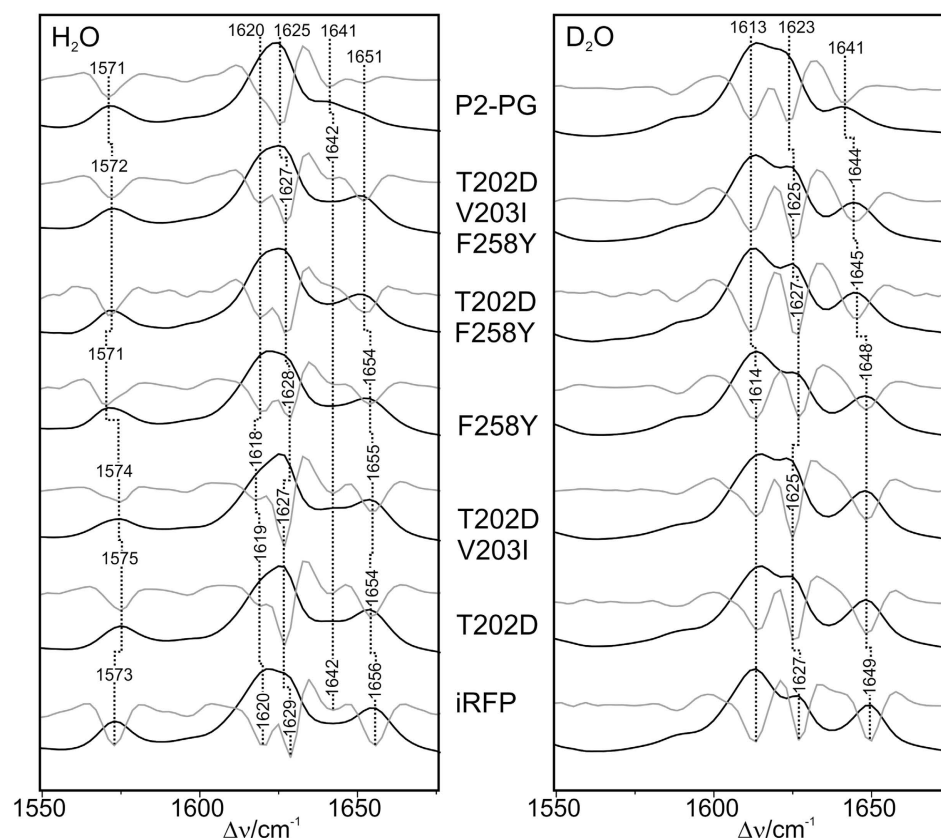


**Figure 5.** RR spectra of the P2PG variants obtained via route B (from bottom to top), compared with the spectra of P2PG WT and iRFP. The spectra, measured from the proteins in H<sub>2</sub>O (left) and D<sub>2</sub>O (right), display the region of the C=C stretching modes. Grey traces represent the second derivatives of the spectra.

previously proposed mechanisms for promoting radiative excited state decay<sup>15,19,21</sup>. A decrease of the tilt angle as indicated by the frequency upshift of the ring *D* and the HOOP mode stabilizes the *Z* vs. the *E* configuration of the *C-D* methine bridge (*vide supra*), consistent with a complete inhibition of photoisomerisation in the P2PG triple mutant which displays the highest ring *D* stretching frequency. This remarkably critical and as yet unrecognized influence of the rather conservative I203V mutation on photoconversion is reflected by the mutants from route B, since introduction of mutation V203I into iRFP-T202D/F258Y marks the transition between constructs that do or do not undergo photoconversion. Also, the concomitantly increased torsion of the *A-B* methine bridge may contribute to the stabilization of *Z* configuration of the chromophore, but – according to the crystallographic analyses<sup>15,16</sup> – it has an additional effect on the H-bond network in the CBP involving the ring *A* carbonyl. However, the latter mode is rather weak in RR and, as far as the technique was applicable, also in the IR difference spectra precluding further analyses of mutation-induced effects (Supplementary Fig. S5).

In addition to the three CBP substitutions, 10 remote replacements account for a further increase of  $\Phi_{fl}$  from 2.5 to 5.9% (Table 1), which is not correlated with frequency shifts of the stretching modes (Supplementary Fig. S7). Instead, we note major intensity redistributions between the two conjugate *A-B* stretching modes such that the high-frequency component (conformer II) clearly dominates in the spectrum of iRFP, corresponding to a distinct decrease of the structural heterogeneity. The mole fractions of the two conformer states I and II ( $x_I$  and  $x_{II}$ ) can be approximated from the ratio  $R = I_{II}/I_I$  of the relative intensities  $I_I$  and  $I_{II}$  of the low- and high-frequency component of the *A-B* stretching mode, yielding  $R/(1 + R)$  for the mole fraction  $x_{II}$  of conformer II, which, e.g., rises from 50% (P2P2-D202T/I203V/Y258F) to 88% in iRFP. We therefore conclude that the remote substitutions primarily affect structural packing of the protein, which strongly favours conformer II.

The simplest explanation of the present results is based on a distribution between two conformers (I, II), which solely differ by their fluorescence quantum yields  $\Phi_I$  and  $\Phi_{II}$ , in analogy to a previous proposal for cyanobacterial phytochromes<sup>31</sup>. Then, the experimentally determined fluorescence quantum yield  $\Phi_{fl}$  is given by

$$\Phi_{fl} = x_I \Phi_I + x_{II} \Phi_{II} \quad (1)$$

Again,  $x_I$  and  $x_{II}$  are the mole fractions of the two conformer states as noted above. Assuming identical Raman cross sections for the conjugate *A-B* stretching modes, eq. (1) can be rewritten to

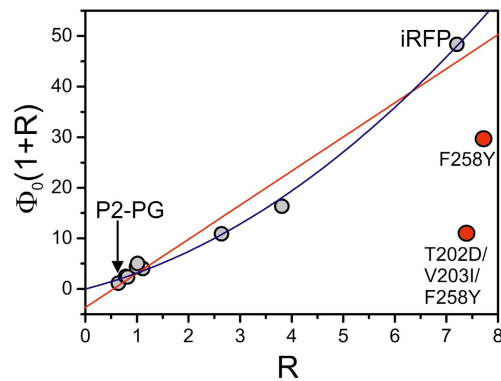


**Figure 6.** Correlation of the experimentally determined fluorescence quantum yield  $\Phi_f$  and the relative population of conformer II according to eq. (2). The red line represents a linear fit of eq. (2) to the experimental data (except for iRFP-F258Y and iRFP-T202D/V203I/F258Y). The blue curve describes a second order polynomial fit to the data to illustrate the deviation from the linear behavior.

$$\Phi_f(1 + R) = \Phi_I + R\Phi_{II} \quad (2)$$

The values for  $R$  were evaluated from the second derivatives in Figs 4 and 5 (left, grey traces; Table 1) to obtain a plot of  $\Phi_f(1 + R)$  vs.  $R$  (Fig. 6).

In fact, except for the iRFP triple mutant and the iRFP-F258Y mutant of route B (red points in Fig. 6), the data are correlated and indicate that  $\Phi_f$  increases with increasing population of conformer II. However, in contrast to the simple expectation from eq. (2), the data follow a parabolic (blue line) rather than a linear function (red line), and a linear fit would afford a physically meaningless negative intercept. These deviations from linear behaviour can be rationalized since eq. (2) assumes that (i) the fluorescence quantum yields of each conformer remain unchanged in the individual protein variants, and (ii) the variations of the experimentally determined  $\Phi_f$  solely depend on the relative populations of the two conformers. However, the increase of  $\Phi_f$  from 0.7% (P2PG) to 2.5% in the P2PG triple mutant (route A) can only partly be attributed to a slightly larger population of the “fluorescent” conformer II (~50% vs. ~40% in P2PG). Instead, the CBP substitutions perturb the chromophore structure, as reflected by the changes of the A-B and ring D stretching modes, and thus affect the fluorescence properties including the fluorescence quantum yields. Additional evidence for this conclusion is derived from the DAS.

Unlike RR spectroscopy, which samples all conformers in the ground state, time-resolved fluorescence spectroscopy monitors radiative processes occurring within the lifetime of the chromophore’s excited state. Accordingly, the DAS spectra predominantly reflect the excited-state processes of the (fluorescent) conformer II, while those of the non-fluorescent conformer I remain largely invisible. Consequently, the substantial excited-state heterogeneity reflected by the DAS of P2PG does not primarily mirror the ground-state heterogeneity of this protein with the comparable populations of the states II (~40%) and I (~60%). Instead, the DAS reveal a variety of possible dissipative decay processes for conformer II. This excited-state heterogeneity is already largely removed by mutation of the two most important residues in the CBP (D202T/Y258F), while the conformer ratio (45%/55%) remains nearly unchanged. Thus, the concomitant increase of  $\Phi_f$  by ~2 is mainly a consequence of the structural changes of conformer II, as discussed above. Following this interpretation, one can readily rationalize that iRFP is endowed with a spectrally homogenous fluorescence emission whereas the triple mutant iRFP-T202D/V203I/F258Y, which has the essential CBP residues of P2PG in place and comprises only the 10 remote mutations, shows a heterogeneous DAS closely resembling P2PG, in line with both having the same CBP residues. The  $\Phi_f$  value of 1.5% for the triple mutant is clearly higher than that of P2PG of (0.7%), which is attributed to the distinctly higher population of the fluorescent conformer II. This can be quantitatively verified by combining eq. (2) for P2PG (superscript “A”) and the triple mutant (superscript “B”) to afford  $\Phi_{II}$  according to

$$\frac{\Phi_f^A(1 + R^A) - \Phi_f^B(1 + R^B)}{R^A - R^B} = \Phi_{II} \quad (3)$$

Thus, one obtains  $\Phi_{II} = 1.7\%$  and, with eq. (2),  $\Phi_I = 0.06\%$ , which confirms the notion of a fluorescent conformer II and a non-fluorescent conformer I.

We now assume that  $\Phi_I \approx 0$  holds for all variants. Even if the CBP substitutions caused an increase of the intrinsic fluorescence quantum yields of both conformers by a similar factor,  $\Phi_I$  would remain distinctly smaller than 1%, such that the contribution of conformer I to the experimentally determined fluorescence quantum yield can be neglected. Then eq. (2) simplifies to

$$\Phi_f \frac{(1 + R)}{R} = \Phi_{II} \quad (4)$$

such that the intrinsic fluorescence quantum yields of conformer II can be evaluated for each mutant (Table 2).

The stepwise substitution of the three CBP residues reveal the expected steady increase of  $\Phi_{II}$  with the strongest increase (from 1.7% to 3.2% or 3.6%, respectively) for the single substitutions of D202 and Y258 (Table 2), in line with the most pronounced changes in the DAS and RR spectra. A further increase (to 4.4%) is noted for the P2PG-D202T/Y258F double mutant, although the contributions by the individual substitutions do not act simply additive. In concert with D202T, the I203V substitution has no effect on  $\Phi_{II}$ , but contributes to the further increase of  $\Phi_{II}$  (to 5%) in the triple mutant P2PG-D202T/I203V/Y258F.

We now compare the variants which only differ by the remote substitutions (Table 2, shaded grey). Except for P2PG and the triple mutant of route B, all other variant pairs reveal an increase of  $\Phi_{II}$  induced by the remote substitutions, particularly pronounced (~34%) for the pair P2PG-D202T/I203V/Y258F and iRFP. These results show that the remote substitutions exert a dual function: a shift of the conformational distribution towards the fluorescent conformer II and a further increase of  $\Phi_{II}$ . The latter effect is not reflected by distinct differences in the respective RR spectra and may be due to a more rigid fixation of conformer II within the protein which is likely to reduce non-radiative excited-state decays<sup>19</sup>. It is interesting to note that the latter effect is not observed for the conjugate pair P2PG and iRFP-T202D/V203I/F258Y. This may be related to the fact that the fluorescence-optimized iRFP was obtained by random mutagenesis starting from the D202H mutant instead of the WT P2PG<sup>11</sup>.

## Conclusions

The present spectroscopic analysis revealed that the chromophore of P2PG-derived variants exists in fluorescent and non-fluorescent conformational states, probably a common feature of the Pr form of prototypical phytochromes<sup>12</sup>. Generating highly fluorescent phytofluors thus requires shifting the conformational distribution towards the fluorescent conformer and optimizing its structure to raise the probability for radiative excited-state decay. This increase of the intrinsic fluorescence quantum yield primarily involves structural changes at the C-D and A-B methine bridges, induced by AA substitutions in the CBP. These structural changes reduce and eventually block photoconversion and might also abolish excited-state proton transfer as a competing decay channel<sup>15,19</sup>. Whereas such structural changes in CBP and their consequences on the excited-state processes may become predictable on the basis of crystallographic, spectroscopic, and theoretical analyses, this will be more difficult for remote substitutions, which in P2PG primarily enrich the population of the fluorescent conformer, but also further increase its intrinsic fluorescence quantum yield, presumably via enhancing the rigidity of the chromophore packing, which lowers the yield for internal conversion. Since the effects particularly of critical remote substitutions are difficult to predict on the atomic level due to the limitations of current computational resources, the complexity of the optimization problem will, for quite some time, need to rely on combinatorial engineering, rather than rational design approaches.

## Materials and Methods

**Site directed mutagenesis, protein expression and purification.** The cDNA templates used in this study were either the plasmid pQE81L containing the cDNA of the RpBphP2 PAS-GAF domains, which was obtained by artificial gene synthesis upon codon optimization for mammalian cells (GeneArt, Regensburg, Germany), or the plasmid pQE81L containing the iRFP cDNA, as described<sup>18</sup>. Mutagenesis was performed using the QuikChange<sup>®</sup> Site-Directed Mutagenesis Kit (Stratagene, La Jolla, USA) according to manufacturer's instructions, which resulted in the following constructs: P2PG-Y258F, P2PG-D202T, P2PG-D202T/Y258F, P2PG-D202T/I203V, P2PG-D202T/I203V/Y258F (for mutational route A, see Fig. 1), and iRFP-T202D, iRFP-F258Y, iRFP-T202D/V203I, iRFP-T202D/F258Y iRFP-T202D/V203I/F258Y (for mutational route B, see Fig. 1). Oligonucleotides were obtained from MWG Eurofins Operon (Ebersberg, Germany) and cDNAs of all constructs were verified by sequencing (MWG Eurofins Operon). The various iRFP and P2PG construct plasmids were co-transformed in NEBturbo cells with the previously described pQE81L-Kan plasmid bearing the gene for the human heme oxygenase type 2 (hHOX2)<sup>18</sup>. The cells were grown overnight at 37 °C on LB-Agar plates containing 100 µg/mL ampicillin and 50 µg/mL kanamycin. The more recently mutated clones (iRFP-T202D/F258Y, P2PG-D202T/I203V, P2PG-D202T/I203V/Y258F) were transformed in DH5 alpha cells with the gene for the hHOX2 stably integrated in the genome using the method described by Kuhlman and Cox<sup>32</sup>. Transformed cells were grown overnight at 37 °C on LB-Agar plates containing 100 µg/mL ampicillin. Details of the protein expression and purification protocol are given elsewhere<sup>18</sup>. According to the SAR values, holoprotein assembly was comparable in the variants of both mutational routes (P2PG and iRFP). Purified proteins were frozen in liquid nitrogen and stored at −80 °C. For spectroscopic measurements, phytochrome samples were prepared in H<sub>2</sub>O or D<sub>2</sub>O (99.95%, Deutero GmbH) Tris buffer (50 mM Tris/Cl, 5 mM EDTA, and 300 mM NaCl). The pH (pD) was adjusted to pH = 7.8 (pD = 7.8) using a 3 M HCl (DCl, 99% in D<sub>2</sub>O, Sigma-Aldrich, Deisenhofen, Germany) pH electrode. Final protein concentrations were ca. 500 µM for RR and IR experiments, but distinctly lower for fluorescence measurements (*vide infra*).

**Vibrational spectroscopy.** RR spectroscopic measurements were carried out as described previously using a Fourier-transform (FT) Raman spectrometer with 1064-nm excitation<sup>18</sup>. All RR spectra shown in this work were measured at −140 °C. Difference IR spectroscopy measurements of photochemically active P2PG and iRFP derivatives were performed at ambient temperature using an IFS28 spectrometer (Bruker) equipped with a liquid nitrogen-cooled MCT detector. Approximately 2–4 µL of protein solution were placed in a 3 µm cavity between two thin CaF<sub>2</sub> windows (d = 20 mm) and sealed with silicone grease. Forward (reverse) conversion from the dark adapted state (photoproduct) was achieved by irradiation with a 660 nm (780 nm) LED array.

**Absorption and static fluorescence spectroscopy.** All measurements were performed at room temperature under protective green light (502 nm). Protein samples were prepared in Tris buffer and measured in disposable cuvettes (10 mm path length). UV/VIS measurements were performed immediately prior to fluorescence measurements with a Cary 1E Varian spectrophotometer (Agilent Technologies). In the case of photochemically active variants, the presence of only the parent Pr state was ensured by LED irradiation at 780 nm. Fluorescence measurements were performed using a Fluoromax 2 spectrometer (Horiba Scientific). Excitation was set to 20 nm blue-shifted from the Q band maximum of the absorption spectra (690–700 nm; see Supplementary Fig. S1). The fluorescence signal was collected, starting from 5 nm above excitation up to 900 nm, and corrected according to the number of absorbed photons (absorbance at the excitation wavelength), using the molar extinction coefficient of iRFP ( $85,000 \text{ M}^{-1} \text{ cm}^{-1}$ )<sup>18</sup> as a reference. Standard solutions of the reference dyes Atto 680 in H<sub>2</sub>O (Attotech) and Nile Blue (Sigma Aldrich) in ethanol ( $\Phi_{\text{fl}} = 0.3/0.27$ ) were used to determine the iRFP quantum yield ( $\Phi_{\text{fl}} = 0.059$ ). Subsequently, iRFP was then used as a reference for determining the fluorescence quantum yields of the other phytochrome variants.

**Time- and wavelength-correlated single photon counting (TWCSPC).** Measurements were performed with the setup as described<sup>33</sup>. Cooling of the measurement cuvette down to 10 K was performed using a metal alloy cuvette holder connected to a home-built variable-temperature cryostat (10–300 K, CTI-Cryogenics 8001/8300) equipped with a thermocouple directly connected to the cooling head for temperature control. In the case of photochemically active variants, in particular P2PG WT, the presence of only the parental Pr state was ensured by continuous LED irradiation at 780 nm during freezing. For TWCSPC, a Hamamatsu R5900 16-channel multi-anode photomultiplier tube (PML-16C, Becker & Hickl, Berlin, Germany) was employed and signals were registered with a SPC-130 (Becker&Hickl) measurement card. A polychromator with a 1200 grooves/mm grating ensured a spectral bandwidth of 6.25 nm per channel. A 632 nm pulsed laser diode (BHL-635, Becker&Hickl, Berlin) was used for excitation. The time- and wavelength-resolved fluorescence spectra were analysed by global fits using three exponentials for all decay curves measured in one spectrum affording common values of lifetimes  $\tau_j$  (linked parameters) for all decay curves and wavelength-dependent pre-exponential factors  $a_j(\lambda)$  (non-linked parameters), thus yielding the decay-associated spectra (DAS) of the individual decay components. The quality of the fit was judged by the value of  $\chi_r^2$  and by the degree of randomness of residuals to check for the absence of any correlation of the deviations in a certain time interval (for further details, see Supporting Information).

## References

- Betzig, E. *et al.* Imaging intracellular fluorescent proteins at nanometer resolution. *Science* **313**, 1642–1645 (2006).
- Giepmans, B. N., Adams, S. R., Ellisman, M. H. & Tsien, R. Y. The fluorescent toolbox for assessing protein location and function. *Science* **312**, 217–224 (2006).
- Hell, S. W. & Wichmann, J. Breaking the diffraction resolution limit by stimulated emission: stimulated-emission-depletion fluorescence microscopy. *Opt. Lett.* **19**, 780–782 (1994).
- Stepanenko, O. V., Shcherbakova, D. M., Kuznetsova, I. M., Turoverov, K. K. & Verkhusha, V. V. Modern fluorescent proteins: from chromophore formation to novel intracellular applications. *Biotechniques* **51**, 313–318 (2011).
- Shcherbakova, D. M., Subach, O. M. & Verkhusha, V. V. Red fluorescent proteins: advanced imaging applications and future design. *Angew. Chem. Int. Ed. Engl.* **51**, 10724–10738 (2012).
- Brakemann, T. *et al.* A reversibly photoswitchable GFP-like protein with fluorescence excitation decoupled from switching. *Nat. Biotechnol.* **29**, 942–947 (2011).
- Hess, S. T., Girirajan, T. P. & Mason, M. D. Ultra-high resolution imaging by fluorescence photoactivation localization microscopy. *Biophys. J.* **91**, 4258–4272 (2006).
- Klar, T. A., Jakobs, S., Dyba, M., Egner, A. & Hell, S. W. Fluorescence microscopy with diffraction resolution barrier broken by stimulated emission. *Proc. Natl. Acad. Sci. USA* **97**, 8206–8210 (2000).
- Rust, M. J., Bates, M. & Zhuang, X. Sub-diffraction-limit imaging by stochastic optical reconstruction microscopy (STORM). *Nat. Methods* **3**, 793–795 (2006).
- Shimomura, O., Johnson, F. H. & Saiga, Y. Extraction, purification and properties of aequorin, a bioluminescent protein from the luminous hydromedusa, *Aequorea*. *J. Cell. Comp. Physiol.* **59**, 223–239 (1962).
- Filonov, G. S. *et al.* Bright and stable near-infrared fluorescent protein for *in vivo* imaging. *Nat. Biotechnol.* **29**, 757–761 (2011).
- Lamparter, T., Michael, N., Mittmann, F. & Esteban, B. Phytochrome from *Agrobacterium tumefaciens* has unusual spectral properties and reveals an N-terminal chromophore attachment site. *Proc. Natl. Acad. Sci. USA* **99**, 11628–11633 (2002).
- Giraud, E. *et al.* A new type of bacteriophytochrome acts in tandem with a classical bacteriophytochrome to control the antennae synthesis in *Rhodospirillum rubrum*. *J. Biol. Chem.* **280**, 32389–32397 (2005).
- Shcherbakova, D. M. & Verkhusha, V. V. Near-infrared fluorescent proteins for multicolor *in vivo* imaging. *Nat. Methods* **10**, 751–754 (2013).
- Auldridge, M. E., Satyshur, K. A., Anstrom, D. M. & Forest, K. T. Structure-guided engineering enhances a phytochrome-based infrared fluorescent protein. *J. Biol. Chem.* **287**, 7000–7009 (2012).
- Lehtivuori, H., Bhattacharya, S., Angenent-Mari, N. M., Satyshur, K. A. & Forest, K. T. Removal of Chromophore-Proximal Polar Atoms Decreases Water Content and Increases Fluorescence in a Near Infrared Phytofluor. *Front. Mol. Biosci.* **2**, 65 (2015).
- Piatkevich, K. D., Subach, F. V. & Verkhusha, V. V. Far-red light photoactivatable near-infrared fluorescent proteins engineered from a bacterial phytochrome. *Nat. Commun.* **4**, 2153 (2013).
- Velazquez Escobar, F. *et al.* Structural parameters controlling the fluorescence properties of phytochromes. *Biochemistry* **53**, 20–29 (2014).
- Bhattacharya, S., Auldridge, M. E., Lehtivuori, H., Ihalaenen, J. A. & Forest, K. T. Origins of fluorescence in evolved bacteriophytochromes. *J. Biol. Chem.* **289**, 32144–32152 (2014).
- Zhu, J., Shcherbakova, D. M., Hontani, Y., Verkhusha, V. V. & Kennis, J. T. Ultrafast excited-state dynamics and fluorescence deactivation of near-infrared fluorescent proteins engineered from bacteriophytochromes. *Sci. Rep.* **5**, 12840 (2015).
- Toh, K. C., Stojkovic, E. A., van Stokkum, I. H., Moffat, K. & Kennis, J. T. Fluorescence quantum yield and photochemistry of bacteriophytochrome constructs. *Phys. Chem. Chem. Phys.* **13**, 11985–11997 (2011).
- von Stetten, D. *et al.* Highly conserved residues Asp-197 and His-250 in Agp1 phytochrome control the proton affinity of the chromophore and Pfr formation. *J. Biol. Chem.* **282**, 2116–2123 (2007).



23. Wagner, J. R. *et al.* Mutational analysis of *Deinococcus radiodurans* bacteriophytochrome reveals key amino acids necessary for the photochromicity and proton exchange cycle of phytochromes. *J. Biol. Chem.* **283**, 12212–12226 (2008).
24. Schmitt, F. J. *Picobiophotonics for the investigation of pigment-pigment and pigment-protein interaction in photosynthetic complexes* Ph.D. thesis, Technical University of Berlin, (2011).
25. Mroginiski, M. A. *et al.* Chromophore structure of cyanobacterial phytochrome Cph1 in the Pr state: reconciling structural and spectroscopic data by QM/MM calculations. *Biophys. J.* **96**, 4153–4163 (2009).
26. Mroginiski, M. A. *et al.* Elucidating photoinduced structural changes in phytochromes by the combined application of resonance Raman spectroscopy and theoretical methods. *J. Mol. Struct.* **993**, 15 (2011).
27. Mroginiski, M. A. *et al.* Determination of the chromophore structures in the photoinduced reaction cycle of phytochrome. *J Am Chem Soc* **126**, 16734–16735 (2004).
28. Kneip, C. *et al.* Protonation state and structural changes of the tetrapyrrole chromophore during the Pr → Pfr phototransformation of phytochrome: a resonance Raman spectroscopic study. *Biochemistry* **38**, 15185–15192 (1999).
29. Bellini, D. & Papiz, M. Z. Dimerization properties of the RpBphP2 chromophore-binding domain crystallized by homologue-directed mutagenesis. *Acta Crystallogr. D Biol. Crystallogr.* **68**, 1058–1066 (2012).
30. Salewski, J. *et al.* Structure of the biliverdin cofactor in the Pfr state of bathy and prototypical phytochromes. *J. Biol. Chem.* **288**, 16800–16814 (2013).
31. Kim, P. W., Rockwell, N. C., Martin, S. S., Lagarias, J. C. & Larsen, D. S. Dynamic inhomogeneity in the photodynamics of cyanobacterial phytochrome Cph1. *Biochemistry* **53**, 2818–2826 (2014).
32. Kuhlman, T. E. & Cox, E. C. Site-specific chromosomal integration of large synthetic constructs. *Nucleic Acids Res.* **38**, e92 (2010).
33. Schmitt, F. J. *et al.* eGFP-pHsens as a highly sensitive fluorophore for cellular pH determination by fluorescence lifetime imaging microscopy (FLIM). *Biochim. Biophys. Acta* **1837**, 1581–1593 (2014).

## Acknowledgements

The authors acknowledge financial support by the DFG via the Sfb1078 (TP B6/P. H.) and the Cluster of Excellence “Unifying concepts in Catalysis”. T.F., F.-J.S. and M.W. gratefully acknowledge support from the Stifterverband für die deutsche Wissenschaft (Study reform project “OPLChem”) and EU support via the COST MP1205 framework.

## Author Contributions

P.H. and T.F. designed the experiments. D.B. performed RR, UV-Vis absorption and static fluorescence measurements and RR data analysis. F.V.E. and A.K. supervised RR measurements. L.S., S.W. and N.H. performed site directed mutagenesis, protein expression and purification under the supervision of N.N.T., M.W. performed time- and wavelength-correlated single photon counting, F.-J.S. and T.F. performed TWCSPEC data analysis. T.U., F.V.E., M.A.M. and P.H. supervised RR data analysis. D.B., F.V.E., T.F. and P.H. wrote the manuscript, and P.H. designed the two-states-model. All the authors discussed the results and commented on the manuscript.

## Additional Information

**Supplementary information** accompanies this paper at <http://www.nature.com/srep>

**Competing financial interests:** The authors declare no competing financial interests.

**How to cite this article:** Buhrke, D. *et al.* The role of local and remote amino acid substitutions for optimizing fluorescence in bacteriophytochromes: A case study on iRFP. *Sci. Rep.* **6**, 28444; doi: 10.1038/srep28444 (2016).



This work is licensed under a Creative Commons Attribution 4.0 International License. The images or other third party material in this article are included in the article's Creative Commons license, unless indicated otherwise in the credit line; if the material is not included under the Creative Commons license, users will need to obtain permission from the license holder to reproduce the material. To view a copy of this license, visit <http://creativecommons.org/licenses/by/4.0/>

## 7.2 Attachment of the Biliverdin Cofactor to two Cysteine Residues

This research was originally published in Scientific Reports:

D. Buhrke, N. Tavraz, D. Shcherbakova, L. Sauthof, M. Moldenhauer, F. Velázquez Escobar, V. Verkhusha, P. Hildebrandt, and T. Friedrich. *Chromophore binding to two cysteines increases quantum yield of near-infrared fluorescent proteins*. In: *Scientific Reports* **9**.Article number: 1866 (2019). DOI: 10.1038/s41598-018-38433-2


- **David Buhrke** performed resonance Raman, UV-Vis absorption, fluorescence and GndHCl denaturation experiments and analyzed spectroscopic data.
- Neslihan N. Tavraz, Marcus Moldenhauer and Luisa Sauthof performed protein expression, purification and SDS-page Gel analysis.
- **David Buhrke**, Peter Hildebrandt, Thomas Friedrich, Vladislav V. Verkhusha and Daria Shcherbakova designed the experiments.
- Peter Hildebrandt, Thomas Friedrich and Francisco Vélazquez Escobar contributed to RR data analysis.
- **David Buhrke**, Peter Hildebrandt, Thomas Friedrich, Vladislav V. Verkhusha and Daria Shcherbakova wrote the manuscript.
- All authors discussed the results and commented on the manuscript.

© This work is licensed under a Creative Commons Attribution 4.0 International License.

# SCIENTIFIC REPORTS

OPEN

## Chromophore binding to two cysteines increases quantum yield of near-infrared fluorescent proteins

David Buhrke<sup>1</sup>, Neslihan N. Tavrız<sup>1</sup>, Daria M. Shcherbakova<sup>2</sup>, Luisa Sauthof<sup>3</sup>, Marcus Moldenhauer<sup>1</sup>, Francisco Vélazquez Escobar<sup>1</sup>, Vladislav V. Verkhusha<sup>2</sup>, Peter Hildebrandt<sup>1</sup> & Thomas Friedrich<sup>1</sup> 

Phytochromes are red/far-red light sensing photoreceptors employing linear tetrapyrroles as chromophores, which are covalently bound to a cysteine (Cys) residue in the chromophore-binding domain (CBD, composed of a PAS and a GAF domain). Recently, near-infrared (NIR) fluorescent proteins (FPs) engineered from bacterial phytochromes binding biliverdin IX $\alpha$  (BV), such as the iRFP series, have become invaluable probes for multicolor fluorescence microscopy and *in vivo* imaging. However, all current NIR FPs suffer from relatively low brightness. Here, by combining biochemical, spectroscopic and resonance Raman (RR) assays, we purified and characterized an iRFP variant that contains a BV chromophore simultaneously bound to two cysteines. This protein with the unusual double-Cys attached BV showed the highest fluorescence quantum yield (FQY) of 16.6% reported for NIR FPs, whereas the initial iRFP appeared to be a mixture of species with a mean FQY of 11.1%. The purified protein was also characterized with 1.3-fold higher extinction coefficient that together with FQY resulted in almost two-fold brighter fluorescence than the original iRFP as isolated. This work shows that the high FQY of iRFPs with two cysteines is a direct consequence of the double attachment. The PAS-Cys, GAF-Cys and double-Cys attachment each entails distinct configurational constraints of the BV adduct, which can be identified by distinct RR spectroscopic features, i.e. the marker band including the C=C stretching coordinate of the ring A-B methine bridge, which was previously identified as being characteristic for rigid chromophore embedment and high FQY. Our findings can be used to rationally engineer iRFP variants with enhanced FQYs.

Phytochromes constitute a class of bimodal photoreceptor proteins, which incorporate linear tetrapyrrole cofactors for red light sensing in plants, fungi, cyanobacteria and non-photosynthetic bacteria<sup>1</sup>. Bacterial phytochromes that incorporate biliverdin IX $\alpha$  (BV) have been extensively used for engineering of fluorescent proteins (FPs)<sup>2–6</sup>. The two advantages of these FPs, their near-infrared (NIR) spectra and the presence of the BV chromophore in mammalian tissue, made them useful probes for non-invasive whole-body imaging and multicolor fluorescence microscopy<sup>7,8</sup>. However, all current NIR FPs suffer from relatively low molecular brightness with the fluorescence quantum yield (FQY) varying from 6–14%. Recent studies found that chromophore attachment in the brightest of engineered NIR FPs differs from the canonical BV binding found in wild-type bacterial phytochromes<sup>9–11</sup>.

In all phytochromes, an open-chain linear tetrapyrrole chromophore is covalently conjugated to a cysteine (Cys) residue in the chromophore-binding domain (CBD) via a thioether bridge in an autocatalytic process termed autolyase activity<sup>12</sup>. Although this fundamental reaction is conserved in all known phytochromes, the chromophore and the attachment site are different in bacterial and plant variants. In the case of bacterial phytochromes (BphPs), biliverdin

<sup>1</sup>Institut für Chemie, Sekr. PC14, Technische Universität Berlin, Straße des 17. Juni 135, 10623, Berlin, Germany.

<sup>2</sup>Department of Anatomy and Structural Biology, Albert Einstein College of Medicine, 1300 Morris Park Avenue, Bronx, NY, 10461, USA. <sup>3</sup>Charité – Universitätsmedizin Berlin, Institute of Medical Physics and Biophysics (CC2), Group Protein X-ray Crystallography and Signal Transduction, Charitéplatz 1, 10117, Berlin, Germany. Correspondence and requests for materials should be addressed to T.F. (email: [friedrich@chem.tu-berlin.de](mailto:friedrich@chem.tu-berlin.de))



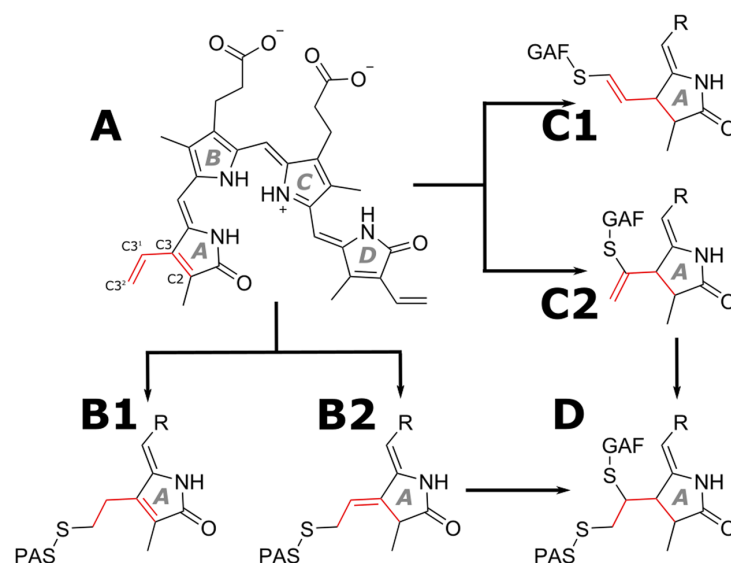


**Figure 1.** Possible modes of chromophore attachment. Free BV (A) can be covalently attached to the conserved PAS-Cys under retention of the endocyclic DB (B1<sup>24</sup>) or exocyclic DB rearrangement (B2<sup>19</sup>), as found in the crystal structures of various BphPs. Attachment to the GAF-Cys results in blue-shifted absorption properties and the remaining DB is not conjugated to the aromatic system, accordingly. Hence, attachment to the GAF domain either results in configuration (C2)<sup>9</sup> like in eukaryotic phytochromes<sup>17</sup> (albeit with a non-conjugated DB) or, possibly also in the configuration (C1), as found in miRFP670<sup>11</sup>. Upon further reaction, only the structures (B2 and C2) can lead to the reported structure of the double-attached species (D), while (B1,C1) represent dead ends in the reaction sequence.

IX $\alpha$  (BV) is attached to a conserved Cys residue upstream of the PAS domain (denoted PAS-Cys in the following)<sup>13</sup>, whereas in cyanobacterial and plant phytochromes the corresponding phycocyanobilin (PCB) or phytochromobilin (P $\Phi$ B) cofactors are linked to a Cys in the GAF domain<sup>14</sup>. Ring A of PCB and P $\Phi$ B contains one exocyclic double bond (DB) at the ethylidene substituent, but no endocyclic DB, and an unambiguous mode of attachment to the GAF-Cys is found in the cyanobacterial phytochromes Cph1<sup>15</sup>, Cph2<sup>16</sup> and in plant phytochrome B<sup>17</sup>. In contrast, ring A of free BV contains an endocyclic DB and a second DB in the vinyl group (Fig. 1, structure A). Consequently, the configuration of the remaining DB in BV after attachment to bacterial phytochromes can vary. In the bacterial phytochrome Agp1<sup>18</sup>, preservation of the endocyclic ring A DB was observed (Fig. 1, structure B1), but investigation of the highly homologous DrBphP revealed an exocyclic DB rearrangement (Fig. 1, structure B2)<sup>19</sup>. Another way of chromophore binding was found in engineered proteins derived from bacterial phytochromes. The first evidence that chromophore binding is possible to the Cys in the GAF domain of BphPs was detected for a Cys exchange mutant of DrBphP that covalently binds PCB via attachment to a GAF-Cys<sup>19</sup>. Later, covalent binding of BV chromophore to the Cys residue in the GAF domain was discovered in blue-shifted near-infrared fluorescent proteins<sup>9</sup>. The resulting chromophore structures are shown in Fig. 1 (structures C1 and C2). In these structures, the DB between the C3<sup>1</sup> and C3<sup>2</sup> atoms is out of conjugation with the rest of the  $\pi$ -electron system, which results in a spectral blue shift in NIR fluorescent proteins containing a Cys in the GAF domain.

Recently, the crystal structure of miRFP670<sup>20</sup>, an engineered version of the CBD fragment of *Rhodospseudomonas palustris* phytochrome P1 (RpBphP1), was determined<sup>11</sup>. This protein contains two Cys residues in spatial proximity to the vinyl group of the BV ring A (Fig. 2A), one located in the PAS and the other in the GAF domain at homologous positions to the conserved Cys for BphPs, and eukaryotic phytochromes, respectively. The crystallographic data for miRFP670 revealed a novel BV binding mode to a BphP. In addition to a single covalent attachment to the GAF-Cys (Fig. 1, structure C1), a novel double attachment to both Cys residues was observed (Fig. 1, structure D). Attachment to a secondary Cys residue also occurs naturally in diverse cyanobacteriochromes, but in these cases, the secondary Cys is also located at different positions in the GAF domain and adds to the A-B or B-C methine bridges<sup>21,22</sup>.

These findings motivated the present study to determine the binding pattern of BV in iRFP682, another iRFP containing two Cys residues, which was derived from the CBD of RpBphP2<sup>4</sup>. The crystal structure of the prototypical phytochrome precursor RpBphP2 is known<sup>23</sup>, and a structural model of the Cys positions in relation to the embedded BV chromophore is shown in Fig. 2A.

## Results and Discussion

**Mutagenesis and protein biochemistry.** Starting from the original construct (denoted iRFP682(CC) in the following) with the Cys residues C15 in the PAS and C249 in the GAF domain (Fig. 2A), we exchanged, first, either of the two cysteines, and second, both cysteines simultaneously for serine, which is non-reactive in chromophore attachment. In this way, the serine exchange variants in the PAS domain (iRFP682(SC)), the GAF

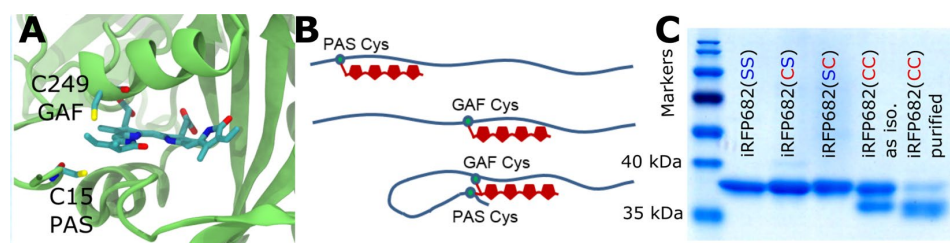


**Figure 2.** Double-Cys chromophore attachment in iRFP682. (A) The positions of the PAS- and GAF-Cys (C15, C249) residues (exchanged for Ser in mutants) relative to the chromophore in the investigated protein constructs. The presented homology model was derived from the iRFP713 homology model<sup>27</sup>. (B) Scheme showing denatured iRFP variant proteins with covalently attached BV. Double attachment results in a covalently linked loop that withstands denaturation and leads to migration of the protein with apparently lower molecular weight. (C) Purification of iRFP682(CC). All protein variants containing only one Cys residue ran as a single band in SDS-PAGE at an apparent molecular mass of 37 kDa. iRFP682(CC) displays a second band characteristic for iRFPs with double-Cys motif<sup>10</sup> at an apparently lower mass, which was assigned to a double attached BV species<sup>11</sup>. This protein species was purified by treatment with GdnHCl and size-exclusion chromatography (Supplementary Fig. S2).

domain (iRFP682(CS)) and the all-serine variant (iRFP682(SS)) were obtained. Except for iRFP682(SS), all protein variants bound BV covalently, as confirmed by  $\text{Zn}^{2+}$  fluorescence (Supplementary Fig. S1) performed in-gel after SDS-PAGE, and a characteristic double-band feature was observed only for iRFP682(CC). Previous observation of this motif for iRFP682<sup>10</sup> was assigned to a compact cross-linked protein species as a result of double Cys attachment. The resulting topological loop in the protein prevents complete denaturation during SDS treatment, and the protein migrates at a lower apparent mass during electrophoresis. These findings were confirmed by biochemical methods and are in line with corresponding crystallographic data for mRFP670, indicating a mixture of a GAF-only and a double attached species<sup>11</sup>.

**Purification of the double attached species.** The two distinct protein species of iRFP682(CC) were not separable by various conventional methods (ion-exchange chromatography, IEC; hydrophobic interaction chromatography, HIC; and size-exclusion chromatography, SEC) due to their identical protein surfaces and, therefore, identical biophysical properties in chromatography experiments. However, iRFP682(CC) showed a spectroscopically heterogeneous denaturation behavior when subjected to high guanidinium hydrochloride (GdnHCl) concentrations. A previous study showed that spectroscopically distinguishable subspecies of iRFP682(CC) denature at different concentrations of GdnHCl. Before the possibility of double-Cys attachment was considered, this behaviour was originally assigned to an allosteric effect caused by dimer-interaction<sup>10</sup>. However, we reasoned that a double-Cys attached and, therefore, cross-linked protein might be more stable under denaturing conditions than the corresponding singly attached variant and could eventually cause this heterogeneity. To confirm that the two species observed in the gel are in fact the reason for the heterogeneous denaturation behaviour, a partially denatured sample (incubation in 2.8 M GdnHCl for 24 h, for detailed protocol on GdnHCl treatment, see Supplementary Fig. S2) was subjected to SEC. After this treatment, a purified sample of a highly enriched double attached species with only minor residual contribution of a singly attached fraction (the densitometric ratio of the gel bands was 4:1) was identified by SDS-PAGE analysis (Fig. 2C, denoted as iRFP682(CC) purified).

**UV/Vis spectroscopy.** iRFP682(CS) displays an absorption pattern in the Q-band (max. 674 nm) and the Soret band region (max. at 383 nm) with the characteristic structure and spectral position of BV-binding BphPs in the Pr state (Fig. 3). Compared to iRFP682(CS), the Q-band maximum in the cysteine-deficient variant iRFP682(SS) is red-shifted (691 nm) towards the absorbance maximum of the free BV, which would also be in line with the increased conjugation length (by one DB) of the free chromophore, and the sample contained considerable amounts of apoprotein, indicated by the high relative intensity in the region of protein absorption (280 nm) due to less effective chromophore assembly without covalent attachment. In contrast, iRFP682(SC) shows a blue-shifted absorption maximum of the Q-band (665 nm). Furthermore, the shape of the Q-band is altered in iRFP682(SC) and iRFP682(CC) as isolated, and a shoulder at 690 nm emerges. After GdnHCl purification, the shoulder is no longer detected, and iRFP682(CC) displays a homogeneous absorption pattern like P<sub>680</sub> bound to a GAF domain Cys in plant phytochromes (see e.g.<sup>17</sup>). However, in case of iRFP682(CC) the BV chromophore is linked to two Cys residues that should result in a more rigid chromophore embedment.

**Fluorescence spectroscopy.** In line with the absorption properties, the fluorescence emission maxima of iRFP682(SS) and (CS) variants are red-shifted (max. 706 and 696 nm), and the intensities are low compared to the other variants. In contrast, iRFP682(SC) and iRFP682(CC) as isolated and purified show the characteristic high-intensity fluorescence peak (max. 682 nm), albeit with different amplitudes. Notably, after the purification procedure, the relative fluorescence intensity of iRFP682(CC) is strongly increased. By integration of the fluorescence signals and extrapolation from the known FQYs of the other variants (CS: 3.2%, SS: 2.2%, CS: 5.0%, CC (as isolated): 11.1%<sup>10</sup>), we estimated an FQY of 16.6% for the purified iRFP682(CC) with double-Cys attachment of the chromophore (Table 1, and Fig. S3). This is the highest FQY reported for the NIR FPs engineered from

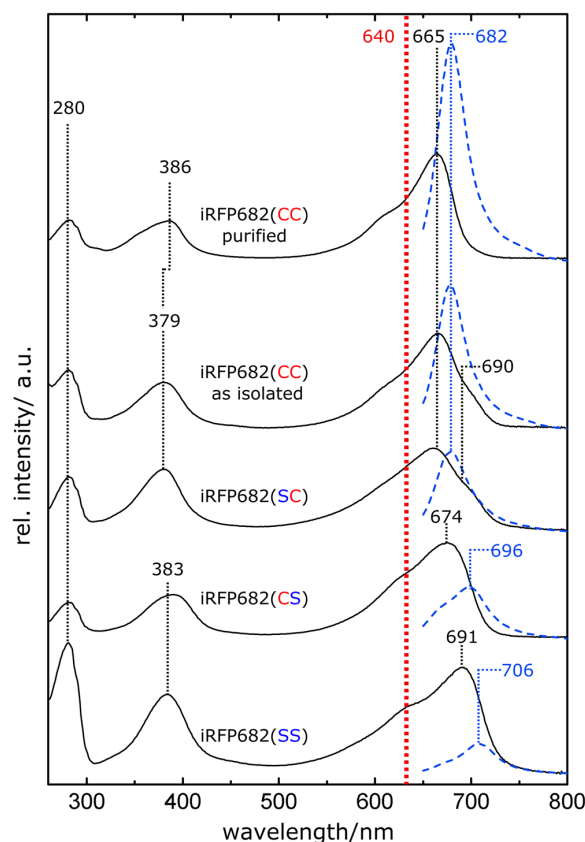


**Figure 3.** Absorption (black lines) and fluorescence (blue dotted lines) spectra of iRFP682 variants and the purified double attached species. The absorption spectra were normalized at 640 nm (red dotted line), which corresponds the fluorescence excitation chosen for all protein samples. Relative fluorescence intensities were normalized according to the number of absorbed photons at 640 nm.

iRFP variant	Absorbance max (nm)	Emission max (nm)	Extinction coefficient at absorbance max <sup>a</sup> (M <sup>-1</sup> ·cm <sup>-1</sup> )	Fluorescence quantum yield (%)	Molecular brightness vs iRFP682(CC) as isolated <sup>d</sup> (%)
iRFP682(SS)	691	706	54400	(2.2) <sup>b</sup>	13
iRFP682(CS)	674	696	87400	(3.2) <sup>b</sup>	30
iRFP682(SC)	665	682	57400	(5.0) <sup>b</sup>	31
iRFP682(CC) as isolated	665	682	84400	(11.1) <sup>b</sup>	100
iRFP682(CC) purified	665	682	112200	16.6 <sup>c</sup>	199

**Table 1.** Properties of the studied iRFP682 protein species. <sup>a</sup>Molecular extinction coefficients were calculated from the ratio of the Soret and Q-band intensity according previous studies<sup>2</sup>. <sup>b</sup>Parameters in parentheses refer to the original publication<sup>10</sup>. <sup>c</sup>The fluorescence quantum yield (FQY) of purified iRFP682(CC) was calculated according to Supplementary Fig. S3. <sup>d</sup>Molecular brightness is the product of extinction coefficient and FQY.

BphPs so far<sup>8</sup>. This variant also has 1.3-fold increased extinction coefficient. Together, this resulted in almost two-fold increase in molecular brightness.

**Resonance Raman spectroscopy.** We restrict the discussion to the spectral region comprising the resonance Raman (RR) bands, which are characteristic of specific structural properties of the chromophore (Fig. 4, for full spectral range, see Supplementary Fig. S4). The protonation state of BV is indicated by the band at 1572/1575 cm<sup>-1</sup>. This band originates from the in-phase in-plane bending of the ring B and C N-H groups and, upon H/D exchange, shifts to the spectral region around 1070 cm<sup>-1</sup>. The band is observed in all variants, indicating that none of the amino acid substitutions affects the normal and fully protonated state of the cofactor. The other bands in this region are assigned to modes mainly including the C=C stretching coordinates of

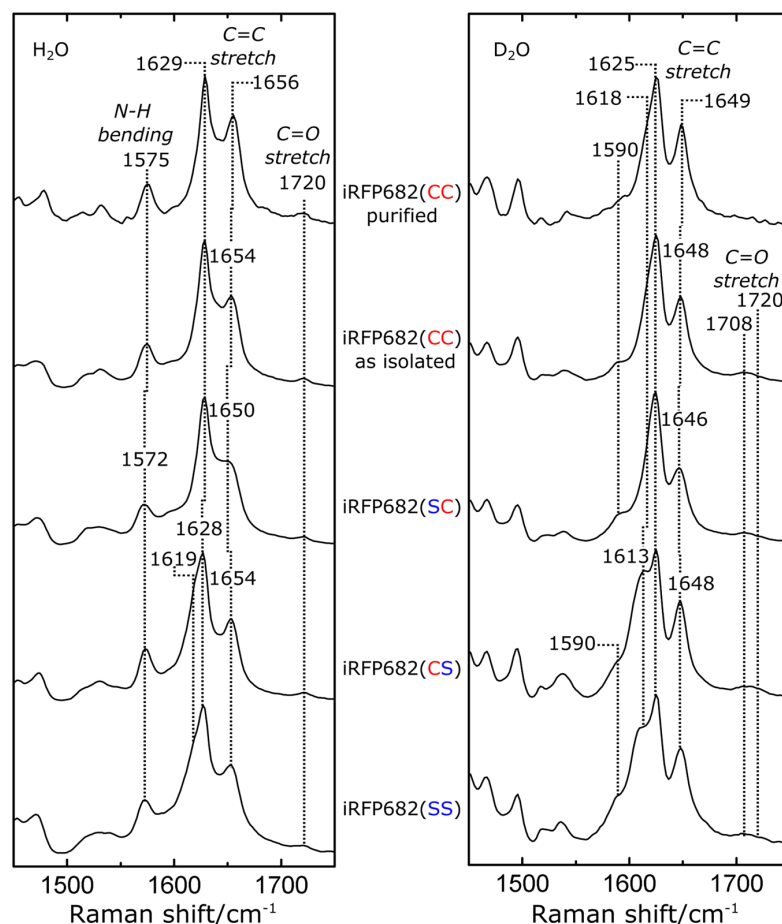


**Figure 4.** Resonance Raman (RR) spectra of the investigated iRFP constructs in the marker region from 1450 to 1750  $\text{cm}^{-1}$ . Left panel: spectra recorded in  $\text{H}_2\text{O}$  buffer, right panel:  $\text{D}_2\text{O}$  buffer. The characteristic modes corresponding to the C=C and C=O stretching modes as well as the (ring B,C) N-H in-plane bending mode are labeled. Band assignment was performed according to previous studies<sup>25,26</sup>. For full spectra, see Supplementary Fig. S4.

the methine bridges, as well as the C=O stretching of rings A and D (1720  $\text{cm}^{-1}$ ). The weak H/D sensitivity of these modes results from the admixture of N-H in-plane bending coordinates of the adjacent pyrrole rings. The corresponding mode of the A-B methine bridge (A-B stretching) remains unchanged by the substitutions and is observed in the spectral region between 1650  $\text{cm}^{-1}$  and 1656  $\text{cm}^{-1}$  and downshifts to the region between 1646  $\text{cm}^{-1}$  and 1649  $\text{cm}^{-1}$  in  $\text{D}_2\text{O}$  buffer. A similar position and H/D effect was observed for the near-infrared fluorescent RbBphP2-derived iRFP713 protein studied previously<sup>24</sup>. The latter study reported that the A-B stretching mode at a frequency above 1650  $\text{cm}^{-1}$  is indicative of a strongly fluorescent conformer, in contrast to the weakly fluorescent species with an A-B stretching mode between 1640 and 1645  $\text{cm}^{-1}$ . The purified iRFP682(CC) shows the most upshifted mode at 1656  $\text{cm}^{-1}$ , indicating that the fluorescence is enhanced by a conformational change at the A-B methine bridge. This should result from the strongest stabilization of the ring A attached to two Cys.

In the spectral region between 1615  $\text{cm}^{-1}$  and 1630  $\text{cm}^{-1}$ , two closely spaced modes are observed, involving the C=C stretching coordinates of the C-D methine bridge (C-D stretching) and of ring D in the low- and high-frequency component, respectively. The lower frequency mode at 1619  $\text{cm}^{-1}$  in iRFP682(CS) also includes small admixtures (about 7%,<sup>25</sup>) of the N-H in-plane bending coordinates of rings C and D. Consequently, removal of these latter contributions upon H/D exchange causes a considerable downshift of this mode (C-D stretching) by 6  $\text{cm}^{-1}$ , in contrast to the nearly invariant high-frequency mode (ring D C=C stretching) such that the frequency separation between both modes increases. Unlike the ring D C=C stretching, the frequency of the C-D stretching mode displays considerable variations among the various species studied here. The lowest frequency at 1619  $\text{cm}^{-1}$  is observed for iRFP682(CS) and (SS), whereas for all GAF-Cys containing variants, this mode is upshifted by nearly 10  $\text{cm}^{-1}$  such that it coincides with the ring D C=C stretching. Therefore, for these iRFP variants, both modes are only separated in the spectra of the samples in  $\text{D}_2\text{O}$ .

The proposed binding pattern for the double attachment (Fig. 1, structure D) lacks the endo- and exocyclic double bonds<sup>11</sup>. Since the stretching mode of the exocyclic DB, predicted to be above  $1650\text{ cm}^{-1}$ , is Raman-inactive<sup>26</sup>, the RR spectrum for the double-Cys attachment is expected to be very similar to that of the GAF-Cys-bound chromophore. In fact, the main peak in the C-D stretching region of iRFP682(CC) is observed at the same position as for the iRFP682(SC) variants at  $1629\text{ cm}^{-1}$ . However, no separated ring D C=C stretching peak is observed in iRFP682(CC) before or after purification, thus, single PAS-Cys attachment can be excluded for the double cysteine variant. This interpretation is supported by the UV/Vis spectra, because there is no indication of a 674-nm absorbance peak in the spectrum of the purified iRFP682(CC). The iRFP682(CC) “as isolated” spectrum comprises, in fact, a spectral superposition of iRFP682(SC) and the purified CC variant. The RR and the fluorescence spectra of iRFP682 “as isolated” can be reproduced as the sum of 45% double- and 55% GAF-only attached species (Supplementary Fig. S5).

## Conclusions

In this study, we report the purification and characterization of a bacteriophytochrome-derived fluorescent protein species containing an unusual double-Cys-attached chromophore for the first time. To isolate this variant, we applied a new purification protocol that takes advantage of the higher stability of the double-attached species against denaturants. Though this study was performed on the near-infrared fluorescent protein iRFP682 derived from RpBphP2<sup>4</sup>, our findings are applicable to other near-infrared fluorescent proteins that contain two chromophore-binding Cys residues in the PAS and the GAF domains, as the double-Cys-attached chromophores were detected in several proteins engineered from different BphPs<sup>10,11</sup>. UV/Vis absorption and fluorescence spectra or RR spectroscopic signatures, which are characteristic for distinct chromophore configurations, are identified. Importantly, the purified double-Cys-attached species is characterized by a FQY of 16.6%, the highest FQY reported for BphP-derived NIR FPs so far. Thus, together with the also increased extinction coefficient, the purified protein containing BV bound to two Cys simultaneously showed two-fold increased molecular brightness than the sample before purification (Table 1).

To improve brightness of future engineered iRFPs, the ratio of single- to double-Cys attachment needs to be shifted towards higher yield of double-attached chromophore. Assuming that the chemical reactions leading to covalent chromophore attachment are irreversible, this is a kinetic problem of two competing reaction pathways leading from free BV to either species C1 or D (Fig. 1). In iRFP682, the reaction kinetics of the two pathways are similar, resulting in an about 50:50 ratio of C1 and D. To increase the amount of species D, either the reaction  $A \rightarrow D$  in Fig. 1 needs to be accelerated or  $A \rightarrow C1$  slowed down. These changes in reactivity could be accomplished by changing the electrostatic environment of the attachment site by further amino acid substitutions. Additionally, highly fluorescent chromophore states are characterized by a high RR signature band in the region around  $1650\text{ cm}^{-1}$ , which is characteristic for the ring A-B methine bridge C=C stretching coordinate and indicates rigid chromophore embedment, as concluded earlier<sup>24</sup>. This rigidity is most likely responsible for the exceptionally high FQY of BphP-derived NIR FPs containing two Cys residues. Analysis of the described spectroscopic features and denaturation behavior combined with rational mutagenesis of amino acids surrounding the two chromophore-binding Cys residues in the PAS and in the GAF domains should facilitate engineering of brighter NIR FPs.

## Materials and Methods

**Site directed mutagenesis, protein expression and purification.** The cDNAs of the various iRFP constructs were subcloned into the pBAD plasmid vector (arabinose-inducible) and transformed into LMG194 *E. coli* cells (Thermo Fisher Scientific, Waltham, MA) that already harbored a plasmid carrying the cDNA of a heme oxygenase under the control of a rhamnose-inducible promoter, as described<sup>10</sup>. Site-directed mutagenesis was performed using the QuikChange II Site-directed mutagenesis kit (Agilent, Santa Clara, CA) according to manufacturer's instructions. Oligonucleotides for mutagenesis were purchased from Eurofins MWG Operon (Ebersberg, Germany). All cDNAs were confirmed by sequencing (Eurofins MWG Operon). Protein expression in LMG194 *E. coli* cells and metal chelate affinity purification of the proteins was performed according to previously published procedures<sup>10,24,27</sup>. Analytical size-exclusion chromatography (SEC) used a Superdex 200 Increase 10/300 column (GE Healthcare Europe, Freiburg, Germany) according to manufacturer's procedures.

**In-gel  $\text{Zn}^{2+}$  fluorescence.** Protein samples were loaded at a concentration of 0.3 mg/ml (determined from the absorption at 280 nm calculated by ProtParam, <https://web.expasy.org/protparam/>) on a SDS gel and separated by electrophoresis prior to  $\text{Zn}^{2+}$  fluorescence. In-gel staining of biliverdin IX $\alpha$  bound to iRFP constructs was carried out as described<sup>28</sup>. The different fluorescence intensities of the samples treated with  $\text{Zn}^{2+}$  (Supplementary Fig. S1) are due to apoprotein contribution and incomplete chromophore assembly<sup>10</sup>. Densitometric analysis of protein bands in gel images was carried out with ImageJ.

**Spectroscopy.** All measurements were performed under protective green light (502 nm). UV/VIS measurements were performed with a Cary E4 spectrophotometer (Agilent, Santa Clara, CA). Fluorescence measurements were performed using a Fluoromax 2 spectrometer (Horiba, Kyoto, Japan). Determination of the fluorescence quantum yield (FQY) was performed as described in the Supplementary Fig. S3. The excitation wavelength was set to 640 nm and the fluorescence signal was collected between 650 nm and 800 nm, and corrected according to the number of absorbed photons (absorbance at 640 nm). RR spectroscopic measurements were carried as described previously using a Fourier-transform (FT) Raman spectrometer with 1064-nm excitation<sup>27</sup>. All RR spectra shown in this work were measured at  $-140^\circ\text{C}$ , all UV/Vis and fluorescence spectra at room temperature ( $20^\circ\text{C}$ ).



## References

1. Rockwell, N. C., Su, Y. S. & Lagarias, J. C. Phytochrome structure and signaling mechanisms. *Annu Rev Plant Biol* **57**, 837–858, <https://doi.org/10.1146/annurev.arplant.56.032604.144208> (2006).
2. Shu, X. *et al.* Mammalian expression of infrared fluorescent proteins engineered from a bacterial phytochrome. *Science* **324**, 804–807, <https://doi.org/10.1126/science.1168683> (2009).
3. Filonov, G. S. *et al.* Bright and stable near-infrared fluorescent protein for *in vivo* imaging. *Nat Biotechnol* **29**, 757–761, <https://doi.org/10.1038/nbt.1918> (2011).
4. Shcherbakova, D. M. & Verkhusha, V. V. Near-infrared fluorescent proteins for multicolor *in vivo* imaging. *Nat Methods* **10**, 751–754, <https://doi.org/10.1038/nmeth.2521> (2013).
5. Auldridge, M. E., Satyshur, K. A., Anstrom, D. M. & Forest, K. T. Structure-guided engineering enhances a phytochrome-based infrared fluorescent protein. *J Biol Chem* **287**, 7000–7009, <https://doi.org/10.1074/jbc.M111.295121> (2012).
6. Fischer, A. J. & Lagarias, J. C. Harnessing phytochrome's glowing potential. *Proc Natl Acad Sci USA* **101**, 17334–17339, <https://doi.org/10.1073/pnas.0407645101> (2004).
7. Shcherbakova, D. M., Baloban, M. & Verkhusha, V. V. Near-infrared fluorescent proteins engineered from bacterial phytochromes. *Curr Opin Chem Biol* **27**, 52–63, <https://doi.org/10.1016/j.cbpa.2015.06.005> (2015).
8. Chernov, K. G., Redchuk, T. A., Omelina, E. S. & Verkhusha, V. V. Near-Infrared Fluorescent Proteins, Biosensors, and Optogenetic Tools Engineered from Phytochromes. *Chem Rev* **117**, 6423–6446, <https://doi.org/10.1021/acs.chemrev.6b00700> (2017).
9. Shcherbakova, D. M. *et al.* Molecular Basis of Spectral Diversity in Near-Infrared Phytochrome-Based Fluorescent Proteins. *Chem Biol* **22**, 1540–1551, <https://doi.org/10.1016/j.chembiol.2015.10.007> (2015).
10. Stepanenko, O. V. *et al.* Allosteric effects of chromophore interaction with dimeric nearinfrared fluorescent proteins engineered from bacterial phytochromes. *Sci Rep* **6**, 18750, <https://doi.org/10.1038/srep18750> (2016).
11. Baloban, M. *et al.* Designing brighter near-infrared fluorescent proteins: insights from structural and biochemical studies. *Chem Sci* **8**, 4546–4557, <https://doi.org/10.1039/c7sc00855d> (2017).
12. Wagner, J. R., Brunzelle, J. S., Forest, K. T. & Vierstra, R. D. A light-sensing knot revealed by the structure of the chromophore-binding domain of phytochrome. *Nature* **438**, 325–331, <https://doi.org/10.1038/nature04118> (2005).
13. Lamparter, T., Michael, N., Mittmann, F. & Esteban, B. Phytochrome from *Agrobacterium tumefaciens* has unusual spectral properties and reveals an N-terminal chromophore attachment site. *Proc Natl Acad Sci USA* **99**, 11628–11633, <https://doi.org/10.1073/pnas.152263999> (2002).
14. Lagarias, J. C. & Rapoport, H. Chromopeptides from Phytochrome - the Structure and Linkage of the Pr Form of the Phytochrome Chromophore. *J Am Chem Soc* **102**, 4821–4828, <https://doi.org/10.1021/ja00534a042> (1980).
15. Essen, L. O., Mailliet, J. & Hughes, J. The structure of a complete phytochrome sensory module in the Pr ground state. *Proc Natl Acad Sci USA* **105**, 14709–14714, <https://doi.org/10.1073/pnas.0806477105> (2008).
16. Anders, K., Daminelli-Widany, G., Mroginiski, M. A., von Stetten, D. & Essen, L. O. Structure of the cyanobacterial phytochrome 2 photosensor implies a tryptophan switch for phytochrome signaling. *J Biol Chem* **288**, 35714–35725, <https://doi.org/10.1074/jbc.M113.510461> (2013).
17. Burgie, E. S., Russell, A. N., Walker, J. M., Dubiel, K. & Vierstra, R. D. Crystal structure of the photosensing module from a red/far-red light-absorbing plant phytochrome. *Proc Natl Acad Sci USA* **111**, 10179–10184, <https://doi.org/10.1073/pnas.1403096111> (2014).
18. Nagano, S. *et al.* The Crystal Structures of the N-terminal Photosensory Core Module of *Agrobacterium* Phytochrome Agp1 as Parallel and Anti-parallel Dimers. *J Biol Chem* **291**, 20674–20691, <https://doi.org/10.1074/jbc.M116.739136> (2016).
19. Wagner, J. R., Zhang, J., Brunzelle, J. S., Vierstra, R. D. & Forest, K. T. High resolution structure of *Deinococcus* bacteriophytochrome yields new insights into phytochrome architecture and evolution. *J Biol Chem* **282**, 12298–12309, <https://doi.org/10.1074/jbc.M611824200> (2007).
20. Shcherbakova, D. M. *et al.* Bright monomeric near-infrared fluorescent proteins as tags and biosensors for multiscale imaging. *Nat Commun* **7**, 12405, <https://doi.org/10.1038/ncomms12405> (2016).
21. Rockwell, N. C., Martin, S. S., Feoktistova, K. & Lagarias, J. C. Diverse two-cysteine photocycles in phytochromes and cyanobacteriophytochromes. *Proc Natl Acad Sci USA* **108**, 11854–11859, <https://doi.org/10.1073/pnas.1107844108> (2011).
22. Ulijasz, A. T. *et al.* Cyanochromes are blue/green light photoreversible photoreceptors defined by a stable double cysteine linkage to a phycoviolobin-type chromophore. *J Biol Chem* **284**, 29757–29772, <https://doi.org/10.1074/jbc.M109.038513> (2009).
23. Yang, X. *et al.* Light Signaling Mechanism of Two Tandem Bacteriophytochromes. *Structure* **23**, 1179–1189, <https://doi.org/10.1016/j.str.2015.04.022> (2015).
24. Buhke, D. *et al.* The role of local and remote amino acid substitutions for optimizing fluorescence in bacteriophytochromes: A case study on iRFP. *Scientific Reports* **6**, 28444, <https://doi.org/10.1038/srep28444> (2016).
25. Mroginiski, M. A. *et al.* Chromophore structure of cyanobacterial phytochrome Cph1 in the Pr state: reconciling structural and spectroscopic data by QM/MM calculations. *Biophys. J.* **96**, 4153–4163, <https://doi.org/10.1016/j.bpj.2009.02.029> (2009).
26. Mroginiski, M. A. *et al.* Elucidating photoinduced structural changes in phytochromes by the combined application of resonance Raman spectroscopy and theoretical methods. *J. Mol. Struct.* **993**, 15–25, <https://doi.org/10.1016/j.molstruc.2011.02.038> (2011).
27. Velazquez Escobar, F. *et al.* Structural parameters controlling the fluorescence properties of phytochromes. *Biochemistry* **53**, 20–29, <https://doi.org/10.1021/bi401287u> (2014).
28. Raps, S. Differentiation between Phycobiliprotein and Colorless Linker Polypeptides by Fluorescence in the Presence of ZnSO<sub>4</sub>. *Plant Physiol* **92**, 358–362 (1990).

## Acknowledgements

The authors thank Mario Willoweit for the help with molecular cloning and Tillmann Utesch for the development of the structure homology model. This work was supported by the German Federal Ministry for Education and Research (BMBF WTZ-RUS grant 01DJ15007 to T.F.), the German Research Foundation (Cluster of Excellence “Unifying Concepts in Catalysis” to P.H. and T.F., and the CRC1078/B6 to P.H.), and the US National Institutes of Health (GM122567 and NS103573 grants to V.V.V.). The authors acknowledge support by the German Research Foundation and the Open Access Publication Funds of Technical University of Berlin for covering publication costs.

## Author Contributions

D.B., P.H., T.F., V.V. and D.S. designed the experiments. D.B. performed resonance Raman, UV-Vis absorption, fluorescence and GndCl denaturation experiments and analyzed spectroscopic data. N.N.T., M.M. and L.S. performed protein expression, purification and protein biochemistry. P.H., T.F. and F.V.E. supervised resonance Raman measurements and analysis. D.B., P.H., T.F., V.V. and D.S. wrote the manuscript, all authors discussed the results and commented on the manuscript.

### Additional Information

**Supplementary information** accompanies this paper at <https://doi.org/10.1038/s41598-018-38433-2>.

**Competing Interests:** The authors declare no competing interests.

**Publisher's note:** Springer Nature remains neutral with regard to jurisdictional claims in published maps and institutional affiliations.



**Open Access** This article is licensed under a Creative Commons Attribution 4.0 International License, which permits use, sharing, adaptation, distribution and reproduction in any medium or format, as long as you give appropriate credit to the original author(s) and the source, provide a link to the Creative Commons license, and indicate if changes were made. The images or other third party material in this article are included in the article's Creative Commons license, unless indicated otherwise in a credit line to the material. If material is not included in the article's Creative Commons license and your intended use is not permitted by statutory regulation or exceeds the permitted use, you will need to obtain permission directly from the copyright holder. To view a copy of this license, visit <http://creativecommons.org/licenses/by/4.0/>.

© The Author(s) 2019

## 8 Conclusions

Within the scope of this thesis, phytochromes from plants, cyanobacteria, bacteria, and bioengineered phytochrome derivatives (iRFPs) were investigated with UV/Vis absorption, fluorescence emission, time-resolved and static pre-resonance Raman and IR difference spectroscopy. In some cases, this combined spectroscopic approach was complemented by biochemical and theoretical studies conducted by co-workers or co-operation partners from other research institutions. All presented studies aimed to contribute to an expansion of the basic knowledge about phytochromes and iRFPs on a molecular level. The important conclusions and implications that were derived based on the experimental results are highlighted in the following.

### **The conformational equilibrium in the Pfr state of plant phytochromes**

The Pfr state in plant phytochromes comprises a conformational equilibrium of two sub-states, Pfr-I and Pfr-II, that differ with respect to their conformation at the C/D methine bridge and are distinguishable by RR spectroscopy.[183] The population ratio of Pfr-I and Pfr-II depends on multiple factors such as the chemical structure of the bilin chromophore (PΦB or PCB), but also the plant species: PhyB from the dicotyledon *Arabidopsis thaliana* and the monocotyledon *Sorghum bicolor* differ with respect to the Pfr-I/II ratio. Indirect factors also contribute to the population of the sub-states: the Pfr equilibrium is changed in NTE-deletion mutants of both SbPhyB and AtPhyB, while the chromophore structure in the Pr state is not affected by the truncation. Hence, there must be some type of interaction between the NTE and the chromophore in the Pfr state, which changes the Pfr-I/Pfr-II equilibrium. Additionally, NTE truncation accelerates the Pfr-to-Pr dark reversion.[26] This opposing effect can be rationalized when different thermal reversion rates for Pfr-I and Pfr-II are considered. The interaction of SbPhyB with PIF3 has also an impact on the ratio between Pfr-I and Pfr-II in samples that were assembled with PCB. But in contrast to NTE-deletion, the effect is reversed: while NTE deletion shifts the equilibrium in favor of Pfr-I, interaction with PIF3 facilitates Pfr-II. Furthermore, the addition of PIF3 to SbPhyB samples decelerates the dark-reversion reaction.[62] This underpins the hypothesis that the dark-reversion depends on the ratio of Pfr-I to Pfr-II and it can be concluded that Pfr-I relaxes faster in darkness to Pr than Pfr-II.

Interestingly, a molecular interaction of PIF3 with the PCB chromophore of SbPhyB was also observed in the Pr state by RR experiments, which seems to contradict the MST results, because here no binding was observed in the Pr state. The different results obtained by the two techniques are probably due to the differences in sample concentration in the RR and MST experiments. The experimental validation or disproof of this working hypothesis is a desirable goal for the future. Biophysical investigations of the interactions of phytochromes with other PIF isoforms also pose an interesting objective in order to find common motifs or differences.

**Characterization of SbPhyB PG** PAS-GAF-PHY or PAS-GAF phytochrome variants are widely used in biochemical, spectroscopic and crystallographic studies because these truncated protein constructs can be concentrated to higher optical densities and protein crystals diffract with higher intensity and up to higher resolutions. However, the use of shortened constructs as models for the FL protein bears the risk to misinterpret experimental results and thus draw wrong or artificial mechanistic conclusions. A comparative RR and IR spectroscopic characterization of SbPhyB PG and PGP was



---

applied to assess the similarities and differences that arise from the domain truncation and crystallization procedure. The RR spectra of the Pr state in the PGP and PG constructs in solution and the PG crystal are nearly identical, suggesting that there are no crystallization or truncation artifacts that impact the chromophore binding pocket in the PG crystal.

The PG photoproduct exhibits a broad Q-band of low intensity in the UV/Vis spectrum, indicating substantial differences to Pfr. RR spectroscopy in solution implies that PCB adopts a geometric configuration similar to the Meta-Rc state of the PGP variant, but the chromophore is protonated at all four pyrrole rings like in Pfr. RR spectroscopy also showed that it is possible to generate the protonated Meta photoproduct *in crystallo* by illumination of the PG crystals. Thus, x-ray crystallography of illuminated SbPhyB PG crystals might yield a structure that can be used as a model for the Meta-Rc state in plant phytochromes. These results can also be compared with PGP crystals, once they are available.

**Temperature effects in Slr-GAF3** The dark-adapted state of the PCB-binding CBCR Slr-GAF3 comprises the typical features of a canonical Pr state, but photoactivation yields a meta-stable green absorbing (Pg) photoproduct. In contrast to DXCF CBCRs, the hypsochromic shift in Slr-GAF3 is not due to the addition of a secondary Cys residue that disrupts the conjugated  $\pi$ -electron-system. The initial photochemical reaction is a Z/E isomerization like in canonical phytochromes, and thus the unusual green absorption properties must originate from distinct molecular interactions of PCB with its molecular environment. UV/Vis and RR spectroscopic data of Slr-GAF3 and the homologous AnPixJg2 were compared and analyzed based on four different models that were proposed for the Pg state.[169] The most likely explanation for the hypsochromic shift is a twisted configuration of the pyrrole rings A and D in combination with a hydrated chromophore binding pocket. In the future, a theoretical modeling on the QM/MM of this state is desirable to facilitate the interpretation of the RR and IR spectra. This approach would become feasible on the basis of a Pg X-ray crystal structure.

Unlike AnPixJg2, Slr-GAF3 does not preserve its UV/Vis and RR spectroscopic properties upon decreasing temperature. Instead, the Pr state converts to an orange-absorbing (Po) state and Pg displays a red shifted absorption spectrum (Pg<sub>2</sub>) when subjected to cryogenic temperatures. The mechanism of these conversions was discussed, and a thermal reaction is the most likely candidate. To understand the exact nature of the Po state and the thermodynamic properties of its formation, further experimental work is necessary. A series of temperature-dependent UV/Vis or Raman measurements allows the exact determination of the reaction enthalpy and entropy with a van, t Hoff plot. Furthermore, the activation energy of the transition can be determined when the kinetics of thermal relaxation to Pr after light-activation are monitored at different temperatures.

**Development of a time-resolved pre-resonance Raman set-up** Ultrafast (FSRS) Raman studies have contributed substantially to the understanding of the initial photoreaction in phytochromes.[35] However, this technique cannot access longer time scales and is therefore not suitable for the investigation of the later photocycle intermediates, such as the Meta states. A novel time-resolved set-up was developed that combines a flow cell system with a commercial FT-Raman spectrometer. The set-up includes continuous-wave pump and probe lasers, pre-resonant NIR excitation

and photochemical back-conversion of the sample in a reservoir to ensure fresh sample conditions for each experiment. The Meta state decay of the canonical Bph Agp1 and the bathy Bph Agp2 in the ms time regime were investigated. The spectroscopic results imply that the photocycle reactions in both systems do not represent linear processes but instead include branching reactions from Meta-Rc and Meta-F back to the initial states (Pr or Pfr, respectively). Thus, only a fraction of the light-activated photoreceptors in an ensemble converts to the signaling state, while another fraction converts back to the dark-adapted state *via* the shunt reaction pathway. This threshold mechanism is consistent with the biological function of phytochromes as sensors for durable changes of light conditions. Interesting objectives for future research include the modeling of time-resolved UV/Vis and IR data with a model that includes the possibility of thermal shunt reactions. It is also desirable to investigate whether this reaction only applies to the investigated PGP constructs, or also to full length proteins and other phytochrome variants.

**Characterization of phytochrome activated cyclase IsPadC** Bioengineered and natural phytochrome chimera constructs with variable catalytic output modules can be used for optogenetic applications, such as second-messenger regulation.[182] One variant, the phytochrome-activated di-guanylyl cyclase IsPadC, was recently crystallized and UV/Vis spectroscopic experiments implied a Pfr/Meta-Rc mixture in the light-activated heterodimer.[60, 61] To test this hypothesis, a complementary approach of RR and IR difference spectroscopy was used to access the state of the BV chromophore and the protein after the phototransformation. While the Pr state of the IsPadC is very similar to the canonical Bph Agp1, the FL photoproduct displays a higher similarity to the IsPadC and Agp1 PG constructs, which can be used as models for the Meta state. The heterodimer hypothesis is also underpinned by the IR results, which show a reduced intensity of the characteristic amide I difference signal. This band is commonly associated with the secondary structure change of the tongue motif and thus the transition from Meta-R to Pfr.

**Fluorescence quantum yield of IRFPs** The Pr state of RpBphP2 PG and derived variants comprises a mixture of fluorescent (conformer I) and non-fluorescent (conformer II) sub-states. Generating variants with high FQY that can be used for fluorescence microscopy thus requires the shift of the conformational distribution towards conformer II and optimizing its structure to raise the probability for radiative excited state decay. The two conformers I and II differ in the dihedral angles at the C,D and A,B methine bridges which can be monitored by RR spectroscopy by the frequency of the corresponding C=C stretching vibrations. The structural differences of conformer I reduce and eventually block photoconversion and might also abolish a proton transfer reaction which is a competing excited-state decay channel. In the fluorescence optimized variants iRFP713 and iRFP682, amino acid substitutions shift the conformational equilibrium towards conformer I and thus enhance the fluorescence quantum yield. Hereby, randomly introduced substitution of amino acids in the chromophore binding pocket and at remote positions in the protein backbone act together in a non-additive way, thus a rational design of fluorescence enhanced iRFPs is aggravated.

---

**Chromophore attachment in iRFPs** Some iRFP variants with very high FQY include an artificial secondary Cys residue in the GAF domain. One variant, miRFP682, was successfully crystallized and a novel double-attachment motif was described where the A ring vinyl group of BV is covalently bound to both, the canonical and the second Cys.[9] This motif represents ca 50 % of the protein ensemble and in the other 50 %, BV is attached to the GAF-Cys. These two fractions are readily detected in the SDS page Gel analysis because the double attachment leads to an internal crosslinking and thus this fraction of proteins unfold less and move through the gel with a lower apparent mass.[9] This enhanced durability against denaturation agents was used for the development of a novel purification protocol. The 50/50 mixture that is obtained when the double-Cys variant is assembled with BV *in vitro* was subjected 24 h to high concentrations (2.8 M) of GdNHCl. After a subsequent SEC run, SDS page gel analysis revealed the prevalence of the double-attached species while most of the GAF-only-attached fraction was removed. The proteins before and after the purification procedure were analyzed by UV/Vis, fluorescence and RR spectroscopy and compared to different Cys/Ser exchange mutant proteins. The purified double-attached species has the highest FQY (16.6 %) that was ever reported for an iRFP. RR spectroscopy revealed that the gain in fluorescence is accompanied by a high frequency of the A,B C=C stretching mode which is a marker band of conformer I (*vide supra*). The double attachment of BV stabilizes conformer I and thus enhances the FQY *via* the mechanism that was described for iRFP713.[23] These findings bear major consequences for the development of rational design strategies for highly fluorescent iRFPs: the 16.6 % represent a desirable benchmark value which can be reached by an improvement of the autolyase reaction selectivity towards the double-attached product.

## Acknowledgements

Diese Arbeit wäre ohne die Hilfe und Unterstützung vieler Menschen nicht möglich gewesen. Mein besonderer Dank gilt folgenden Personen:

- Prof. Dr. Peter Hildebrandt und Prof. Dr. Thomas Friedrich für die sorgfältige Betreuung und Begutachtung meiner Arbeit sowie die exzellente Zusammenarbeit während der letzten Jahre.
- Prof. Dr. Franz Bartl für die Begutachtung meiner Arbeit.
- Den Kollegen und Kooperationspartnern Norbert Michael, Marcus Moldenhauer, Dr. Neslihan Tavraz, Svea Wilkening, Luisa Sauthof, Geoffrey Gourinchas, Dr. Soshichiro Nagano, Dr. Silke von Horsten und Christine Kupschus für die Bereitstellung diverser farbiger Proteinlösungen.
- Der BIG-NSE, dem Sfb 1078 und der DAAD für die großzügige Finanzierung.
- Meinen Kollegen im Phytochrombereich, die ein hervorragendes Team bilden: Dr. Francisco Velázquez Escobar, Anastasia Kraskov, Prof. Dr. Maria-Andrea Mroginski, Dr. Tilmann Utesch, Giovanni Battocchio, Maria Fernandez Lopez, Prof. Dr. Jon Hughes, Prof. Dr. Lars-Oliver Essen, Dr. Patrick Scheerer, Dr. Patrick Piwowarski, Andrea Schmidt, Dr. Michal Szczepek, Anh Duc Nguyen und Zaneta Nogacz.
- Prof. Dr. Vladislav V. Verkhusha and Dr. Daria Shcherbakova for helpful discussions on iRPFs.
- Dr. Eugene Maksimov and Dr. Nikolai Sluchanko for the very fruitful collaboration on carotenoid-binding proteins.
- Dr. Franz-Josef Schmitt, Dr. Uwe Kuhlmann, Dr. Eberhard Schlodder, Dr. Ingo Zebger, Jürgen Krauss, Lars Paasche, Marina Böttcher und Claudia Schulz für den ausgezeichneten technischen Support im MVL.
- My BIG-NSE friends Ernie, Arita, Chengyue, and Min Ha for mental support.
- My friends from UW Madison: Katy, Kevin and Jeff for helping me through a hard time during my PhD.
- Prof. Dr. Fritz Siebert, meinem Mentor für die IR-Spektroskopie.
- My friends and (ex-)co-workers from the MVL: Sagie, Jacek, Alex, Christian, Patrycja, Enrico, Cathi, An, Jana, Johannes, Marius, Christine, Khoa, Murat, Stefan, Konstantin... nicht zu vergessen: danke, Anke!
- Meinen Eltern Conny und Thorsten, Oma Inge und Opa Karl und meinen Geschwistern Elisabeth und Benjamin. David ist jetzt auch fertig mit "Doktorarbeit machen".
- Meinen Lieblingsmusikern: Franz, Terry, Paul, Max, Fabi und allen Bandkellerkindern: ohne euch und die Musik hätte das nur halb so viel Spaß gemacht. Dazu gehört natürlich Kim - danke für die Musik, aber vor allem für die Liebe und Unterstützung in allen Lebenslagen und für einfach alles!

---

## 9 Supplementary Data

### 9.1 Supplements: Plant Phytochromes

## **Supporting Information**

### **Structural communication between the chromophore binding pocket and the N-terminal extension in plant phytochrome phyB**

**Francisco Velázquez Escobar<sup>1\*</sup>, David Buhrke<sup>1</sup>, Maria Fernandez Lopez<sup>1</sup>, Sintayehu Manaye  
Shenkutie<sup>2</sup>, Silke von Horsten<sup>3</sup>, Lars-Oliver Essen<sup>3,4</sup>, Jon Hughes<sup>2</sup>, and Peter Hildebrandt<sup>1</sup>**

1 Technische Universität Berlin, Institut für Chemie, Sekr. PC14, Straße des 17. Juni 135, D-10623  
Berlin, Germany

2 Plant Physiology, Justus-Liebig University Gießen, Senckenbergstr. 3, D-35390 Giessen, Germany

3 Philipps-Universität Marburg, Fachbereich Chemie, Strukturbiochemie, Hans-Meerwein-Strasse 4,  
D-35032 Marburg, Germany.

4 LOEWE Center for Synthetic Microbiology, Philipps-Universität, D 35032 Marburg, Germany

#### **Content:**

**Fig. S1. Absorption spectra of *Sb*-phyB**

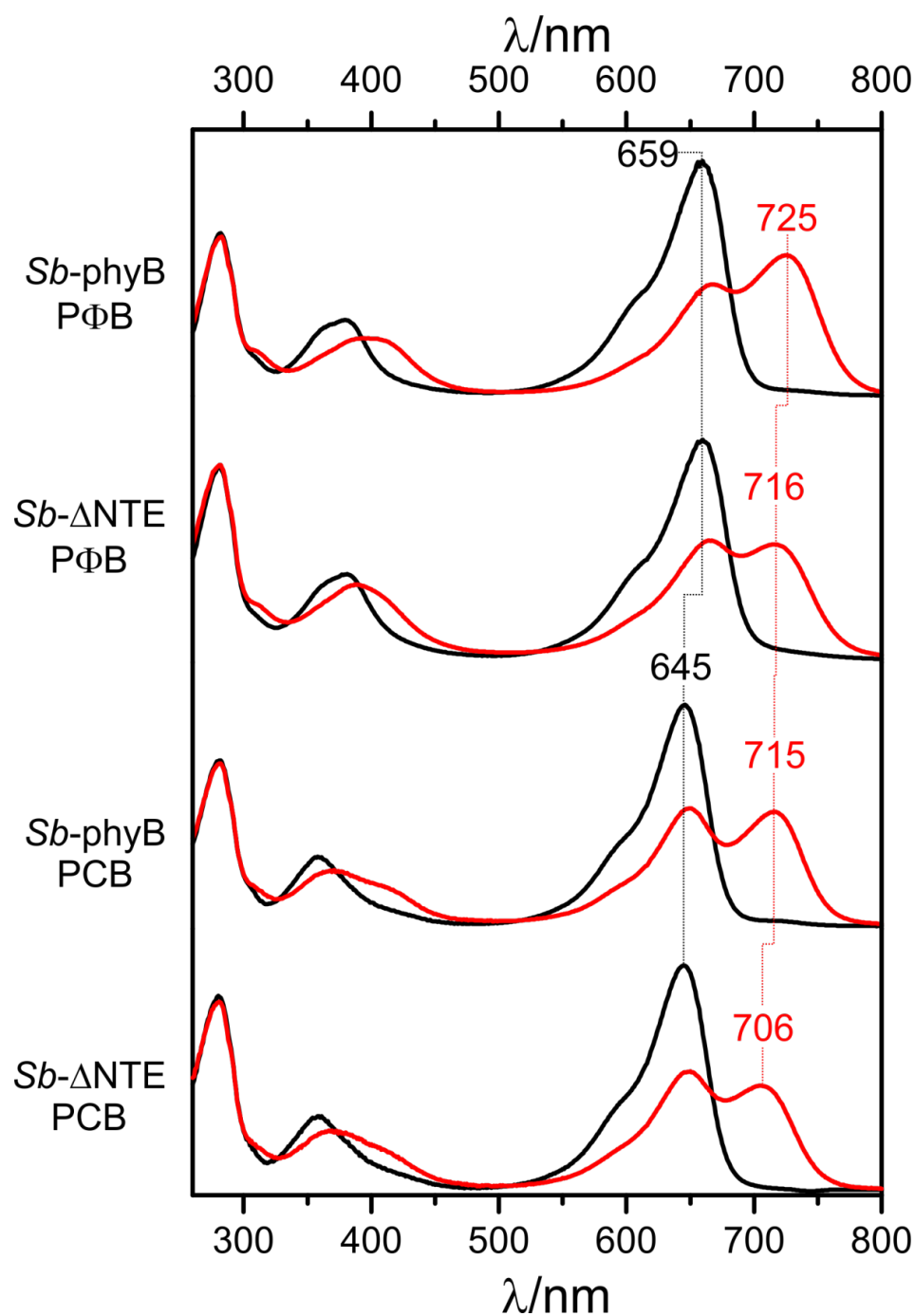


**Fig. S1. Absorption spectra of *Sb-phyB* and *Sb- $\Delta$ NTE* assembled with *P $\Phi$ B* and *PCB*.**

The black and red traces refer to the spectra obtained after irradiation with far-red and red light, respectively. The corresponding absorption spectra of *At-phyB* and *At- $\Delta$ NTE* are reported in ref. 8 (Supporting Information).

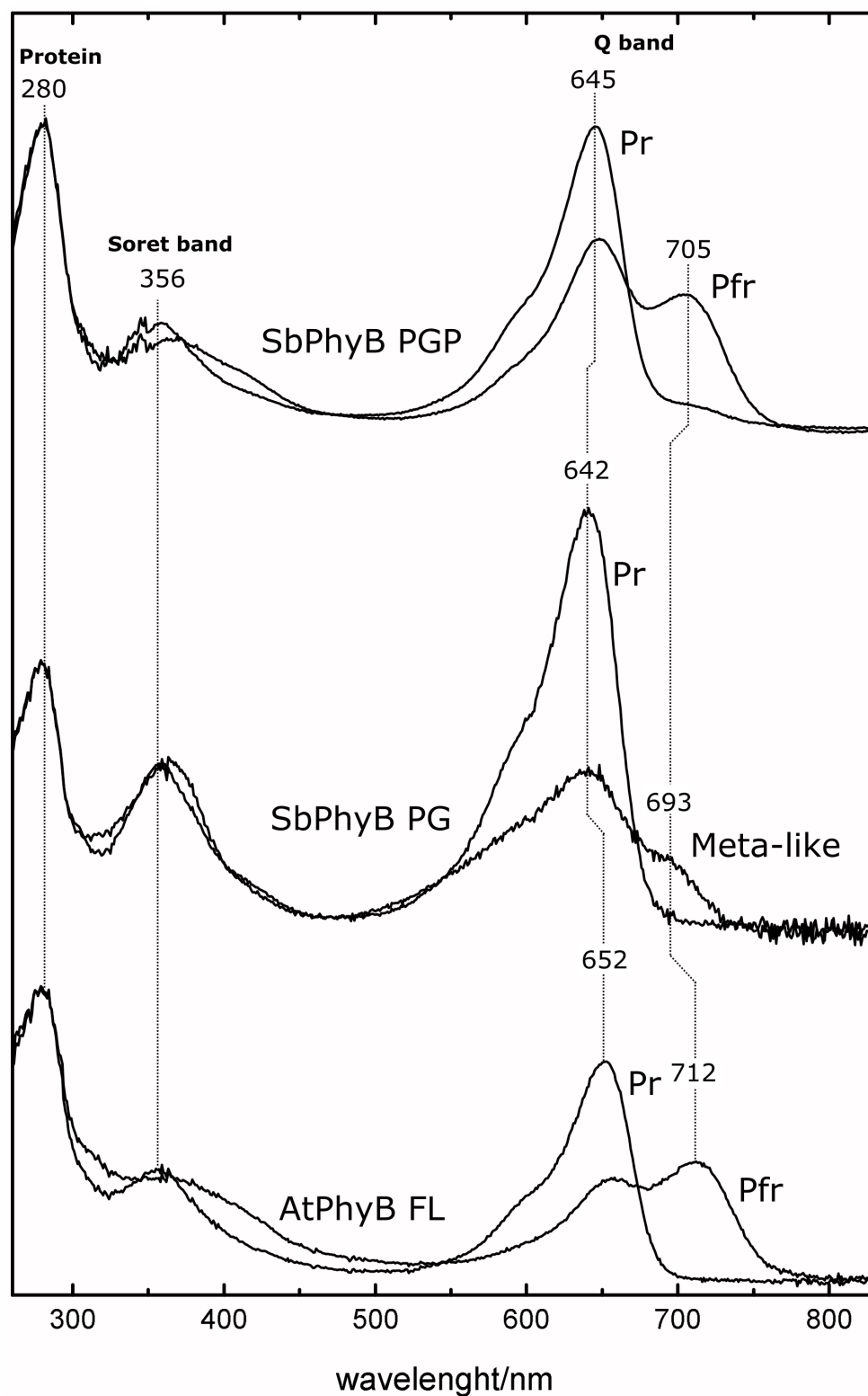


**Figure 9.1.1:** From bottom to top: Unsubtracted UV/Vis spectra of AtPhyB FL, SbPhyB PG and SbPhyB PGP in their dark (Pr) and photo-activated states (Pfr in the case of FL and Meta for the SbPhyB PG construct).



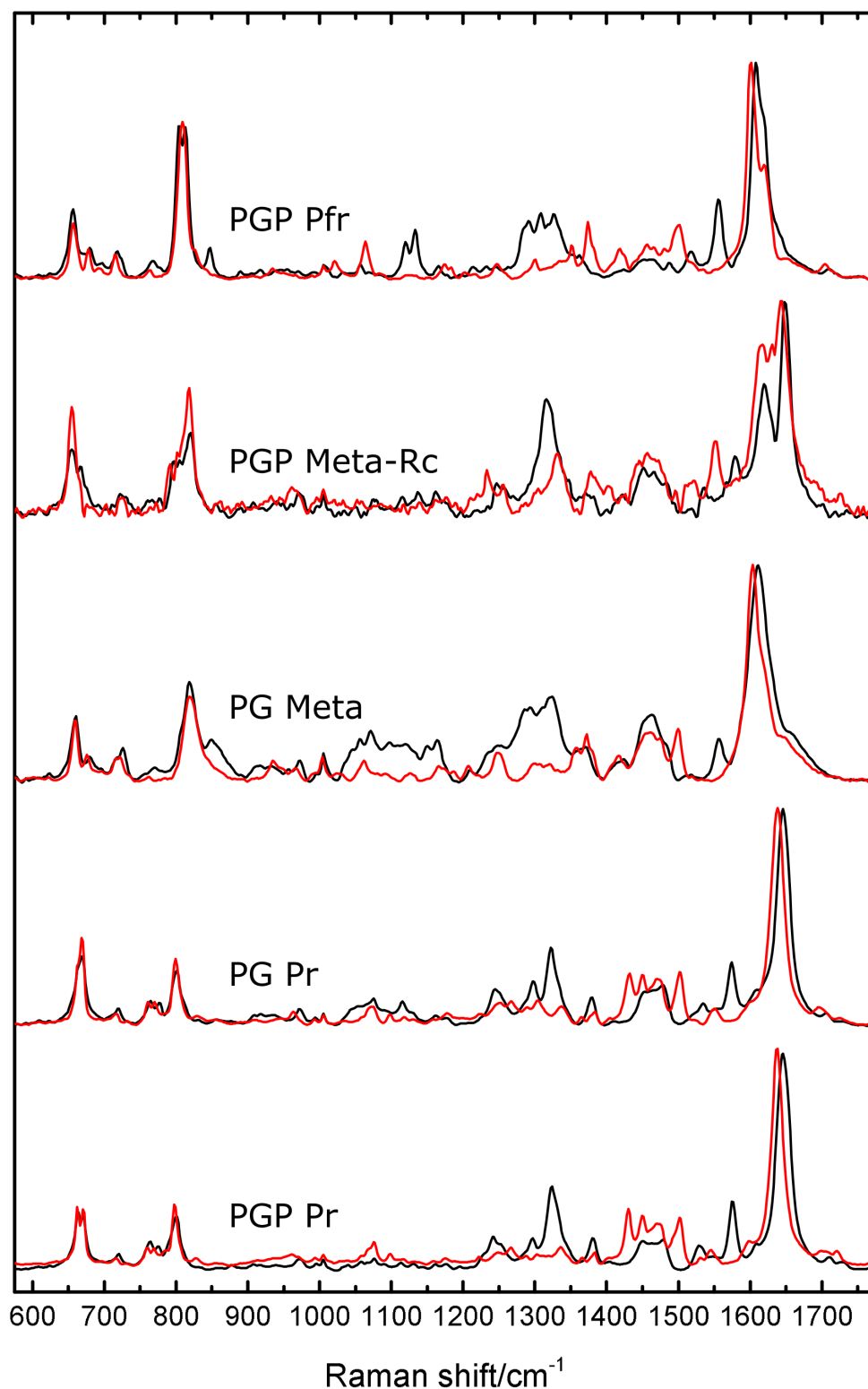


**Figure 9.1.2:** Full range RR spectra of SbPhyB. From bottom to top: the Pr states of the PGP and PG constructs, followed by the room-temperature photoproduct of PG (Meta). This photoproduct can be compared to the cryo-trapped Meta-Rc intermediate and the Pfr spectrum of the PGP variant. Spectra were recorded in H<sub>2</sub>O and D<sub>2</sub>O buffer.

## 9.2 Supplements: Cyanobacterial Phytochromes

**Protein expression and purification** The cDNA constructs used in this study comprised a plasmid harboring the cDNA for Slr-GAF3 (pJOE5751 Rhamnose promotor, Ampicillin resistance), and another one carrying the cDNAs of human heme oxygenase type 2 (hHox2) and the PCB:ferredoxin oxidoreductase PcyA from *Anabaena* sp. PCC7120 (both subcloned into the two MCS regions of the pRSFDuet plasmid, which carries a T7 promotor and kanamycin resistance). Slr-GAF3 cDNA was synthesized by artificial gene synthesis (GeneArt, Regensburg, Germany) based on the PDB amino acid sequence (amino acids 417 to 577 of GenBank entry BAM50929.1, plus N-terminal 6xHis tag) with codon usage optimized for expression in human cell lines (cDNA sequence available on request). Both plasmids were co-transformed in Rosetta(DE3) pLysS cells (Chloramphenicol resistance). Cell cultures were grown in TB medium, harvested and resuspended in PBS buffer. The cells were lysed in three cycles of freeze/thaw in dry ice and hot water. After removal of the cell debris by centrifugation (20000g, 4 °C), the clarified supernatant was purified on a Talon Co<sup>2+</sup> affinity column (GE Healthcare) and eluted with buffer containing 1x PBS, 300 mM NaCl and 300 mM imidazole. Purest fractions were pooled and concentrated (3 kDa Macrosep protein filter). In a last step, the concentrated protein solution was desalted (Sephadex column) and eluted with 1x PBS buffer.

**Interaction with imidazole** The spectral changes upon imidazole addition are pronounced in the Po state, comprising a downshift of the marker band by 23 cm<sup>-1</sup> accompanied by a vanishing of the B,C N-H in plane bending mode at 1585 cm<sup>-1</sup> (fig. 9.2.5), implying a deprotonation of PCB upon interaction with the base. In the Pg' state, only a small shift of the marker band (- 3 cm<sup>-1</sup>), changes in band width and relative intensities are observed (data not shown). To further characterize the interaction of PCB with imidazole, a RR titration experiment was performed. First, the amount of GAF3 in the highly concentrated solution for the RR experiment was calculated using the specific absorption properties of the protein at 280 nm. The Expasy prot-parameter tool calculates a specific absorption  $Abs_{280nm}$  (1 g/l)=1.6 and a molecular weight of M=22100 g/mol from the sequence of Slr-GAF3.[54] The UV/Vis absorption spectrum at 100x dilution was measured (Cary E4 Spectrometer, Varian). A value of  $Abs_{280nm}$ =0.4 was obtained, corresponding to a concentration of 0.4 mg/ml in the diluted, and of 40 mg/ml in the undiluted (RR) sample, respectively. This yields a molar concentration for Slr-GAF3 of  $c_{molar} = c/M = 1.8 \mu mol/ml$ . 3  $\mu L$  of the sample solution were diluted 1:1 in Tris-Cl Buffer (pH=7.8), and used for the RR experiment, corresponding to 5.4 nmol of Slr-GAF3. The concentration of imidazole in the standard solution was adjusted to 4 nmol/ $\mu L$ , (elution buffer/Tris-Cl buffer 1:75) and then added to the Slr-GAF3 sample in 1  $\mu L$  steps. This leads to a dilution of the sample, and for comparability the resulting spectra were normalized to the phenylalanine ring-breathing mode at 1004 cm<sup>-1</sup>. Since this mode originates from the protein backbone possible changes of the PCB scattering cross-section upon imidazole interaction are taken into account by the normalization procedure.

The interaction with imidazole is specific for Slr-GAF3 and could neither be observed in AnPixJg2, nor in the canonical phytochrome Agp1 PGP (fig. 9.2.2). The effect is also reversible with the buffer exchange method described in the materials and methods (see chapter 3.3). Since imidazole is a base and red/green CBCRs were described

to be protochromic[73], the UV/Vis and RR spectra of Slr-GAF3 as well as the imidazole effect were investigated for potential pH-dependence. UV/Vis and RR spectra in the Pr and Pg state with and without imidazole addition were recorded in TrisCl buffer at pH values of 6 and 9. The RR spectra of Agp1 PGP and AnpJg2 in Tris Cl Buffer (pH=7.8) were measured according to the standard conditions described in the materials and methods (see chapter 3.3). Agp1 and AnpJ do not show any imidazole dependence at 10-fold imidazole excess in the parent states (see fig. 9.2.2).

**PH-dependence** The imidazole effect was tested in Po and Pg' in Tris-Cl buffer at pH=6 and pH=9 (see fig. 9.2.3). Without imidazole, the Pr spectrum remains unchanged at pH=6 (compared to pH=7.8), Pg shows neglectable differences (marker band  $-2\text{ cm}^{-1}$ ). The interaction pattern with imidazole is the same in both parent states as at pH=7.8. A change to pH=6 has no effect on the sample. Without imidazole, no pH effect in Pr or Pg are observed at pH=9, the protein and chromophore environment are in a stable configuration in a range from pH=6 to pH=9. With imidazole, large deviations over the whole spectral range are observed in the Pr as well as in the Pg state. At pH=9, the imidazole interaction is altered. imidazole has a  $\text{pK}_a=7$  for the first protonation and Tris buffer is adjusted to a pH=7.8, so at pH=7.8 as well as at pH=9, histidine and imidazole are single protonated, in contrast to pH=6, where significantly more double protonated His/imidazole should be present. These contradictions point to a distinct molecular interaction of PCB with imidazole, instead of a general pH-effect.

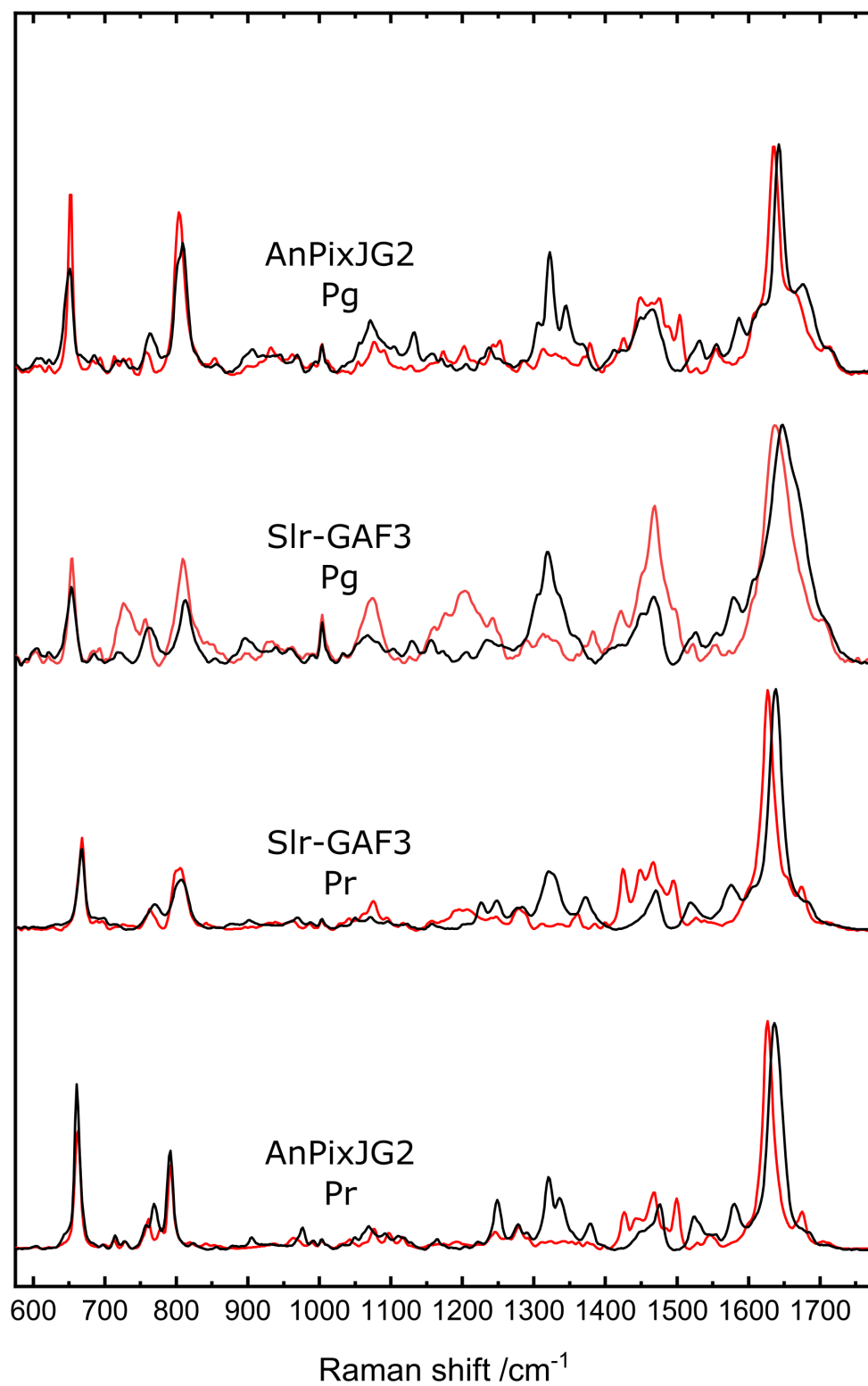


**Figure 9.2.1:** Full range RR spectra of Slr-GAF3 and AnpixJG2 in the Pr (bottom) and the Pg states (top). Spectra were recorded in H<sub>2</sub>O and D<sub>2</sub>O buffer.

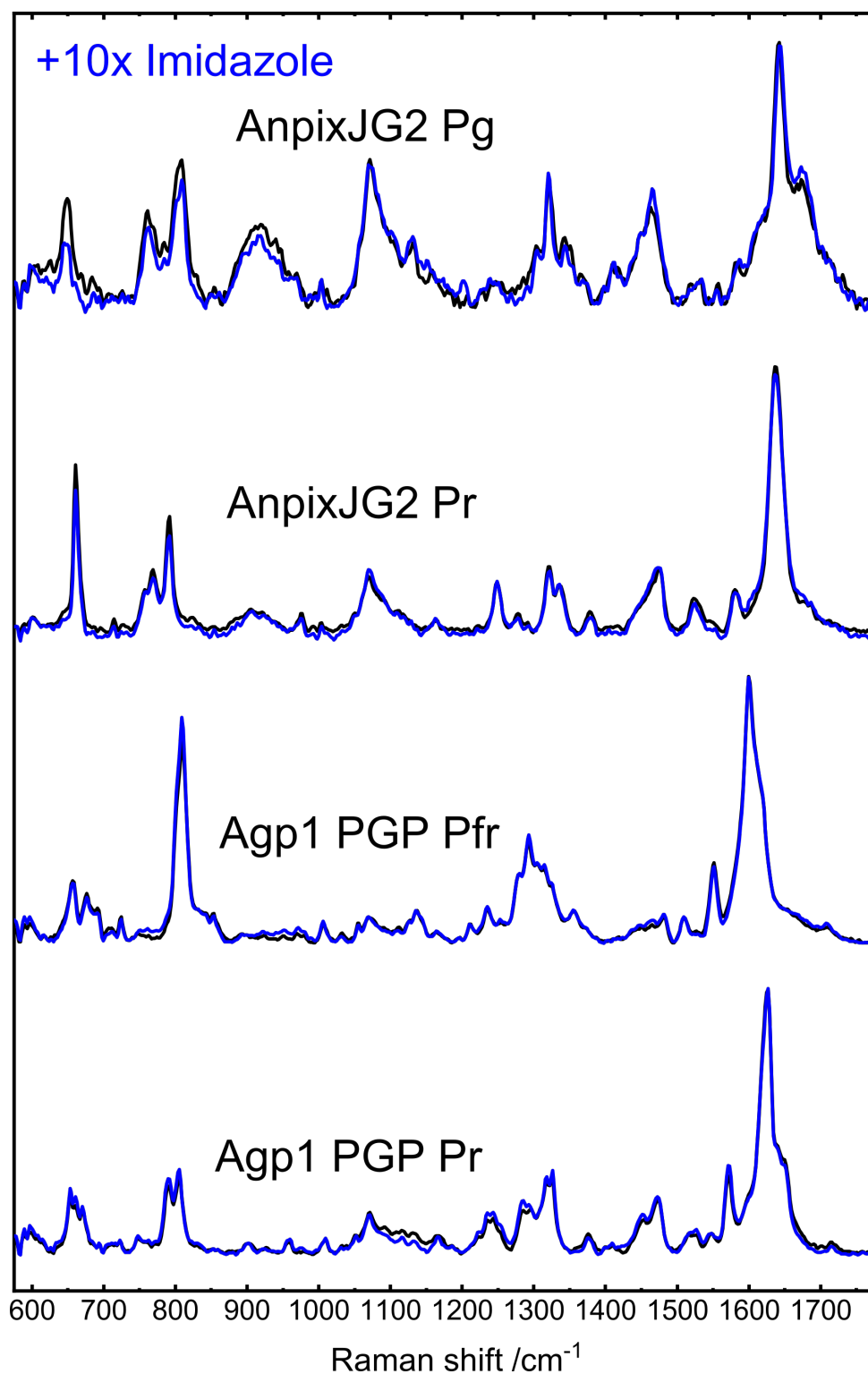


**Figure 9.2.2:** RR spectra of AnpixonJ (Pr and Pg states, top) and Agp1 (Pr and Pfr states, bottom) with and without 10x imidazole excess. Black traces refer to samples without imidazole, blue spectra were recorded after addition of 10x imidazole excess to the solution.

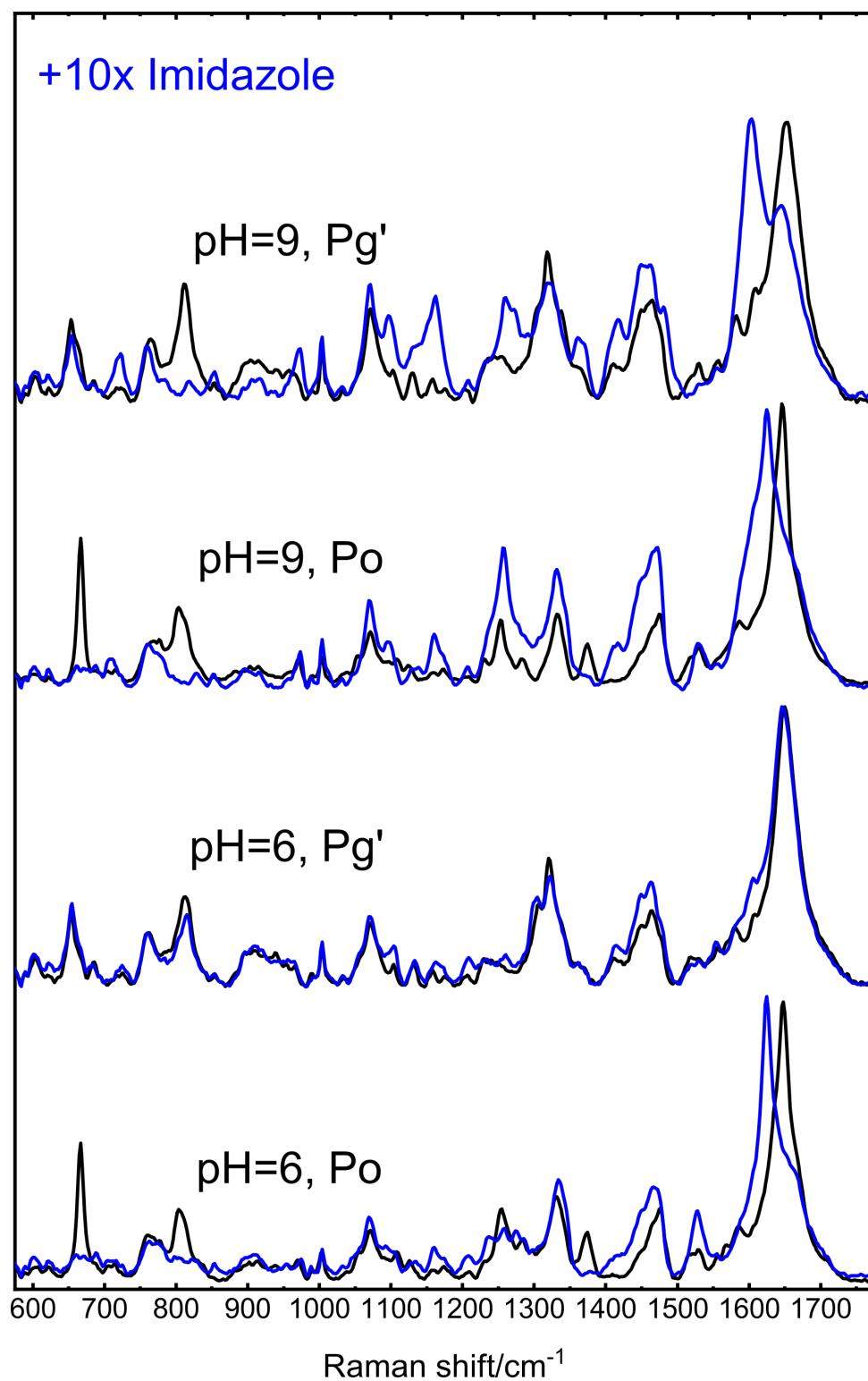


**Figure 9.2.3:** RR spectra of Slr-GAF3 with 10x imidazole excess at pH=9 (Pg and Pr, top) and pH=6 (Pg and Pr, bottom). Black traces refer to samples without imidazole, blue spectra were recorded after addition of 10x imidazole excess to the solution.

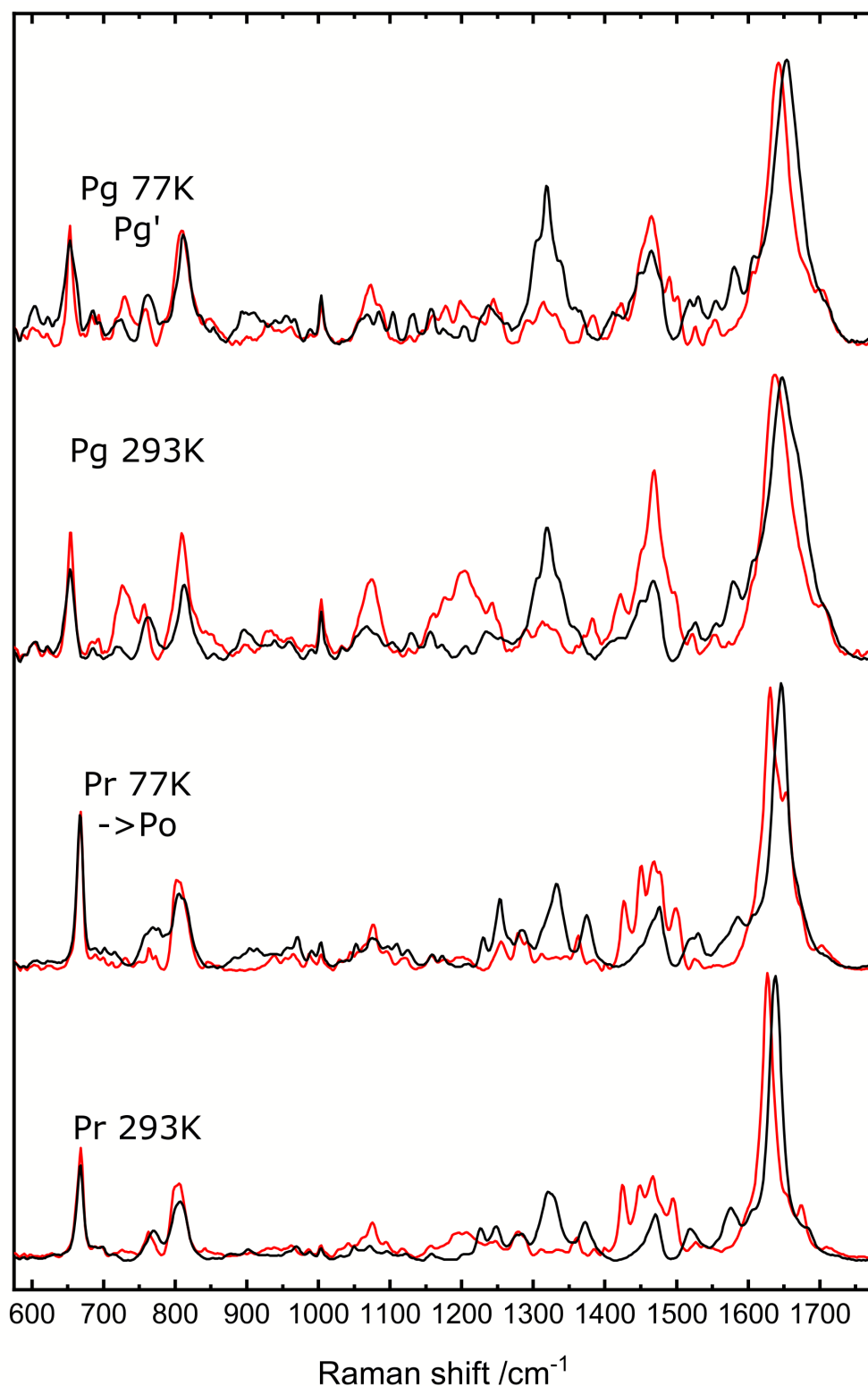


**Figure 9.2.4:** Full range temperature dependent RR spectra of Slr-GAF3. Spectra were recorded in H<sub>2</sub>O and D<sub>2</sub>O buffer. From bottom to top: the Pr spectrum of Slr-GAF3 at 293 K changes when it is frozen in the dark (77 K). The product is assigned to the Po state that is also observed in the UV/Vis spectra at low temperatures (see chapter 5.1). The Pg state is also changed during freezing in a similar manner, and is converted to the Pg' state at 77 K (top).

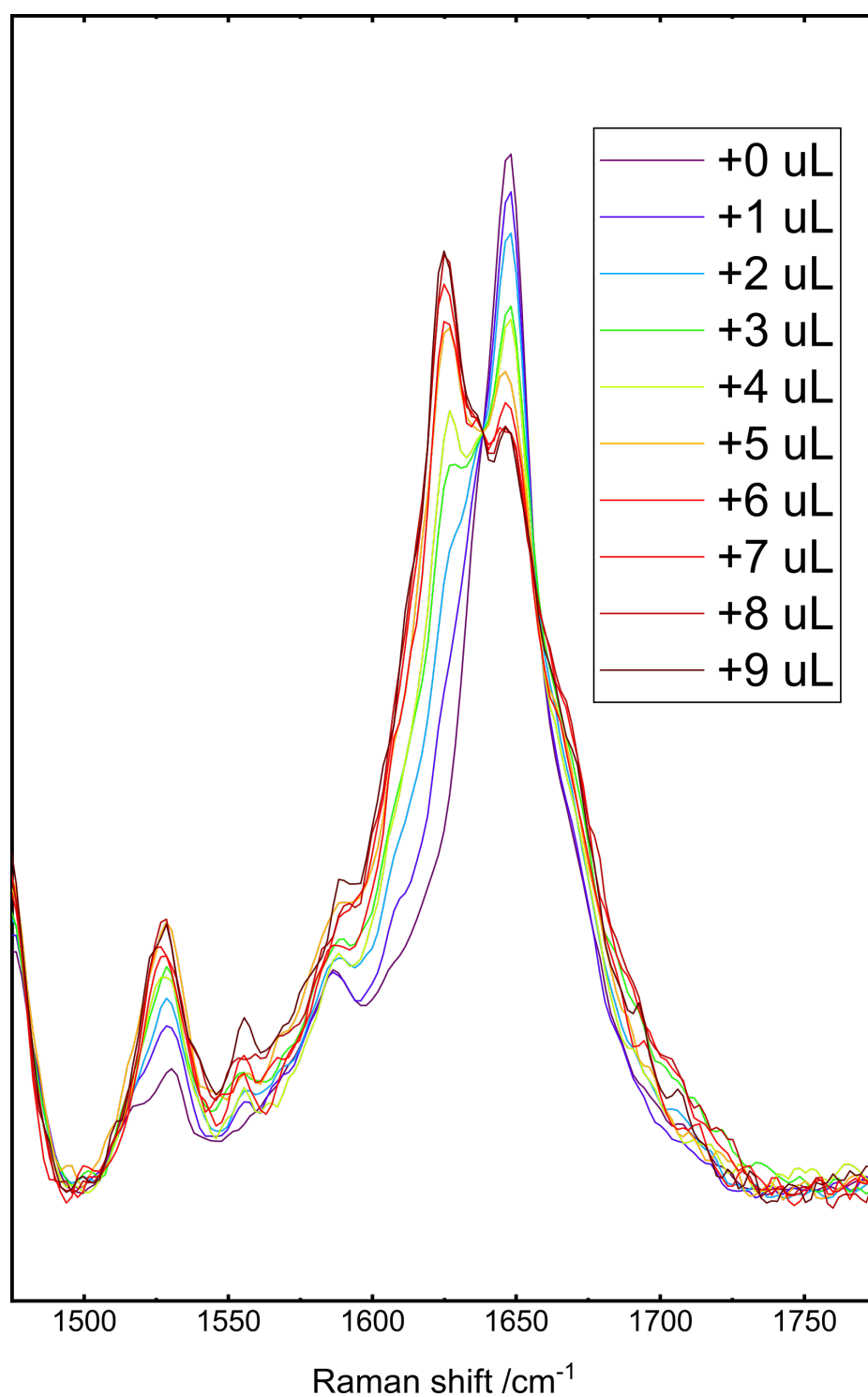


**Figure 9.2.5:** RR spectra of Slr-GAF3 titration with imidazole. The color code refers to different excess amounts of imidazole solution added to the RR sample and is given in the inset figure legend.



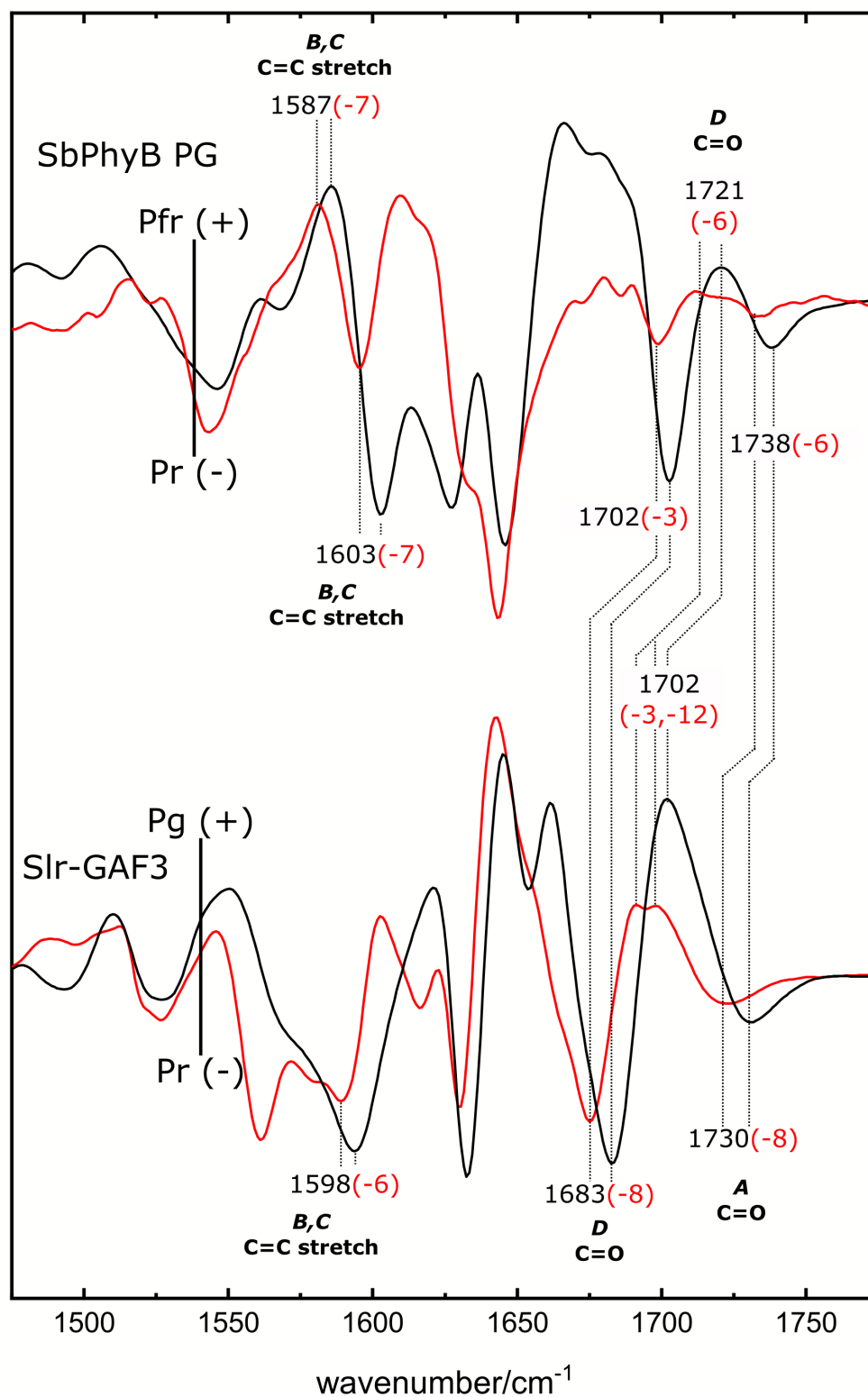


**Figure 9.2.6:** Difference IR spectra of Slr-GAF3 (bottom) and SbPhyB PG (top). Spectra were recorded in H<sub>2</sub>O and D<sub>2</sub>O buffer.

### **9.3 Supplements: Bacteriophytochromes**

# CHEMPHYSCHEM

## Supporting Information

### **The Photoconversion of Phytochrome Includes an Unproductive Shunt Reaction Pathway**

David Buhrke, Uwe Kuhlmann, Norbert Michael, and Peter Hildebrandt\*<sup>[a]</sup>

[cphc\\_201701311\\_sm\\_miscellaneous\\_information.pdf](#)

### **Author Contributions**

*P.H. Conceptualization: Lead; Project administration: Lead; Supervision: Lead; Writing – review & editing: Lead*

*D.B. Conceptualization: Supporting; Investigation: Lead; Methodology: Equal; Writing – original draft: Lead*

*N.M. Investigation: Lead*

*U.K. Methodology: Lead.*

Supporting Information  
©Wiley-VCH 2016  
69451 Weinheim, Germany

## The photoconversions of phytochromes include an unproductive shunt reaction pathway

David Buhrke, Uwe Kuhlmann, Norbert Michael and Peter Hildebrandt\*

\*Technische Universität Berlin, Institut für Chemie, Straße des 17. Juni 135, Sekr. PC14, D-10623 Berlin, Germany

Correspondence should be addressed to P.H. (email: [hildebrandt@chem.tu-berlin.de](mailto:hildebrandt@chem.tu-berlin.de))

**Abstract:** Phytochromes are modular bimodal photoswitches that control gene expression for morphogenetic processes in plants. These functions are triggered by the photoinduced conversions between the inactive and active states of the photosensory module, denoted as Pr and Pfr, respectively. In the present time-resolved resonance Raman spectroscopic study of bacterial representatives of this photoreceptor family, we demonstrate for the first time that these phototransformations do not represent linear processes but include a branching reaction back to the initial state, prior to (de)activation of the output module. Thus, only a fraction of the photoreceptors undergoing the phototransformations can initiate the downstream signaling process, consistent with phytochrome's function as a sensor for more durable changes of light conditions.

DOI: XXXXX

### Table of Contents

1. Supplementary Note 1; Figure S1 and S2: Experimental part
2. Supplementary Note 2: Interpretation of the slow Pfr recovery kinetics in Agp2
3. Supplementary note 3: Quality of the RR spectra
4. Figure S3: Time-resolved RR spectra of Agp1
5. Figure S4: Time-resolved RR spectra of Agp2
6. References

**Supplementary note 1: Experimental Part**

The photosensor (PAS-GAF-PHY) modules of Agp1 and Agp2 were expressed and purified as described previously.<sup>[1]</sup> For RR experiments, the protein solutions (buffered to pH 7.8 by Tris-HCl) were concentrated to yield a final concentration of ca. 0.7 mg/mL. A 15 mL conical vessel including the concentrated protein solution (ca. 0.7 mg/mL; ca. 10 mL) was placed in a light-sealed thermostable (20 °C) water bath. To slow down sample degradation, the sample reservoir was kept under inert N<sub>2</sub> atmosphere. However, degradation mainly due to shear forces generated by pumping the solution through the capillary could not be completely avoided. After a series of measurements, a pellet of degraded protein sample was usually found at the tip of the conical vessel. (Figure S1). Glass capillary micropipettes (Brand Blaubrand intraMark 200 µL) with an inner diameter of 1.6 mm and an outer diameter of 2 mm were used for applying the pump-probe (c1 in Figure S1) sequence as well as for photoinduced regeneration to the initial state (c2 in Figure S1). The flow of the sample was controlled by a peristaltic pump equipped with an easy-load 3 pump head (Masterflex L/S precision pump system, Cole Parmer/Novodirect). Since significant degradation of the sample was noted for higher pump frequencies ( $v_{\text{pump}} > 20$  rpm),  $v_{\text{pump}} = 6$  rpm and  $v_{\text{pump}} = 20$  rpm defined the accessible range of flow rates from 0.1 to 0.03 mm/ms in the capillary.

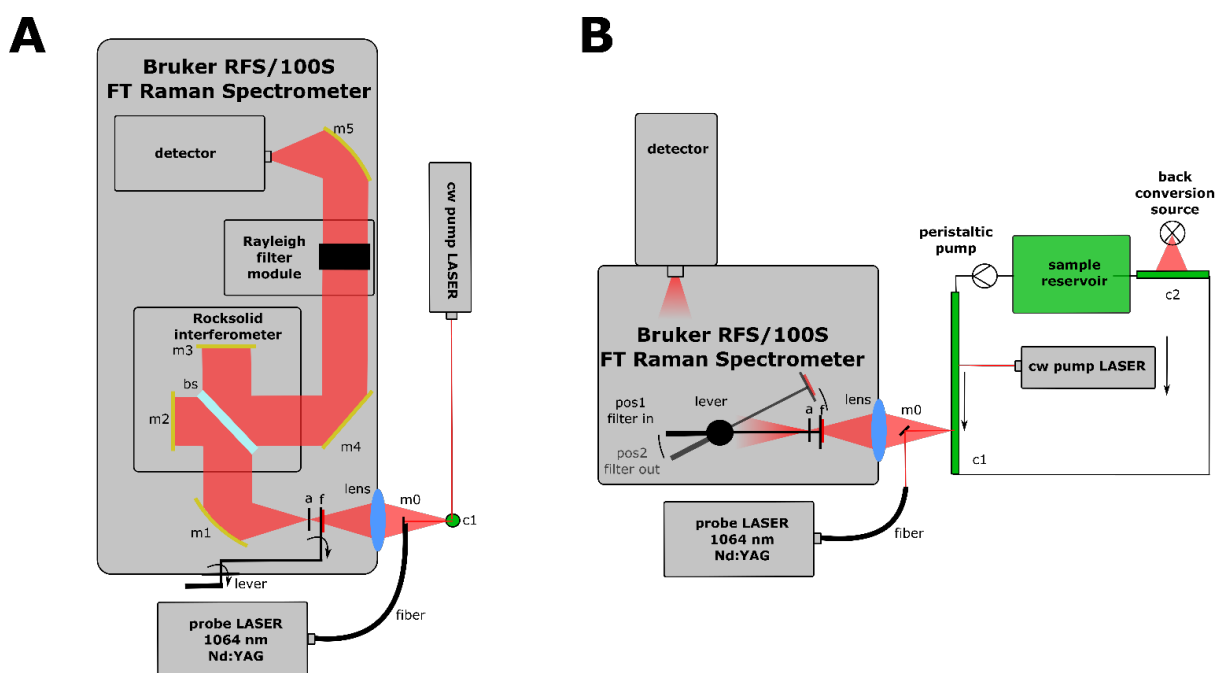
The spectra were measured with a FT Raman spectrometer RFS 100/S (Bruker) that was slightly modified for the time-resolved set-up. A 1064 nm Nd:YAG continuous wave (cw) Raman laser (line width 1 cm<sup>-1</sup>, laser spot size  $d_{\text{probe}} = 1$  mm) was directed through an optical fiber and a prism (m0) onto the capillary (c1) (Figure S1). The scattered radiation was collected in a 180° back-scattering geometry. The cw pump laser beam ( $d_{\text{pump}} = 1$  mm) was focused onto the capillary in 90° with respect to the probe laser beam. The spot size was adjusted for uniform illumination of the sample in the capillary to achieve maximum photoconversion. The laser spot position was spatially adjustable up to 20 mm relative to the probe beam. This configuration provides the range of time-resolution with 10 - 200 ms for  $v_{\text{pump}} = 20$  rpm, and 33 - 670 ms for 6 rpm. To induce the photochemical reaction cascade, a wavelength close to the absorption maximum of the first electronic transition of Agp1 and Agp2 was chosen. In the case of the Pfr state of Agp2, a solid state laser with output at 785 nm was used (CrystaLaser), providing an unfocussed spot size of  $d_{\text{pump}} = 1$  mm and a power of 65 mW. For photoconversion of the Pr state of Agp1, the 20 mW output of a 685 nm laser diode (Thorlabs, HL6750MG) was focused onto the capillary with an aspheric lens (LT110P) collimation optics to achieve a spot size of 1 mm in diameter. With  $d_{\text{pump}} = d_{\text{probe}} = 1$  mm, the closest possible distance of the two laser spot centers is 1mm, i. e., when the two laser spots touch each other. At this small spatial separation, the entrance optics of the spectrometer also collects scattered light from the pump laser hitting the capillary, resulting in an increased noise level in the spectra. Thus, a 785 nm edge filter (Semrock 785 nm razor edge ultra steep long-pass edge filter, cut-off wavelength around 790 nm) was attached to a lever in the spectrometer to remove unwanted stray light (Figure S1 and Figure S2). The lever allows access to the filter from outside of the spectrometer.

The photosensor module of Agp2 undergoes a fast dark reversion from Pr to Pfr with a time constant of ca. 5 s<sup>[2]</sup> that is distinctly shorter than the residence time in the reservoir. Thus, no additional photoinduced recovery of the initial state was required to achieve fresh-sample conditions. Agp1 displays a much slower dark relaxation kinetics<sup>[3]</sup> and, therefore, Pr regeneration had to be accelerated via photoinduced conversion of Pfr, using the 785 nm laser (65 mW) to illuminate the sample downstream of the probe laser focus (c2 in Figure S1). For Agp2, each pump-probe spectrum was averaged over 500 scans. Between the measurements of two pump-probe spectra, a probe-only spectrum of 100 scans was recorded as a reference for the respective difference spectrum and to check if fresh-sample conditions were established. Because of the slower reversion kinetics, each single pump-probe spectrum of Agp1 consisted of only 30 scans. To improve the signal-to-noise ratio, for each delay time eight spectra were co-added corresponding to a total of 240 scans. Between the

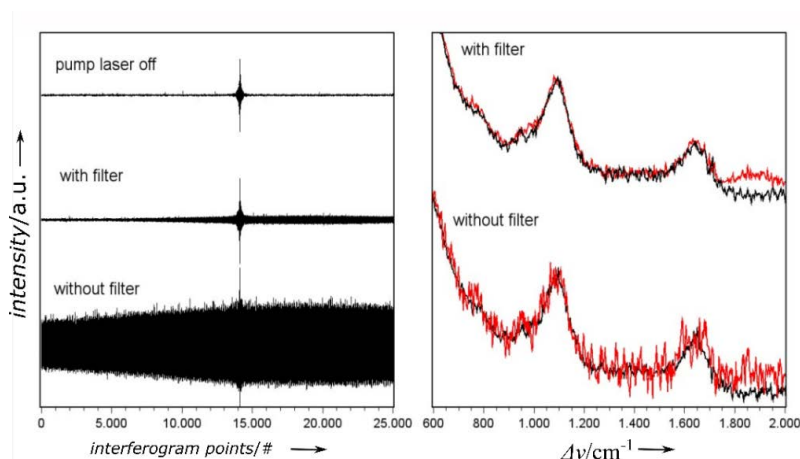
acquisitions of two pump-probe spectra, a probe-only spectrum of 100 scans was measured that served as a reference to generate the time-resolved difference spectra (“pump-probe” minus “probe only”), and as a control for checking “fresh sample” conditions. The RR spectra of the initial states shown in Figure 2 represent the sum of all probe-only RR spectra of the corresponding series of measurements. To avoid systematic errors (e.g. from sample degradation) the sequence of spectra acquisition at specific delay times was randomized for both proteins. Pump-probe and probe-only spectra were measured with 670 mW of the 1064 nm probe laser.

The flow speed was varied in the accessible range between 10 – 670 ms for both systems, resulting in different residence times of the sample in the pump beam. Longer residual times in the pump laser spot did not speed up the kinetics of the branching reactions, thus ruling out the possibility of a secondary photoreaction. The background spectrum (2000 scans) of the glass capillary (c1 in Figure S1) filled with buffer solution (cf. Figure S2) was subtracted from each RR spectrum, using the OPUS software package (Bruker). “Pump-probe” minus “probe-only” difference spectra were generated with the Origin software package (Origin labs).

**Figure S1**



**Figure S1.** Experimental set-up for the time-resolved RR measurements viewed from the top (A) and from the side (B). Mirrors and capillaries are denoted by “m” and “c”, respectively. The 785-nm edge filter (f) is placed in front of the aperture (a), where the collected light beam has a small diameter, and is attached to a lever, enabling positioning of the filter into and out of the light pathway from outside the spectrometer.

**Figure S2**

**Figure S2.** Effect of the 785 nm edge filter on the signal-to-noise ratio. Interferograms and the corresponding Raman spectra (average of 100 scans), taking from capillary including the buffer solution, are shown on the left and right panel, respectively. Right panel: Spectra in the presence of the pump beam are shown in red, the reference spectrum (probe only) is shown in black for comparison.

### Supplementary note 2: Interpretation of the slow Pfr recovery kinetics in Agp2

The slow phase of the Pfr recovery in Agp2 (Figure 3) can be assigned to the reaction sequence Meta-F  $\rightarrow$  Pr  $\rightarrow$  Pfr. For the first step, flash photolysis experiments have revealed a time constant of ca. 500 ms.<sup>[4]</sup> This time constant most likely refers to formation of the “normal” keto form of the chromophore that shows an RR spectrum that is nearly indistinguishable from that of Meta-F,<sup>[2]</sup> such that reaction step Meta-F  $\rightarrow$  Pr cannot be directly monitored by time-resolved RR spectroscopy. This reaction step includes the secondary structure change and can only be monitored by IR spectroscopy.<sup>[2]</sup> Thus, the time-dependent evolution of the 1618 cm<sup>-1</sup> actually reflects the superposition of formation and decay of the keto-form of Pr and the decay of Meta-F. The keto-form of Pr is involved in an equilibrium with the corresponding enol tautomer (70% at pH 7.8), which exhibits very low RR cross sections at 1064 nm excitation,<sup>[2]</sup> and thus cannot be detected in the time-resolved RR spectra. The enol form of Pr then constitutes the starting point for the dark reversion of to Pfr for which a time constant of ca. 5 s was determined.<sup>[2,4]</sup> These individual reaction steps may in fact account for the complex kinetics of the slow Pfr recovery.

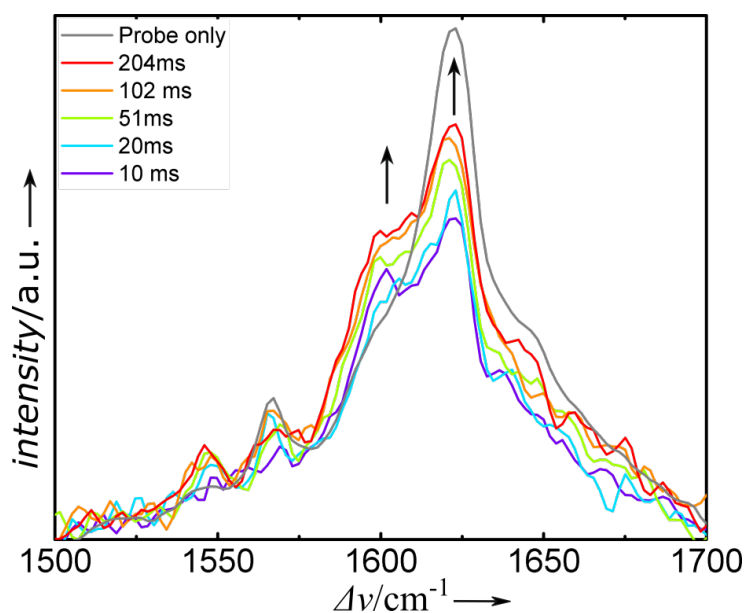


**Supplementary note 3: Quality of the RR spectra**

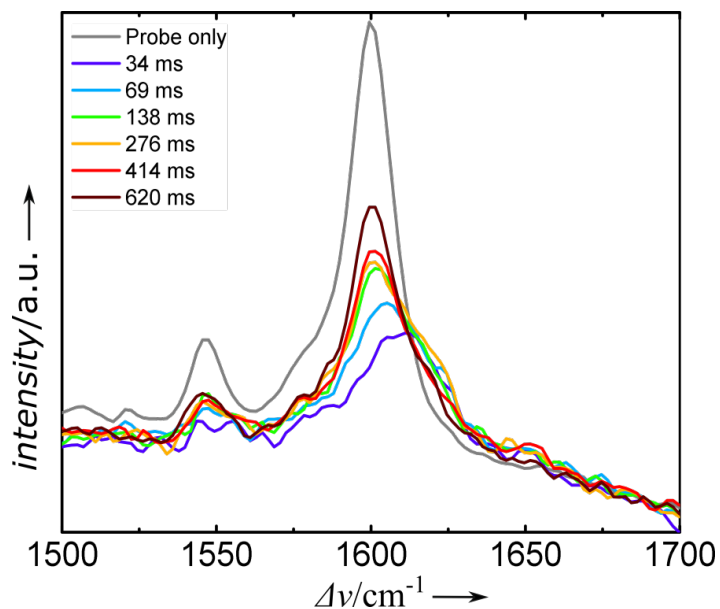
The RR spectroscopic analysis of phytochromes suffers from the fact that phytochrome states with protonated chromophores exhibit a distinctly more intense RR spectrum than those with deprotonated chromophores. This is due to the different Raman cross sections of the prominent bands. Using the  $1004\text{ cm}^{-1}$  of Phe as an internal standard one may estimate that the cross section of the strongest RR band of Meta-R (C-D methine bridge stretching) is at least 6 times smaller than that of Pr or Pfr upon excitation in (pre)resonance with the first electronic transition (here  $1064\text{ nm}$ ). Thus, one can calculate that an improvement of the time-resolved RR spectra of Agp1 (Fig. S3) up to a level that allows for the identification of Meta-Rc would require ca. 50 further series of measurements corresponding to a minimum of 350 mg of the protein. This amount of sample by far exceeds the current capacities of our protein production.

Using excitation lines in resonance with the second electronic transition causes a slight improvement of the relative intensities of the RR spectrum of Meta-Rc compared to Pr. However, in that case (unlike to  $1064\text{ nm}$  excitation) the Raman probe beam is not photo-“innocent” but causes photoconversion of the sample in the probe beam. For a reliable kinetic analysis, photolysis in the probe beam must be minimized which in turn is only possible with (i) high flow rates of the sample and (ii) a low photon flux of the Raman probe beam (for details see [5]). High flow rates do not only per se require a larger amount of protein for each experiment. It also facilitates protein denaturation due to the higher shear forces at the exit of the optical capillaries. These drawbacks and the restriction to a low photon flux of the probe beam further increase the necessary accumulation time such that, altogether, the advantage of using lower protein concentrations is not only destroyed but turned into the opposite. Thus, we have discarded this experimental option. For similar reasons, red excitation (in rigorous resonance with the Q-band) was also not an acceptable option. Here, also the interference by the fluorescence impairs the measurement of the RR spectra.

Thus, the best results were finally obtained with  $1064\text{-nm}$  excitation since the probe beam does not induce any photoreactions of the parent states or the intermediates. Here the disadvantage is the use of high concentrations (due to the low overall resonance enhancement), however, the sample demands in these experiments were much more modest compared to the other options with rigorous resonance enhancement. Nevertheless, also in this case, the sample demand is the limiting factor as we have described above.

**Figure S3: Time-resolved RR spectra of Agp1**

**Figure S3.** Time-resolved RR spectra of the Pr→Pfr phototransformation of Agp1, measured at different delay times. The corresponding difference spectra are shown in Figure 2.

**Figure S4: Time-resolved RR spectra of Agp2**

**Figure S4.** Time-resolved RR spectra of the Pfr→Pr phototransformation of Agp2, measured at different delay times. The corresponding difference spectra are shown in Figure 2.

## References

- [1] T. Lamparter, N. Michael, *Biochemistry* 2005, 44, 8461–8469.
- [2] F. Velazquez Escobar, P. Piwowarski, J. Salewski, N. Michael, M. Fernandez Lopez, A. Rupp, Q. B. Qureshi, P. Scheerer, F. Bartl, N. Frankenberg-Dinkel, F. Siebert, M. A. Mrogiński, P. Hildebrandt, *Nature Chem.* **2015**, 7, 423-430.
- [3] B. Borucki, D. von Stetten, S. Seibeck, T. Lamparter, N. Michael, M. A. Mrogiński, H. Otto, D. H. Murgida, M. P. Heyn, P. Hildebrandt, *J. Biol. Chem.* **2005**, 280, 34358-34364.
- [4] B. Zienicke, I. Molina, R. Glenz, P. Singer, D. Ehmer, F. Velazquez Escobar, P. Hildebrandt, R. Diller, T. Lamparter, *J. Biol. Chem.* **2013**, 288, 31738-31751
- [5] F. Siebert and P. Hildebrandt "Vibrational Spectroscopy in Life Science" (2007), Wiley-VCH, Weinheim.

## Author Contributions

N. M. prepared the protein samples, D. B. and U.K. designed and assembled the set-up for time-resolved RR experiments, D. B. carried out the spectroscopic measurements. D.B. and P.H. designed the project, analysed the data, and wrote the manuscript, with contribution by all other authors.

## 9.4 Supplements: IsPadC

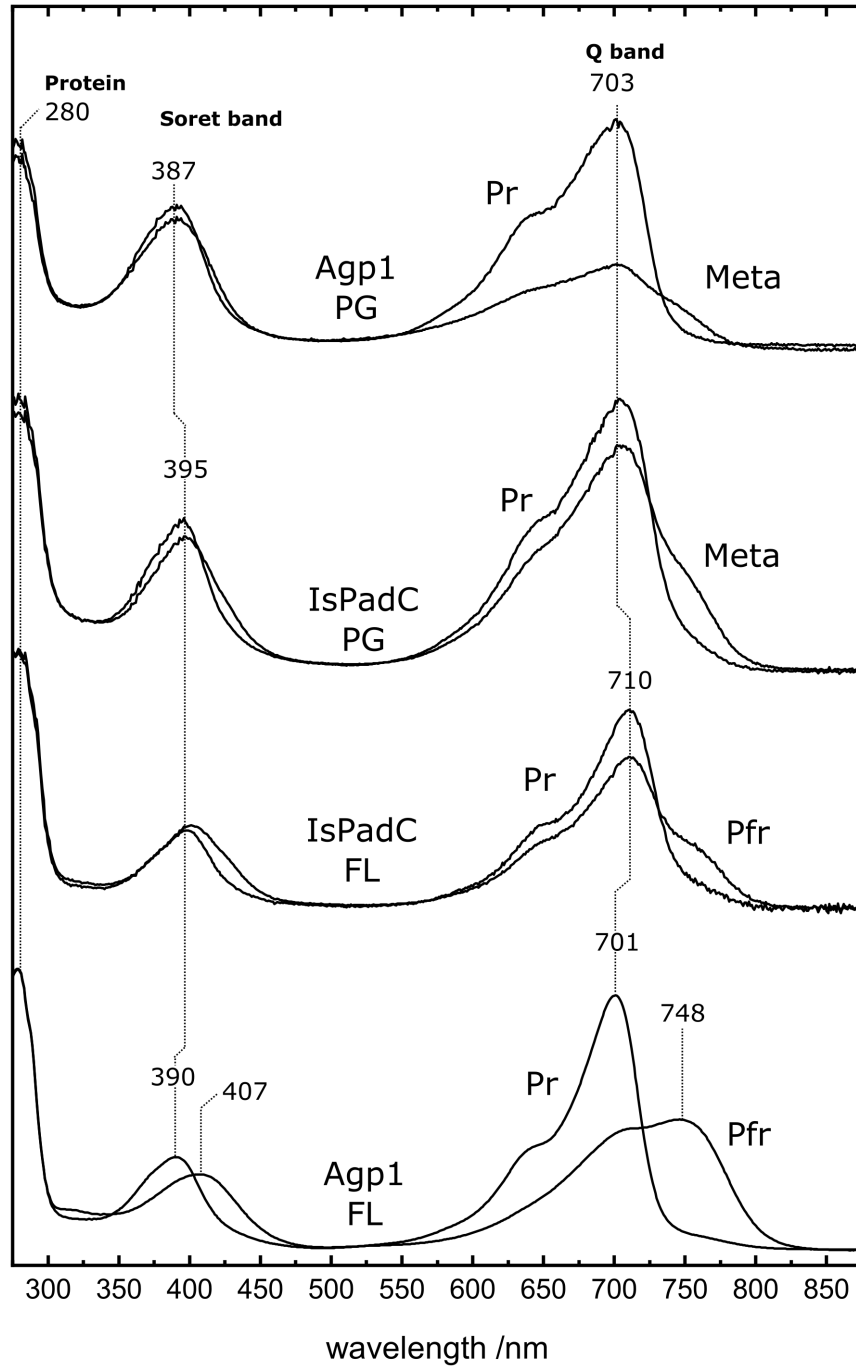


**Figure 9.4.1:** From bottom to top: Unsubtracted UV/Vis spectra of Agp1 and IsPadC FL, IsPadC PG and Agp1 PG. The Pr spectra are recorded in the dark and the respective Meta and Pfr spectra were generated *via* illumination with a 660 nm LED.

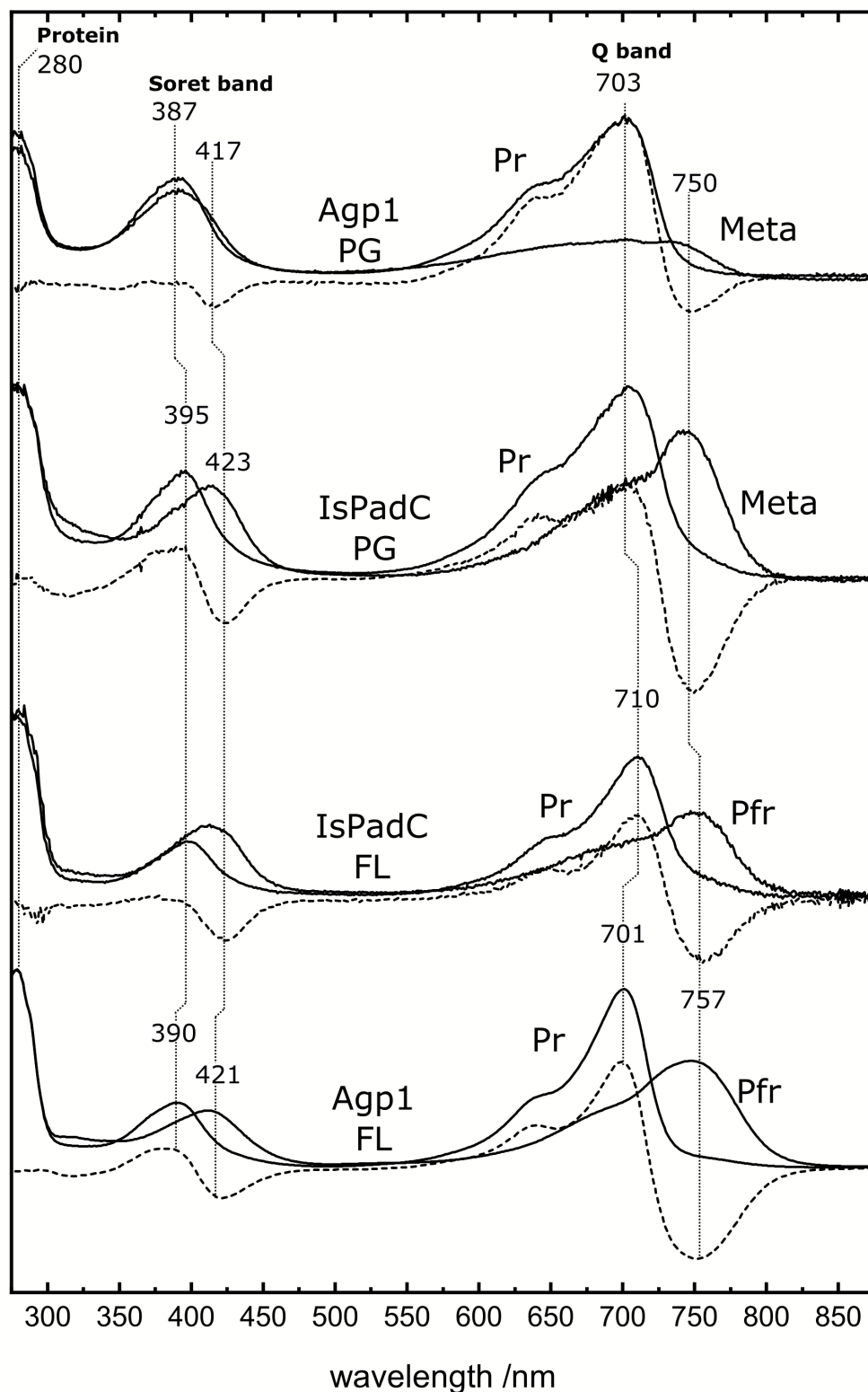


**Figure 9.4.2:** From bottom to top: Unsubtracted UV/Vis spectra of Agp1 and IsPadC FL, IsPadC PG and Agp1 PG. The Pr spectra are recorded in the dark and the respective Meta and Pfr spectra were generated *via* illumination with a 660 nm LED. Remaining Pr contributions (see fig. 9.4.1) were removed by spectral subtraction. Dashed lines indicate Pr-minus-photoproduct difference spectra.

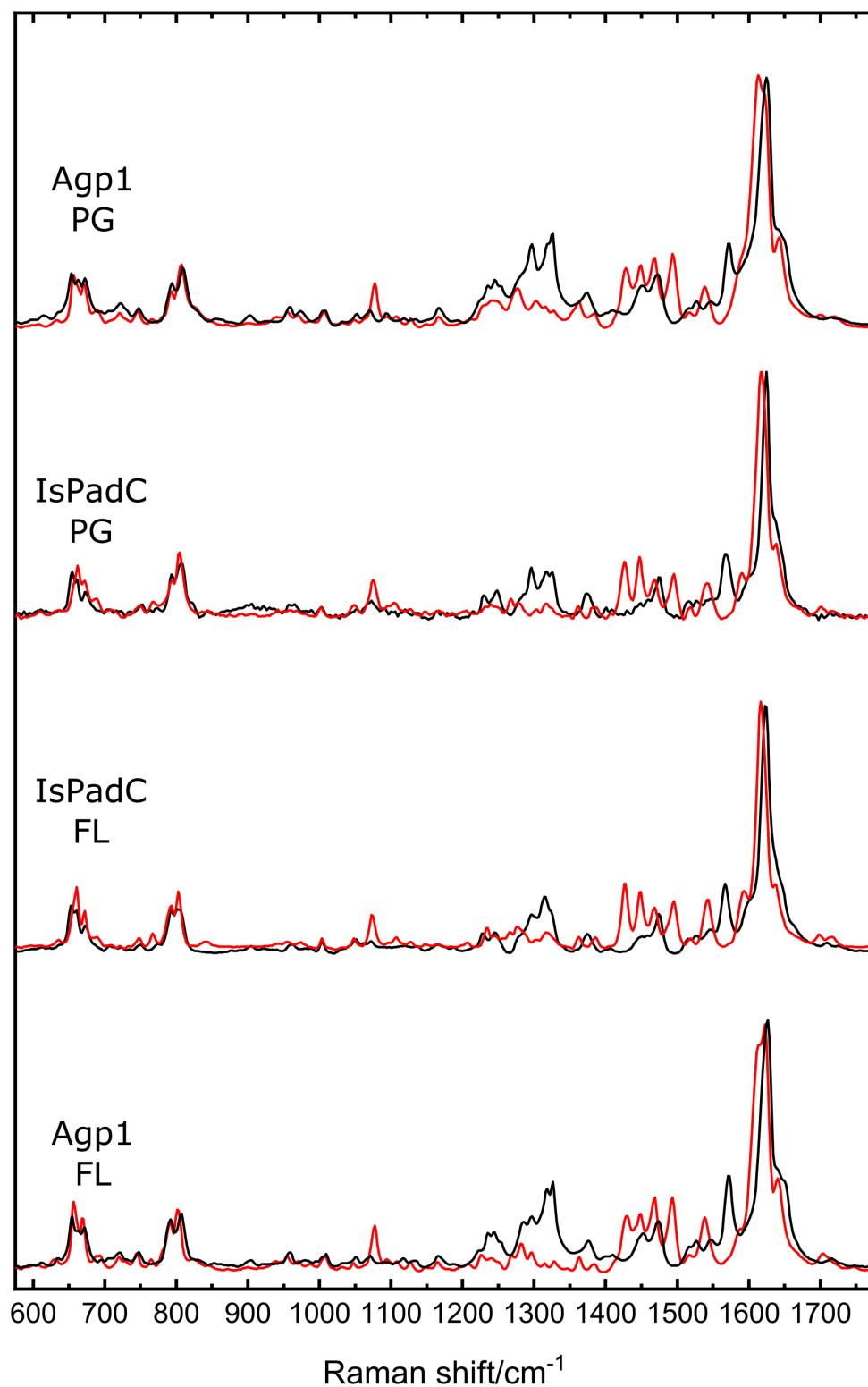


**Figure 9.4.3:** Full range IsPadC and Agp1 RR spectra in the Pr state. From bottom to top: Agp1 FL, IsPadC FL, IsPadC PG and Agp1 PG. Spectra were recorded in H<sub>2</sub>O and D<sub>2</sub>O buffer.

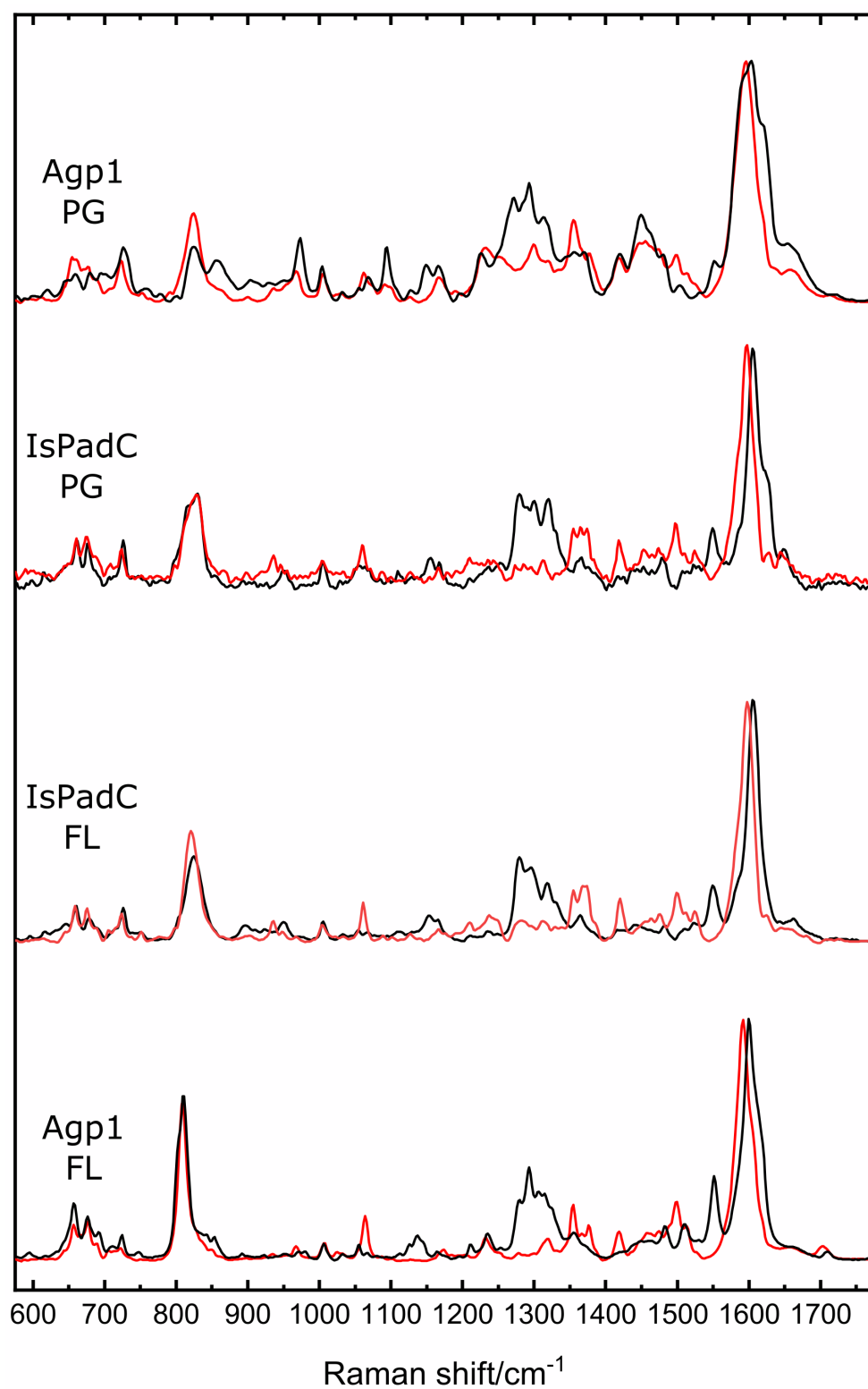


**Figure 9.4.4:** Full range IsPadC RR spectra in the photo activated (Pfr and Meta) state. From bottom to top: Agp1 FL, IsPadC FL, IsPadC PG and Agp1 PG. Spectra were recorded in  $\text{H}_2\text{O}$  and  $\text{D}_2\text{O}$  buffer.



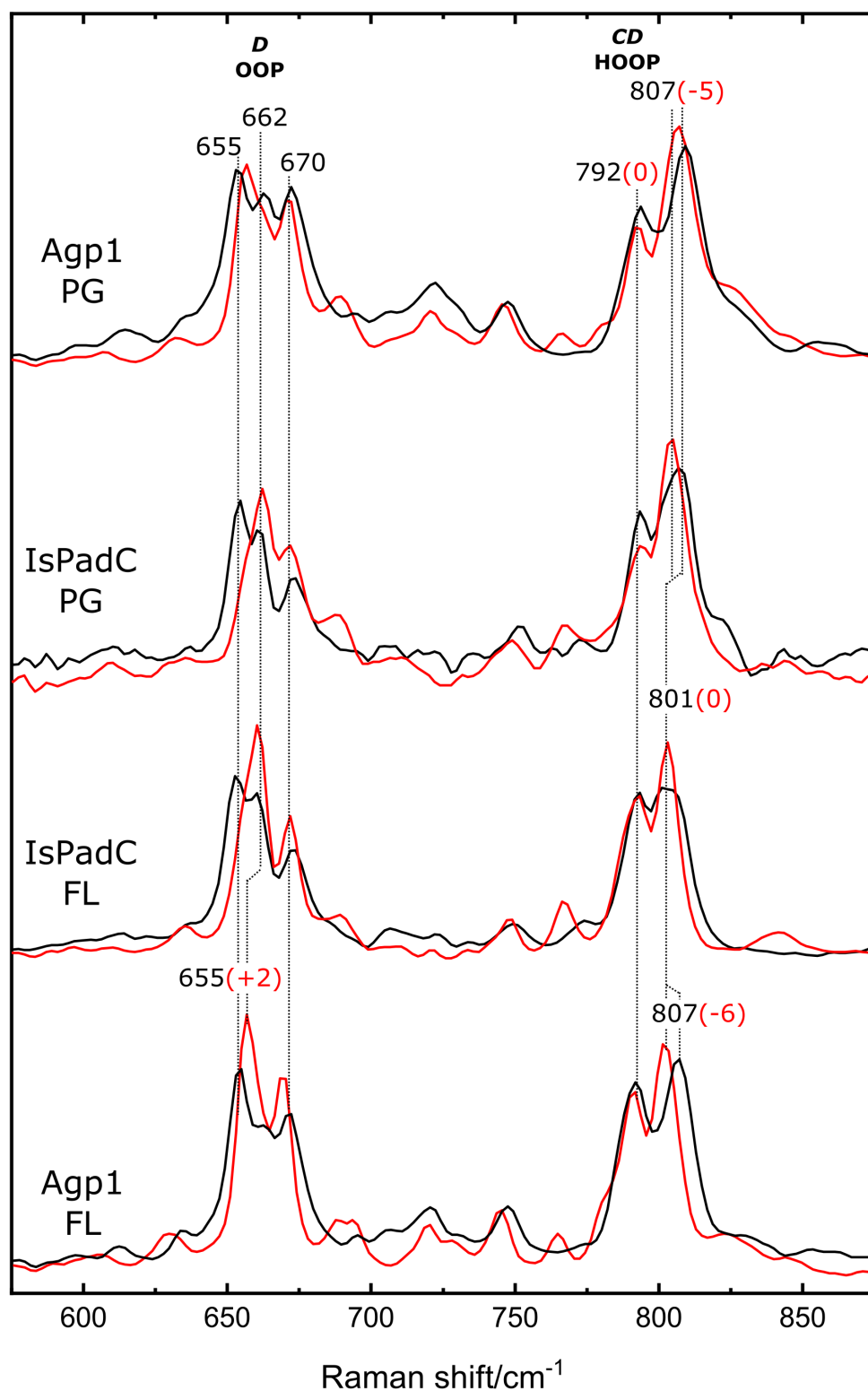


**Figure 9.4.5:** IsPadC RR spectra in the HOOP region in the Pr state. From bottom to top: Agp1 FL, IsPadC FL, IsPadC PG and Agp1 PG. Spectra were recorded in H<sub>2</sub>O and D<sub>2</sub>O buffer.

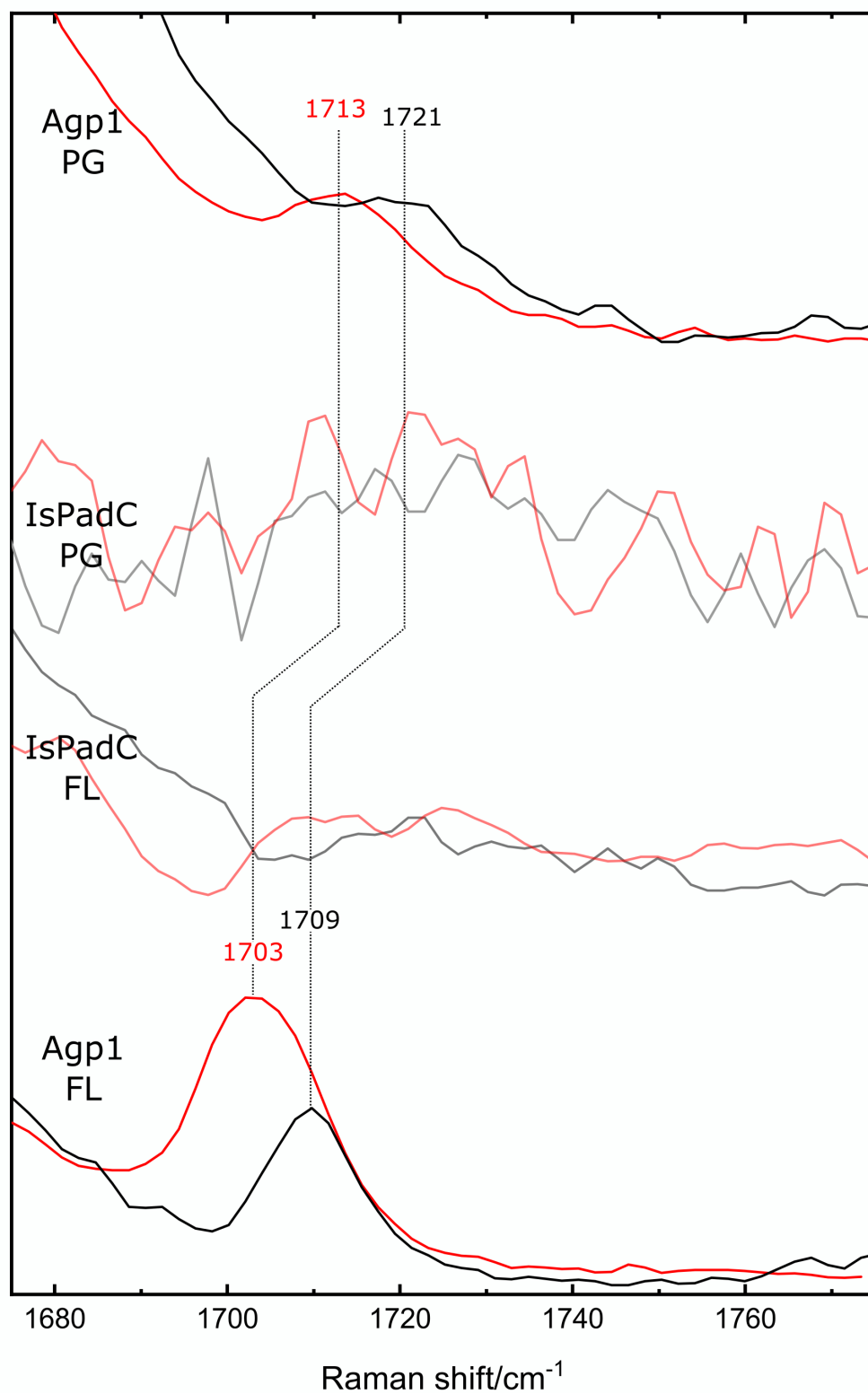


**Figure 9.4.6:** IsPadC RR spectra in the CO region in the photo activated (Pfr and Meta) states. From bottom to top: Agp1 FL, IsPadC FL, IsPadC PG and Agp1 PG. IsPadC spectra are faded because of the high noise level. Spectra were recorded in  $\text{H}_2\text{O}$  and  $\text{D}_2\text{O}$  buffer.

## 9.5 Supplements: IRFPs

iRFP sequence alignment is given below:

```

RpP6   1 MPR-----KVDLTSCDREPIHIPGSIQPCGCLLACDAQAVRITRISENAG
iRFP702 1 MAR-----KVDLTSCDREPIHIPGSIQPCGCLLACDAQAVRITRITENAG
iRFP670 1 MAR-----KVDLTSCDREPIHIPGSIQPCGCLLACDAQAVRITRITENAG
RpP2   1 MTEGSVARQPDLSTCDDEPIHIPGAIQPHGLLLALAADMTIVAG-SDNLP
iRFP713 1 MAEGSVARQPDLSTCDDEPIHIPGAIQPHGLLLALAADMTIVAG-SDNLP
iRFP720 1 MAEGSVARQPDLSTCDDEPIHIPGAIQPHGLLLALAADMTIVAG-SDNLP
iRFP682 1 MAEGSVARQPDLSTCDDEPIHIPGAIQPHGLLLALAADMTIVAG-SDNLP

RpP6   45 AFFGRET-PRVGELLADYFGETEHAHLRNALAQSSDPKRPALIFGWRDGL
iRFP702 45 AFFGRET-PRVGELLADYFGETEHAHLRNALAQSSDPKRPALIFGWRDGL
iRFP670 45 AFFGRET-PRVGELLADYFGETEHAHLRNALAQSSDPKRPALIFGWRDGL
RpP2   49 ELTGLAIGALIGRSAADVDFDSETHNRLTIALAEPGAAVGAPIAVGFTMR-
iRFP713 49 ELTGLAIGALIGRSAADVDFDSETHNRLTIALAEPGAAVGAPITVGFTMR-
iRFP720 49 ELTGLAIGALIGRSAADVDFDSETHNRLTIALAEPGAAVGAPITVGFTMR-
iRFP682 49 ELTGLAIGALIGRSAADVDFDSETHNRLTIALAEPGAAVGAPITVGFTMR-

RpP6   94 TGRTFDISLHRHDGTSIVEFEPAAADQADNPLRLTR---QIIARTKELKS
iRFP702 94 TGRTFDISLHRHDGTSIIIEFEPAAAEQADNPLRLTR---QIIARTKELKS
iRFP670 94 TGRTFDISLHRHDGTSIIIEFEPAAAEQADNPLRLTR---QIIARTKELKS
RpP2   98 KDAGFIGSWHRHDQLIFLELEPPQRD-VAEPQAFFRRTNSAIRRLQAAET
iRFP713 98 KDAGFIGSWHRHDQLIFLELEPPQRD-VAEPQAFFRRTNSAIRRLQAAET
iRFP720 98 KDAGFIGSWHRHDQLIFLELEPPQRD-VAEPQAFFRRTNSAIRRLQAAET
iRFP682 98 KDAGFIGSWHRHDQLIFLELEPPQRD-VAEPQAFFRRTNSAIRRLQAAET

RpP6   141 LEEMAARVPRYLQAMLGYHRVMYRFADDGSGKVICEAKRSDLESFLGQH
iRFP702 141 LEEMAARVPRYLQAMLGYHRVMYRFADDGSGKVICEAKRSDLESFLGQH
iRFP670 141 LEEMAARVPRYLQAMLGYHRVMYRFADDGSGMVIGEAKRSDLESFLGQH
RpP2   147 LESACAAAQEVREITGFDRVMYRFASDFSGEVIAEDRCAEVESYLGHLH
iRFP713 147 LESACAAAQEVRKITGFDRVMYRFASDFSGEVIAEDRCAEVESKLGHLH
iRFP720 147 LESACAAAQEVRKITGFDRVMYRFASDFSGSVIAEDRCAEVESKLGHLH
iRFP682 147 LESACAAAQEVRKITGFDRVMYRFASDFSQVIAEDRCAEVESKLGHLH

RpP6   191 FPASDIPQARLLYLKNAIRVISDSRGISSRIVPERD-ASGAALDLSFAH
iRFP702 191 FPASLVPQARLLYLKNAIRVVSDSRGISSRIVPEHD-ASGAALDLSFAH
iRFP670 191 FPASLVPQARLLYLKNAIRVVSDSRGISSRIVPEHD-ASGAALDLSFAH
RpP2   197 FPASDIPAQARRLYTINPVRIIPDINYRPVPVTPDLNPVTGRPIDLSFAI
iRFP713 197 YPASTVPAQARRLYTINPVRIIPDINYRPVPVTPDLNPVTGRPIDLSFAI
iRFP720 197 YPASFIPAQARRLYTINPVRIIPDINYRPVPVTPDLNPVTGRPIDLSFAI
iRFP682 197 YPASAVPAQARRLYTINPVRIIPDINYRPVPVTPDLNPVTGRPIDLSFAI

RpP6   240 LRSVSPHLEYLRNMGVSASMSLSIIDGTLWGLIACHHYEPRAVPMAGR
iRFP702 240 LRSISPIHLEFLRNMGVSASMSLSIIDGTLWGLIICHHYEPRAVPMAGR
iRFP670 240 LRSISPCHLEFLRNMGVSASMSLSIIDGTLWGLIICHHYEPRAVPMAGR
RpP2   247 LRSVSPVHLEYMRNIGMHGTMSISILRGERLWGLIACHHRKPNYVDLDGR
iRFP713 247 LRSVSPVHLEFMRNIGMHGTMSISILRGERLWGLIVCHHRTPPYVDLDGR
iRFP720 247 LRSVSPNHLEFMRNIGMHGTMSISILRGERLWGLIVCHHRTPPYVDLDGR

```

iRFP682 247 LRSVSPCHLEFMRNIGMHGTMSISILRGERLWGLIVCHHRTPIYYVDLDGR

RpP6	290	VAAEMFADFFSLHFTAHHQR-----	311
iRFP702	290	VAAEMFADFLSLHFTAHHQR-----	311
iRFP670	290	VAAEMFADFLSLHFTAHHQR-----	311
iRFP713	297	QACELVAQVLAWQIGVMEE-----	316
iRFP720	297	QACELVAQVLAWQIGVMEE-----	316
iRFP682	297	QACELVAQVLAWQIGVMEE-----	316

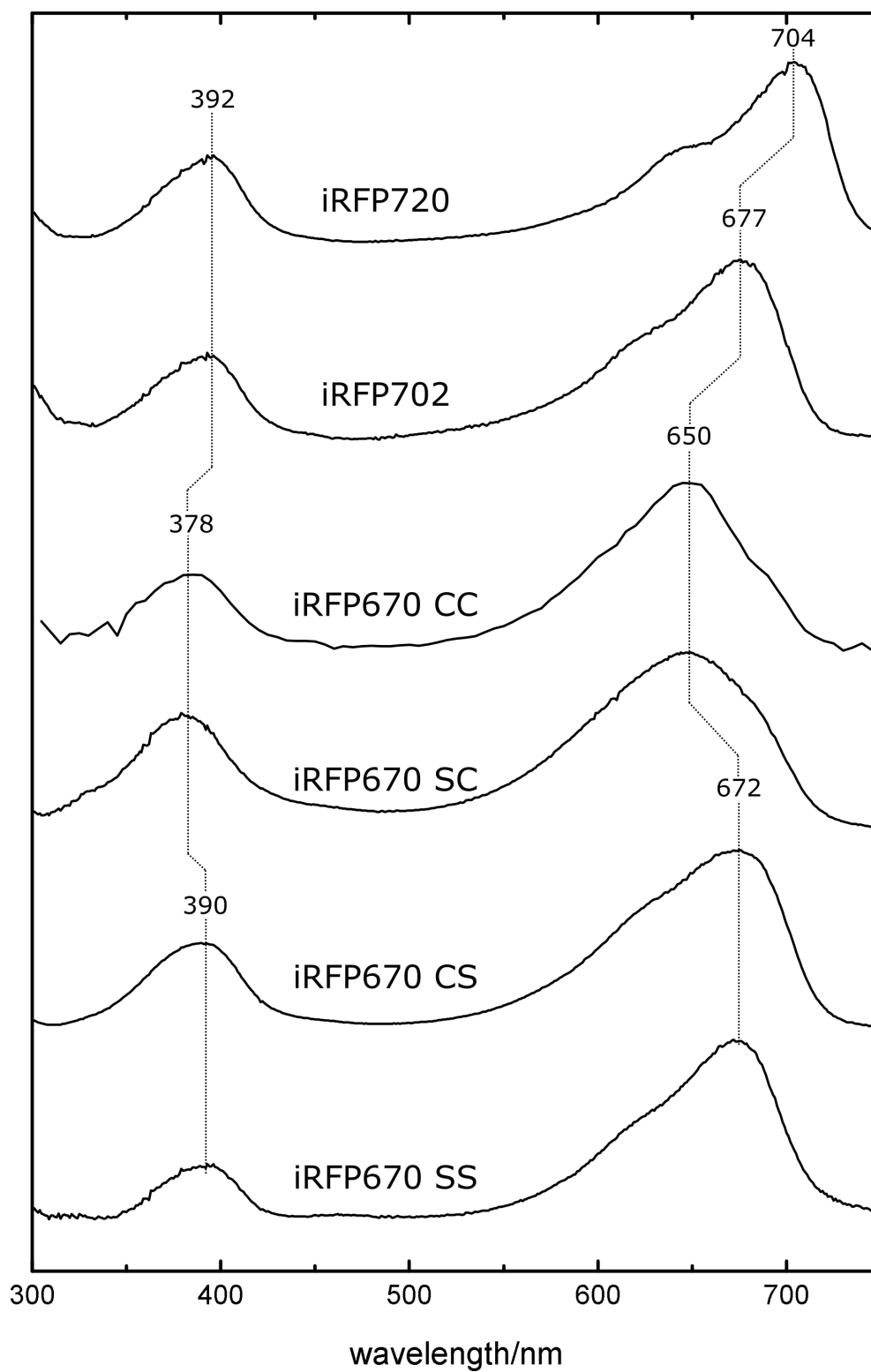


**Figure 9.5.1:** UV/Vis spectra of iRFP702, iRFP720, iRFP670 and Cys/Ser exchange variants of iRFP670.

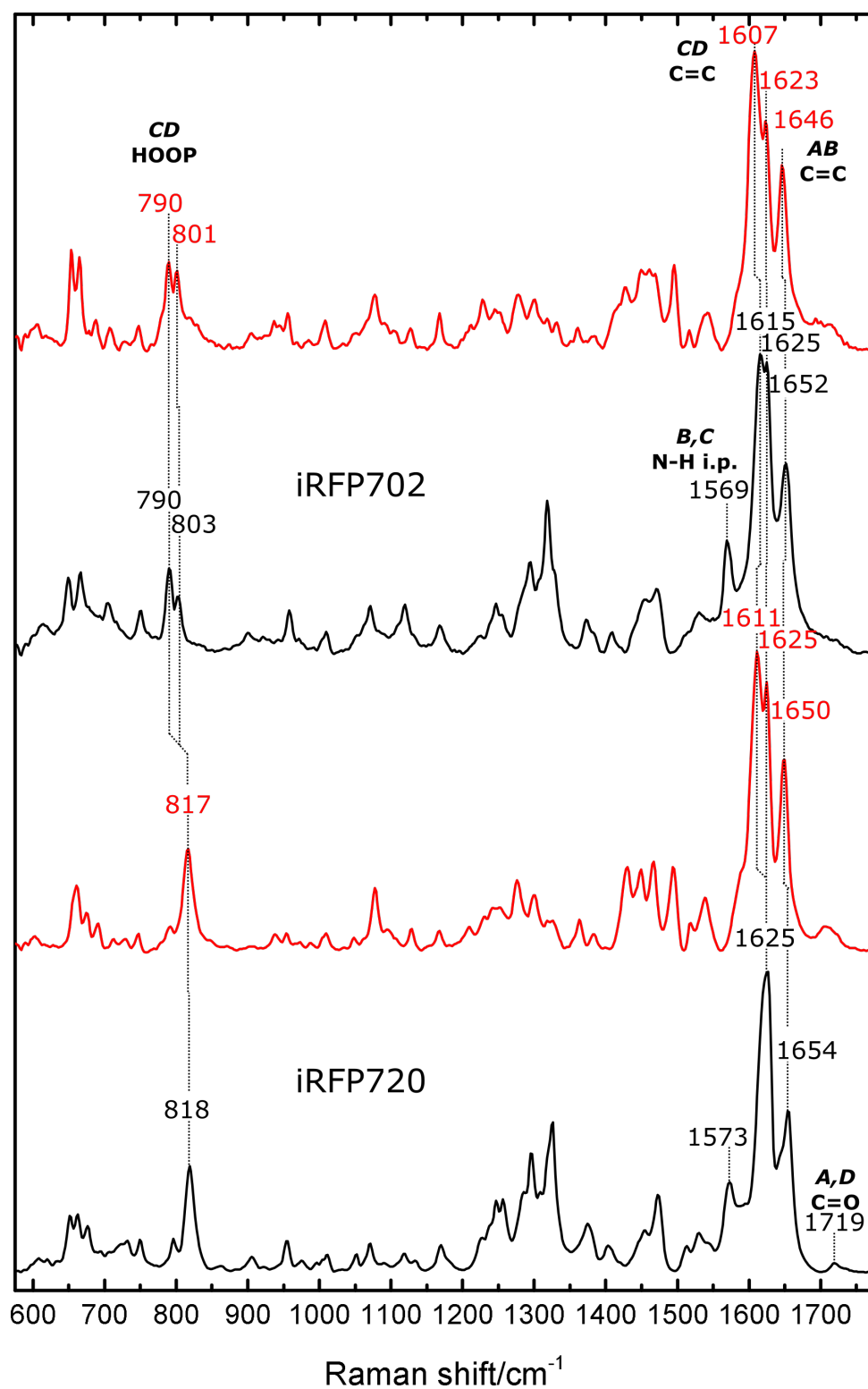
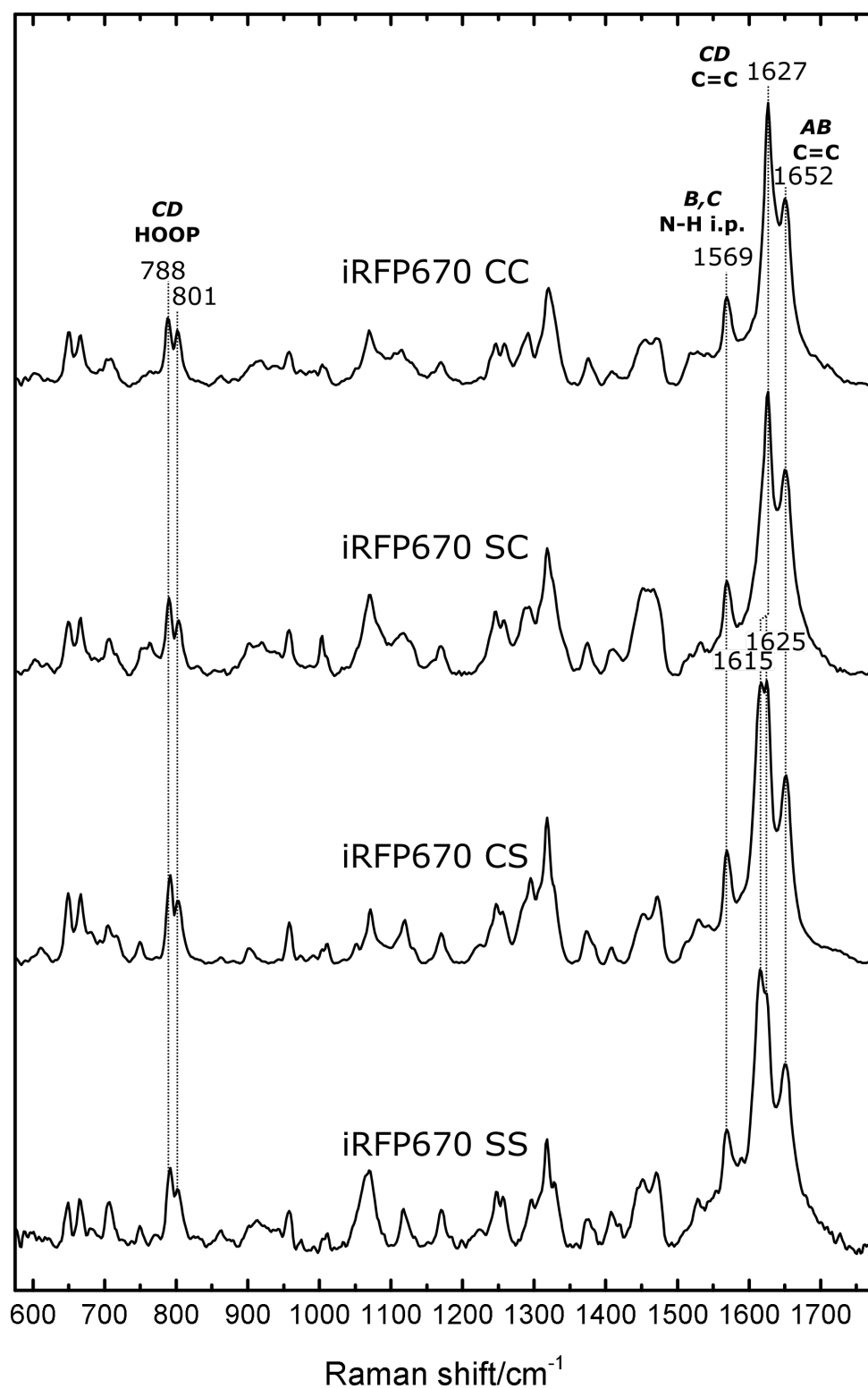
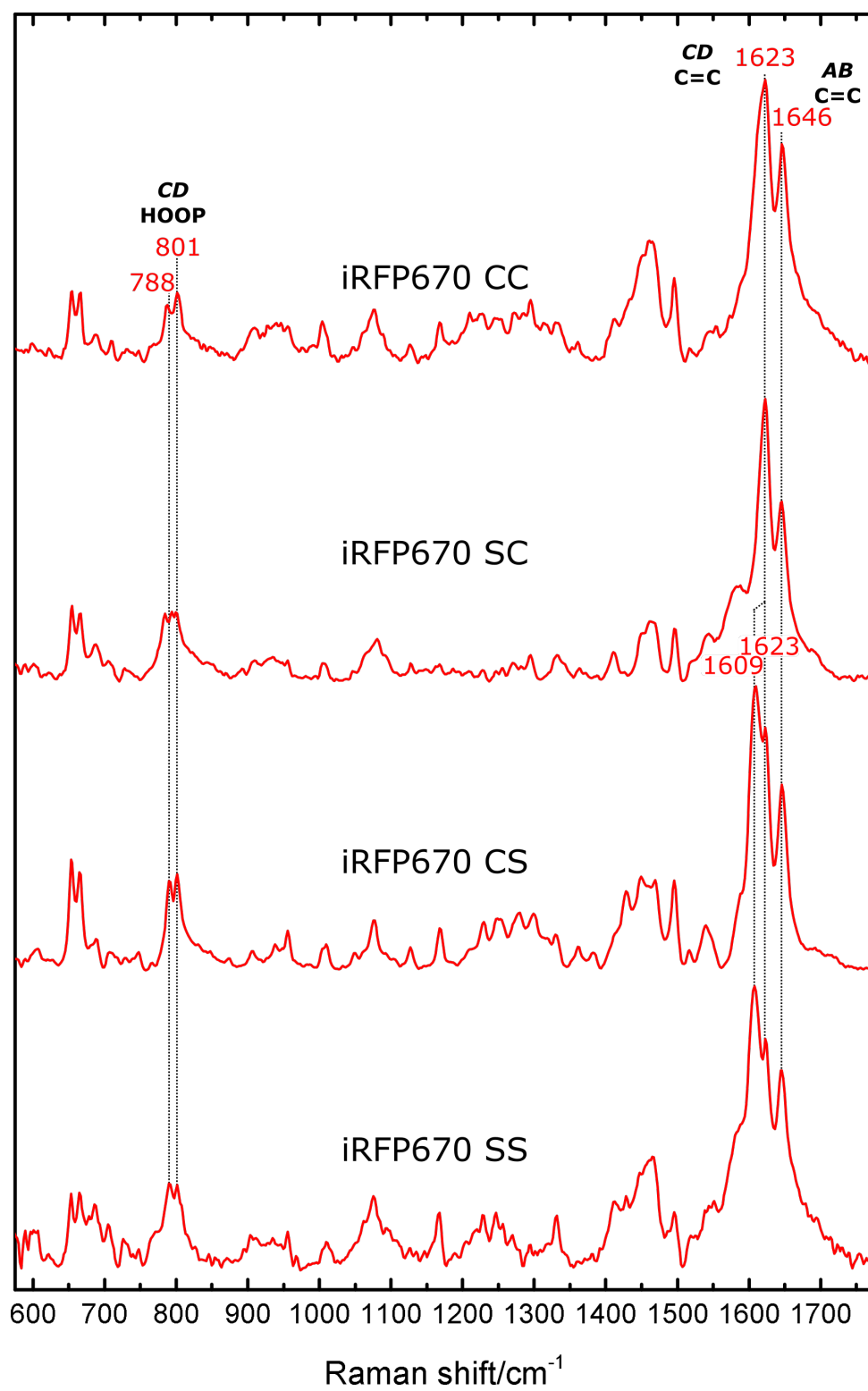


Figure 9.5.2: RR spectra of iRFP 702 and 720 in  $\text{H}_2\text{O}$  and  $\text{D}_2\text{O}$  buffer.



**Figure 9.5.3:** RR spectra of iRFP670 and Cys/Ser exchange variants recorded in  $\text{H}_2\text{O}$  buffer.



**Figure 9.5.4:** RR spectra of iRFP670 and Cys/Ser exchange variants recorded in D<sub>2</sub>O buffer.



## Supporting information

### The role of local and remote amino acid substitutions for optimizing fluorescence in bacteriophytochromes: A case study on iRFP

David Buhrke, Francisco Velazquez Escobar, Luisa Sauthof, Svea Wilkening, Nico Herder, Neslihan N. Tavraz, Mario Willoweit, Anke Keidel, Tillmann Utesch, Maria-Andrea Mroginski, Franz-Josef Schmitt, Peter Hildebrandt\*, and Thomas Friedrich\*

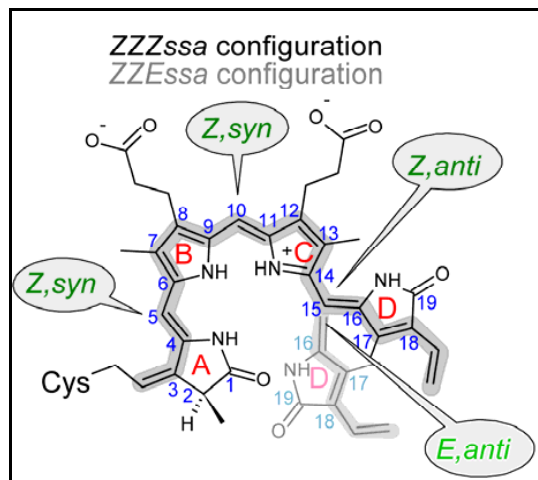
Technische Universität Berlin, Institut für Chemie, Sekr. PC 14, Straße des 17. Juni 135, D-10623 Berlin, Germany

**\*Corresponding authors:** Thomas Friedrich, Peter Hildebrandt, Technische Universität Berlin, Institut f. Chemie, Sekr. PC 14, Straße des 17. Juni 135, D-10623 Berlin, Germany, Tel: +49-(30)-31421419, Fax: +49-(30)-31421122, Email: [hildebrandt@chem.tu-berlin.de](mailto:hildebrandt@chem.tu-berlin.de)  
Tel: +49-(30)-31424128, Fax: +49-(30)-31478600, E-mail: [friedrich@chem.tu-berlin.de](mailto:friedrich@chem.tu-berlin.de)

#### Content:

1. Nomenclature of chromophore configurations
2. Fluorescence data analysis
3. Absorption spectra and photoconversion (Fig. S1)
4. Fluorescence spectra (Fig. S2)
5. RR spectra in the low frequency region (Figs. S3, S4)
6. IR difference spectra (Fig. S5)
7. RR spectra of further mutants (Figs. S6)
8. Correlation of Raman shifts with fluorescence quantum yields (Fig. S7)

## 1. Nomenclature of chromophore geometry



The geometry of the biliverdin chromophore is denoted according to the configuration (Z/E; Z - “zusammen”, E - “entgegen”) and conformation (s/a; s - syn, a - anti) of the methine bridges between the pyrrole rings A, B, C, and D. In the Pr ground state, the configuration is ZZZssa, in the Pfr state ZZEssa. In the protein, the cofactor is covalently attached to a cysteine via the ethylidene substituent at ring A. The C atoms in rings A–D are numbered for reference. Photon absorption leads to a photoinduced Z/E isomerization of the chromophore around the methine bridge between rings C and D. The figure was modified based on Fig. 1a from (Nieder et al., 2011).

Nieder, J.B., Stojkovic, E.A., Moffat, K., Forest, K.T., Lamparter, T., Bittl, R., and Kennis, J.T. (2011). Pigment-protein interactions in phytochromes probed by fluorescence line narrowing spectroscopy. *J. Phys. Chem. B* 117, 14940-14950.

## 2. Fluorescence data analysis

The fluorescence decays were analyzed employing a Levenberg-Marquardt algorithm for the minimization of the reduced  $\chi_r^2$  after iterative reconvolution with the instrumental response function (IRF). The value of  $\chi_r^2$  depends on a parameter set  $(p_1, \dots, p_n)$  of the chosen continuous fit function  $A(t, \lambda, p_1, \dots, p_n)$  for the temporally discrete fluorescence points  $F(t_v, \lambda)$ . The function  $\chi_r^2$  is evaluated in each time  $t_v$  channel ( $v = 1, 4096$ ) after convolution of the determined fit function  $A(t, \lambda, p_1, \dots, p_n)$  with the IRF and averaged over all time channels:

$$(S1) \quad \chi_r^2(p_1, \dots, p_n, \lambda) = \sum_{v=1}^{4096} \frac{1}{\sqrt{F(t_v, \lambda)}} \left( \frac{F(t_v, \lambda) - A(t_v, \lambda, p_1, \dots, p_n)}{\sqrt{F(t_v, \lambda)}} \right)^2$$

$A(t, \lambda, p_1, \dots, p_n)$  was chosen as a triexponential decay function

$$(S2) \quad A(t, \lambda) = \sum_{j=1}^3 a_j(\lambda) e^{-t/\tau_j},$$

with the parameters  $a_j(\lambda)$  and  $\tau_j$  denoting wavelength-dependent amplitude  $a_j(\lambda)$  and time constant  $\tau_j$  of the  $j^{\text{th}}$  exponential decay component for two components ( $n = 3$ ). The triexponential fits of all decay curves measured in one time- and wavelength resolved fluorescence spectrum were performed as global fits with common values of lifetimes  $\tau_j$  (linked parameters) for all decay curves and wavelength-dependent pre-exponential factors  $a_j(\lambda)$  (non-linked parameters). The result of this analysis is usually plotted as a graph of  $a_j(\lambda)$  for all wavelength independent lifetimes  $\tau_j$  representing so-called decay associated spectra (DAS) thus revealing the energetic position of individual decay components.

The quality of the fit was judged by the value of  $\chi_r^2$  and by the degree of randomness of residuals (difference between the experimental data points and the fit at each time point  $t_v$ ) to check for the absence of any correlation of the deviations in a certain time interval. For this judgment, the autocorrelation function of the residuals was calculated, which was around 1.0 for the whole time interval. For these calculations, the software of Globals Unlimited® (University of Illinois, Urbana, USA) was used. It was found that a sufficient quality of the fit could be achieved for fitting with  $n=3$  decay components ( $\chi_r^2 = 1.05$ ). No significant improvement was obtained with  $n>3$  decay components.

## 2. Absorption spectra and photoconversion

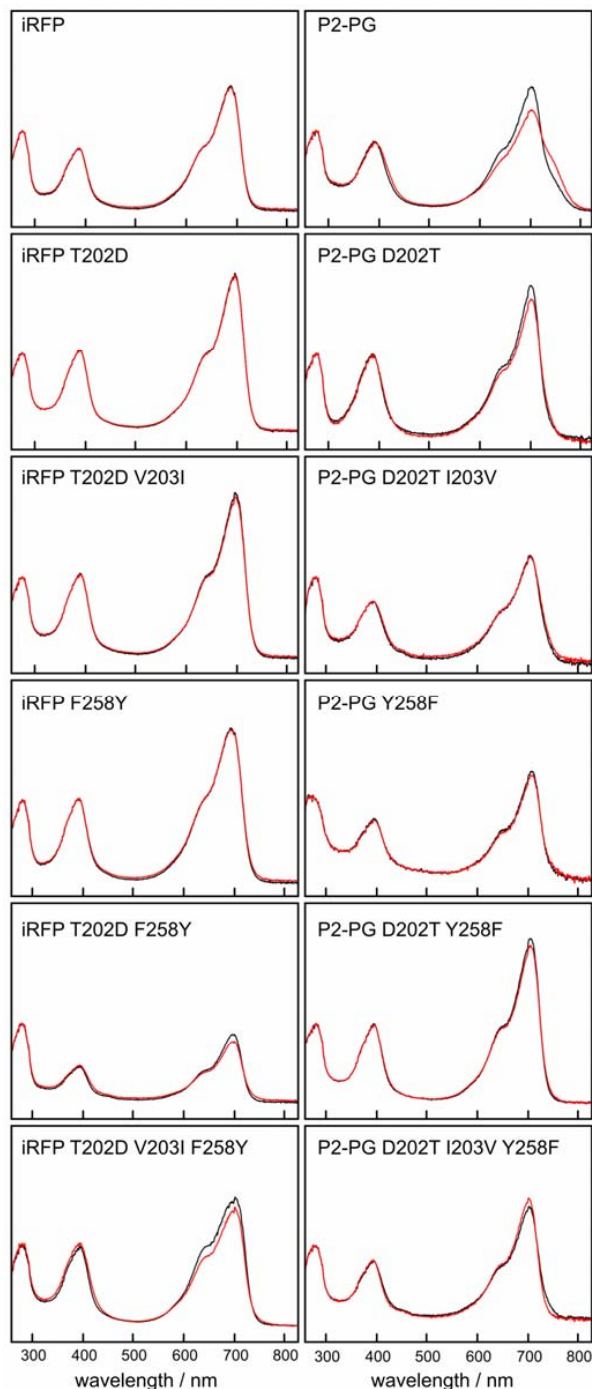


**Figure S1.** Normalized absorption spectra of P2PG, iRFP, and the mutants obtained via route A (right) and route B (left) showing the typical Soret (around 400 nm) and Q bands (around 700 nm) due to absorption of the biliverdin chromophore. Spectra measured before and after red-light irradiation (660 nm LED) are shown in black and red, respectively. Note that the photoactive variants only undergo a phototransformation to the Meta-R state which, due to the low extent of photoconversion, is typically reflected only by a decrease of the Q-band absorption. All spectra were normalized to the protein absorption peak at 280 nm.

### 3. Fluorescence spectra

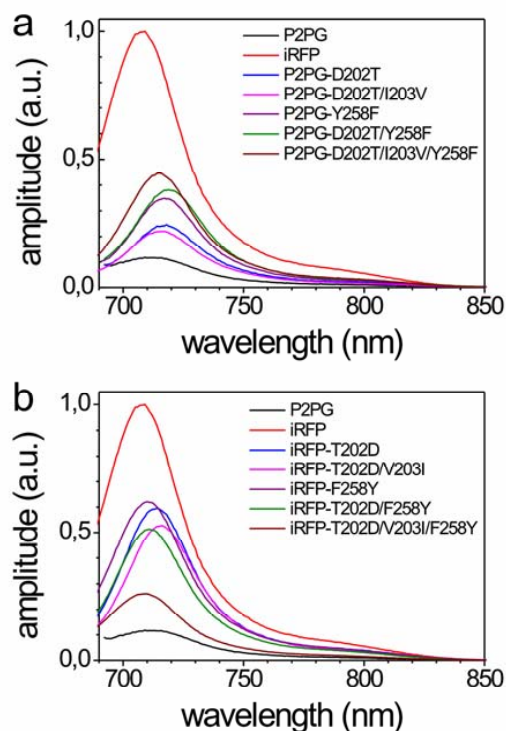


**Figure S2.** Fluorescence spectra measured for the various mutants, obtained via route A (left) and route B (right). For normalization, the fluorescence spectra were corrected according to the number of absorbed photons at the excitation wavelength according to the recorded UV/Vis absorption spectra using as a reference the published extinction coefficient of iRFP ( $85,000 \text{ M}^{-1} \text{ cm}^{-1}$ ) from ref. 11. Standard solutions of the dyes Atto 680 (Attotech) in  $\text{H}_2\text{O}$  and Nile Blue (Sigma Aldrich) in ethanol ( $\Phi_{\text{fl}} = 0.3/0.27$ ) were used as references to determine the iRFP quantum yield ( $\Phi_{\text{fl}} = 0.059$ ). Subsequently, iRFP was used as a reference for determining the fluorescence quantum yields of the other phytochrome variants.

#### 4. RR spectra in the low frequency region

Below  $700\text{ cm}^{-1}$  there are three medium intense Raman bands which may be assigned in analogy to previous vibrational analysis of the BV chromophore in the Pfr state of Agp2 (see manuscript). In that case, theoretical calculations predicted modes of considerable Raman intensity in this region that involve torsional and out-of-plane deformation coordinates of rings D, C, and ring B, as well as the N-H out-of-plane coordinate of ring B. Guided by the predicted Raman intensities and frequencies, we assign the peak at  $673\text{ cm}^{-1}$  ( $674\text{ cm}^{-1}$ ) of iRFP (P2-PG) to two closely spaced modes involving mainly torsional and out-of-plane deformation coordinates of rings C and D (Figure S3). The  $651\text{ cm}^{-1}$  band in the spectrum of iRFP ( $656\text{ cm}^{-1}$  for P2-PG) displays a small upshift upon H/D exchange which can be rationalized in terms of the involvement of the N-H out-of-plane coordinates in  $\text{H}_2\text{O}$  but not in  $\text{D}_2\text{O}$ . An even larger contribution of this coordinate is likely to be the origin for the disappearance of the  $659\text{ cm}^{-1}$  band of iRFP ( $663\text{ cm}^{-1}$  in P2-PG) in  $\text{D}_2\text{O}$ , where a new band at distinctly higher frequencies ( $690\text{ cm}^{-1}$ ) is detected instead. We therefore tentatively assign the  $659\text{-cm}^{-1}$  band (iRFP) to a mode of significant N-H out-of-plane character, presumably localized at ring B, and the  $651\text{-cm}^{-1}$  band to a torsional and out-of-plane deformation mode involving ring D (*vide supra*).

Inspection of the spectral changes brought about by the substitutions according to route A and B shows that the upshift of the HOOP mode from  $810\text{ cm}^{-1}$  (P2-PG) to  $813\text{ cm}^{-1}$  (iRFP) is produced by the single mutations at either the position 202 (D202T) or 258 (Y258F) (Figure S4). The latter replacement is also responsible for the intensity increase of the  $663\text{ cm}^{-1}$  band whereas the frequency shift of this band largely depend on the remote amino acid substitutions.

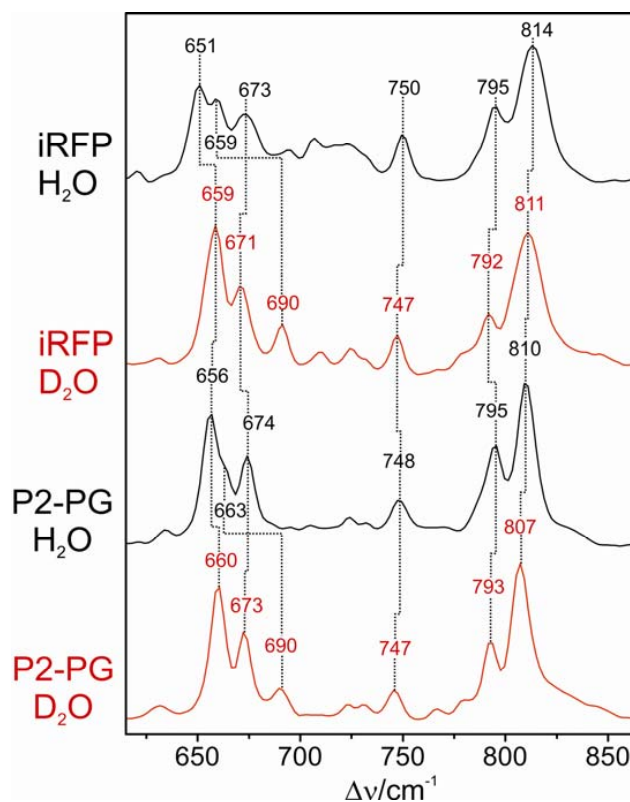


**Figure S3.** RR spectra of P2PG and iRFP in the HOOP region, measured from samples in  $\text{H}_2\text{O}$  (black) and  $\text{D}_2\text{O}$  (red).



## 5. IR difference spectra

### *Infrared difference spectroscopy*

IR difference spectroscopy can be employed only to those variants which undergo a photoisomerisation (Figure S5). Due to the lack of the PHY domain, the spectra of these variants do not display any major difference signals in the amide I and amide II region. However, the C=O stretching mode of ring D, which in the Pr state of P2PG is observed at  $1711\text{ cm}^{-1}$ , can clearly be identified in all photoactive variants, albeit at slightly higher frequencies. The corresponding ring A C=O stretching at  $1737\text{ cm}^{-1}$  (P2PG) can barely be detected suggesting that the position of this mode remains largely unchanged upon photoconversion.

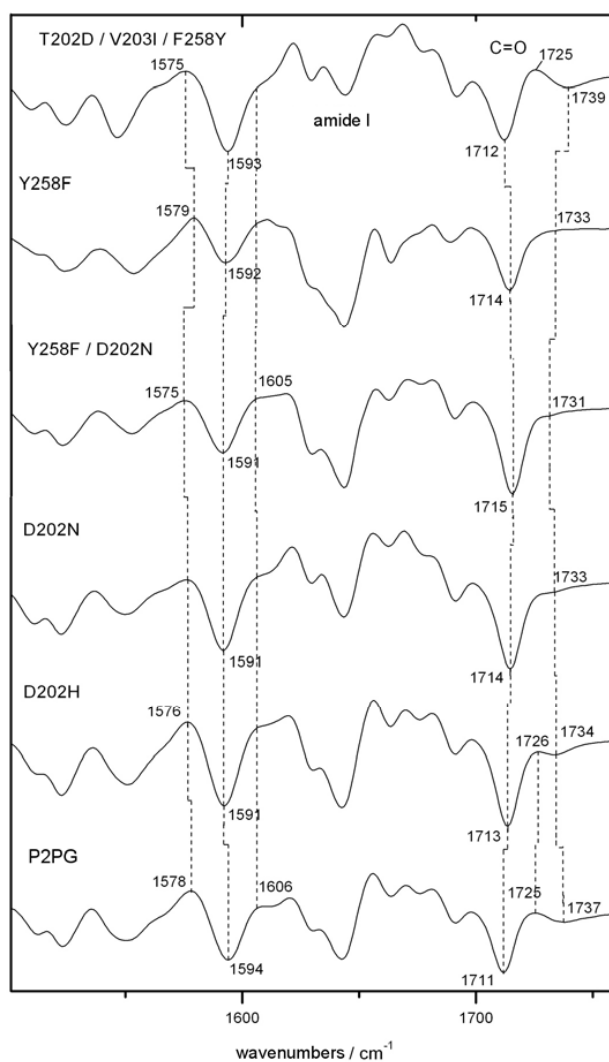


**Figure S5.** IR difference spectra obtained by subtracting the spectrum of the parent Pr state from that of the photoproduct obtained by 660 nm LED irradiation. Thus, negative and positive bands refer to the parent state and the photoproduct (usually a Meta-R state), respectively. The signals of the ring D and A carbonyl functions are observed between  $1710$  and  $1725\text{ cm}^{-1}$  and above  $1730\text{ cm}^{-1}$ , respectively. As expected, no major signals are observed in the amide I region.



## 6. RR spectra of further mutants

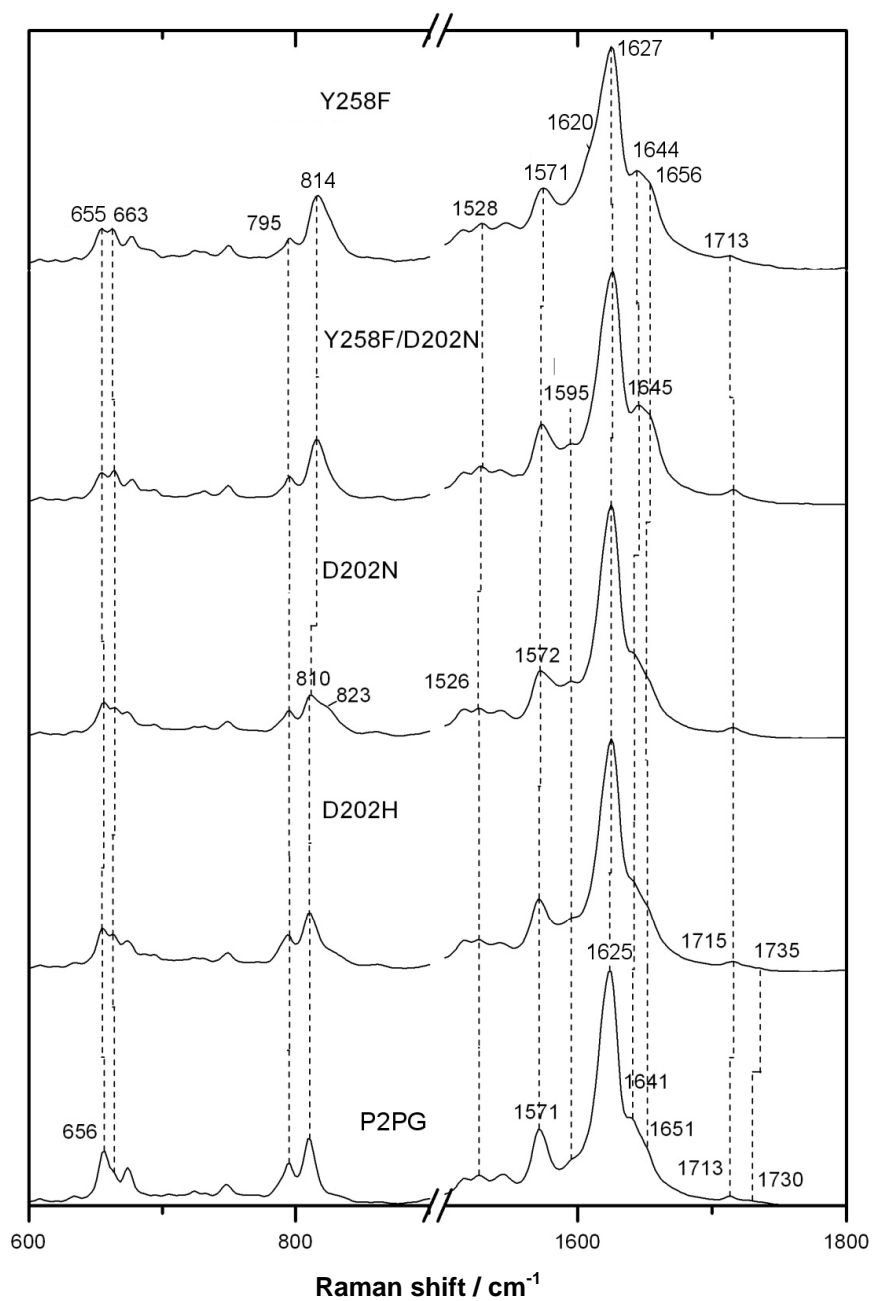


**Figure S6.** RR spectra of various mutants derived from P2PG.

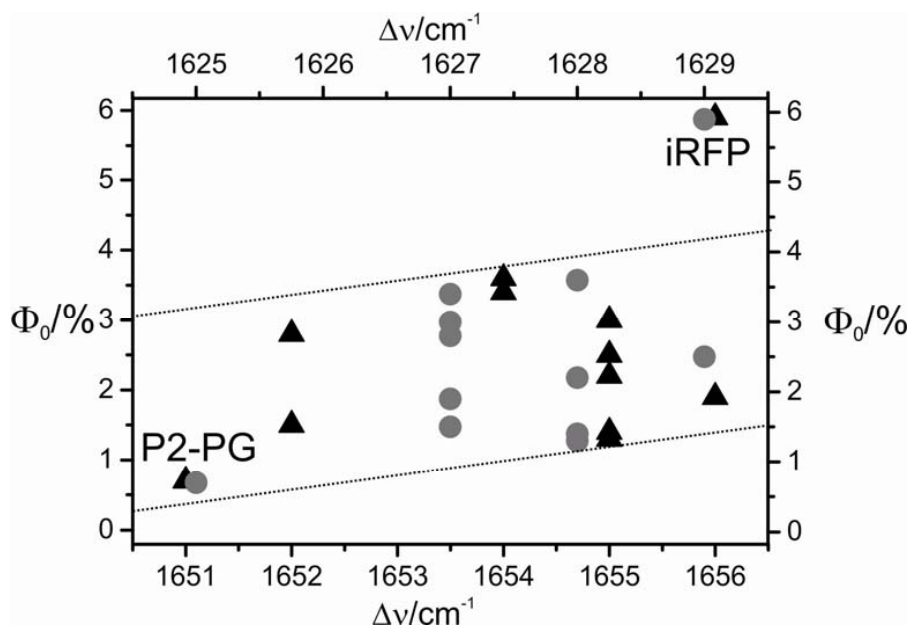


**Figure S7.** Correlation between the C=C stretching frequency of ring *D* (grey circles, upper abscissa) and the *A-B* methine bridge (high frequency component, black triangle, lower abscissa) and the experimentally determined fluorescence quantum yield  $\Phi_f$ .

## Supporting Information

### **Chromophore binding to two cysteines increases quantum yield of near-infrared fluorescent proteins**

David Buhrke<sup>1</sup>, Neslihan N. Tavraz<sup>1</sup>, Daria M. Shcherbakova<sup>2</sup>, Luisa Sauthof<sup>3</sup>, Marcus Moldenhauer<sup>1</sup>, Francisco Vélazquez Escobar<sup>1</sup>, Vladislav V. Verkhusha<sup>2</sup>, Peter Hildebrandt<sup>1</sup> and Thomas Friedrich<sup>1\*</sup>

<sup>1</sup> Institut für Chemie, Sekr. PC14, Technische Universität Berlin, Straße des 17. Juni 135, 10623 Berlin, Germany.

<sup>2</sup> Department of Anatomy and Structural Biology, Albert Einstein College of Medicine, 1300 Morris Park Avenue, Bronx, NY 10461, USA.

<sup>3</sup> Charité – Universitätsmedizin Berlin, Institute of Medical Physics and Biophysics (CC2), Group Protein X-ray Crystallography and Signal Transduction, Charitéplatz 1, 10117 Berlin, Germany.

\* Correspondence: [friedrich@chem.tu-berlin.de](mailto:friedrich@chem.tu-berlin.de)

#### **Contents**

1. Figure S1: SDS page and Zn<sup>2+</sup> fluorescence
2. Figure S2: Absorbance curves during GdnHCl denaturation
3. Figure S3: Calculation of the fluorescence quantum yield
4. Figure S4: Full-range resonance Raman spectra
5. Figure S5: iRFP682(CC) as isolated is a mixture of species containing double-attached chromophore and species with chromophore attached to the GAF domain.
6. Figure S6: Original photographs of gel images shown in Figure S1 and Figure 2C
7. Literature cited

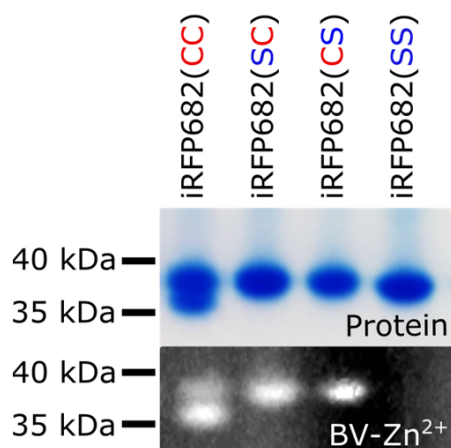


**Figure S1:** To investigate whether the chromophore was covalently attached to the respective apoproteins, SDS-PAGE with subsequent in-gel  $\text{Zn}^{2+}$  fluorescence assay was performed <sup>1</sup>. Upper panel: Coomassie blue staining shows a single band for all protein variants containing one Cys. iRFP682(CC) displays a second band characteristic for iRFPs with a double-Cys motif. Lower Panel: Except for the iRFP682(SS) variant, the chromophore is covalently attached to the protein, as indicated by the characteristic fluorescence of the BV- $\text{Zn}^{2+}$  complex. In-gel staining of biliverdin IX $\alpha$  bound to iRFP constructs was carried out as described <sup>1</sup>. The concentration of the protein samples loaded on the gel was 0.3 mg/ml (determined from the absorption at 280 nm calculated by ProtParam).

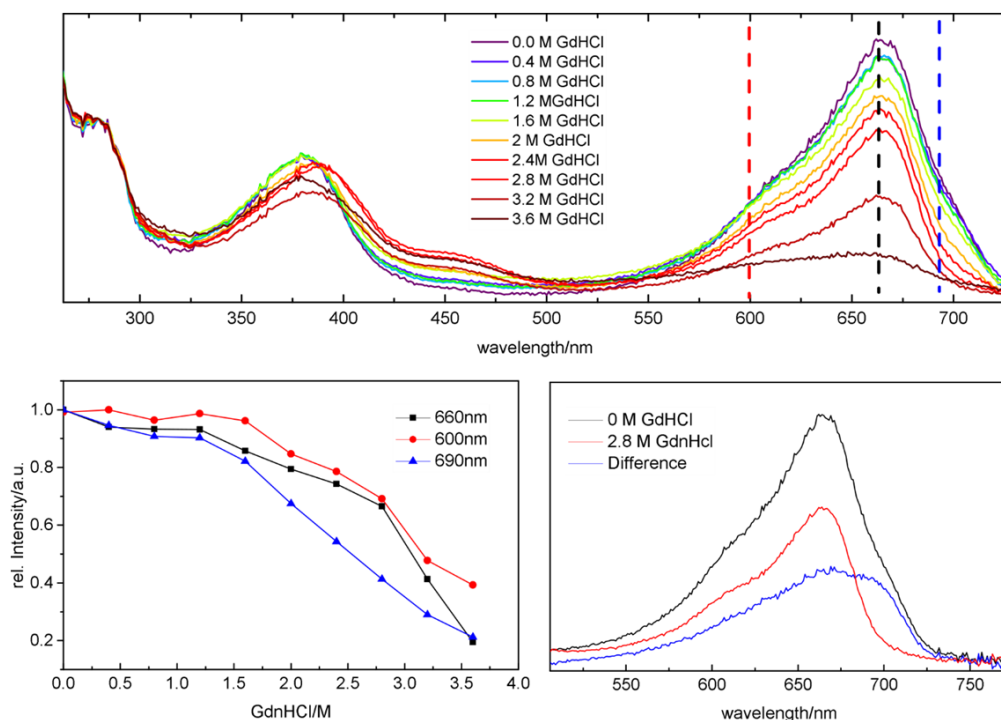


**Figure S2:** The affinity-purified iRFP682(CC) protein was titrated with GdnHCl as described previously<sup>2</sup> and the heterogeneous denaturation behavior, affecting contributions of the protein species with different chromophore attachment differently (i.e. those hypothesized to be due to the single- and double-attached form, and small fraction of the species with non-covalently bound chromophore absorbing at 690 nm), was reproduced (upper panel). At 2.8 M GdnHCl, the deviation of the relative absorption intensities at 660 nm and 690 nm is the largest (lower left panel), indicating that the more stable double-attached species could be maximally enriched under these conditions, whereas the least stable form with non-covalently attached chromophore absorbing at 690 nm is denatured together with less stable single-attached form. Therefore, these conditions were chosen to induce denaturation of the single-attachment species and size-exclusion chromatography was performed subsequently in order to isolate the non-denatured (double-attached) species (see Fig. 1 in main article). The absorption spectra of the iRFP682(CC) “as isolated”, of the sample enriched in double-attached species after the denaturation purification scheme, and the difference spectrum (corresponding to the single-attached species lost during purification) is shown in the lower right panel.

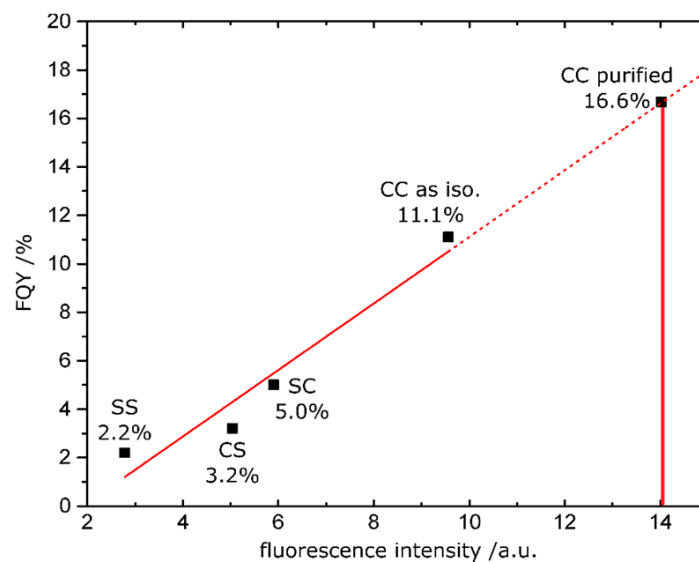


**Figure S3:** Calculation of the FQY of purified iRFP682(CC) from published data on the basis of FQY values determined for other protein variants in the literature (see Table 1 for references). The published FQY values were plotted against the experimentally determined integrated fluorescence intensities measured in a fluorescence spectrometer at defined protein concentrations (based on characteristic extinction coefficients). Linear extrapolation to the integrated fluorescence intensity measured for purified iRFP682(CC) yields an FQY of 16.6%.

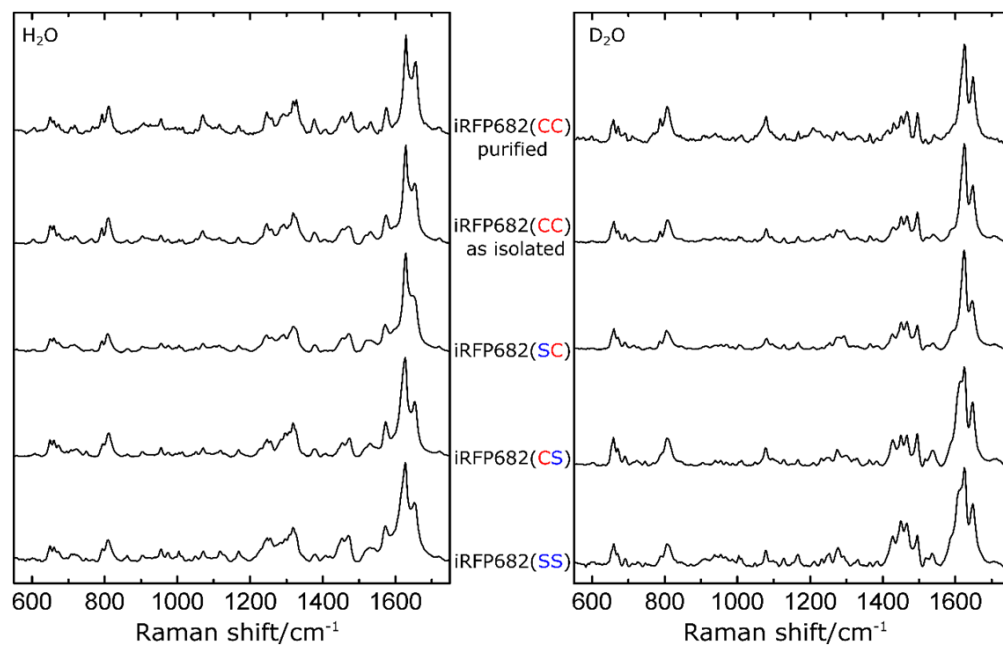


**Figure S4:** Full-range resonance Raman spectra of all investigated protein variants. The left panel shows measurements performed in H<sub>2</sub>O buffer, the right panel in D<sub>2</sub>O buffer.

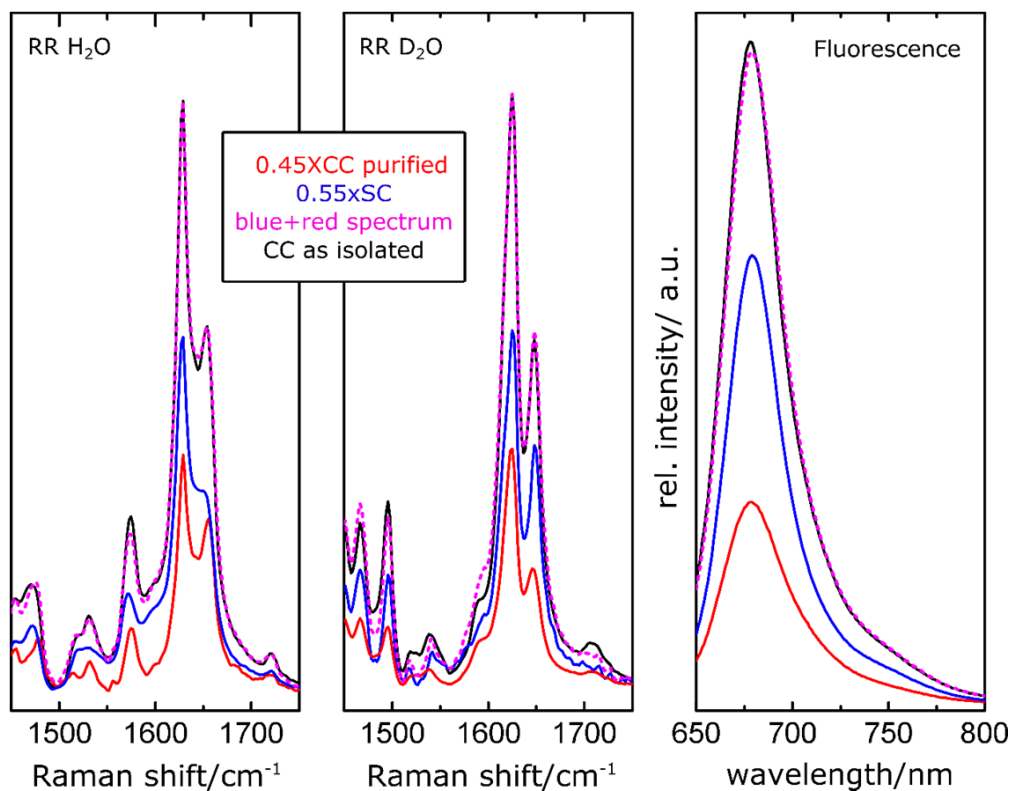


**Figure S5:** iRFP682(CC) as isolated is a mixture of species containing double-attached chromophore and species with chromophore attached to the GAF domain. The RR spectrum of iRFP682(CC) as isolated (black lines) represents a superposition of the pure double-attached species (red lines) and the single-attached species iRFP682(SC) (blue lines). The ratio of the spectral contributions is 0.45:0.55, as represented by the corresponding sum (magenta lines) of the spectra of single- and double-attached species, which matches the spectra of the “as isolated” species. Left panel: RR spectra in H<sub>2</sub>O, middle: in D<sub>2</sub>O. Right panel: fluorescence spectra according to the same color code.



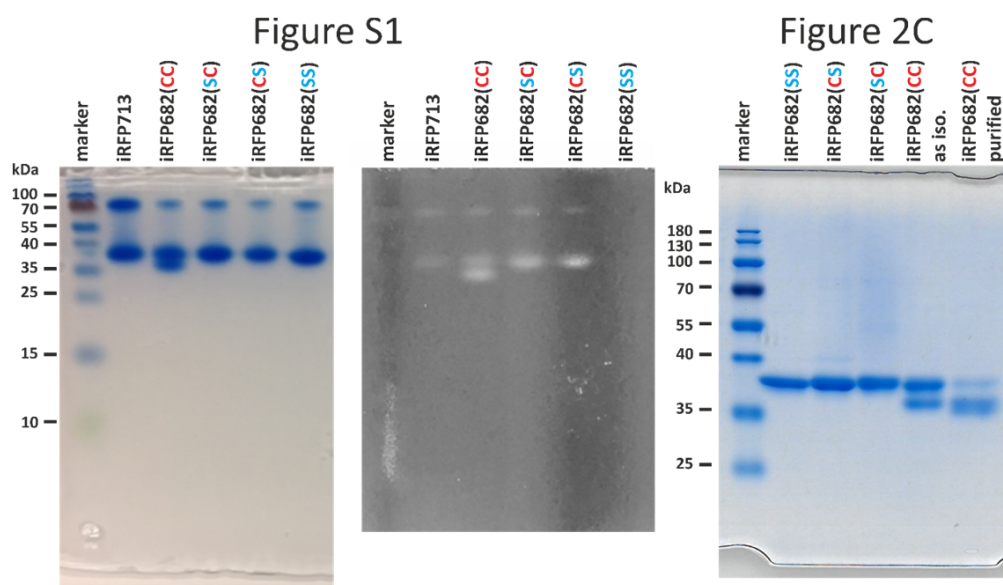


**Figure S6:** Original gel photographs of the Coomassie-stained SDS gel shown in Figure S1 (left panel), the corresponding in-gel  $\text{Zn}^{2+}$  staining fluorescence image (middle panel) and of the Coomassie-stained SDS gel shown in Figure 2C of the main manuscript.

#### Literature cited:

- 1 Raps, S. Differentiation between Phycobiliprotein and Colorless Linker Polypeptides by Fluorescence in the Presence of  $\text{ZnSO}_4$ . *Plant Physiol* **92**, 358-362 (1990).
- 2 Stepanenko, O. V. *et al.* Allosteric effects of chromophore interaction with dimeric near-infrared fluorescent proteins engineered from bacterial phytochromes. *Sci Rep* **6**, 18750, doi:10.1038/srep18750 (2016).

## List of Figures

1.2.1 Chemical formulae of the tetrapyrrole chromophores . . . . .	18
1.3.1 Phytochrome domain structure . . . . .	19
1.3.2 Modes of chromophore attachment . . . . .	20
1.3.3 PSM crystal structures of the Pr and Pfr state of phytochromes. . . . .	21
1.3.4 UV/Vis spectra of PCB SbPhyB . . . . .	22
1.3.5 Photocycle scheme of plant phytochromes . . . . .	23
1.4.1 UV/Vis spectra of Slr-GAF3 . . . . .	27
1.5.1 Chromophore binding pocket in canonical and bathy phytochromes . . . . .	29
1.6.1 Fluorescence imaging with iRFPs. . . . .	33
2.1.1 Jablonski diagram of vibrational absorption and scattering processes . . . . .	35
2.6.1 Pump-probe flowcell system for time-resolved RR spectroscopy . . . . .	47
2.7.1 Jablonski diagram of excited-state processes . . . . .	49
3.5.1 Schematic drawing of the Bruker RFS/100S FTR spectrometer . . . . .	58
3.6.1 Schematic drawing of the Bruker Tensor27 FTIR spectrometer . . . . .	59
4.2.1 Unsubtracted RR spectra of PIF3 and AtPhyB . . . . .	73
4.2.2 Full range RR spectra of AtPhyB with and without PIF3 (subtracted). . . . .	74
4.2.3 RR spectra of AtPhyB with PIF3 in the marker region . . . . .	76
4.2.4 RR spectra of AtphyB with PIF3 in the HOOP region . . . . .	77
4.3.1 SbPhyB PG crystal structure . . . . .	79
4.3.2 SbPhyB UV/Vis spectra . . . . .	80
4.3.3 SbPhyB RR spectra marker region . . . . .	82
4.3.4 SbPhyB RR spectra CO region . . . . .	83
4.3.5 SbPhyB RR spectra HOOP region . . . . .	85
4.3.6 SbPhyB IR difference spectra . . . . .	88
4.3.7 SbPhyB crystal spectra . . . . .	90
5.1.1 UV/Vis spectra of Slr-GAF3 . . . . .	93
5.1.2 T-dependent RR spectra of Slr-GAF3 in the marker region . . . . .	94
5.1.3 RR spectra of Slr-GAF3 and AnPixJg2 in the marker region . . . . .	95
5.1.4 Crystal structure of Slr-GAF3 PCB chromophore in the Pr and the Pg states . . . . .	99
6.2.1 IsPadC RR spectra marker region Pr state . . . . .	109
6.2.2 IsPadC RR spectra marker region photoactivated state . . . . .	110
6.2.3 IsPadC RR spectra HOOP region photoactivated state . . . . .	112
6.2.4 IsPadC RR spectra CO region Pr state . . . . .	113
6.2.5 IsPadC diff. IR spectra . . . . .	115
9.1.1 UV/Vis spectra of AtPhyB and SbPhyB . . . . .	148
9.1.2 Full range RR spectra of SbPhyB . . . . .	149
9.2.1 Full range RR spectra of Slr-GAF3 . . . . .	152
9.2.2 RR spectra of AnpoxJ and Agp1 with and without 10x imidazole excess . . . . .	153
9.2.3 pH-dependent RR spectra of Slr-GAF3 with imidazole excess . . . . .	154
9.2.4 Full range T dependent RR spectra of Slr-GAF3 . . . . .	155
9.2.5 RR spectra of Slr-GAF3 titration with imidazole . . . . .	156
9.2.6 Diff. IR spectra of Slr-GAF3 . . . . .	157
9.4.1 Unsubtracted IsPadC UV/Vis spectra . . . . .	169
9.4.2 Subtracted IsPadC UV/Vis spectra . . . . .	170
9.4.3 Full range IsPadC RR spectra in the Pr state . . . . .	171
9.4.4 Full range IsPadC RR spectra in the photo activated states . . . . .	172

9.4.5 IsPadC RR spectra HOOP region Pr state . . . . .	173
9.4.6 IsPadC RR spectra CO region photo activated state . . . . .	174
9.5.1 UV/Vis spectra of iRFP702, iRFP720, iRFP670 and cysteine mutants	177
9.5.2 RR spectra of iRFP 702 and 720 . . . . .	178
9.5.3 H <sub>2</sub> O RR spectra of iRFP670 and cysteine mutants . . . . .	179
9.5.4 D <sub>2</sub> O RR spectra of iRFP670 and cysteine mutants . . . . .	180

**List of Tables**

3.1	List of phytochrome samples . . . . .	52
3.2	List of iRFP samples . . . . .	54

## References

- [1] A. C. Albrecht and M. C. Hutley. *On the Dependence of Vibrational Raman Intensity on the Wavelength of Incident Light*. In: *J. Chem. Phys.* **55**.9 (1971), pp. 4438–4443.
- [2] A. C. Albrecht. *On the Theory of Raman Intensities*. In: *J. Chem. Phys.* **34**.5 (1961), pp. 1476–1484.
- [3] F. Andel, K. C. Hasson, F. Gai, P. A. Anfinrud, and R. A. Mathies. *Femtosecond time-resolved spectroscopy of the primary photochemistry of phytochrome*. In: *Biospectroscopy* **3**.6 (1997), pp. 421–433.
- [4] F. Andel, J. C. Lagarias, and R. A. Mathies. *Resonance Raman analysis of chromophore structure in the lumi-R photoproduct of phytochrome*. In: *Biochemistry* **35**.50 (1996), pp. 15997–16008.
- [5] K. Anders and L. O. Essen. *The family of phytochrome-like photoreceptors: Diverse, complex and multi-colored, but very useful*. In: *Curr. Opin. Struct. Biol.* **35** (2015), pp. 7–16.
- [6] K. Anders, G. Daminelli-Widany, M.-A. Mroginiski, D. von Stetten, and L. O. Essen. *Structure of the cyanobacterial phytochrome 2 photosensor implies a tryptophan switch for phytochrome signaling*. In: *J. Biol. Chem.* **288**.50 (2013), pp. 35714–35725.
- [7] P. W. Atkins. *Physical Chemistry*. **4**. Oxford University Press, 1990.
- [8] M. E. Auldridge, K. A. Satyshur, D. M. Anstrom, and K. T. Forest. *Structure-guided engineering enhances a phytochrome-based infrared fluorescent protein*. In: *J. Biol. Chem.* **287**.10 (2012), pp. 7000–7009.
- [9] M. Baloban, D. M. Shcherbakova, S. Pletnev, V. Z. Pletnev, J. C. Lagarias, and V. V. Verkhusha. *Designing brighter near-infrared fluorescent proteins: insights from structural and biochemical studies*. In: *Chem. Sci.* **00** (2017), pp. 1–12.
- [10] A. Barth and C. Zscherp. *What vibrations tell about proteins*. In: *Q. Rev. Biophys.* **35**.4 (2002).
- [11] D. Bellini and M. Z. Papiz. *Dimerization properties of the RpBphP2 chromophore-binding domain crystallized by homologue-directed mutagenesis*. In: *Acta Crystallogr. Sect. D Biol. Crystallogr.* **68**.8 (2012), pp. 1058–1066.
- [12] E. Betzig, R. Sougrat, W. Lindwasser, S. Olenych, J. S. Bonifacino, M. W. Davidson, J. Lippincott-Schwartz, H. F. Hess, and G. H. Patterson. *Imaging Intracellular Fluorescent Proteins at Nanometer Resolution*. In: *Science (80-. )*. **313**.2006 (2006), pp. 1642–1645.
- [13] S. Bhattacharya, M. E. Auldridge, H. Lehtivuori, J. A. Ihalainen, and K. T. Forest. *Origins of fluorescence in evolved bacteriophytochromes*. In: *J. Biol. Chem.* **289**.46 (2014), pp. 32144–32152.
- [14] S. H. Bhoo, S. J. Davis, J. Walker, B. Karniol, and R. D. Vierstra. *Bacteriophytochromes are photochromic histidine kinases using a biliverdin chromophore*. In: *Nature* **414**.6865 (2001), pp. 776–779.
- [15] A. Björling, O. Berntsson, H. Lehtivuori, H. Takala, A. J. Hughes, M. Panman, M. Hoernke, S. Niebling, L. Henry, R. Henning, I. Kosheleva, V. Chukharev, N. V. Tkachenko, A. Menzel, G. Newby, D. Khakhulin, M. Wulff, J. A. Ihalainen, and S. Westenhoff. *Structural photoactivation of a full-length bacterial phytochrome*. In: *Sci. Adv.* **2**.8 (2016), e1600920–e1600920.
- [16] A. Blumenstein, K. Vienken, R. Tasler, J. Purschwitz, D. Veith, N. Frankenberg-Dinkel, and R. Fischer. *The Aspergillus nidulans phytochrome FphA represses sexual development in red light*. In: *Curr. Biol.* **15**.20 (2005), pp. 1833–1838.
- [17] H. R. Bonomi, L. Toum, G. Sycz, R. Sieira, A. M. Toscani, G. E. Gudesblat, F. C. Leskow, F. A. Goldbaum, A. A. Vojnov, and F. Malamud. *Xanthomonas campestris attenuates virulence by sensing light through a bacteriophytochrome photoreceptor*. In: *EMBO Rep.* **17**.11 (2016), pp. 1565–1577.
- [18] B. Borucki, D. von Stetten, S. Seibeck, T. Lamparter, N. Michael, M.-A. Mroginiski, H. Otto, D. H. Murgida, M. P. Heyn, and P. Hildebrandt. *Light-induced proton release of phytochrome is coupled to the transient deprotonation of the tetrapyrrole chromophore*. In: *J. Biol. Chem.* **280**.40 (2005), pp. 34358–34364.

- [19] M. T. Boylan and P. H. Quail. *Oat Phytochrome Is Biologically Active in Transgenic Tomatoes*. In: *Plant Cell* **1.8** (1989), pp. 765–773.
- [20] S. Bretschneider, C. Eggeling, and S. W. Hell. *Breaking the diffraction barrier in fluorescence microscopy by optical shelving*. In: *Phys. Rev. Lett.* **98.21** (2007), p. 218103.
- [21] D. Buhrke, N. Tavraz, D. Shcherbakova, L. Sauthof, M. Moldenhauer, F. Velázquez Escobar, V. Verkhusha, P. Hildebrandt, and T. Friedrich. *Chromophore binding to two cysteines increases quantum yield of near-infrared fluorescent proteins*. In: *Scientific Reports* **9**.Article number: 1866 (2019). DOI: 10.1038/s41598-018-38433-2.
- [22] D. Buhrke, U. Kuhlmann, N. Michael, and P. Hildebrandt. *The Photoconversion of Phytochrome Includes an Unproductive Shunt Reaction Pathway*. In: *ChemPhysChem* **Volume 19**.Issue 5 (2018). DOI: 10.1002/cphc.201701311.
- [23] D. Buhrke, F. Velázquez Escobar, L. Sauthof, S. Wilkening, N. Herder, N. N. Tavraz, M. Willoweit, A. Keidel, T. Utesch, M. Mroginski, F. Schmitt, P. Hildebrandt, and T. Friedrich. *The role of local and remote amino acid substitutions for optimizing fluorescence in bacterio-phytochromes : A case study on iRFP*. In: *Scientific Reports* **6**.Article number: 28444 (2016). DOI: 10.1038/srep28444.
- [24] E. S. Burgie, J. Zhang, and R. D. Vierstra. *Crystal Structure of Deinococcus Phytochrome in the Photoactivated State Reveals a Cascade of Structural Rearrangements during Photoconversion*. In: *Structure* **24.3** (2016), pp. 448–457.
- [25] E. S. Burgie, J. M. Walker, G. N. Phillips, and R. D. Vierstra. *A photo-labile thioether linkage to phycoviolobilin provides the foundation for the blue/green photocycles in DXCF-cyanobacteriochromes*. In: *Structure* **21.1** (2013), pp. 88–97.
- [26] E. S. Burgie, A. N. Bussell, J. M. Walker, K. Dubiel, and R. D. Vierstra. *Crystal structure of the photosensing module from a red/far-red light-absorbing plant phytochrome*. In: *Proc. Natl. Acad. Sci. U. S. A.* **111.28** (2014), pp. 10179–84.
- [27] E. S. Burgie, T. Wang, A. N. Bussell, J. M. Walker, H. Li, and R. D. Vierstra. *Crystallographic and electron microscopic analyses of a bacterial phytochrome reveal local and global rearrangements during photoconversion*. In: *J. Biol. Chem.* **289.35** (2014), pp. 24573–24587.
- [28] E. S. Burgie, A. N. Bussell, S.-H. Lye, T. Wang, W. Hu, K. E. McLoughlin, E. L. Weber, H. Li, and R. D. Vierstra. *Photosensing and Thermosensing by Phytochrome B Require Both Proximal and Distal Allosteric Features within the Dimeric Photoreceptor*. In: *Sci. Rep.* **7.1** (2017), p. 13648.
- [29] W. L. Butler, K. H. Norris, H. W. Siegelman, and S. B. Hendricks. *Detection, assay, and preliminary purification of the pigment controlling photoresponsive development of plants*. In: *Proc. Natl. Acad. Sci. U. S. A.* **45.12** (1959), pp. 1703–8.
- [30] a. L. H. C. Butler, W.L. *Dark transformations of phytochromes in vivo. II*. In: *Plant Physiol* **40** (1965), pp. 13–17.
- [31] M. Chen and J. Chory. *Phytochrome signaling mechanisms and the control of plant development*. In: **21.11** (2012), pp. 664–671.
- [32] K. G. Chernov, T. A. Redchuk, E. S. Omelina, and V. V. Verkhusha. *Near-Infrared Fluorescent Proteins, Biosensors, and Optogenetic Tools Engineered from Phytochromes*. In: *Chem. Rev.* **117.9** (2017), pp. 6423–6446.
- [33] I. Chizhov, B. Zorn, D. J. Manstein, and W. Gärtner. *Kinetic and thermodynamic analysis of the light-induced processes in plant and cyanobacterial phytochromes*. In: *Biophys. J.* **105.9** (2013), pp. 2210–2220.
- [34] T. Clack, S. Mathews, and R. A. Sharrock. *The phytochrome apoprotein family in Arabidopsis is encoded by five genes: the sequences and expression of PHYD and PHYE*. In: *Plant Mol. Biol.* **25.3** (1994), pp. 413–427.
- [35] J. Dasgupta, R. R. Frontiera, K. C. Taylor, J. C. Lagarias, and R. A. Mathies. *Ultrafast excited-state isomerization in phytochrome revealed by femtosecond stimulated Raman spectroscopy*. In: *Proc. Natl. Acad. Sci. U. S. A.* **106.6** (2009), pp. 1784–1789.

- [36] S. J. Davis, A. V. Vener, and R. D. Vierstra. *Bacteriophytochromes: phytochrome-like photoreceptors from nonphotosynthetic eubacteria*. In: *Science (80-. )*. **286**.5449 (1999), pp. 2517–2520.
- [37] D. Duanmu, C. Bachy, S. Sudek, C.-H. Wong, V. Jimenez, N. C. Rockwell, S. S. Martin, C. Y. Ngan, E. N. Reistetter, M. J. van Baren, D. C. Price, C.-L. Wei, A. Reyes-Prieto, J. C. Lagarias, and A. Z. Worden. *Marine algae and land plants share conserved phytochrome signaling systems*. In: *Proc. Natl. Acad. Sci.* **111**.44 (2014), pp. 15827–15832.
- [38] P. Edlund, H. Takala, E. Claesson, L. Henry, R. Dods, H. Lehtivuori, M. Panman, K. Pande, T. White, T. Nakane, O. Berntsson, E. Gustavsson, P. B  th, V. Modi, S. Roy-Chowdhury, J. Zook, P. Berntsen, S. Pandey, I. Poudyal, J. Tenboer, C. Kupitz, A. Barty, P. Fromme, J. D. Koralek, T. Tanaka, J. Spence, M. Liang, M. S. Hunter, S. Boutet, E. Nango, K. Moffat, G. Groenhof, J. Ihalainen, E. A. Stojkovi  , M. Schmidt, and S. Westenhoff. *The room temperature crystal structure of a bacterial phytochrome determined by serial femtosecond crystallography*. In: *Sci. Rep.* **6**.October (2016), p. 35279.
- [39] P. Eilfeld and W. R  diger. *Absorption spectra of phytochrome intermediates*. In: *Zeitschrift f  r Naturforsch. - Sect. C J. Biosci.* **40**.1-2 (1985), pp. 109–114.
- [40] F. V. Escobar. *Vibrational spectroscopy of phytochromes and phytochrome-related photoreceptors*. PhD thesis. TU Berlin, 2015.
- [41] L.-O. Essen, J. Mailliet, and J. Hughes. *The structure of a complete phytochrome sensory module in the Pr ground state*. In: *Proc. Natl. Acad. Sci. U. S. A.* **105**.38 (2008), pp. 14709–14714.
- [42] K. Evans, A. P. Fordham-Skelton, H. Mistry, C. D. Reynolds, A. M. Lawless, and M. Z. Papiz. *A bacteriophytochrome regulates the synthesis of LH4 complexes in Rhodospseudomonas palustris*. In: *Photosynth. Res.* **85**.2 (2005), pp. 169–180.
- [43] R. P. Feynman. *QED - Die seltsame Theorie des Lichts und der Materie*. Piper M  nchen Z  rich, 1985.
- [44] G. S. Filonov, K. D. Piatkevich, L. M. Ting, J. Zhang, K. Kim, and V. V. Verkhusha. *Bright and stable near-infrared fluorescent protein for in vivo imaging*. In: *Nat Biotechnol* **29**.8 (2011), pp. 757–761.
- [45] A. J. Fischer and J. C. Lagarias. *Harnessing phytochrome’s glowing potential*. In: *Proc. Natl. Acad. Sci. U. S. A.* **101**.50 (2004), pp. 17334–17339.
- [46] A. E. Fitzpatrick, C. N. Lincoln, L. J. G. W. van Wilderen, and J. J. van Thor. *Pump-dump-probe and pump-repump-probe ultrafast spectroscopy resolves cross section of an early ground state intermediate and stimulated emission in the photoreactions of the Pr ground state of the cyanobacterial phytochrome Cph1*. In: *J. Phys. Chem. B* **116**.3 (2012), pp. 1077–1088.
- [47] S. P. Fodor, J. C. Lagarias, and R. A. Mathies. *Resonance Raman Analysis of the Pr and Pfr Forms of Phytochrome*. In: *Biochemistry* **29**.50 (1990), pp. 11141–11146.
- [48] A. E. Fortunato, M. Jaubert, G. Enomoto, J.-P. Bouly, R. Raniello, M. Thaler, S. Malviya, J. S. Bernardes, F. Rappaport, B. Gentili, M. J. Huysman, A. Carbone, C. Bowler, M. R. D’Alcal  , M. Ikeuchi, and A. Falciatore. *Diatom Phytochromes Reveal the Existence of Far-Red-Light-Based Sensing in the Ocean*. In: *Plant Cell* **28**.3 (2016), pp. 616–628.
- [49] A. Froehlich, B. Noh, and R. Vierstra. *Genetic and molecular analysis of phytochromes from the filamentous fungus Neurospora crassa*. In: *Eukaryot. Cell* **4**.12 (2005), p. 2140.
- [50] Y. Fukushima, M. Iwaki, R. Narikawa, M. Ikeuchi, Y. Tomita, and S. Itoh. *Photoconversion mechanism of a green/red photosensory cyanobacteriochrome AnPixJ: Time-resolved optical spectroscopy and FTIR analysis of the AnPixJ-GAF2 domain*. In: *Biochemistry* **50**.29 (2011), pp. 6328–6339.
- [51] K. Fushimi, N. C. Rockwell, G. Enomoto, Ni-Ni-Win, S. S. Martin, F. Gan, D. A. Bryant, M. Ikeuchi, J. C. Lagarias, and R. Narikawa. *Cyanobacteriochrome Photoreceptors Lacking the Canonical Cys Residue*. In: *Biochemistry* **55**.50 (2016), pp. 6981–6995.
- [52] F. Gan and D. A. Bryant. *Adaptive and acclimative responses of cyanobacteria to far-red light*. In: *Environ. Microbiol.* **17**.10 (2015), pp. 3450–3465.

- [53] F. Gan, S. Zhang, N. C. Rockwell, S. S. Martin, C. Lagarias, and D. a. Bryant. *Extensive remodeling of a cyanobacterial photosynthetic apparatus in far-red light*. In: *Science (80-. )*. **345**.August (2014), pp. 1–11.
- [54] E. Gasteiger, C. Hoogland, A. Gattiker, S. Duvaud, M. R. Wilkins, R. D. Appel, and A. Bairoch. *The Proteomics Protocols Handbook*. In: *Proteomics Protoc. Handb.* (2005), pp. 571–607.
- [55] B. N. G. Giepmans, S. R. Adams, M. H. Ellisman, and R. Y. Tsien. *The Fluorescent Toolbox for Assessing Protein Location and Function*. In: *Science (80-. )*. **312**.5771 (2006), pp. 217–224.
- [56] E. Giraud and A. Verméglio. *Bacteriophytochromes in anoxygenic photosynthetic bacteria*. In: *Photosynth. Res.* **97**.2 (2008), pp. 141–153.
- [57] E. Giraud, S. Zappa, L. Vuillet, J. M. Adriano, L. Hannibal, J. Fardoux, C. Berthomieu, P. Bouyer, D. Pignol, and A. Verméglio. *A new type of bacteriophytochrome acts in tandem with a classical bacteriophytochrome to control the antennae synthesis in Rhodopseudomonas palustris*. In: *J. Biol. Chem.* **280**.37 (2005), pp. 32389–32397.
- [58] J. Goedhart, D. von Stetten, M. Noirclerc-Savoye, M. Lelimosin, L. Joosen, M. A. Hink, L. van Weeren, T. W. Gadella, and A. Royant. *Structure-guided evolution of cyan fluorescent proteins towards a quantum yield of 93%*. In: *Nat. Commun.* **3** (2012), p. 751.
- [59] S. B. Gould, R. F. Waller, and G. I. McFadden. *Plastid Evolution*. In: *Annu. Rev. Plant Biol.* **59**.1 (2008), pp. 491–517.
- [60] G. Gourinchas, U. Heintz, and A. Winkler. *Asymmetric activation mechanism of a homodimeric red light-regulated photoreceptor*. In: *Elife* **7** (2018), pp. 1–25.
- [61] G. Gourinchas, S. Etzl, C. Göbl, U. Vide, T. Madl, and A. Winkler. *Long-range allosteric signaling in red light-regulated diguanylyl cyclases*. In: *Sci. Adv.* **3**.3 (2017), pp. 1–12.
- [62] V. Gruth. *Biophysikalische Interaktionsanalysen zwischen dem pflanzlichen Phytochrom B und Phytochrom Interaktionsfaktoren*. MA thesis. Philipps-Universität Marburg, 2016.
- [63] J. Hahn, H. M. Strauss, and P. Schmieder. *Heteronuclear NMR investigation on the structure and dynamics of the chromophore binding pocket of the cyanobacterial phytochrome Cph1*. In: *J. Am. Chem. Soc.* **130**.33 (2008), pp. 11170–11178.
- [64] J. Hahn, H. M. Strauss, F. T. Landgraf, H. F. Gimenez, G. Lochnit, P. Schmieder, and J. Hughes. *Probing protein-chromophore interactions in Cph1 phytochrome by mutagenesis*. In: *FEBS J.* **273**.7 (2006), pp. 1415–1429.
- [65] W. Herres and J. Gronholz. *Understanding FT-IR Data Processing*. In: *Comp. Anw. Lab.* **6** (1984), p. 3.
- [66] H. P. Hershey, J. T. Colbert, J. L. Lissemore, R. F. Barker, and P. H. Quail. *Molecular cloning of cDNA for Avena phytochrome*. In: *Proc. Natl. Acad. Sci. U. S. A.* **81**.8 (1984), pp. 2332–2336.
- [67] H. P. Hershey, R. F. Barker, K. B. Idler, J. L. Lissemore, and P. H. Quail. *Analysis of cloned cDNA and genomic sequences for pfaytochrome: complete amino acid sequences for two gene products expressed in etiolated Avena*. In: *Nucleic Acids Res.* **13**.23 (1985).
- [68] D. J. Heyes, B. Khara, M. Sakuma, S. J. O. Hardman, R. O’Cualain, S. E. J. Rigby, and N. S. Scrutton. *Ultrafast Red Light Activation of Synechocystis Phytochrome Cph1 Triggers Major Structural Change to Form the Pfr Signalling-Competent State*. In: *PLoS One* **7**.12 (2012).
- [69] P. Hildebrandt, A. Hoffmann, P. Lindemann, G. Heibel, S. E. Braslavsky, K. Schaffner, and B. Schrader. *Fourier transform resonance Raman spectroscopy of phytochrome*. In: *Biochemistry* **31**.34 (1992), pp. 7957–62.
- [70] P. Hildebrandt and F. Siebert. *Vibrational Spectroscopy in Life Science*. Wiley-VCH, 2008.
- [71] J. P. Hill and P. D. Buckley. *The use of pH indicators to identify suitable environments for freezing samples in aqueous and mixed aqueous/nonaqueous solutions*. In: *Analytical Biochemistry* **192**.2 (1991), pp. 358–361.



- 
- [72] Y. Hirose, R. Narikawa, M. Katayama, and M. Ikeuchi. *Cyanobacteriochrome CcaS regulates phycoerythrin accumulation in Nostoc punctiforme, a group II chromatic adapter*. In: *Proc. Natl. Acad. Sci.* **107**.19 (2010), pp. 8854–8859.
  - [73] Y. Hirose, N. C. Rockwell, K. Nishiyama, R. Narikawa, Y. Ukaji, K. Inomata, J. C. Lagarias, and M. Ikeuchi. *Green/red cyanobacteriochromes regulate complementary chromatic acclimation via a protochromic photocycle*. In: *Proc. Natl. Acad. Sci. U. S. A.* **110**.13 (2013), pp. 4974–9.
  - [74] Y. Hontani, D. M. Shcherbakova, M. Baloban, J. Zhu, V. V. Verkhusha, and J. T. M. Kennis. *Bright blue-shifted fluorescent proteins with Cys in the GAF domain engineered from bacterial phytochromes: fluorescence mechanisms and excited-state dynamics*. In: *Sci. Rep.* **6**.August (2016), p. 37362.
  - [75] M. Horch. *Structure-function Relationships of Metalloenzymes*. PhD thesis. TU Berlin, 2015.
  - [76] S. v. Horsten, S. Straß, N. Hellwig, V. Gruth, R. Klasen, A. Mielcarek, U. Linne, N. Morgner, and L.-O. Essen. *Mapping light-driven conformational changes within the photosensory module of plant phytochrome B*. In: *Nat. Publ. Gr.* June (2016), pp. 1–8.
  - [77] T. Hübschmann, T. Börner, E. Hartmann, and T. Lamparter. *Characterization of the Cph1 holo-phytochrome from Synechocystis sp. PCC 6803*. In: *Eur. J. Biochem.* **268**.7 (2001), pp. 2055–2063.
  - [78] J. Hughes. *Phytochrome Cytoplasmic Signaling*. In: *Annu. Rev. Plant Biol* **64**.1 (2013), pp. 377–402.
  - [79] J. Hughes. *Phytochrome three-dimensional structures and functions*. In: *Biochem. Soc. Trans.* **38** (2010), pp. 710–716.
  - [80] J. Hughes, T. Lamparter, F. Mittmann, E. Hartmann, and W. Gärtner. *A procariotic phytochrome*. In: *Nature* **386**.17 (1997), p. 663.
  - [81] J. A. Ihalainen, H. Takala, and H. Lehtivuori. *Fast Photochemistry of Prototypical Phytochromes-A Species vs. Subunit Specific Comparison*. In: *Front. Mol. Biosci.* **2**.December (2015), pp. 1–10.
  - [82] Inkscape. In: <http://inkscape.org> (2018).
  - [83] K. Inomata, S. Noack, M. A. S. Hammam, H. Khawn, H. Kinoshita, Y. Murata, N. Michael, P. Scheerer, N. Krauss, and T. Lamparter. *Assembly of synthetic locked chromophores with Agrobacterium phytochromes Agp1 and Agp2*. In: *Journal of Biological Chemistry* **281**.38 (2006), pp. 28162–28173.
  - [84] T. Ishizuka, R. Narikawa, T. Kohchi, M. Katayama, and M. Ikeuchi. *Cyanobacteriochrome TePixJ of Thermosynechococcus elongatus harbors phycoviolobin as a chromophore*. In: *Plant Cell Physiol.* **48**.9 (2007), pp. 1385–1390.
  - [85] T. Ishizuka, A. Kamiya, H. Suzuki, R. Narikawa, T. Noguchi, T. Kohchi, K. Inomata, and M. Ikeuchi. *The cyanobacteriochrome, TePixJ, isomerizes its own chromophore by converting phycocyanobilin to phycoviolobin*. In: *Biochemistry* **50**.6 (2011), pp. 953–961.
  - [86] Z. Jiang. *Bacterial Photoreceptor with Similarity to Photoactive Yellow Protein and Plant Phytochromes*. In: *Science (80-. )*. **285**.5426 (1999), pp. 406–409.
  - [87] J.-H. Jung, M. Domijan, C. Klose, S. Biswas, D. Ezer, M. Gao, A. K. Khattak, M. S. Box, V. Charoensawan, S. Cortijo, M. Kumar, A. Grant, J. C. W. Locke, E. Schäfer, K. E. Jaeger, and P. A. Wigge. *Phytochromes function as thermosensors in Arabidopsis*. In: *Science (80-. )*. **354**.6314 (2016), pp. 886–889.
  - [88] A. A. Kaberniuk, A. A. Shemetov, and V. V. Verkhusha. *An optogenetic system based on bacterial phytochrome controllable with near-infrared light*. In: *Nat Methods* **13**.7 (2016), pp. 591–597.
  - [89] S. Kacprzak, I. Njimonu, A. Renz, J. Feng, E. Reijerse, W. Lubitz, N. Krauss, P. Scheerer, S. Nagano, T. Lamparter, and S. Weber. *Intersubunit distances in full-length, dimeric, bacterial phytochrome Agp1, as measured by pulsed electron-electron double resonance (PELDOR) between different spin label positions, remain unchanged upon photoconversion*. In: *J. Biol. Chem.* **292**.18 (2017), pp. 7598–7606.

- [90] B. Karniol and R. D. Vierstra. *The pair of bacteriophytochromes from Agrobacterium tumefaciens are histidine kinases with opposing photobiological properties*. In: *Proc. Natl. Acad. Sci.* **100.5** (2003), pp. 2807–2812.
- [91] B. Karniol, J. R. Wagner, J. M. Walker, and R. D. Vierstra. *Phylogenetic analysis of the phytochrome superfamily reveals distinct microbial subfamilies of photoreceptors*. In: *Biochem. J.* **392**.Pt 1 (2005), pp. 103–116.
- [92] D. M. Kehoe and A. R. Grossman. *Complementary chromatic adaptation: photoperception to gene regulation*. 1994.
- [93] P. W. Kim, J. Pan, N. C. Rockwell, C. W. Chang, K. C. Taylor, J. Clark Lagarias, and D. S. Larsen. *Ultrafast E to Z photoisomerization dynamics of the Cph1 phytochrome*. In: *Chem. Phys. Lett.* **549** (2012), pp. 86–92.
- [94] P. W. Kim, N. C. Rockwell, L. H. Freer, C. W. Chang, S. S. Martin, J. C. Lagarias, and D. S. Larsen. *Unraveling the primary isomerization dynamics in cyanobacterial phytochrome Cph1 with multipulse manipulations*. In: *J. Phys. Chem. Lett.* **4.16** (2013), pp. 2605–2609.
- [95] J. Kirpich, L. T. Mix, S. S. Martin, N. C. Rockwell, J. C. Lagarias, and D. S. Larsen. *Protonation Heterogeneity Modulates the Ultrafast Photocycle Initiation Dynamics of Phytochrome Cph1*. In: *J. Phys. Chem. Lett.* (2018).
- [96] E. Kish, M. M. M. Pinto, D. Kirilovsky, R. Spezia, and B. Robert. *Echinenone vibrational properties: From solvents to the orange carotenoid protein*. In: *Biochim. Biophys. Acta - Bioenerg.* **1847.10** (2015), pp. 1044–1054.
- [97] T. A. Klar, E. Engel, and S. W. Hell. *Breaking Abbe’s diffraction resolution limit in fluorescence microscopy with stimulated emission depletion beams of various shapes*. In: *Phys. Rev.* **64.6** Pt 2 (2001), p. 066613.
- [98] C. Kneip. *FT-NIR-Resonanz-Raman-spektroskopische Untersuchungen an Phytochrom und Tetrapyrrolpigmenten aus Cyanobakterien*. PhD thesis. Gesamthochschule Duisburg, 1998.
- [99] C. Kneip, P. Hildebrandt, W. Schlamann, S. E. Braslavsky, F. Mark, and K. Schaffner. *Protonation state and structural changes of the tetrapyrrole chromophore during the Pr to Pfr phototransformation of phytochrome: A resonance raman spectroscopic study*. In: *Biochemistry* **38.46** (1999), pp. 15185–15192.
- [100] L. Koenig and A. C. Angood. *Spectra of Poly(ethylene Glycols) in Solution*. In: *Journal of Polymer ScienceE* **8** (1970), pp. 1787–1796.
- [101] I. Kraiselburd, L. Moyano, A. Carrau, J. Tano, and E. G. Orellano. *Bacterial Photosensory Proteins and Their Role in Plant-pathogen Interactions*. In: *Photochem. Photobiol.* **93.3** (2017), pp. 666–674.
- [102] H. A. Kramers and W. Heisenberg. *Über die Streuung von Strahlung durch Atome*. In: *Zeitschrift für Phys.* **31.1** (1925), pp. 681–708.
- [103] N. Krauss, S. Nagano, P. Scheerer, K. Zubow, N. Michael, K. Inomata, and T. Lamparter. *Structures of the photosensory core module of bacteriophytochrome Agp1 from two crystal forms reveal plasticity of the Pr state*. In: *Acta Crystallogr. Sect. A Found. Adv.* **72.a1** (2016), s228–s229.
- [104] J. L.-Yao, A. Kaberniuk, L. Li, D. Shcherbakova, R. Zhang, L. Wang, G. Li, and V. V. Verkhusha. *Multiscale photoacoustic tomography using reversibly switchable bacterial phytochrome as a near-infrared photochromic probe*. 2015.
- [105] J. C. Lagarias and H. Rapoport. *Chromopeptides from phytochrome. The structure and linkage of the PR form of the phytochrome chromophore*. In: *J. Am. Chem. Soc.* **102.6** (1980), pp. 4821–4828.
- [106] T. Lamparter, F. Mittmann, W. Gärtner, T. Börner, E. Hartmann, and J. Hughes. *Characterization of recombinant phytochrome from the cyanobacterium Synechocystis*. In: *Proc. Natl. Acad. Sci. U. S. A.* **94.22** (1997), pp. 11792–7.
- [107] T. Lamparter. *Evolution of cyanobacterial and plant phytochromes*. In: *FEBS Lett.* **573.1-3** (2004), pp. 1–5.

- [108] T. Lamparter, N. Krauß, and P. Scheerer. *Phytochromes from Agrobacterium fabrum*. In: *Photochem. Photobiol.* **93.3** (2017), pp. 642–655.
- [109] T. Lamparter and N. Michael. *Agrobacterium phytochrome as an enzyme for the production of ZZE bilins*. In: *Biochemistry* **44.23** (2005), pp. 8461–8469.
- [110] T. Lamparter, M. Carrascal, N. Michael, E. Martinez, G. Rottwinkel, and J. Abian. *The Biliverdin Chromophore Binds Covalently to a Conserved Cysteine Residue in the N-Terminus of Agrobacterium Phytochrome Agp1*. In: *Biochemistry* **43.12** (2004), pp. 3659–3669.
- [111] F. W. Larimer, P. Chain, L. Hauser, J. Lamerdin, S. Malfatti, L. Do, M. L. Land, D. A. Pelletier, J. T. Beatty, A. S. Lang, F. R. Tabita, J. L. Gibson, T. E. Hanson, C. Bobst, J. L. T. Y. Torres, C. Peres, F. H. Harrison, J. Gibson, and C. S. Harwood. *Complete genome sequence of the metabolically versatile photosynthetic bacterium Rhodospseudomonas palustris*. In: *Nat. Biotechnol.* **22.1** (2004), pp. 55–61.
- [112] M. Legris, C. Klose, E. S. Burgie, C. C. R. Rojas, M. Neme, A. Hiltbrunner, P. A. Wigge, E. Schäfer, R. D. Vierstra, and J. J. Casal. *Phytochrome B integrates light and temperature signals in Arabidopsis*. In: *Science* **354.6314** (2016), pp. 897–900.
- [113] H. Lehtivuori, I. Rissanen, H. Takala, J. Bamford, N. V. Tkachenko, and J. A. Ihalainen. *Fluorescence properties of the chromophore-binding domain of bacteriophytochrome from Deinococcus radiodurans*. In: *J. Phys. Chem. B* **117.38** (2013), pp. 11049–11057.
- [114] H. Lehtivuori, S. Bhattacharya, N. M. Angenent-Mari, K. A. Satyshur, and K. T. Forest. *Removal of Chromophore-Proximal Polar Atoms Decreases Water Content and Increases Fluorescence in a Near Infrared Phytofluor*. In: *Front. Mol. Biosci.* **2**.November (2015), pp. 65–69.
- [115] A. Levskaya, A. A. Chevalier, J. J. Tabor, Z. B. Simpson, L. A. Lavery, E. A. D. Matthew Levy, A. Scouras, A. D. Ellington, E. M. Marcotte, and C. A. Voigt. *Engineering Escherichia coli to see light*. In: *Nature* **438.7067** (2005), p. 441.
- [116] F.-W. Li, M. Melkonian, C. J. Rothfels, J. C. Villarreal, D. W. Stevenson, S. W. Graham, G. K.-S. Wong, K. M. Pryer, and S. Mathews. *Phytochrome diversity in green plants and the origin of canonical plant phytochromes*. In: *Nat. Commun.* **6** (2015), p. 7852.
- [117] F. Li, E. S. Burgie, T. Yu, A. Héroux, G. C. Schatz, R. D. Vierstra, and A. M. Orville. *X-ray radiation induces deprotonation of the bilin chromophore in crystalline D. Radiodurans phytochrome*. In: *J. Am. Chem. Soc.* **137.8** (2015), pp. 2792–2795.
- [118] S. W. Lin, G. G. Kochendoerfer, K. S. Carroll, D. Wang, R. A. Mathies, and T. P. Sakmar. *Mechanisms of Spectral Tuning in Blue Cone Visual Pigments*. In: **273.38** (1998), pp. 24583–24591.
- [119] M. Linke, Y. Yang, B. Zienicke, M. A. S. Hammam, T. von Haimberger, A. Zacarias, K. Inomata, T. Lamparter, and K. Heyne. *Electronic transitions and heterogeneity of the bacteriophytochrome Pr absorption band: An angle balanced polarization resolved femtosecond VIS pump-IR probe study*. In: *Biophys. J.* **105.8** (2013), pp. 1756–1766.
- [120] D. A. Long. *The Raman Effect: A Unified Treatment of the Theory of Raman Scattering by Molecules*. John Wiley and Sons Ltd, 2002.
- [121] M. Luck, S. Bruun, A. Keidel, P. Hegemann, and P. Hildebrandt. *Photochemical chromophore isomerization in histidine kinase rhodopsin HKR1*. In: *FEBS Lett.* **589.10** (2015), pp. 1067–1071.
- [122] J. Mailliet, G. Psakis, K. Feilke, V. Sineshchekov, L. O. Essen, and J. Hughes. *Spectroscopy and a high-resolution crystal structure of Tyr263 mutants of cyanobacterial phytochrome Cph1*. In: *J. Mol. Biol.* **413.1** (2011), pp. 115–127.
- [123] E. G. Maksimov, N. N. Sluchanko, Y. B. Slonimskiy, E. A. Slutskaya, A. V. Stepanov, A. M. Argentova-Stevens, E. A. Shirshin, G. V. Tsoraev, K. E. Klementiev, O. V. Slatinskaya, E. P. Lukashev, T. Friedrich, V. Z. Paschenko, and A. B. Rubin. *The photocycle of orange carotenoid protein conceals distinct intermediates and asynchronous changes in the carotenoid and protein components*. In: *Sci. Rep.* **7.1** (2017), p. 15548.

- [124] T. Mathes, J. Ravensbergen, M. Klotz, T. Gleichmann, K. D. Gallagher, N. C. Weitowich, R. St. Peter, S. E. Kovaleva, E. A. Stojković, and J. T. Kennis. *Femto- to Microsecond Photodynamics of an Unusual Bacteriophytochrome*. In: *J. Phys. Chem. Lett.* **6**.2 (2015), pp. 239–243.
- [125] S. Mathews. *Algae hold clues to eukaryotic origins of plant phytochromes*. In: *Proc. Natl. Acad. Sci.* **111**.44 (2014), pp. 15608–15609.
- [126] S. Mathews. *Evolutionary Studies Illuminate the Structural-Functional Model of Plant Phytochromes*. In: *Plant Cell* **22**.1 (2010), pp. 4–16.
- [127] M. Medzihradszky, J. Bindics, E. Adam, A. Viczian, E. Klement, S. Lorrain, P. Gyula, Z. Merai, C. Fankhauser, K. F. Medzihradszky, T. Kunkel, E. Schafer, and F. Nagy. *Phosphorylation of Phytochrome B Inhibits Light-Induced Signaling via Accelerated Dark Reversion in Arabidopsis*. In: *Plant Cell* **25**.2 (2013), pp. 535–544.
- [128] A. Miyawaki, D. M. Shcherbakova, and V. V. Verkhusha. *Red fluorescent proteins: Chromophore formation and cellular applications*. In: *Curr. Opin. Struct. Biol.* **22**.5 (2012), pp. 679–688.
- [129] A. Möglich, X. Yang, R. A. Ayers, and K. Moffat. *Structure and function of plant photoreceptors*. In: *Annu Rev Plant Biol* **61** (2010), pp. 21–47.
- [130] A. Möglich and K. Moffat. *Engineered photoreceptors as novel optogenetic tools*. In: *Photochem. Photobiol. Sci.* **9**.10 (2010), pp. 1286–1300.
- [131] M. Moldenhauer, N. N. Sluchanko, D. Buhrke, D. V. Zlenko, N. N. Tavraz, F.-J. Schmitt, P. Hildebrandt, E. G. Maksimov, and T. Friedrich. *Assembly of photoactive orange carotenoid protein from its domains unravels a carotenoid shuttle mechanism*. In: *Photosynth. Res.* (2017), pp. 1–15. DOI: 10.1007/s11120-017-0353-3.
- [132] M. Moldenhauer, N. N. Sluchanko, N. N. Tavraz, C. Junghans, D. Buhrke, M. Willoweit, L. Chiappisi, F.-J. Schmitt, V. Vukojevic, E. A. Shirshin, V. Y. Ponomarev, V. Z. Paschenko, M. Gradzielski, E. G. Maksimov, and T. Friedrich. *Interaction of the signaling state analog and the apoprotein form of the orange carotenoid protein with the fluorescence recovery protein*. In: *Photosynth. Res.* (2017), pp. 1–15. DOI: 10.1007/s11120-017-0346-2.
- [133] B. L. Montgomery and J. C. Lagarias. *Phytochrome ancestry: Sensors of bilins and light*. In: *Trends Plant Sci.* **7**.8 (2002), pp. 357–366.
- [134] M. A. Mroginiski, D. von Stetten, S. Kaminski, F. Velázquez Escobar, N. Michael, G. Daminelli-Widany, and P. Hildebrandt. *Elucidating photoinduced structural changes in phytochromes by the combined application of resonance Raman spectroscopy and theoretical methods*. In: *J. Mol. Struct.* **993**.1-3 (2011), pp. 15–25.
- [135] M.-A. Mroginiski, D. von Stetten, F. Velázquez Escobar, H. M. Strauss, S. Kaminski, P. Scheerer, M. Günther, D. H. Murgida, P. Schmieder, C. Bongards, W. Gärtner, J. Maillet, J. Hughes, L. O. Essen, and P. Hildebrandt. *Chromophore structure of cyanobacterial phytochrome Cph1 in the Pr state: Reconciling structural and spectroscopic data by QM/MM calculations*. In: *Biophys. J.* **96**.10 (2009), pp. 4153–4163.
- [136] M.-A. Mroginiski, S. Kaminski, D. von Stetten, S. Ringsdorf, W. Gärtner, L. O. Essen, and P. Hildebrandt. *Structure of the chromophore binding pocket in the Pr state of plant phytochrome phyA*. In: *J. Phys. Chem. B* **115**.5 (2011), pp. 1220–1231.
- [137] K. Müller, R. Engesser, J. Timmer, F. Nagy, M. D. Zurbriggen, and W. Weber. *Synthesis of phycocyanobilin in mammalian cells*. In: *Chem. Commun.* **49**.79 (2013), p. 8970.
- [138] S. Nagano, P. Scheerer, K. Zubow, N. Michael, K. Inomata, T. Lamparter, and N. Krauß. *The crystal structures of the N-terminal photosensory core module of Agrobacterium phytochrome App1 as parallel and anti-parallel dimers*. In: *J. Biol. Chem.* **291**.39 (2016), pp. 20674–20691.
- [139] R. Narikawa, G. Enomoto, Ni-Ni-Win, K. Fushimi, and M. Ikeuchi. *A new type of dual-cys cyanobacteriochrome GAF domain found in cyanobacterium Acaryochloris marina, which has an unusual red/blue reversible photoconversion cycle*. In: *Biochemistry* **53**.31 (2014), pp. 5051–5059.
- [140] R. Narikawa, Y. Fukushima, T. Ishizuka, S. Itoh, and M. Ikeuchi. *A Novel Photoactive GAF Domain of Cyanobacteriochrome AnPixJ That Shows Reversible Green/Red Photoconversion*. In: *J. Mol. Biol.* **380**.5 (2008), pp. 844–855.

- 
- [141] R. Narikawa, K. Fushimi, Ni-Ni-Win, and M. Ikeuchi. *Red-shifted red/green-type cyanobacteriochrome AM1-1870g3 from the chlorophyll d-bearing cyanobacterium Acaryochloris marina*. In: *Biochem. Biophys. Res. Commun.* **461**.2 (2015), pp. 390–395.
  - [142] R. Narikawa, T. Ishizuka, N. Muraki, T. Shiba, G. Kurisu, and M. Ikeuchi. *Structures of cyanobacteriochromes from phototaxis regulators AnPixJ and TePixJ reveal general and specific photoconversion mechanism*. In: *Proc. Natl. Acad. Sci. U. S. A.* **110** (2013), pp. 918–923.
  - [143] H. Naumann, D. H. Murgida, M. Engelhard, J. P. Klare, and P. Hildebrandt. *Time-resolved resonance Raman spectroscopy of sensory rhodopsin II in the micro- and millisecond time range using gated cw excitation*. In: *J. Raman Spectrosc.* **37**.1-3 (2006), pp. 436–441.
  - [144] W. Ni, S.-L. Xu, R. J. Chalkley, T. N. D. Pham, S. Guan, D. A. Maltby, A. L. Burlingame, Z.-Y. Wang, and P. H. Quail. *Multisite light-induced phosphorylation of the transcription factor PIF3 is necessary for both its rapid degradation and concomitant negative feedback modulation of photoreceptor phyB levels in Arabidopsis*. In: *Plant Cell* **25**.7 (2013), pp. 2679–98.
  - [145] J. B. Nieder, E. A. Stojković, K. Moffat, K. T. Forest, T. Lamparter, R. Bittl, and J. T. M. Kennis. *Pigment-protein interactions in phytochromes probed by fluorescence line narrowing spectroscopy*. In: *J. Phys. Chem. B* **117**.48 (2013), pp. 14940–14950.
  - [146] M. B. Nielsen. *Model systems for understanding absorption tuning by opsin proteins*. In: (2009).
  - [147] K. Nito, C. C. L. Wong, J. R. Yates, and J. Chory. *Tyrosine Phosphorylation Regulates the Activity of Phytochrome Photoreceptors*. In: *Cell Rep.* **3**.6 (2013), pp. 1970–1979.
  - [148] I. Njimonu and T. Lamparter. *Temperature effects on agrobacterium phytochrome agp1*. In: *PLoS One* **6**.10 (2011).
  - [149] S. Noack, N. Michael, R. Rosen, and T. Lamparter. *Protein conformational changes of Agrobacterium phytochrome Agp1 during chromophore assembly and photoconversion*. In: *Biochemistry* **46**.13 (2007), pp. 4164–4176.
  - [150] I. Oberpichler, R. Rosen, A. Rasouly, M. Vugman, E. Z. Ron, and T. Lamparter. *Light affects motility and infectivity of Agrobacterium tumefaciens*. In: *Environ. Microbiol.* **10**.8 (2008), pp. 2020–2029.
  - [151] Origin. In: *OriginLab, Northampton, MA* (2018).
  - [152] Y. Orii and M. Morita. *Measurement of the pH of frozen buffer solutions by using pH indicators*. In: *Journal of biochemistry* (1977).
  - [153] L. H. Otero, S. Klinke, J. Rinaldi, F. Velázquez Escobar, M. A. Mroginski, M. Fernández López, F. Malamud, A. A. Vojnov, P. Hildebrandt, F. A. Goldbaum, and H. R. Bonomi. *Structure of the Full-Length Bacteriophytochrome from the Plant Pathogen Xanthomonas campestris Provides Clues to its Long-Range Signaling Mechanism*. In: *J. Mol. Biol.* **428**.19 (2016), pp. 3702–3720.
  - [154] N. Pandey, B. E. Kuypers, B. Nassif, E. E. Thomas, R. N. Alnahhas, L. Segatori, and J. J. Silberg. *Tolerance of a Knotted Near-Infrared Fluorescent Protein to Random Circular Permutation*. In: *Biochemistry* **55**.27 (2016), pp. 3763–3773.
  - [155] F. Pennacchietti, A. Losi, X.-l. Xu, K.-h. Zhao, W. Gartner, C. Viappiani, F. Cella, A. Diaspro, and S. Abbruzzetti. *Photochromic conversion in a red/green cyanobacteriochrome from Synechocystis PCC6803: quantum yields in solution and photoswitching dynamics in living E. coli cells*. In: *Photochem. Photobiol. Sci.* **14**.2 (2015), pp. 229–237.
  - [156] B.-K. Phee, J.-I. Kim, D. H. Shin, J. Yoo, K.-J. Park, Y.-J. Han, Y.-K. Kwon, M.-H. Cho, J.-S. Jeon, S. H. Bhoo, and T.-R. Hahn. *A novel protein phosphatase indirectly regulates phytochrome-interacting factor 3 via phytochrome*. In: *Biochem. J.* **415**.2 (2008), pp. 247–255.
  - [157] K. D. Piatkevich, F. V. Subach, and V. V. Verkhusha. *Engineering of bacterial phytochromes for near-infrared imaging, sensing, and light-control in mammals*. In: *Chem. Soc. Rev.* **42**.8 (2013), pp. 3441–52.
  - [158] K. D. Piatkevich, F. V. Subach, and V. V. Verkhusha. *Far-red light photoactivatable near-infrared fluorescent proteins engineered from a bacterial phytochrome*. In: *Nat. Commun.* **4** (2013), p. 2153.

- [159] P. Piwowarski, E. Ritter, K. P. Hofmann, P. Hildebrandt, D. von Stetten, P. Scheerer, N. Michael, T. Lamparter, and F. Bartl. *Light-induced activation of bacterial phytochrome Agp1 monitored by static and time-resolved FTIR spectroscopy*. In: *ChemPhysChem* **11.6** (2010), pp. 1207–1214.
- [160] L. H. Pratt. *Molecular properties of phytochrome. Review Article*. In: *Photochem. Photobiol.* **27** (1978), pp. 105–811.
- [161] F. G. Prendergast and K. G. Manni. *Chemical and Physical Properties of Aequorin and the Green Fluorescent Protein Isolated from Aequorea forskilea*. In: *Biochemistry* **17.17** (1978), pp. 3448–3453.
- [162] P. H. Quail. *Phytochrome photosensory signalling networks*. In: *Nat. Rev. Mol. Cell Biol.* **3.2** (2002), pp. 85–93.
- [163] E. Reichhart, A. Ingles-Prieto, A. M. Tichy, C. McKenzie, and H. Janovjak. *A phytochrome sensory domain permits receptor activation by red light*. In: *Angew. Chemie - Int. Ed.* **55.21** (2016), pp. 6339–6342.
- [164] C. Rivetti, A. Mozzarelli, G. L. Rossi, E. R. Henry, and W. A. Eaton. *Oxygen Binding by Single Crystals of Hemoglobin*. In: *Biochemistry* **32.11** (1993), pp. 2888–2906.
- [165] N. C. Rockwell and J. C. Lagarias. *A brief history of phytochromes*. In: *ChemPhysChem* **11.6** (2010), pp. 1172–1180.
- [166] N. C. Rockwell and J. C. Lagarias. *Phytochrome diversification in cyanobacteria and eukaryotic algae*. In: *Curr. Opin. Plant Biol.* **37** (2017), pp. 87–93.
- [167] N. C. Rockwell, S. S. Martin, and J. C. Lagarias. *Identification of Cyanobacteriochromes Detecting Far-Red Light*. In: *Biochemistry* **55.28** (2016), pp. 3907–3919.
- [168] N. C. Rockwell, S. S. Martin, and J. C. Lagarias. *Mechanistic insight into the photosensory versatility of DXCF cyanobacteriochromes*. In: *Biochemistry* **51.17** (2012), pp. 3576–3585.
- [169] N. C. Rockwell, S. S. Martin, A. G. Gulevich, and J. C. Lagarias. *Conserved phenylalanine residues are required for blue-shifting of cyanobacteriochrome photoproducts*. In: *Biochemistry* **53.19** (2014), pp. 3118–3130.
- [170] N. C. Rockwell, D. Duanmu, S. Shelley, C. Bachy, D. C. Price, D. Bhattacharya, A. Z. Worden, J. C. Lagarias, N. C. Rockwell, D. Duanmu, S. S. Martin, C. Bachy, D. C. Price, and D. Bhattacharya. *Correction for Rockwell et al., Eukaryotic algal phytochromes span the visible spectrum*. In: *Proc. Natl. Acad. Sci.* **112.9** (2015), E1051–E1051.
- [171] N. C. Rockwell, L. Shang, S. S. Martin, and J. C. Lagarias. *Distinct classes of red/far-red photochemistry within the phytochrome superfamily*. In: *Proc. Natl. Acad. Sci. U. S. A.* **106.15** (2009), pp. 6123–7.
- [172] N. C. Rockwell, S. S. Martin, K. Feoktistova, and J. C. Lagarias. *Diverse two-cysteine photocycles in phytochromes and cyanobacteriochromes*. In: *Proc. Natl. Acad. Sci. U. S. A.* **108.29** (2011), pp. 11854–11859.
- [173] N. C. Rockwell, S. S. Martin, F. Gan, D. A. Bryant, and J. C. Lagarias. *NpR3784 is the prototype for a distinctive group of red/green cyanobacteriochromes using alternative Phe residues for photoproduct tuning*. In: *Photochem. Photobiol. Sci.* **14.2** (2015), pp. 258–269.
- [174] N. C. Rockwell, S. S. Martin, A. G. Gulevich, and J. C. Lagarias. *Phycoviolobin formation and spectral tuning in the DXCF cyanobacteriochrome subfamily*. In: *Biochemistry* **51.7** (2012), pp. 1449–1463.
- [175] E. A. Rodriguez, G. N. Tran, L. A. Gross, J. L. Crisp, J. Y. Lin, and R. Y. Tsien. *A far-red fluorescent protein evolved from a cyanobacterial phycobiliprotein*. In: *Nat Methods* **13.9** (2017), pp. 763–769.
- [176] E. A. Rodriguez, R. E. Campbell, J. Y. Lin, M. Z. Lin, A. Miyawaki, A. E. Palmer, X. Shu, J. Zhang, and R. Y. Tsien. *The Growing and Glowing Toolbox of Fluorescent and Photoactive Proteins*. In: *Trends Biochem. Sci.* **42.2** (2017), pp. 111–129.
- [177] G. Rottwinkel, I. Oberpichler, and T. Lamparter. *Bathy phytochromes in rhizobial soil bacteria*. In: *J. Bacteriol.* **192.19** (2010), pp. 5124–5133.

- 
- [178] W. Rüdiger, F. Thümmel, E. Cmiel, and S. Schneider. *Chromophore structure of the physiologically active form (Pfr) of phytochrome*. In: *Proc. Natl. Acad. Sci. U. S. A.* **80**.20 (1983), pp. 6244–6248.
  - [179] K. A. Rumyantsev, D. M. Shcherbakova, N. I. Zakharova, A. V. Emelyanov, K. K. Turoverov, and V. V. Verkhusha. *Minimal domain of bacterial phytochrome required for chromophore binding and fluorescence*. In: *Sci. Rep.* **5**.November (2015), p. 18348.
  - [180] M. J. Rust, M. Bates, and X. W. Zhuang. *Sub-diffraction-limit imaging by stochastic optical reconstruction microscopy (STORM)*. In: *Nat Methods* **3**.10 (2006), pp. 793–795.
  - [181] J. S. Ryu, J. I. Kim, T. Kunkel, B. C. Kim, D. S. Cho, S. H. Hong, S. H. Kim, A. P. Fernández, Y. Kim, J. M. Alonso, J. R. Ecker, F. Nagy, P. O. Lim, P. S. Song, E. Schäfer, and H. G. Nam. *Phytochrome-specific type 5 phosphatase controls light signal flux by enhancing phytochrome stability and affinity for a signal transducer*. In: *Cell* **120**.3 (2005), pp. 395–406.
  - [182] M. H. Ryu and M. Gomelsky. *Near-infrared light responsive synthetic c-di-GMP module for optogenetic applications*. In: *ACS Synth. Biol.* **3**.11 (2014), pp. 802–810.
  - [183] J. Salewski, F. Velázquez Escobar, S. Kaminski, D. von Stetten, A. Keidel, Y. Rippers, N. Michael, P. Scheerer, P. Piwowarski, F. Bartl, N. Frankenberg-Dinkel, S. Ringsdorf, W. Gärtner, T. Lamparter, M.-A. Mrogiński, and P. Hildebrandt. *Structure of the biliverdin cofactor in the Pfr state of bathy and prototypical phytochromes*. In: *J. Biol. Chem.* **288**.23 (2013), pp. 16800–16814.
  - [184] A. A. Samma, C. K. Johnson, S. Song, S. Alvarez, and M. Zimmer. *On the origin of fluorescence in bacteriophytochrome infrared fluorescent proteins*. In: *J. Phys. Chem. B* **114**.46 (2010), pp. 15362–15369.
  - [185] A. Schmidt, L. Sauthof, M. Szczepek, M. Fernández López, F. Velázquez Escobar, B. M. Qureshi, N. Michael, D. Buhrke, T. Stevens, D. Kwiatkowski, D. von Stetten, M. Mrogiński, N. Krauss, T. Lamparter, P. Hildebrandt, and P. Scheerer. *Structural snapshot of a bacterial phytochrome in its functional intermediate state*. In: *Nat. Commun.* **9**.4912 (2018), pp. 1–13. DOI: 10.1038/s41467-018-07392-7.
  - [186] C. Schumann, R. Groß, N. Michael, T. Lamparter, and R. Diller. *Sub-picosecond mid-infrared spectroscopy of phytochrome Agp1 from Agrobacterium tumefaciens*. In: *ChemPhysChem* **8**.11 (2007), pp. 1657–1663.
  - [187] R. A. Sharrock and P. H. Quail. *Novel phytochrome sequences in Arabidopsis thaliana: structure, evolution, and differential expression of a plant regulatory photoreceptor family*. In: *Genes Dev.* **3**.11 (1989), pp. 1745–1757.
  - [188] D. M. Shcherbakova, M. Baloban, and V. V. Verkhusha. *Near-infrared fluorescent proteins engineered from bacterial phytochromes*. In: *Curr. Opin. Chem. Biol.* **27** (2015), pp. 52–63.
  - [189] D. M. Shcherbakova, O. M. Subach, and V. V. Verkhusha. *Red fluorescent proteins: Advanced imaging applications and future design*. In: *Angew. Chemie - Int. Ed.* **51**.43 (2012), pp. 10724–10738.
  - [190] D. M. Shcherbakova and V. V. Verkhusha. *Near-infrared fluorescent proteins for multicolor in vivo imaging*. In: *Nat. Methods* **10**.8 (2013), pp. 751–754.
  - [191] D. M. Shcherbakova, M. Baloban, A. V. Emelyanov, M. Brenowitz, P. Guo, and V. V. Verkhusha. *Bright monomeric near-infrared fluorescent proteins as tags and biosensors for multiscale imaging*. In: *Nat. Commun.* **7** (2016), p. 12405.
  - [192] D. M. Shcherbakova, M. Baloban, S. Pletnev, V. N. Malashkevich, H. Xiao, Z. Dauter, and V. V. Verkhusha. *Molecular Basis of Spectral Diversity in Near-Infrared Phytochrome-Based Fluorescent Proteins*. In: *Chem. Biol.* **22**.11 (2015), pp. 1540–1551.
  - [193] D. M. Shcherbakova, A. A. Shemetov, A. A. Kaberniuk, and V. V. Verkhusha. *Natural Photoreceptors as a Source of Fluorescent Proteins, Biosensors, and Optogenetic Tools*. In: *Annu. Rev. Biochem.* **84**.1 (2014), p. 150223145439006.
  - [194] O. Shimomura, F. H. Johnson, and Y. Saiga. *Extraction, Purification and Properties of Aequorin, a Bioluminescent Protein from the Luminous Hydromedusan, Aequorea*. In: *J. Cell. Comp. Physiol.* **59**.3 (1962), pp. 223–239.

- [195] A.-Y. Shin, Y.-J. Han, A. Baek, T. Ahn, S. Y. Kim, T. S. Nguyen, M. Son, K. W. Lee, Y. Shen, P.-S. Song, and J.-I. Kim. *Evidence that phytochrome functions as a protein kinase in plant light signalling*. In: *Nat. Commun.* **7**.May (2016), p. 11545.
- [196] X. Shu, A. Ryan, M. Z. Lin, T. A. Aguilera, V. Lev-Ram, P. A. Steinbach, and R. Y. Tsien. *Mammalian Expression of Fluorescent Proteins Engineered from a Bacterial Phytochrome*. In: *Science (80-. )*. **324**.5928 (2009), pp. 804–807.
- [197] V. Sineshchekov, J. Mailliet, G. Psakis, K. Feilke, J. Kopycki, M. Zeidler, L. O. Essen, and J. Hughes. *Tyrosine 263 in cyanobacterial phytochrome Cph1 optimizes photochemistry at the prelum-R→lum-R step*. In: *Photochem. Photobiol.* **90**.4 (2014), pp. 786–795.
- [198] C. Slavov, X. Xu, K. H. Zhao, W. Gärtner, and J. Wachtveitl. *Detailed insight into the ultra-fast photoconversion of the cyanobacteriochrome Slr1393 from Synechocystis sp.* In: *Biochim. Biophys. Acta - Bioenerg.* **1847**.10 (2015), pp. 1335–1344.
- [199] H. Smith. *Phytochromes and light signal perception by plants - An emerging synthesis*. In: *Nature* **407**.6804 (2000), pp. 585–591.
- [200] C. Song, M.-A. Mroginiski, C. Lang, J. Kopycki, W. Gärtner, J. Matysik, J. Hughes, and J. C. Lagarias. *3D Structures of Plant Phytochrome A as Pr and Pfr From Solid-State NMR : Implications for Molecular Function Chemical Shift Assignments of the*. In: *Front. Plant Sci.* **9**.April (2018), pp. 1–15.
- [201] C. Song, F. Velázquez Escobar, X. L. Xu, R. Narikawa, M. Ikeuchi, F. Siebert, W. Gärtner, J. Matysik, and P. Hildebrandt. *A Red/Green Cyanobacteriochrome Sustains Its Color Despite a Change in the Bilin Chromophors Protonation State*. In: *Biochemistry* **54**.38 (2015), pp. 5839–5848.
- [202] C. Song, L.-O. Essen, W. Gärtner, J. Hughes, and J. Matysik. *Solid-state NMR spectroscopic study of chromophore-protein interactions in the Pr ground state of plant phytochrome A*. In: *Mol. Plant* **5**.3 (2012), pp. 698–715.
- [203] C. Song, G. Psakis, J. Kopycki, C. Lang, J. Matysik, and J. Hughes. *The D-ring, not the A-ring, rotates in Synechococcus OS-B' phytochrome*. In: *J. Biol. Chem.* **289**.5 (2014), pp. 2552–2562.
- [204] K. M. Spillane, J. Dasgupta, and R. A. Mathies. *Conformational homogeneity and excited-state isomerization dynamics of the bilin chromophore in phytochrome cph1 from resonance raman intensities*. In: *Biophys. J.* **102**.3 (2012), pp. 709–717.
- [205] K. M. Spillane, J. Dasgupta, J. C. Lagarias, and R. A. Mathies. *Homogeneity of phytochrome Cph1 vibronic absorption revealed by resonance raman intensity analysis*. In: *J. Am. Chem. Soc.* **131**.39 (2009), pp. 13946–13948.
- [206] O. V. Stepanenko, G. S. Bublikov, O. V. Stepanenko, D. M. Shcherbakova, V. V. Verkhusha, K. K. Turoverov, and I. M. Kuznetsova. *A knot in the protein structure - Probing the near-infrared fluorescent protein iRFP designed from a bacterial phytochrome*. In: *FEBS J.* **281**.9 (2014), pp. 2284–2298.
- [207] O. V. Stepanenko, M. Baloban, G. S. Bublikov, D. M. Shcherbakova, O. V. Stepanenko, K. K. Turoverov, I. M. Kuznetsova, and V. V. Verkhusha. *Allosteric effects of chromophore interaction with dimeric near-infrared fluorescent proteins engineered from bacterial phytochromes*. In: *Sci. Rep.* **6**.November 2015 (2016), p. 18750.
- [208] O. V. Stepanenko, O. V. Stepanenko, I. M. Kuznetsova, D. M. Shcherbakova, V. V. Verkhusha, and K. K. Turoverov. *Interaction of biliverdin chromophore with near-infrared fluorescent protein BphP1-FP engineered from bacterial phytochrome*. In: *Int. J. Mol. Sci.* **18**.5 (2017).
- [209] A. M. Stock, V. L. Robinson, and P. N. Goudreau. *Two-Component Signal Transduction*. In: *Annu. Rev. Biochem.* **69**.1 (2000), pp. 183–215.
- [210] E. A. Stojković, K. C. Toh, M. T. A. Alexandre, M. Baclayon, K. Moffat, and J. T. M. Kennis. *FTIR spectroscopy revealing light-dependent refolding of the conserved tongue region of bacteriophytochrome*. In: *J. Phys. Chem. Lett.* **5**.15 (2014), pp. 2512–2515.



- [211] D. Stöppler, C. Song, B. J. van Rossum, M. A. Geiger, C. Lang, M.-A. Mroginiski, A. P. Jagtap, S. T. Sigurdsson, J. Matysik, J. Hughes, and H. Oschkinat. *Dynamic Nuclear Polarization Provides New Insights into Chromophore Structure in Phytochrome Photoreceptors*. In: *Angew. Chemie - Int. Ed.* **55**.52 (2016), pp. 16017–16020.
- [212] F. V. Subach, K. D. Piatkevich, and V. V. Verkhusha. *Directed molecular evolution to design advanced red fluorescent proteins*. In: *Nat Methods* **8**.12 (2011), p. 1026.
- [213] H. Takala, H. Lehtivuori, H. Hammarén, V. P. Hytönen, J. A. Ihalainen, R. D. Vierstra, M. Weik, E. F. Garman, P. V. Konarev, D. I. Svergun, A. J. McCoy, N. W. Moriarty, R. Oeffner, R. J. Read, D. C. Richardson, J. S. Richardson, T. C. Terwilliger, P. H. Zwart, and S. Westenhoff. *Connection between Absorption Properties and Conformational Changes in Deinococcus radiodurans Phytochrome*. In: *Biochemistry* **53**.45 (2014), pp. 7076–7085.
- [214] H. Takala, A. Björling, M. Linna, S. Westenhoff, and J. A. Ihalainen. *Light-induced changes in the dimerization interface of bacteriophytochromes*. In: *J. Biol. Chem.* **290**.26 (2015), pp. 16383–16392.
- [215] H. Takala, S. Niebling, O. Berntsson, A. Björling, H. Lehtivuori, H. Häkkänen, M. Panman, E. Gustavsson, M. Hoernke, G. Newby, F. Zontone, M. Wulff, A. Menzel, J. A. Ihalainen, and S. Westenhoff. *Light-induced structural changes in a monomeric bacteriophytochrome*. In: *Struct. Dyn.* **3**.5 (2016).
- [216] H. Takala, H. Lehtivuori, O. Berntsson, A. Hughes, R. Nanekar, S. Niebling, M. Panman, L. Henry, A. Menzel, S. Westenhoff, and J. A. Ihalainen. *On the (un)coupling of the chromophore, tongue interactions and overall conformation in a bacterial phytochrome*. In: *J. Biol. Chem.* (2018), jbc.RA118.001794.
- [217] H. Takala, A. Björling, O. Berntsson, H. Lehtivuori, S. Niebling, M. Hoernke, I. Kosheleva, R. Henning, A. Menzel, J. A. Ihalainen, and S. Westenhoff. *Signal amplification and transduction in phytochrome photosensors*. In: *Nature* **509**.7499 (2014), pp. 245–8.
- [218] A. Takiden, F. Velázquez Escobar, J. Dragelj, A. L. Woelke, E. W. Knapp, P. Piwowarski, F. Bartl, P. Hildebrandt, and M.-A. Mroginiski. *Structural and Vibrational Characterization of the Chromophore Binding Site of Bacterial Phytochrome Agp1*. In: *Photochem. Photobiol.* **93**.3 (2017), pp. 713–723.
- [219] K. C. Toh, E. A. Stojković, I. H. M. van Stokkum, K. Moffat, and J. T. M. Kennis. *Fluorescence quantum yield and photochemistry of bacteriophytochrome constructs*. In: *Phys. Chem. Chem. Phys.* **13**.25 (2011), pp. 11985–97.
- [220] K. C. Toh, E. A. Stojković, A. B. Rupenyan, I. H. M. van Stokkum, M. Salumbides, M. L. Groot, K. Moffat, and J. T. M. Kennis. *Primary reactions of bacteriophytochrome observed with ultrafast mid-infrared spectroscopy*. In: *J. Phys. Chem. A* **115**.16 (2011), pp. 3778–3786.
- [221] K. C. Toh, E. A. Stojković, I. H. M. van Stokkum, K. Moffat, and J. T. M. Kennis. *Proton-transfer and hydrogen-bond interactions determine fluorescence quantum yield and photochemical efficiency of bacteriophytochrome*. In: *Proc. Natl. Acad. Sci. U. S. A.* **107**.20 (2010), pp. 9170–5.
- [222] A. T. Ulijasz, G. Cornilescu, D. von Stetten, S. Kaminski, M.-A. Mroginiski, J. Zhang, D. Bhaya, P. Hildebrandt, and R. D. Vierstra. *Characterization of two thermostable cyanobacterial phytochromes reveals global movements in the chromophore-binding domain during photo-conversion*. In: *J. Biol. Chem.* **283**.30 (2008), pp. 21251–21256.
- [223] A. T. Ulijasz, G. Cornilescu, D. v. Stetten, C. Cornilescu, F. Velázquez Escobar, J. Zhang, R. J. Stankey, M. Rivera, P. Hildebrandt, and R. D. Vierstra. *Cyanochromes Are Blue / Green Light Photoreversible Photoreceptors Defined by a Stable Double Cysteine Linkage to a Phycoviolobilin-type Chromophore*. In: **284**.43 (2009), pp. 29757–29772.
- [224] A. T. Ulijasz, G. Cornilescu, C. C. Cornilescu, J. Zhang, M. Rivera, J. L. Markley, and R. D. Vierstra. *Structural basis for the photoconversion of a phytochrome to the activated Pfr form*. In: *Nature* **463**.7278 (2010), pp. 250–254.
- [225] J. J. van Thor, B. Borucki, W. Crielaard, H. Otto, T. Lamparter, J. Hughes, K. J. Hellingwerf, and M. P. Heyn. *Light-induced proton release and proton uptake reactions in the cyanobacterial phytochrome Cph1*. In: *Biochemistry* **40**.38 (2001), pp. 11460–11471.

- [226] J. J. van Thor, N. Fisher, and P. R. Rich. *Assignments of the Pfr - Pr FTIR difference spectrum of cyanobacterial phytochrome Cph1 using  $^{15}\text{N}$  and  $^{13}\text{C}$  isotopically labeled phyco-cyanobilin chromophore*. In: *J. Phys. Chem. B* **109**.43 (2005), pp. 20597–20604.
- [227] F. Velázquez Escobar, P. Piwowarski, J. Salewski, N. Michael, M. Fernández López, A. Rupp, B. Muhammad Qureshi, P. Scheerer, F. Bartl, N. Frankenberg-Dinkel, F. Siebert, M. Andrea Mroginski, and P. Hildebrandt. *A protonation-coupled feedback mechanism controls the signalling process in bathy phytochromes*. In: *Nat. Chem.* **7**.5 (2015), pp. 423–30.
- [228] F. Velázquez Escobar, D. Buhrke, N. Michael, L. Sauthof, S. Wilkening, N. N. Tavraz, J. Salewski, N. Frankenberg-Dinkel, M.-A. Mroginski, P. Scheerer, T. Friedrich, F. Siebert, and P. Hildebrandt. *Common Structural Elements in the Chromophore Binding Pocket of the Pfr State of Bathy Phytochromes*. In: *Photochem. Photobiol.* **93**.3 (2017), pp. 724–732. DOI: 10.1111/php.12742.
- [229] F. Velázquez Escobar, D. von Stetten, M. Günther-Lütken, A. Keidel, N. Michael, T. Lamparter, L.-O. Essen, J. Hughes, W. Gärtner, Y. Yang, K. Heyne, M. a. Mroginski, and P. Hildebrandt. *Conformational heterogeneity of the Pfr chromophore in plant and cyanobacterial phytochromes*. In: *Front. Mol. Biosci.* **2**.July (2015), p. 37.
- [230] F. Velázquez Escobar, T. Utesch, R. Narikawa, M. Ikeuchi, M.-A. Mroginski, W. Gärtner, and P. Hildebrandt. *Photoconversion mechanism of the second GAF domain of cyanobacteriochrome AnPixJ and the cofactor structure of its green-absorbing state*. In: *Biochemistry* **52**.29 (2013), pp. 4871–4880.
- [231] F. Velázquez Escobar, D. Buhrke, M. Fernández López, S. M. Shenkutie, S. von Horsten, L. O. Essen, J. Hughes, and P. Hildebrandt. *Structural communication between the chromophore-binding pocket and the N-terminal extension in plant phytochrome phyB*. In: *FEBS Letters* **Volume 591**.Issue 9 (2017), pp. 1258–1265. DOI: 10.1002/1873-3468.12642.
- [232] F. Velázquez Escobar, T. Hildebrandt, T. Utesch, F.-J. Schmitt, I. Seuffert, N. Michael, C. Schulz, M.-A. Mroginski, T. Friedrich, and P. Hildebrandt. *Structural parameters controlling the fluorescence properties of phytochromes*. In: *Biochemistry* **53**.1 (2014), pp. 20–29.
- [233] R. D. Vierstra and P. H. Quail. *Native phytochrome: Inhibition of proteolysis yields a homogeneous monomer of 124 kilodaltons from Avena*. In: *Proc. Natl. Acad. Sci. U. S. A.* **79**.17 (1982), pp. 5272–6.
- [234] R. D. Vierstra and P. H. Quail. *Photochemistry of 124 kilodalton Avena phytochrome in vitro*. In: *Plant Physiol.* **72**.1 (1983), pp. 264–267.
- [235] R. D. Vierstra and S. J. Davis. *Bacteriophytochromes: new tools for understanding phytochrome signal transduction*. In: *Semin. Cell Dev. Biol.* **11**.6 (2000), pp. 511–521.
- [236] D. von Stetten. *Investigation of the chromophore structure in plant and bacterial phytochromes by comparison of experimental and calculated Raman spectra*. PhD thesis. TU Berlin, 2008.
- [237] D. von Stetten, M. Günther, P. Scheerer, D. H. Murgida, M.-A. Mroginski, N. Krauß, T. Lamparter, J. Zhang, D. M. Anstrom, R. D. Vierstra, K. T. Forest, and P. Hildebrandt. *Chromophore heterogeneity and photoconversion in phytochrome crystals and solution studied by resonance Raman spectroscopy*. In: *Angew. Chemie - Int. Ed.* **47**.25 (2008), pp. 4753–4755.
- [238] D. von Stetten, S. Seibeck, N. Michael, P. Scheerer, M.-A. Mroginski, D. H. Murgida, N. Krauss, M. P. Heyn, P. Hildebrandt, B. Borucki, and T. Lamparter. *Highly conserved residues Asp-197 and His-250 in Agp1 phytochrome control the proton affinity of the chromophore and Pfr formation*. In: *J. Biol. Chem.* **282**.3 (2007), pp. 2116–2123.
- [239] J. R. Wagner, J. S. Brunzelle, K. T. Forest, and R. D. Vierstra. *A light-sensing knot revealed by the structure of the chromophore-binding domain of phytochrome*. In: *Nature* **438**.7066 (2005), pp. 325–331.
- [240] J. R. Wagner, J. Zhang, J. S. Brunzelle, R. D. Vierstra, and K. T. Forest. *High resolution structure of Deinococcus bacteriophytochrome yields new insights into phytochrome architecture and evolution*. In: *J. Biol. Chem.* **282**.16 (2007), pp. 12298–12309.

- [241] J. R. Wagner, J. Zhang, D. von Stetten, M. Günther, D. H. Murgida, M.-A. Mroginski, J. M. Walker, K. T. Forest, P. Hildebrandt, and R. D. Vierstra. *Mutational analysis of Deinococcus radiodurans bacteriophytochrome reveals key amino acids necessary for the photochromicity and proton exchange cycle of phytochromes*. In: *J. Biol. Chem.* **283**.18 (2008), pp. 12212–12226.
- [242] S. H. Wu and J. C. Lagarias. *Defining the bilin lyase domain: Lessons from the extended phytochrome superfamily*. In: *Biochemistry* **39**.44 (2000), pp. 13487–13495.
- [243] X. L. Xu, A. Gutt, J. Mechelke, S. Raffelberg, K. Tang, D. Miao, L. Valle, C. D. Borsarelli, K. H. Zhao, and W. Gärtner. *Combined mutagenesis and kinetics characterization of the bilin-binding GAF domain of the protein Slr1393 from the cyanobacterium synechocystis PCC6803*. In: *ChemBioChem* **15**.8 (2014), pp. 1190–1199.
- [244] X. Yang, J. Kuk, and K. Moffat. *Crystal structure of Pseudomonas aeruginosa bacteriophytochrome: photoconversion and signal transduction*. In: *Proc. Natl. Acad. Sci. U. S. A.* **105**.38 (2008), pp. 14715–20.
- [245] X. Yang, E. A. Stojković, J. Kuk, and K. Moffat. *Crystal structure of the chromophore binding domain of an unusual bacteriophytochrome, RpBphP3, reveals residues that modulate photoconversion*. In: *Proc. Natl. Acad. Sci. U. S. A.* **104**.30 (2007), pp. 12571–12576.
- [246] X. Yang, E. A. Stojković, W. B. Ozarowski, J. Kuk, E. Davydova, and K. Moffat. *Light Signaling Mechanism of Two Tandem Bacteriophytochromes*. In: *Structure* **23**.7 (2015), pp. 1179–1189.
- [247] X. Yang, Z. Ren, J. Kuk, and K. Moffat. *Temperature-scan cryocrystallography reveals reaction intermediates in bacteriophytochrome*. In: *Nature* **479**.7373 (2011), pp. 428–32.
- [248] Y. Yang, K. Heyne, R. A. Mathies, and J. Dasgupta. *Non-Bonded Interactions Drive the Sub-Picosecond Bilin Photoisomerization in the Pfr State of Phytochrome Cph1*. In: *ChemPhysChem* **17**.3 (2016), pp. 369–374.
- [249] Y. Yang, M. Linke, T. von Haimberger, J. Hahn, R. Matute, L. González, P. Schmieder, and K. Heyne. *Real-time tracking of phytochrome’s orientational changes during Pr photoisomerization*. In: *J. Am. Chem. Soc.* **134**.3 (2012), pp. 1408–1411.
- [250] K. Yeh, S.-H. Wu, J. T. Murphy, and J. C. Lagarias. *A Cyanobacterial Phytochrome Two-Component Light Sensory System*. In: *Science (80-. )*. **277**.5331 (1997), pp. 1505–1508.
- [251] D. Yu, W. C. Gustafson, C. Han, C. Lafaye, M. Noirclerc-Savoye, W.-P. Ge, D. A. Thayer, H. Huang, T. B. Kornberg, A. Royant, L. Y. Jan, Y. N. Jan, W. A. Weiss, and X. Shu. *An improved monomeric infrared fluorescent protein for neuronal and tumour brain imaging*. In: *Nat. Commun.* **5**.May (2014), pp. 1–7.
- [252] D. Yu, Z. Dong, W. C. Gustafson, R. Ruiz-González, L. Signor, F. Marzocca, F. Borel, M. P. Klassen, K. Makhijani, A. Royant, Y. N. Jan, W. A. Weiss, S. Guo, and X. Shu. *Rational design of a monomeric and photostable far-red fluorescent protein for fluorescence imaging in vivo*. In: *Protein Sci.* **25** (2016), pp. 308–315.
- [253] A. H. Zewail. *Femtochemistry: Atomic-Scale Dynamics of the Chemical Bond*. In: *J. Phys. Chem. A* **104**.24 (2000), pp. 5660–5694.
- [254] J. Zhang, R. J. Stankey, and R. D. Vierstra. *Structure-Guided Engineering of Plant Phytochrome B with Altered Photochemistry and Light Signaling*. In: *Plant Physiol.* **161**.3 (2013), pp. 1445–1457.
- [255] J. Zhu, D. M. Shcherbakova, Y. Hontani, V. V. Verkhusha, and J. T. M. Kennis. *Ultrafast excited-state dynamics and fluorescence deactivation of near-infrared fluorescent proteins engineered from bacteriophytochromes*. In: *Sci. Rep.* **5**.August (2015), p. 12840.
- [256] B. Zienicke, I. Molina, R. Glenz, P. Singer, D. Ehmer, F. Velázquez Escobar, P. Hildebrandt, R. Diller, and T. Lamparter. *Unusual spectral properties of bacteriophytochrome Agp2 result from a deprotonation of the chromophore in the red-absorbing form Pr*. In: *J. Biol. Chem.* **288**.44 (2013), pp. 31738–31751.